Modelling, Characterisation and Design Optimisation of an Ironless Inductive Position Sensor

Adrian Grima

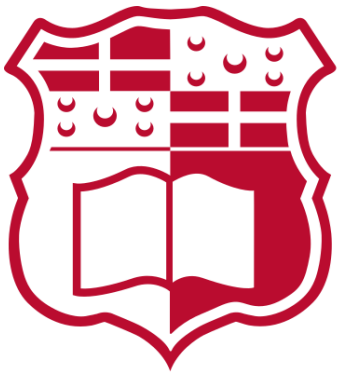

University of Malta

Under the supervision of Dr. Ing. Nicholas Sammut

Department of Microelectronics and Nanoelectronics
Faculty of Information and Communication Technology

January 2019

A dissertation submitted to the University of Malta for the degree of Doctor of Philosophy

The research leading to the results of this thesis has been supported by the European Organization for Nuclear Research (CERN) and the University of Malta.

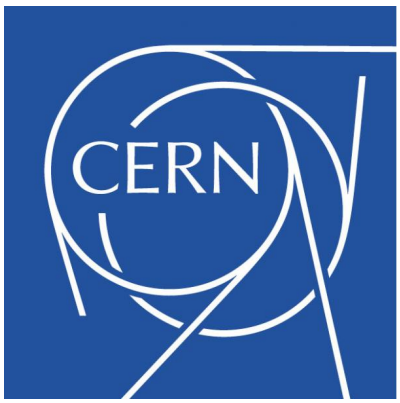

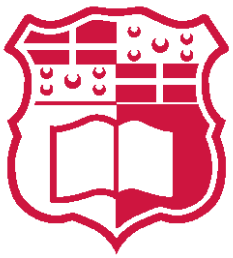

L-Università ta' Malta

L-Università ta' Malta

FACULTY/~~INSTITUTE/CENTRE/SCHOOL~~ of Information and Communication Technology

DECLARATION OF AUTHENTICITY FOR DOCTORAL STUDENTS

Student's I.D. /Code 31592 (G)

Student's Name & Surname Adrian Grima

Course Doctor of Philosopy

Title of Dissertation/Thesis
Modelling, Characterisation, and Design Optimisation of an Ironless Inductive Position Sensor

(a) Authenticity of Thesis/Dissertation

I hereby declare that I am the legitimate author of this Thesis/Dissertation and that it is my original work.

No portion of this work has been submitted in support of an application for another degree or qualification of this or any other university or institution of higher education.

I hold the University of Malta harmless against any third party claims with regard to copyright violation, breach of confidentiality, defamation and any other third party right infringement.

(b) Research Code of Practice and Ethics Review Procedure

I declare that I have abided by the University's Research Ethics Review Procedures.

□ As a Ph.D. student, as per Regulation 49 of the Doctor of Philosophy Regulations, I accept that my thesis be made publicly available on the University of Malta Institutional Repository.

□ As a Doctor of Sacred Theology student, as per Regulation 17 of the Doctor of Sacred Theology Regulations, I accept that my thesis be made publicly available on the University of Malta Institutional Repository.

□ As a Doctor of Music student, as per Regulation 24 of the Doctor of Music Regulations, I accept that my dissertation be made publicly available on the University of Malta Institutional Repository.

□ As a Professional Doctorate student, as per Regulation 54 of the Professional Doctorate Regulations, I accept that my dissertation be made publicly available on the University of Malta Institutional Repository.

Adrian Grima .
Signature of Student

ADRIAN GRIMA
Name of Student (in Caps)

20/1/2019
Date

"Success is walking from failure to failure with no loss of enthusiasm."

Winston Churchill

Abstract

Safety critical systems such as particle accelerators and nuclear plants strongly depend on the sensors that control the system. The Large Hadron Collider (LHC) found at the European Organisation for Nuclear Research (CERN) depends on a collimation system to control the beam. The jaw position with respect to the beam of particles is measured with linear position sensors. The traditional transducer used for this task is the Linear Variable Differential Transformer (LVDT) while a newer transducer called the Ironless Inductive Position Sensor (I2PS) is taking up the LVDT's place, in areas characterised with magnetic interference.

An electrical metrological characterisation of the transducer, with long cables, is first presented. The frequency response of the sensor is conducted to assess the I2PS sensitivity at different frequencies with different cable lengths. Moreover, a set of experimental results are performed to assess the I2PS's sensitivity to cable capacitance change. Comparison with a commercial off-the-shelf LVDT is presented, knowing that this was required to gain a better understanding. A novel SPICE simulation that models the I2PS sensor and its electronics is consequently developed. Furthermore, a countermeasure circuit is presented to eliminate the effects of cable capacitance. A detailed thermal analysis is then presented which characterises the impact of ambient temperature change on the sensor. This study itself becomes an important step in developing changes and defining guidelines, which optimise the stability of the I2PS. A number of modifications to the sensor are proposed to reduce the drift, making the sensor more robust. Nevertheless, not all solutions lead to sensor immunisation, given the unavoidable design of the transducer. Furthermore, a detailed study of operating multiple I2PS in close proximity at the same frequency is presented. Finally, this work also identifies the optimisation parameters and constants required when manually designing an I2PS. Consequently, it presents an automated design procedure, which when powered by a multi-objective optimisation algorithm, it automatically produces an I2PS, tailor-made to the user's specifications, very quickly by a user with minimal training.

The research provided in this thesis presents a more thorough characterisation of the thermal and electrical behaviour of the transducer. This is accomplished by taking into consideration typical and infrequent circumstances of the operation of the LHC collimator system.

Acknowledgements

The study is the result of three years of research which have been both a constant challenge and, at the same time, a very rewarding experience.

I would like to convey my thanks to my supervisor Nicholas Sammut at the University of Malta who closely followed my progress. He has had to cope with me from the first days of this journey, always examining my work with a critical eye. I would like to thank Alessandro Masi at the European Organisation for Nuclear Research (CERN) for his expert advice and support throughout this difficult project. I would also like to show my gratitude towards Mario Di Castro, for his honest and precious support. I greatly appreciate his counsel and expertise. Furthermore, I have to convey my thanks to the staff working at CERN.

Among the many young people I have met during these three years, I would like to thank the guys from my section with whom I not only had the pleasure to work with but also share countless and well needed breaks from the work. I am sure that if I name everyone I will end up forgetting someone, so a big thanks to all. Also thank you goes to the other colleagues at CERN who never made me feel alone and shared great and funny experiences.

Ultimately, a special thanks to Gabriele Piscopo. You had to cope with me everyday at the office. Moreover, I cannot forget a great friend who has embarked on the same path, at the same time and who has been with me from the very beginning of engineering, even though the last four years have been from far away. For this reason a special thanks goes to Nathalie Cauchi for her support and long discussions.

I have to admit, the combination of challenging research and working far from home brought many grim days. However, in all the good and the bad moments, I could always count on the support of my family. My sincere gratitude goes to them for their unconditional love and for teaching me that anything is possible with faith, hard work and determination.

This thesis is in fact dedicated to my parents and my brother to whom I wish to convey the greatest gratitude for always being there even though from far away.

Journal Publications

Part of this dissertation have been published:

1. **Adrian Grima**, Mario Di Castro, Alessandro Masi, and Nicholas Sammut, "Electrical Metrological Characterization of Ironless Inductive Position Sensors with Long Cables", *IEEE Sensors Journal*, vol. 18, no. 17, pp. 7114 - 7121, 2018.

2. **Adrian Grima**, Mario Di Castro, Alessandro Masi, and Nicholas Sammut, "A Novel Holistic Design Optimisation Algorithm for the Ironless Inductive Position Sensor", *International Journal of Computer and Electrical Engineering*,vol. 10, no. 2, pp. 116-126, 2018.

3. **Adrian Grima**, M. Di Castro, A. Masi, and N. Sammut, "Frequency Response Characterization of Ironless Inductive Position Sensors with Long Cables", *MATEC Web of Conferences.* vol. 208, pp. 3007, EDP Sciences Journal, 2018

4. **Adrian Grima**, Mario Di Castro, and Nicholas Sammut, "Experimental Thermal Characterisation of an Ironless Inductive Position Sensor", *Case Studies in Thermal Engineering.* Elsevier, vol. 13, pp. 100411, 2018

5. **Adrian Grima**, Mario Di Castro, Alessandro Masi, and Nicholas Sammut, "Design Enhancements of an Ironless Inductive Position Sensor", *IEEE Transactions on Instrumentation and Measurement* vol.69, pp. 2505

6. **Adrian Grima**, Mario Di Castro, Alessandro Masi, and Nicholas Sammut, "Thermal Study of the Ironless inductive Position Sensor Installed on the LHC collimators", *IEEE Transactions in Nuclear Science*, vol. 66, no. 4, pp. 688-695.

Awards

The paper "A Novel Holistic Design Optimisation Algorithm for the Ironless Inductive Position Sensor" received the **best presentation award** when presented at the *2018 2nd International Conference On Computer, Software and Modelling, in Nice, France*

Contents

Abstract iv

Acknowledgements v

List of Publications vi

Contents x

List of Figures xvii

List of Tables xviii

List of Acronyms xxi

Dedicatory xxii

1 Introduction 1

1.1 The European Organisation for Nuclear Research 1

1.1.1 The Large Hadron Collider 2

1.2 Project description and objectives 10

1.3 Thesis Structure 12

2 The LHC Collimation System and its Position Sensors 15

2.1 Introduction 15

2.1.1 General layout and design 16

2.1.2 Low Level Control System 19

2.2 The Linear Variable Differential Transformer 21

2.3 Review of position sensing techniques 26

2.4 The Ironless Inductive Position Sensor 30

2.4.1 Design 30

2.4.2 Working principle 31

2.4.3 The electromagnetic and electrical model 33

2.5 Summary 37

3 Electrical Characterisation of the I2PS with Cable 38

3.1 Introduction 38

3.1.1 Transfer function with cable 39

3.1.2 Supply Coils Transfer Function 40

3.1.3 Sense coil Transfer Function 42
3.1.4 Result Verification 44
3.2 I2PS Characterisation at Different Frequencies 46
3.2.1 Characteristic Curve at different Frequencies 46
3.2.2 Frequency analysis 48
3.3 Simulation 51
3.3.1 Simulation Results 54
3.4 Sensitivity to Change in Cable Parasitic Capacitance 57
3.4.1 Test-bench Results 59
3.5 Capacitance Sensitivity Correction 64
3.5.1 Countermeasure design and simulation results 64
3.5.2 Test-bench Results 69
3.6 Summary 71

4 Thermal and Compensation Algorithm Characterisation 73
4.1 Introduction 73
4.1.1 Problem Definition 74
4.2 Test-bench Setup 76
4.3 Acquired Voltage Drift due to Temperature Change 77
4.3.1 The Sense Voltages 77
4.3.2 The Supply dc Voltage 79
4.3.3 The Supply ac Voltage 81
4.3.4 The Supply Coils 82
4.3.5 The Sense Coils 83
4.3.6 The Moving Coil 84
4.3.7 Manual Change of Parameters 89
4.4 Position Change due to Temperature Change 91
4.4.1 State-of-the-art of the Compensation Algorithm 93
4.4.2 Thermal Characterisation and Review 94
4.5 Summary 106

5 Design Modifications 109
5.1 Introduction 109
5.2 Behaviour of Ironless Inductive Position Sensor (I2PS) in Close Proximity to Each Other 110
5.2.1 Sensor's Finite Element Model 110
5.2.2 Numerical Simulation Results 113
5.2.3 Test-bench Results 117
5.3 Design Modifications of the I2PS 120
5.3.1 Substituting the Moving Coil Copper Winding with Brass . 121

5.3.2 Substituting the Moving Coil with a Solid Brass Core 125
5.3.3 Resining the Moving Coil 128
5.4 Tests on the collimator test system 129
5.4.1 Testing same frequency operation 129
5.4.2 Thermal analysis in collimator environment 130
5.5 Summary 140

6 Design engine development 141
6.1 Optimisation Algorithms 143
6.1.1 Single-Objective Optimisation 144
6.1.2 Multi-Objective optimisation 146
6.1.3 The Genetic Algorithm 148
6.2 I2PS variables and dependencies 152
6.2.1 Constants 152
6.2.2 Variables to be optimised / calculated 152
6.3 Algorithm and Methods Implemented 155
6.4 Summary 163

7 Conclusions and Outlook 164
7.1 Achieved results 164
7.1.1 Analysis 165
7.1.2 Summary of scientific contributions 170
7.2 Future Work 171

References 185

List of Figures

1.1 The Standard Model of Particle Physics, describing the elementary subatomic particles of the universe, which have been observed experimentally. Top rim: Quarks. Bottom rim: Leptons. Inner circle: Gauge Bosons. Central circle: Scalar Boson. 2

1.2 CERN Accelerator Complex. Legend: *p (protons) RIBS (Radioactive Ion Beams)* $\bar{p}$ *(antiprotons)* e^-*(electrons) Large Hadron Collider (LHC) (Large Hadron Collider) SPS (Super Proton Synchrotron) PS (Proton Synchrotron) AD (Antiproton Decelerator) CTF3 (Clic Test Facility) AWAKE (Advanced WAKefieId Experiment) ISOLDE (Isotope Separator OnLine) REX/HIE (Radioactive EXperiment/High Intensity and Energy ISOLDE) LEIR (Low Energy Ion Ring) LINAC (LINear ACcelerator) n-ToF (Neutrons Time Of Flight) HiRadMat(High-Radiation to Materials) CHARM (Cern High energy AcceleRator Mixed field facility) IRRAD (proton IRRADiation facility) GIF++ *(Gamma Irradiation Facility) CENF (CErn Neutrino platForm)* 3

1.3 A basic schematic layout of the LHC. It shows the position of the four main experiments and the experimental insertions. Furthermore, it shows the radio frequency cavities and utility insertions which are found in octants not occupied by the experiments. 4

1.4 LHC operational cycle with the magnet strengths and beam energy. 5

1.5 A particle beam modelled as a 2D double Gaussian distribution. Showing a scenario, where the core makes up 95% of the beam, and the tail 5%. The top plot show the histogram of the distribution, and the probability density function divided into core (blue) and tail (red). 6

1.6 (a) Beam loss monitor at LHC. (b) Photograph of the inside of an ionization chamber. 7

1.7 Layout of the LHC, showing the collimator locations around the ring 8

1.8 Photograph of a collimator in the LHC tunnel 9

2.1 Collimator mechanical assembly (cross-section of a horizontal TCSG). 16

2.2 Front view of the 3D drawing of a collimator 17

2.3 The layout of the collimators control system. 19

2.4 Structure and working principle of an Linear Variable Differential Transformer . . . 21
2.5 A photo of a Linear Variable Differential Transformer (LVDT) . . . 22
2.6 Typical cross section of an LHC tunnel . . . 24
2.7 Correlation between the current signal and the position read by an LVDT . . . 25
2.8 I2PS Diagram. A quarter of the I2PS design is presented since the sensor is symmetrical in the x and y domain . . . 31
2.9 A photo of the I2PS pre-assembly . . . 32
2.10 Longitudinal cross-section of the ironless inductive position sensor structure. The sensor is symmetric about the y-axis. Coils 1 & 2 are the supply coils. (Note that they are wound opposite to each other.) Coils 3 & 4 are the sense coils. Coil 5 is the moving coil. . . . 33

3.1 Cable model with I2PS supply coil as load . . . 41
3.2 Cable model with I2PS sense coil as supply and acquisition bias resistor as load . . . 42
3.3 I2PS characteristic curve . . . 47
3.4 I2PS ratiometric index . . . 47
3.5 Comparison between the effect of the cable on the frequency response of the I2PS and the LVDT, as obtained from test bench . . . 49
3.6 Varying the moving coil position with a 200 m cable . . . 50
3.7 Varying the moving coil position with a 1 km cable . . . 50
3.8 Block diagram of the simulation circuit . . . 54
3.9 Comparison of the I2PS sense voltages at different positions from the test-bench with the simulation. Obtained at 50 mA at 1 kHz. 55
3.10 Effect of cable on the frequency response with different cable lengths with comparison to simulation . . . 56
3.11 Existent capacitances between cables in a multi-shielded-twisted pair cable . . . 58
3.12 I2PS position change due to a change in cable capacitance, as obtained from the test bench. . . . 60
3.13 All mutual and cable-to-shield capacitances . . . 61
3.14 LVDT position change due to an increase in the mutual and cable-shield capacitance, as obtained from the test bench. . . . 62
3.15 Comparison between some of the test-bench and simulation results for the mutual capacitance change . . . 63

3.16 The countermeasure circuit simulated and added at the end of the long cable. Circuit (b) is the equivalent circuit of the highlighted circuit. 65
3.17 Comparison between the simulated I2PS position change due to a change in cable capacitance with and without the countermeasure . 68
3.18 I2PS position change due to a change in cable capacitance with the countermeasure, as obtained from the test bench. 70
3.19 Comparison between the I2PS position change due to a change in cable capacitance with and without the countermeasure, as obtained from the test bench. 71

4.1 Comparison between the position measured by the I2PS in a collimator and the I2PS dc voltage from 2018 run. The sensor position is the position of the jaw as measured by the I2PS while the reference position is the position as measured by the resolver in the collimator setup. V_{dc} is the measured primary voltage of the I2PS which represents the temperature of the sensor. As explained in Chapter 1. 74
4.2 Comparison between the position measured by the I2PS in a collimator and the I2PS dc voltage from 2017 run. The sensor position is the position of the jaw as measured by the I2PS while the reference position is the position as measured by the resolver. As explained in Chapter 1. Therefore the calculated difference presented is between the as read resolver position and the I2PS. 75
4.3 Sense coils voltage 78
4.4 V_{dc} for different sensor and cable conditions at $I_{dc} = 10\ mA$ 80
4.5 V_{dc} at different I_{dc} for the same moving coil position 80
4.6 V_{ac} at different I_{dc} and I_{ac} 81
4.7 V_{ac} at different moving coil positions 81
4.8 Supply Coil 82
4.9 Supply coil inductance at 1 kHz and at 2 kHz with respect to temperature 83
4.10 Sense Coil 84
4.11 Sense coil inductance at 1 kHz and at 2 kHz with respect to temperature 84
4.12 Moving Coil 85
4.13 Moving coil inductance at 1 kHz and at 2 kHz with respect to temperature 85
4.14 Comparison between theoretical resistance change and experimental resistance change 86

4.15 Manual change in Supply coils 90
4.16 Manual change in Sense coils 90
4.17 Manual Resistance change in Moving coil at different frequencies and position 91
4.18 Position change for different moving coil positions at 1 kHz 92
4.19 Position change for different moving coil positions at 2 kHz 93
4.20 Comparing the position change due to change in temperature at different moving coil positions and operating frequencies 93
4.21 Comparing compensated position readout with $\zeta = 0.3$ to that of the uncompensated position readout at $I_{dc} = 10\ mA$ 94
4.22 Comparing the maximum change of sense 1 and sense 2 with the change in V_{dc} 95
4.23 Comparing the maximum change of the ratiometric index with the change in V_{dc} 95
4.24 V_{dc} with different input currents 96
4.25 Variable compensation algorithm 97
4.26 Temperature and ζ readings during the long temperature profile . . 97
4.27 Position change for a long temperature profile at 1 kHz with high I_{dc}. The uncompensated position is compared to the normal compensation settings and to the cubic and linear adaptation. . . . 98
4.28 Different ζ requirements for different moving coil positions at 1 kHz with same cable length 200 m and supply $I_{ac} = 20\ mA$ $I_{dc} = 40\ mA$ 99
4.29 Position readout change and ζ required when the operating frequency is set at 2 kHz with same cable length 200 m and supply $I_{ac} = 20\ mA$ $I_{dc} = 40\ mA$ 100
4.30 Position readout change and ζ required when the operating frequency is set at 1250 Hz with same cable length 200 m and but different dc supply 101
4.31 Position readout change and ζ required when the operating frequency is set at 1250 Hz with same cable length 200 m and but different dc supply 102
4.32 Position readout change and ζ required when the operating frequency is set at 1.5 kHz with same cable length 200 m and supply $I_{ac} = 40\ mA$ $I_{dc} = 10\ mA$ 103
4.33 Position readout change and ζ required when the operating frequency is set at 1.5 kHz with same cable length 200 m and supply $I_{ac} = 18\ mA$ $I_{dc} = 40$ mA 104

4.34 Position readout change and ζ required when the operating frequency is set at 1750 Hz with same cable length 200 m and but different dc supply 105
4.35 Position readout change and ζ required when the operating frequency is set at 1750 Hz with same cable length 200 m and but different dc supply 106

5.1 A diagram showing the positioning of the I2PS with respect to each other. 111
5.2 FEM meshing scenario highlighting a crossection of the coils and the paths, as in the 3D scenario, used for the graphs. 112
5.3 A detailed representation magnetic field escaping the sensor at the peak of the supply. 113
5.4 Magnetic field at increasing distances from the sensor at the peak of the supply voltage 114
5.5 Presents a more detailed representation magnetic field escaping the sensor. 115
5.6 A detailed representation magnetic field escaping the sensor at the zero crossing of the supply. 115
5.7 The magnetic field at peak amplitude outside when the sensors are adjacent to each other 116
5.8 Magnetic field around the transducers when the I2PS are on top of each other 117
5.9 Picture showing the parallel I2PS used for the experiment. $I2PS_{S1}$ is moved to the origin of the drawn ruler and $I2PS_{S2}$ is moved away from the former. The moving coils shown outside the sensor are placed inside. 118
5.10 The sense coils' voltage with interference when $\Delta x = 1\ cm$. Note that for the first two seconds the second I2PS is un-powered and hence there is no interference. 118
5.11 Interference magnitude on the position reading at different Δx . . . 119
5.12 Comparison of the position reading with interference at different distances between the two I2PS 119
5.13 Comparison of the normal moving coil (Coil 1), the new coil made out of brass cable (Coil 2), a normal moving coil which is encased in resined (Coil 3) and a brass core (4). 120
5.14 A comparison between the simulated characteristic curve of a copper wound moving coil and a simulated brass wound moving coil. 122

5.15 Characteristic curves and ratiometric of the 3 new brass wound moving coils. MC 1 and 2 are composed of 18 winding layers of 0.457 mm brass magnet wire adding to a total of 1852 turns and MC 3 is composed of 18 layers but with a total of 1950 turns. . . . 123
5.16 Thermal test comparison between the copper and the brass wound moving coils. 124
5.17 Characteristic curves of the solid cores, as obtained from the FEM simulation 126
5.18 Characterisation of a solid brass core at different frequencies 127
5.19 Comparison of the normal moving coil with a solid brass core. The same sense and supply coils are used for the test. 127
5.20 Thermal test with the solid brass core 128
5.21 Thermal test with a resined moving coil 129
5.22 A diagram of the collimator setup accommodating three of six I2PS installed for testing. Two such blocks are required. One for the upstream and another for the downstream. [1] 130
5.23 Position reading of the I2PS installed on test collimator 130
5.24 A test where the room temperature was varied very slowly with the sensors at outer position. 131
5.25 A test where the room temperature was varied very slowly with the sensors at outer position. 132
5.26 Thermal image of the Left Upstream sensor after jaw movement. . 133
5.27 Thermal image of the Gap Downstream sensor after jaw movement. 133
5.28 A test where the room temperature was varied very slowly with the sensors at outer position. 134
5.29 The read I2PS position from collimator during technical stop with respect to the read resolver position taken as the reference. 135
5.30 Position drift after short movement during operation 136
5.31 Photo of the plastic encased I2PS as installed on test setup with a plastic 3-Dimensional (3D) printed flange. 137
5.32 Thermal images of modified I2PS 138
5.33 Comparison of the position change of the I2PS with and without modification with respect to temperature 138
5.34 Difference between I2PS position and reference with respect to temperature. Comparison between RD which is a standard I2PS and LU which is a modified one. 139
5.35 Temperature and dc voltage variation with time for stability test. . 140

6.1 The taxonomy of global optimisation algorithms. 144

6.2 Convexity test per variable 156
6.3 The optimisation algorithm 158
6.4 3D plot representing the fitness of each chromosome for each generation 160
6.5 Example of a graph showing the normalised fitness of all values to be considered in optimisation and the final fitness value 161
6.6 Comparison between the characteristic curves of the manual design and the result from the tool. 162
6.7 Comparison between the ratiometric index curves of the manual design and the result from the tool. 163

List of Tables

2.1 Summary of existing position sensing techniques and their respective drawbacks from an LHC implementation point of view. 29
2.2 Progression of I2PS development 30

3.1 Table comparing the sense coil voltages obtained from the experimental test-bench with different cable lengths with respect to those obtained from the model and from the simulation. All the values are obtained with a current supply of 50 mA at 1 kHz at a sampling rate of 250kS/s while using sine fit for signal demodulation as presented in [53, 56] 45
3.2 I2PS settings for 5 V at electrical zero and the respective sensitivity and Non Linearity Error (NLE) 46
3.3 Electrical properties of an I2PS and cable parameters as measured by LCR meter with 0.01% accuracy 53
3.4 Comparison of the sense coil voltages obtained from the experimental test-bench with respect to those obtained from the simulation. The table also provides the percentage difference between simulation and experiment. 55
3.5 Comparison of the average sensitivity for the I2PS and LVDT as obtained from the test-bench 59
3.6 Measured audio transformer values 69

5.1 Physical characteristics of the sensor 112
5.2 Table of materials and their respective temperature coefficient and resistivity. 121
5.3 Sensor design with brass winding 122

6.1 List of constraints 154
6.2 Example of a combination, with input/output values and fitness . . 161

List of Acronyms

2D	2-Dimensional
3D	3-Dimensional
A/D	Analogue to Digital
AD	Antiproton Decelerator
ac	Semi-length of the Moving Coil
ap/as	Semi-length of the Supply and Sense Coil
ALICE	A Large Ion Collider Experiment
ATLAS	A Toroidal LHC Apparatus
AWAKE	Advanced WAKefieId Experiment
BLMs	Beam Loss Monitors
C/C	carbon-carbon composite
CCA	Central Control Application
CENF	CErn Neutrino platForm
CERN	Conseil Européen pour la Recherche Nucléaire
CHARM	Cern High energy AcceleRator Mixed field facility
CMS	Compact Muon Solenoid
CSS	Collimator Supervisory System
CTF3	Clic Test Facility
DAQ	Data Acquisition Board
EA	Evolutionary Algorithms
ESS	Environmental Survey System
FEM	Finite Element Model
FESA	Front End Software Architecture

GA	Genetic Algorithm
GD	Gap Downstream
GU	Gap Upstream
GIF++ *	Gamma Irradiation Facility
GUI	Graphical User Interface
HiRadMat	High-Radiation to Materials
HL-LHC	High-Luminosity Large Hadron Collider
I2PS	Ironless Inductive Position Sensor
IRRAD	proton IRRADiation facility
IRs	interaction regions
IRs	Insertion Region
ISOLDE	Isotope Separator OnLine
LEIR	Low Energy Ion Ring
LEP	Large Electron-Proton Collider
LD	Left Downstream
LU	Left Upstream
LHC	Large Hadron Collider
LHCb	Large Hadron Collider beauty
LHCf	Large Hadron Collider forward
LINAC	LINear ACcelerator
LVDT	Linear Variable Differential Transformer
MDC	Motor Drive Control
MoEDAL	Monopole and Exotics Detector at the LHC
n-ToF	Neutrons Time Of Flight
NLP	Number of Layers of the Supply Coil

NLS	Number of Layers of the Sense Coil
NLC	Number of Layers of the Moving Coil
NLE	Non Linearity Error
NI	National Instruments
OFC	Oxygen-Free Copper
PRS	Position Readout and Survey
PS	Proton Synchrotron
PSO	Particle Swarm Optimisation
PSB	Proton Synchrotron Booster
REX/HIE	Radioactive EXperiment/High Intensity and Energy ISOLDE
RF	Radio Frequency
RIBS	Radioactive Ion Beams
RD	Right Downstream
RU	Right Upstream
SC	superconducting
SM	Standard Model
SPS	Super Proton Synchrotron
SPICE	Simulation Program with Integrated Circuit Emphasis
TOTEM	Total, elastic and diffractive cross-section measurement
UHV	Ultra-High Vacuum
VNA	Vector Network Analyser
wire dP	Supply Coil Wire Diameter
wire dS	Sense Coil Wire Diameter
wire dC	Moving Coil Wire Diameter

To Mum, Dad & Nicholas
... for always being there

Chapter 1

Introduction

1.1 The European Organisation for Nuclear Research

High-energy physics involves the study of the elementary constituents of the universe and the forces by which they interact [2, 3]. The two main goals of particle physics are to discover all the rudimentary particles and to unify the fundamental forces. Indeed, this collective understanding is referred to as the Standard Model (SM) of particle physics [2] (Figure 1.1). High-energy machines particle accelerators are used to study these subatomic particles by accelerating beams of common, stable particles (protons or electrons and their anti-particles) that make up ordinary matter, to very high energies.

The European Organisation for Nuclear Research, also known as CERN [4], is one of Europe's first joint ventures. It is aimed at scrutinising the fundamental structure of the universe where it studies the basic components of matter.

CERN's particle accelerator is more than just one machine that accelerates the particles. In fact, it is better referred to as a particle accelerator complex [6] (Figure 1.2), where a sequence of machines accelerate particles to progressively higher energies. This is done through an elaborate arrangement of beam lines. It all

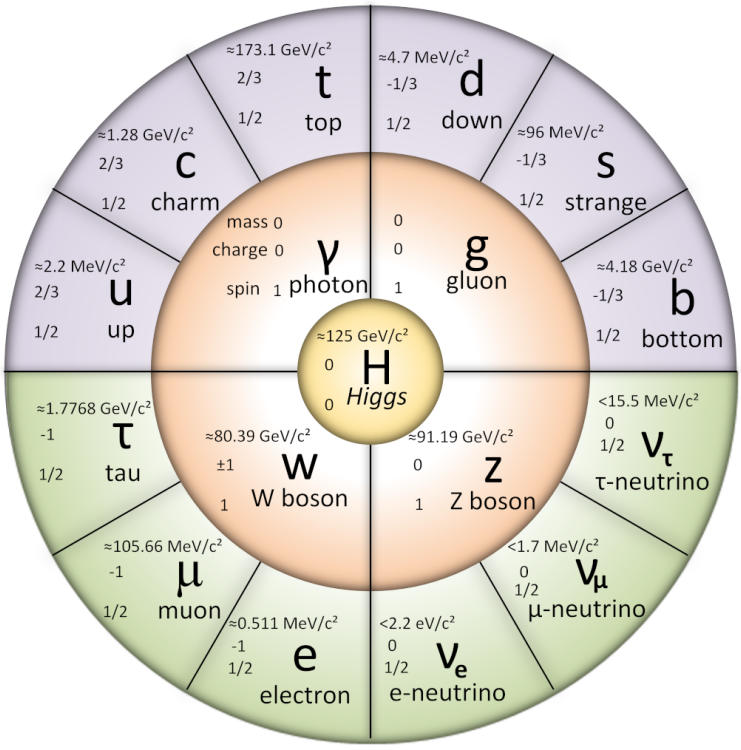

Figure 1.1: The Standard Model of Particle Physics, describing the elementary subatomic particles of the universe, which have been observed experimentally. Top rim: Quarks. Bottom rim: Leptons. Inner circle: Gauge Bosons. Central circle: Scalar Boson. (Adapted from [5])

starts from the proton source, which is a simple tank of hydrogen gas. The electrons are stripped from the hydrogen atoms with an electric field yielding protons. The first accelerator, Linac 2, accelerates the protons to the energy of 50 MeV. Once this energy is achieved, the beam is then injected into the Proton Synchrotron Booster (PSB), which in turn accelerates the protons to 1.4 GeV. This is followed by the Proton Synchrotron (PS), which accelerates the beam to 25 GeV. The accelerated protons are then sent to the Super Proton Synchrotron (SPS) where they are accelerated to 450 GeV. Then they are finally transferred to the two beam pipes of the LHC to reach their maximum energy of 6.5 TeV. Finally, the two beams collide inside the detectors where the total energy at the collision point is equal to 13 TeV.

1.1.1 The Large Hadron Collider

Both the previous particle-antiparticle colliders, such as Large Electron-Proton Collider (LEP) [7, 8] and also the Tevatron shared the same phase space in a single ring. CERN's flagship project, the Large Hadron Collider is a two-ring-

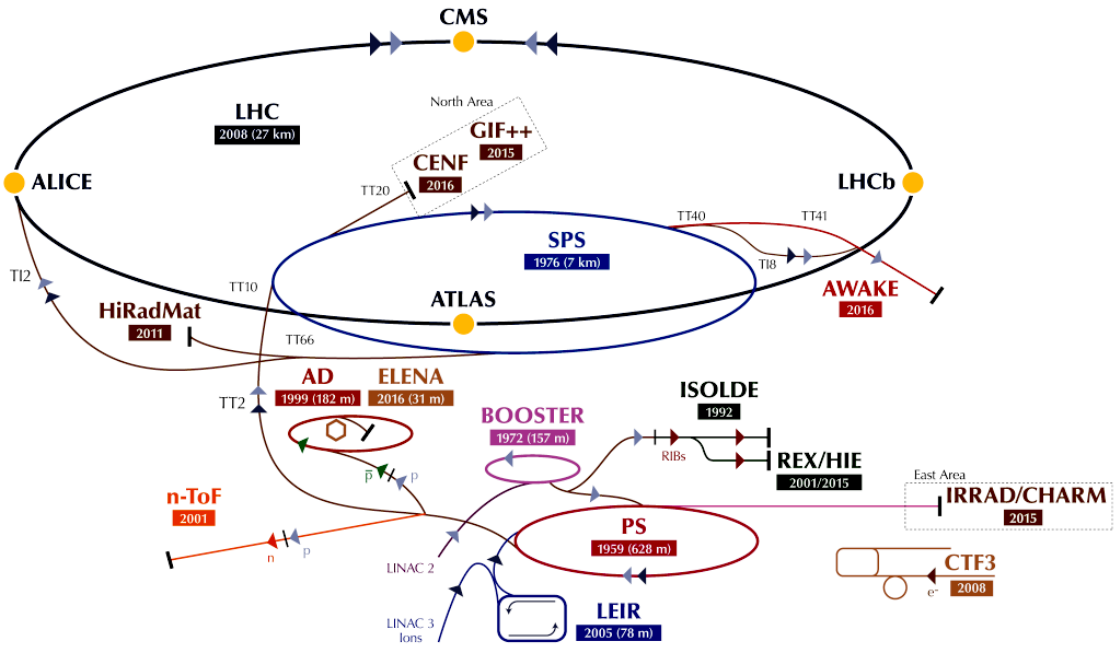

Figure 1.2: CERN Accelerator Complex.
Legend: *p (protons) RIBS (Radioactive Ion Beams) $\bar{p}$ (antiprotons) e^- (electrons) LHC (Large Hadron Collider) SPS (Super Proton Synchrotron) PS (Proton Synchrotron) AD (Antiproton Decelerator) CTF3 (Clic Test Facility) AWAKE (Advanced WAKefieId Experiment) ISOLDE (Isotope Separator OnLine) REX/HIE (Radioactive EXperiment/High Intensity and Energy ISOLDE) LEIR (Low Energy Ion Ring) LINAC (LINear ACcelerator) n-ToF (Neutrons Time Of Flight) HiRadMat(High-Radiation to Materials) CHARM (Cern High energy AcceleRator Mixed field facility) IRRAD (proton IRRADiation facility) GIF++ *(Gamma Irradiation Facility) CENF (CErn Neutrino platForm).* [6]

superconducting proton/ion accelerator installed in the pre-existing 26.659 *km* tunnel built for the LEP under the border between France and Switzerland. The LHC is CERN's newest and most powerful accelerator in the accelerator complex. The latter has seven unique experiments, each characterised by its detectors, where the machines particles are collided in. The four main experiments are A Toroidal LHC Apparatus (ATLAS) [9], A Large Ion Collider Experiment (ALICE) [10], Compact Muon Solenoid (CMS) [11] and Large Hadron Collider beauty (LHCb) [12], and each contributes in its own way to the discoveries made in the particle physics world. On the other hand, the smallest experiments on the LHC are Total, elastic and diffractive cross-section measurement (TOTEM) [13] and Large Hadron Collider forward (LHCf) [14]. These experiments focus on protons or heavy ions that brush past each other rather than meeting head on when the beams collide. Finally, there is Monopole and Exotics Detector at the LHC (MoEDAL) [15] that is aimed at searching for a hypothetical particle called the magnetic monopole.

Inside the accelerator [17, 18], the two high-energy particle beams travel in two counter-rotating beam pipes, each kept at an Ultra-High Vacuum (UHV) (Figure 1.3). The LHC is not a perfect ring and in fact, it is made of eight 2.45 *km*

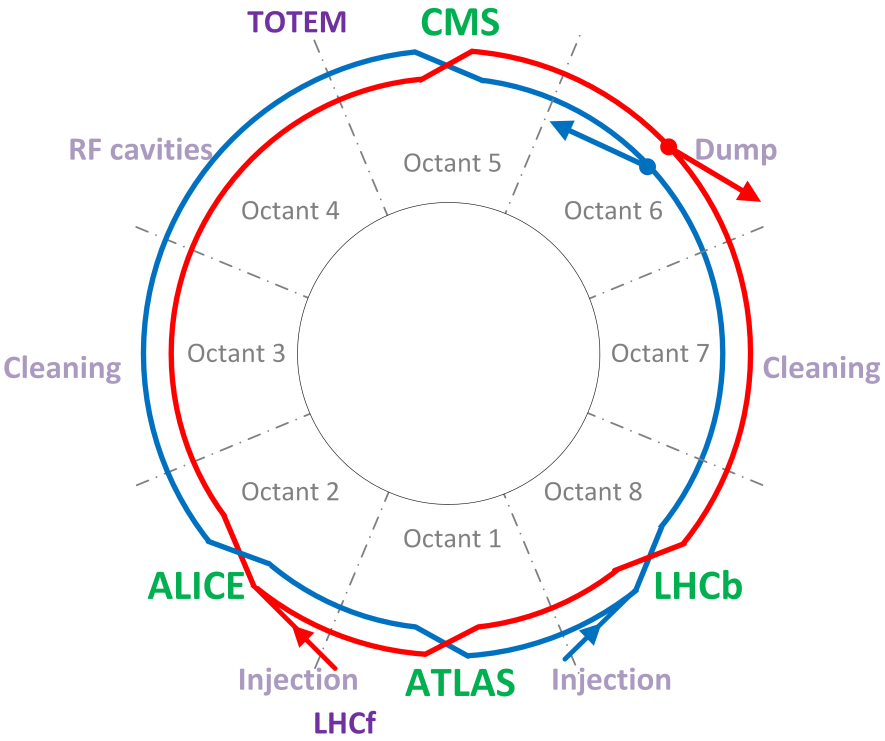

Figure 1.3: A basic schematic layout of the LHC. It shows the position of the four main experiments and the experimental insertions. Furthermore, it shows the radio frequency cavities and utility insertions which are found in octants not occupied by the experiments. (The layout reproduced by author from [16] is not to scale).

arcs and eight 545 m straight sections crossing in eight different Insertion Region (IRs). The latter are flanked by superconducting (SC) Radio Frequency (RF) cavities, which are used to accelerate particles and compensate the high synchrotron radiation [1] losses. Dipole and quadrupole SC magnets respectively achieve steering and focusing of the beams. In order to keep the particle beams on course, electromagnets with a magnetic field of around 8 T are required. Consequently, approximately 12 kA are required in the magnet coils. Most of the LHC's SC magnets are needed to be maintained at a temperature of 1.9 K which is achieved with a closed liquid-helium system [19]. This is done such that niobium-titanium (Nb-Ti) material used for the SC magnets reaches negligible electrical resistance, hence allowing the magnets to efficiently conduct electricity with very low energy loss.

Ultimately, this leads to the capability of the LHC beam pipes to handle a stored beam energy of up to 362 MJ that is equivalent to 2808 *bunches* of 1.15×10^{11} protons per bunch at 7 TeV each. This is such that the LHC can achieve centre-of-mass collision of energies up to 14 TeV. With transverse energy densities of

[1] Synchrotron radiation is an electromagnetic radiation generated by radially accelerated charged particles; in circular colliders the main contributions to this phenomenon comes from the dipole magnets used to bend the charged particles trajectory.

1 GJ/mm^2 [20, 21], the LHC beams are highly destructive. Moreover, in 2017, the LHC achieved record luminosity [22]. The instantaneous luminosity record was smashed, reaching $2.06 \times 10^{34}\ cm^{-2}s^{-1}$, which is twice the nominal value. If particles are squeezed enough through a given space in a given time, there is a higher probability that they will collide when two beams meet. Therefore, instantaneous luminosity corresponds to the potential number of collisions per second [23]. This is why the High-Luminosity Large Hadron Collider (HL-LHC) [17, 24] aims at increasing tenfold the LHC annual integrated luminosity and thus providing the high-energy physics community with an unprecedented data sample.

Having said this, the beams are collided during *stable beams* or the *physics phase* of the LHC operational cycle, shown in Figure 1.4. The cycle starts when the beams are injected in the LHC from the SPS at 450 GeV, after verifying the correct behaviour of the machine with a safe beam probe. The magnet strengths are then ramped-up in order to accelerate the beams to maximum energy. Finally, the beam is then squeezed to reduce the beam size and adjusted for collision [25].

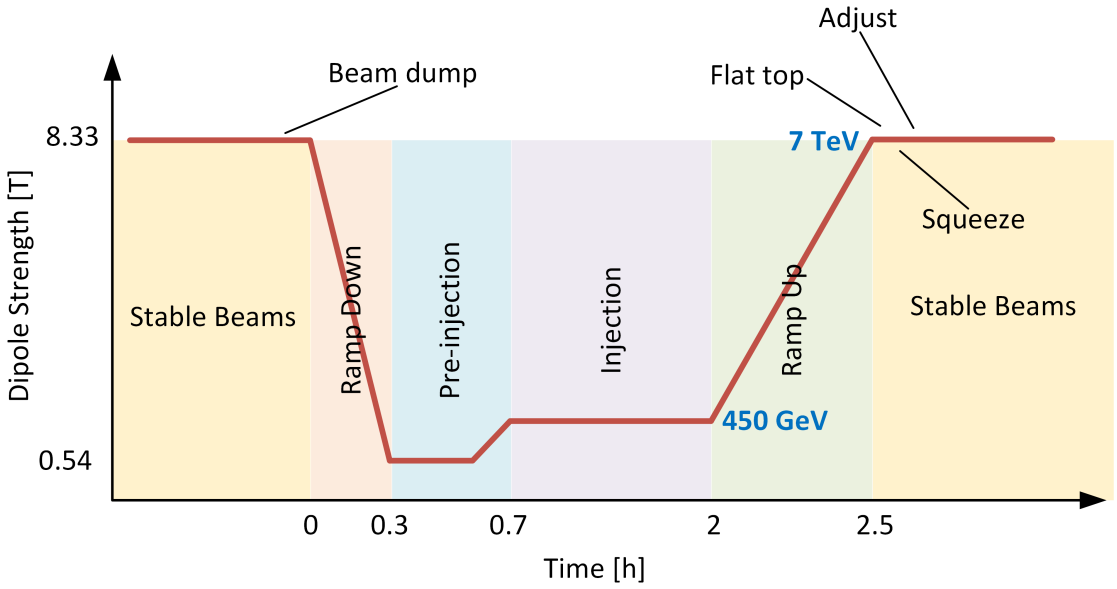

Figure 1.4: LHC operational cycle with the magnet strengths and beam energy. Reproduced by author from [26].

It can also be expected that the beam lifetime is not fixed [27] through the operational cycle due to various sources of beam loss. These can be listed as:

- collision with residual gas molecules in the beam pipe;
- intra-beam scattering;
- beam instabilities;

- synchrotron radiation damping;
- beam-beam effects, and;
- dynamic changes during the operational cycle.

These diffusion mechanisms shift particles from the bunch core to higher amplitudes, creating what is known as the beam halo. Generally, the core of a LHC proton bunch in the transverse plane can be modelled as a four-dimensional (x, x', y, y') Gaussian distribution. In order to account for the halo particles, a tail or a second Gaussian distribution is considered. Indeed, it will have a larger standard deviation σ and a smaller number of particles than the core, as depicted in Figure 1.5. It is generally considered that the particles with an amplitude $> 3\sigma$ comprise the beam halo and, by elimination, $< 3\sigma$ the core. As expected, the core contributes to the absolute majority of the luminosity [26, 28].

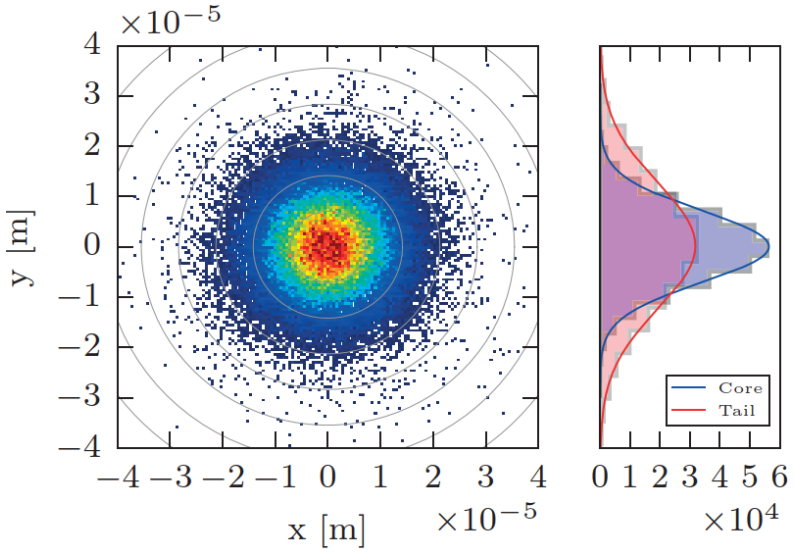

Figure 1.5: A particle beam modelled as a 2D double Gaussian distribution. Showing a scenario, where the core makes up 95% of the beam, and the tail 5%. The top plot show the histogram of the distribution, and the probability density function divided into core (blue) and tail (red). Reproduced by author from [26, 28, 29].

The beam halo and beam losses are a very important problem and each needs to be handled with caution. If small amounts of energy, induced by a local transient beam loss of a 10^{-9} fraction of the full beam at 7 TeV, are deposited into the SC magnet coils, the SC magnets in the LHC would quench[2]. Such events can lead to the destruction of parts of the accelerator. Since the repair time of a

[2]As already mentioned, one of the LHC operational requirements is that the SC magnets must be kept at cryogenic temperatures in order to benefit from their SC state. A magnet quench represents a transition of the magnet from a SC to a normal-conducting state. This will result in very high resistances and unstable magnetic fields.

superconducting magnet would cause a down time of several weeks or months, it is of utmost importance that the beam of particles is monitored and controlled at all times [30]. Considering all this, the need for a system of more than 4000 Beam Loss Monitors (BLMs) to be installed around the ring, was established.

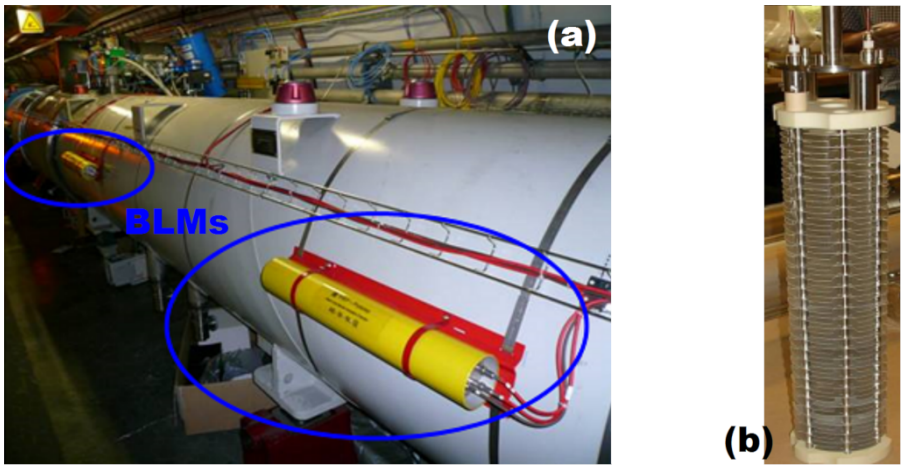

Figure 1.6: (a) Beam loss monitor at LHC. (b) Photograph of the inside of an ionization chamber [30, 31].

Protection of the equipment from beam particle loss is achieved by the monitoring and subsequent generation of a beam dump trigger when the losses measured by the BLMs exceed certain thresholds. The thresholds depend on the:

- momentum of the stored beam,
- the duration of the beam loss and
- on the location of the beam loss monitor.

In addition to the quench prevention and damage protection, the loss detection allows the observation of local aperture restrictions, orbit distortions, beam oscillations, and particle diffusion. As shown in Figure 1.6, BLMs are mounted on elements that have been identified as potentially critical such as the quadrupoles and the collimators. There are four different types of BLMs [31]. The standard ones are 50 *cm* long ionization chambers with parallel aluminium electrodes. The chambers are filled with nitrogen at 100 *mbar* overpressure. The properties of the chamber gas are close enough to the ones of air at ambient pressure such that if a detector develops a leak it would not compromise the precision of the BLM system. On the other hand, they are sufficiently different to detect a leak during the scheduled annual test of all the chambers with a radioactive source. Apart from the use of BLMs, a powerful collimation mechanism is set in place in order to ensure stable running conditions.

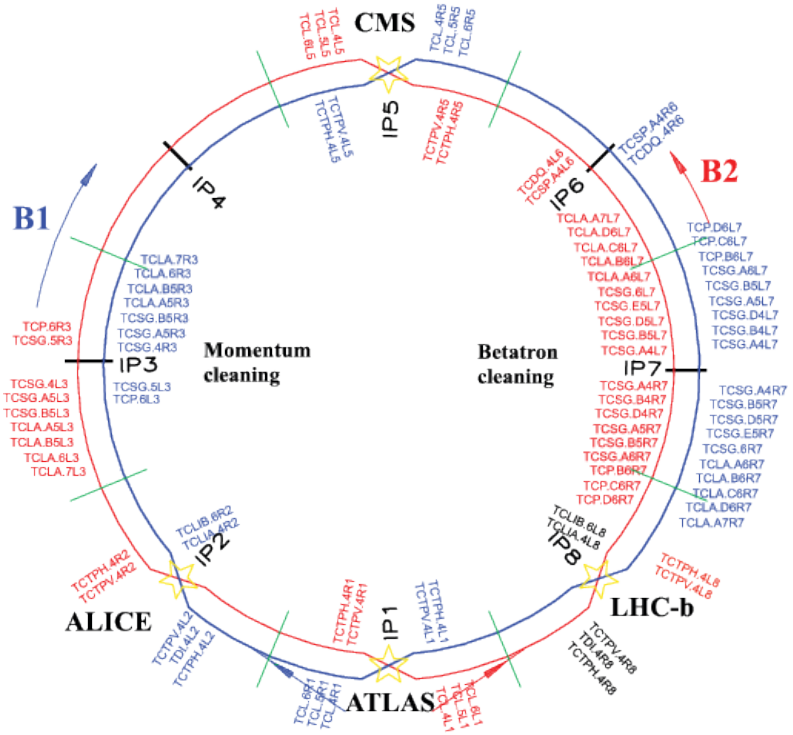

Figure 1.7: Layout of the LHC, showing the collimator locations around the ring [32]

In general, to collimate rays of particles means to make the beam accurately parallel. The LHC collimation system is the most advanced cleaning system built for an accelerator. Unlike previous colliders, such as the Tevatron, where the main purpose of collimation was to reduce experimental background, the LHC requires collimation during all stages of operation to protect its elements. It is made up of 108 collimators [1] and absorbers, of which 100 are movable collimators installed in seven of the LHC IRs as well as in the transfer lines [20,33]. The collimation system used in Run 2 is shown in Figure 1.7. The movable collimators are subdivided into two single sided and ninety-eight double sided collimators of different designs and materials, providing 396 degrees of freedom (two motors per collimator jaw), that produce a multi-stage scrubbing of the beam halo [32]. The latter also plays a crucial role in the LHC machine protection. Moreover, the collimation system must ensure, in all conditions, more than 99% cleaning of the beam halo during the full beam cycle [34]. In the context of the luminosity performance, this is crucial since it enables the LHC to reach its full potential during regular operation [35–37].

Since there is no collimator solution that fulfils all the design requirements for LHC collimation, the design of the LHC collimation system has been a complex task. Therefore, a huge and consequential, multi department effort is undertaken to continuously design, develop, optimise, operate, maintain and monitor the powerful LHC collimation mechanism. In fact, the work on a state-of-the-art collimation

system has been ongoing since the 1990's and is continuously evolving depending to new requirements. Each design must encompass all pertinent requirements concerning robustness, performance, fabrication requirements, costs, installation, maintenance, machine protection and beam operation. This reflects the challenge posed by the advancement of the required beam cleaning and collimation and the difficulties involved to meet the ever evolving LHC requirements. [1, 20, 36–38]

Figure 1.8: Photograph of a collimator in the LHC tunnel [32]

As already highlighted, collimators (as the one shown in Figure 1.8) are designed to protect the LHC accelerator from beam particles travelling outside the nominal trajectory. This is achieved by physically blocking the particles that are outside the beam halo, thus cleaning the excess particles in the outer part. This also implies that collimators are also adept at narrowing the beam of particles in the horizontal plane. The nominal beam size at the collimator is 200 μm. Since a collimator directly influences the size of the beam of particles, it is very important that its jaws position with respect to the beam is accurately known. Linear position sensors are installed for this specific task. Moreover, the target uncertainty of the position reading, of any linear position sensor installed, needs to be one tenth of the nominal beam size implying that the jaws have to be measured with a 20 μm, maximum target position uncertainty. Apart from high accuracy, it is also imperative that the collimation position measurements are not influenced by nuclear radiation or by magnetic fields [39, 40] coming from surrounding devices [41–43]. Furthermore, due to the several MGrays/year of radiation expected in

the proximity of the collimators, no electronics could be embedded in the sensors or in the motors. This is why all the electronics are placed hundreds of meters away and are connected to the sensors through long cables. This poses a challenge when designing sensor and electronics for the collimators because the cable and its properties affect the signals sent and received. The two sensors used to determine the jaw position of the collimators are the I2PS and the LVDT.

1.2 Project description and objectives

As already highlighted, the safety and reliability of the LHC depends on the correct performance of the collimators. Indeed, an incorrect reading of any one of the sensors installed on the collimator leads to a beam dump or damage to the machinery. In the field of safety critical applications, such as the one in this case and also in the industry, it is vital that a transducer is stable and reliable over a wide range of environmental changes. On the other hand, a transducer such as the I2PS which is highly requested in the industry as it has features like long lifetime, robustness, radiation hardness and high resolution, should be optimised and industrialised for the use in other fields apart from the LHC at CERN.

The main aim of this work is twofold: increase the reliability/accuracy of the measured position and optimise the I2PS. This is achieved by modelling and characterising the transducer in conditions which perturb the position reading. Indeed, this work can be divided into three parts:

1. Electrical characterisation of the I2PS with long cables:
   (a) understand the effect of parasitic capacitance on the coils and hence the implications on the position reading;
   (b) develop a model that replicates this phenomenon; and
   (c) develop, build and test a solution to counteract this phenomenon.
2. Examine and reduce position drifts related to temperature:
   (a) understand the cause for this phenomenon and hence prove that the compensation algorithm is correct;
   (b) define a set of guidelines and a procedure to be used when selecting the compensation factors; and

(c) investigate possible modifications to the sensor in order to obtain higher temperature stability.

3. Obtain a general model and develop a design engine for the manufacturing of optimised I2PS:

   (a) provide an autonomous algorithm that holistically optimises the sensor's specifications with minimal direct intervention by the user;

   (b) use a generalised programming language independent of proprietary software like Matlab; and

   (c) provide an intuitive interface for a non-professional to use.

The I2PS is connected to the electronics for the supply and acquisition by a long cable. This cable is usually a few hundred meters long and it passes alongside other cables in the LHC tunnel racks or floor. It is also noted, from the past dataset that in abnormal cases the capacitance of the long cable connecting the sensor to the electronics changes. This leads to a different parasitic capacitance with respect to the one calibrated during commissioning, leading to position change. This work aims at obtaining a detailed study on the impact which the long cable leaves on the position reading and provide a solution to the position change caused by this phenomenon.

Moreover, while it is noted that the sensor is not affected by electromagnetic interference, as the LVDT, it is noted that it drifts with time as the surrounding temperature changes. Similar to the LVDT, the I2PS has a temperature compensation algorithm which compensates for the drift but it seems that in this case the compensation factors are not enough or correct for this purpose. Although it is noted that the temperature drift in this case is small, and the LHC collimators can still be operated with it, it is important that this issue is resolved so that the reliability of the reading is increased. Indeed, this work presents a detailed study of the sensor when the ambient temperature is changed and moreover presents possible solutions.

Finally, the need to industrialise the I2PS comes from the fact that its predecessor, the LVDT, is a widely sought after and highly used linear position sensor in the industry. The only drawback of the I2PS is the fact that it has been designed, continuously optimised and manufactured for one particular function. Tailor-making such a product involves a long design phase, followed by a testing period by a professional in the field. Hence, unlike the LVDT, only one sensor design

exists with a set of defined specifications. Furthermore, the task of designing an I2PS has until now been done manually by an electromagnetic engineer, which by knowing the characteristics of the transducer; through trial and error, defines a set of design specifications by using the electromagnetic model and the Finite Element Model (FEM) simulator. The available electromagnetic model is implemented in Matlab by Mathworks, which although is a good interface for testing models it is heavy on the computational resources. As expected, the summation of all this results in a design task that takes a long time of finish. Therefore, in order to be used to its full potential by the industry, this work aims at industrialising the available models by obtaining a design engine that produces optimised design specifications for the manufacturer.

This work will therefore help increase the knowledge about the I2PS and so achieve a stronger understanding of the inner workings of this transducer. Moreover, apart from the new guidelines, and countermeasure circuits for the thermal and capacitance effects respectively, it will provide a new simulation and a tool for design of a new I2PS.

1.3 Thesis Structure

This thesis is divided into seven chapters, with the first chapter aimed at giving a general introduction. Indeed, this chapter provides a description of CERN's infrastructure and the LHC. The LHC experiments, the luminosity in context of the beam, the beam and the eventual beam losses are ultimately also discussed. Moreover, the beam loss monitoring system is introduced and consequently, the LHC collimation system is put forward as the backbone of the structure that protects the accelerator from the inevitable beam losses. A brief description of the accuracy and requirements of the collimator is also explained. The aim of this thesis which is that of fully characterising, enhancing and industrialising a collimator tailor-made linear position sensor, the I2PS, is then presented together with the motivation for this work and the expected project objectives.

The next chapter follows a more detailed explanation of the mechanical and electrical design of the collimator which is built upon the description presented in Chapter 1. This is done by explaining the movement and protection algorithms embedded in the collimator software and hardware. A detailed description on how

the linear position sensors are operated and how the accuracy of the collimator is achieved is also presented. Moreover, the work done on the LVDT is highlighted. This is important since the LVDT is used as a reference in the majority of the studies, which are related to the I2PS. Finally this chapter introduces the I2PS, giving a detailed description of the design and working principle while comparing it to the LVDT. It is shown that various detailed studies have been carried out over the years to define this transducer. An overview of the work presented in this thesis in relation to these studies is also provided in this chapter.

One of the challenges electronics designers face are long tracks and long cables. Cable length is usually kept as short as possible hence reducing introduction of noise in the system. With this in mind, Chapter 3 explains how the I2PS is sensitive to cable capacitance change. It presents a novel spice simulation, which models this phenomenon and also an electromagnetic model. This model is very important since unlike FEM models it is fast and other circuits can be simulated as well. This simulation leads to the development of a countermeasure against the sensor's cable sensitivity.

Thermal sensitivity is an issue almost every sensor exhibits and a compensation system is always investigated and implemented, the I2PS being no exception. For this reason, Chapter 4 presents the detailed and exhaustive study carried out in relation to the thermal sensitivity of the sensor. It is shown how the sensor behaves in different operating conditions. Furthermore, a thorough characterisation of the performance of the compensation algorithm is unveiled in this chapter.

Chapter 5 builds on the previous chapter and presents variations implemented in the I2PS structure with the aim of decreasing thermal sensitivity. To complement the conclusions obtained in the thermal studies, an interference study was conducted such that guidelines on the operation of multiple I2PS in close proximity could be defined. The latter was used with the former to conduct a set of experiments on the collimators to obtain a deeper understanding of the thermal behaviour of the I2PS in operation.

Ultimately, Chapter 6 gives a detailed description of the optimisation tools available. This is followed by an analysis of the sensor's variables and dependencies with the aim of designing an automated optimisation design engine to industrialise the sensor. Once a sensor is developed, it is not always easy to re-optimise with modifications to the design for other implementations manually. This usually involves precious resources and dedicated professional manpower. An algorithm,

which generates new sensor specifications and its results, are then presented and discussed at the end of this chapter.

Finally, a summary of the work accomplishments and the main contributions of this study to the further development of this research field are presented in the last chapter. Furthermore, this chapter provides suggestions for future work and concluding remarks.

Chapter 2

The LHC Collimation System and its Position Sensors

2.1 Introduction

As briefly highlighted in Chapter 1, CERN houses over one hundred collimators to help with the protection and control of the beams in the LHC. Furthermore, to ensure the multi-beam cleaning by the collimation system, various types of collimators are installed in the LHC. In fact, the mechanical design depends on the collimator's function. The jaws of the primary collimators are typically shorter than the secondary collimators, whilst the aperture of secondary collimators must be larger than that of the primary but small enough to maximise its efficiency in catching the particles out-scattered by the primaries. Other collimator types also exist, namely, the tertiary, absorbers, dump protection and injection which are all different depending on their particular function [32].

Since this study deals with the linear position sensors which have the same function on all the collimator types, and are installed in the same manner, this chapter provides a detailed explanation of the general mechanical and electronic design and layout of a collimator. It also provides, a detailed description of the LVDT and the I2PS, as well as a comparison between the two. An overview of the up-to-date development of the I2PS at time of the work presented in this thesis, in relation to the development of the research field, is finally given.

2.1.1 General layout and design

Collimators are designed to withstand the high intensity of the LHC beam. It is a challenge to create a large machine, which is not only very robust, but at the same time very precise. Furthermore, the jaws have to be remotely movable with good precision and high reproducibility of settings. Finally, the absolute opening of the collimator gap is safety-critical and must be known at all times with good accuracy.

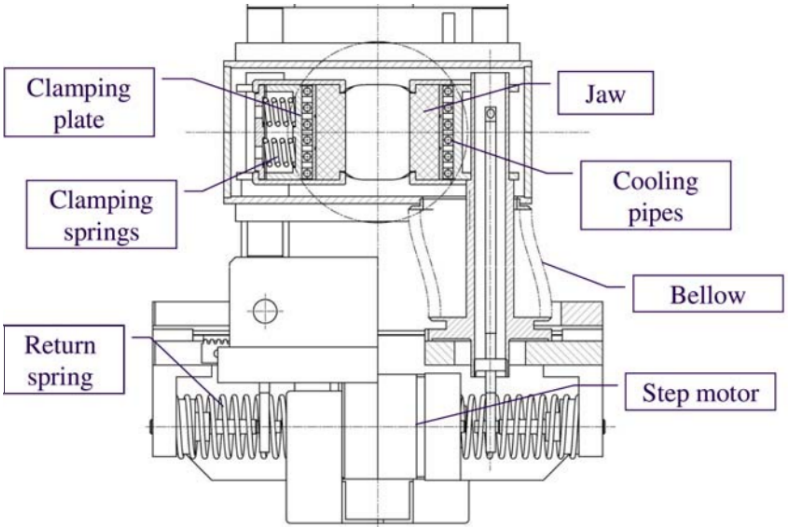

Figure 2.1: Collimator mechanical assembly (cross-section of a horizontal TCSG) [44]

The jaw assembly design is based on the clamping concept [1]. A graphite or a carbon-carbon composite (C/C) jaw is pressed against a heat exchanger made out of copper by a steel bar, which is kept under pressure by a series of springs. Steel plates hold the jaw assembly together, as can be noted from Figure 2.1. The jaw width is set to 25 mm, which is the minimum allowable dimension, as demanded by preliminary thermo-mechanical analysis. This is done in order to minimise the thermal path from the place where the beam impact takes place i.e. the hottest spot, to the cooling pipes. Since copper expands at a rate of 16 to 17 $10^{-6}m/mK$ and graphite expands at a rate of 4 to 8 $10^{-6}m/mK$, a fixed joint between the jaw and the copper plate is not possible. To avoid unacceptable distortions, the contact between the two surfaces must allow for relative sliding. At the same time, proper heat conduction at the contact point must be ensured. Consequently, a nominal pressure of five bar has to be applied between these surfaces. While a higher pressure leads to better conductance, it increases the mechanical stresses on the jaw. The pressure required was estimated through a semi-analytical model developed by Fuller and Marotta [45]. The effect of differential thermal expansion

on the jaw surface precision is minimised by setting the transverse distance from the two supporting axles to the internal reference surface of the jaw to 40 mm. [1]

Two Oxygen-Free Copper (OFC) pipes per jaw, which are brazed on one side to the copper plate and on the other side to the stainless steel bar, make up the heat exchanger. Each pipe has three turns of square pipe section to increase the heat exchange, ease the brazing procedure and to avoid harmful air traps. A maximum operating temperature of 50°C for the jaw material is required due to the graphitic materials specifications. This imposes the use of water at 12°C with a water flow rate of 5 l/min per pipe. [46]

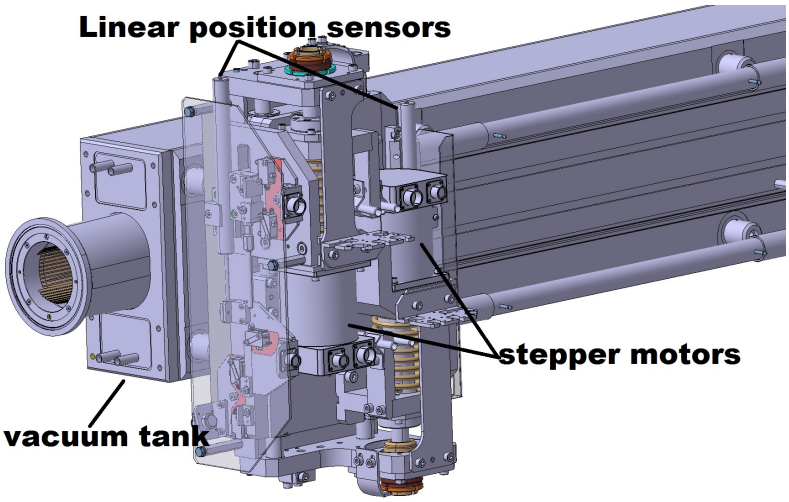

Figure 2.2: Front view of the 3D drawing of a collimator

Two stepper-motors independently actuate each jaw. This allows both lateral displacement and angular adjustment. Indeed, a rack and pinion system avoids excessive tilt of the jaw. In fact the relative difference between the two axes cannot be larger than 2 mm. Rotational movement of the each motor is converted to linear motion by a lead screw system, which when connected to a table mounted on anti-friction linear guide-ways, allows the precise positioning of the jaw supporting axle. The smallest motor step is 10 μm. Four bellows, which can be bent sideways, guarantee vacuum tightness. Then, a return spring pre-loads the system hence making it play-free. The return spring also provides a semi-automatic back driving of the jaw, in case of motor failure.

End-stop and anti-collision switches are installed to stop the jaw before colliding with each other or to the end plates. The position control is guaranteed by motor encoders and by six linear position sensors. Furthermore, the vacuum tank, which has a traditional design, is manufactured out of 316L stainless steel and is mainly electron-beam welded (Figure 2.2). The whole system is pre-aligned and then

placed on a support table via a plug-in system. Another stepper motor with the same setup adjusts the whole assembly by $\pm 10\ mm$ in order to move the jaws on the plane of collimation and present a fresher surface in the beam impact area, in case the initial impact area is damaged. A linear position sensor monitors this position and end-stop switches limit further movement. [44]

The stepper motors are controlled in open loop. This implies that they follow predetermined trajectories without feedback from a position sensor. This is possible due to the precision of the kinematic chain that has been designed to be free of mechanical play. The collimators are therefore equipped with electronics such that the following diagnostics can be obtained [1]:

- the position of each motor and jaw support point through motor encoders,
- independent measurement of collimator gap dimension, at both extremities of collimator tank with linear position sensors,
- independent measurement of each jaw position at both extremities of collimator tank with linear position sensors as well as the position of the tank with respect to the pre-aligned position. (Five position sensors installed for this purpose, bringing to seven the total number of linear position sensor per collimator),
- temperature of each jaw at both of its extremities,
- temperature of cooling water at inlet and outlet,
- signals from various limit switches (end stop in and out and anti-collision),
- one microphonic sensor per jaw for detection of beam-induced shock waves,
- flow of cooling water per collimator.

The extensive diagnostic measurements allow fail-safe setting of collimator gaps. It is also important since it allows for self-consistency checks and detection of abnormal beam load conditions.

2.1.2 Low Level Control System

Similar to the mechanical design, the control system for the collimator has a strict list of requirements. The system must run in real-time and is required to be fast (<10 ms), accurate and reliable. Hence, the system is divided into low level, supervisory level and application level.

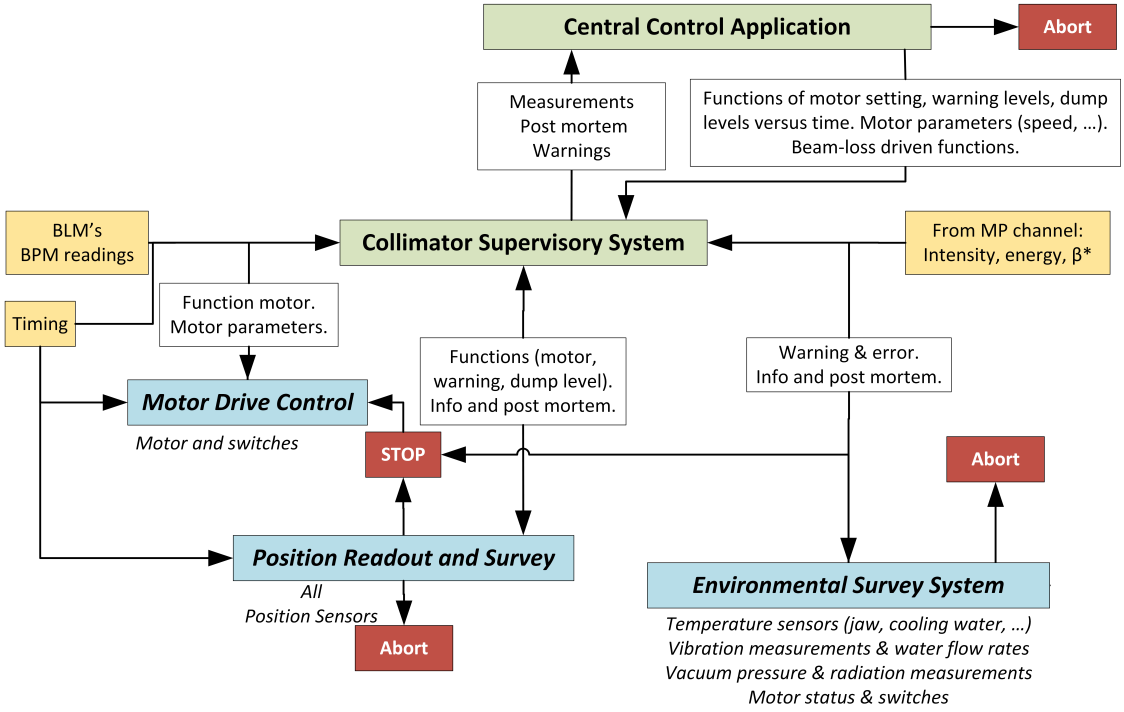

Figure 2.3: The layout of the collimators control system. Reproduced by author from [47].

Figure 2.3 presents a layout of the collimators' control system. The operator's interface in the control room includes the high-level module of the system and is referred to as the Central Control Application (CCA) [47,48]. The role of the CCA is twofold: it presents an efficient Graphical User Interface (GUI), which allows the supervision of about 120 collimators in one screen, and it provides special functions like trimming [49,50].

The Collimator Supervisory System (CSS) takes care of all time critical actions and runs on several Linux PCs, henceforth referred to gateway, which are installed close to the low-level racks. Every gateway manages approximately thirty collimators by means of commands sent to the low-level system through the CERN middleware framework called Front End Software Architecture (FESA) [51]. The low-level system triggers all time critical actions by pulses sent through a dedicated optic fibre. The latter serves as a link between the gateway and the different low-level

systems of the collimators supervised by the CSS to trigger time sensitive actions triggered on the low-level system. The standard CERN timing system is used to synchronise the different gateways among themselves [48].

The low-level function subdivides into three parts:

- The **Motor Drive Control (MDC)** controls the motion aspect of the collimators. This system receives the motion commands from the supervisory system and is charged with the transmission of the acknowledgement of commands received and end-of-action notifications. This system is also tasked with the pre-processing of these commands. Hence, the commands include performing tasks such as coherence checks and protocol checks and the generation of the smooth profile movement trajectory set-points to be executed by the FPGA motor controller. It also provides interlocks to eventually abort the beam in the LHC in case a problem occurs during the movement.
- The **Environmental Survey System (ESS)** reads all environmental parameters such as the temperatures of the jaws and cooling, the vacuum gauges and more. Moreover, it is able to trigger a beam abort if it meets specific conditions.
- The **Position Readout and Survey (PRS)** is responsible of verifying in real time that the actual position corresponds to the desired one within a well-defined tolerance received by the supervisory system. Apart from executing coherence and protocol checks of the commands received from the CSS, the PRS also prepares the upper and lower thresholds of the profile for the collimator axes position and the two gaps. The position of the linear position sensors is read with an accuracy of 20 μm at a rate of up to 100 Hz [52]. In [53], the I2PS algorithms are found to have a processing time of less then 0.3 ms. Taking into account a signal acquisition of 2000 samples acquired at 250 kS/s, an acquisition time of 8 ms is obtained. Depending on the type and energy of the circulating beams, the PRS can issue a beam abort in case of difference between the desired and the measured position of the jaw.

As already mentioned, linear position sensors have been chosen to measure the jaw position at each extremity, the distance between the two jaws and the position of the tank. Since 2013, two linear position sensors are installed in the LHC collimators. The Linear Variable Differential Transformer (LVDT) and the Ironless Inductive Position Sensor (I2PS).

2.2 The Linear Variable Differential Transformer

The Linear Variable Differential Transformer (LVDT) is a common type of inductive transducer that can convert the rectilinear motion of an object, to which it is coupled mechanically, into a corresponding electrical signal [54–57]. A basic LVDT consists of a movable core and three coils, a primary coil and two secondary coils. The coils are wound onto a cylindrical bobbin, which is usually made out of some insulator material. Since inductive coupling is the source of communication between the moving and stationary parts of the transducer, these coils are usually inter-penetrated rather than lined end-to-end. An LVDT core is normally a cylinder of permeable material and provides inductive coupling between the primary coil and the secondary coils. The core moves within the bore of the LVDT. The core material is usually made of the nickel-iron alloy, which is threaded to enable one to attach it to the element that is to be measured. After the core is in the final shape, size, and is threaded, it is annealed. The annealing process removes mechanical stress and makes the permeability uniform [57]. This aids the completed LVDT to obtain a low null, unit-to-unit repeatability, lower non-linearity and better temperature performance.

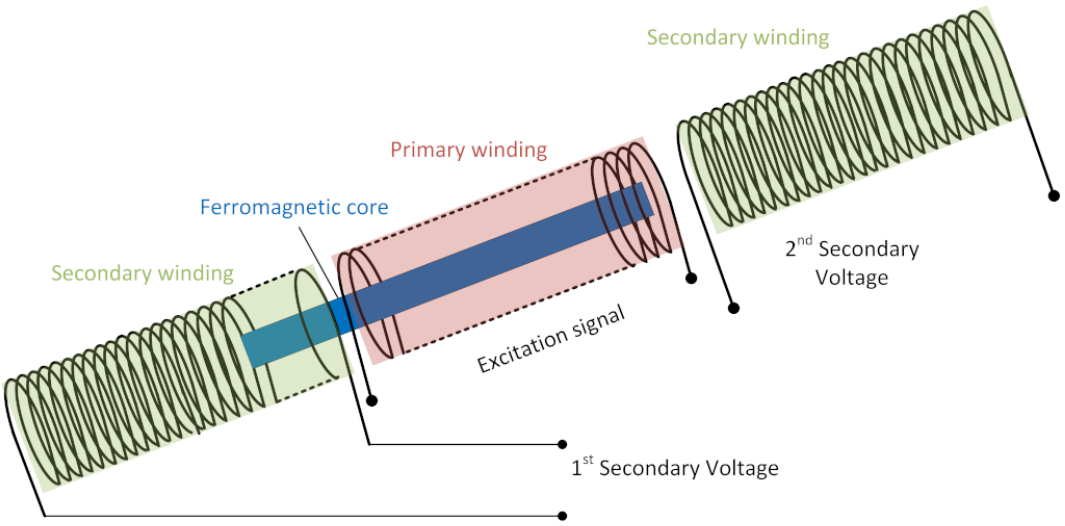

Figure 2.4: Structure and working principle of an Linear Variable Differential Transformer

Movement of the core triggers the linkage from primary to both the secondary coils, which changes the induced voltages. The coil, onto which the voltage is impressed, is henceforth referred to as the primary. The coils that produce the relative outputs are henceforth referred to as the secondaries. In transformer theory, two or more adjacent coils are coupled by mutual inductance. Therefore, if a voltage is supplied to one coil (the primary), the voltage produced at a second coil (a secondary) is related to the magnitude of the primary voltage by the ratio of the number

of turns of the respective coils. The LVDT's primary is energised by a constant amplitude ac supply. The magnetic flux develops coupling through the core to the adjacent secondary windings. If the core is located midway, equidistant from the secondary coils, equal flux is coupled to each secondary. This implies that the voltages induced by transformer theory in the secondary windings are equal. This midway core position is known as the null point, where the differential voltage output, is practically zero. If the core is moved closer to the first secondary than to the other, the flux distribution is shifted favouring the first secondary coil. This implies that a higher voltage is induced in the first secondary coil while the voltage in the second secondary is decreased. The opposite happens if the core is moved closer to the second secondary coil. The phase angle of this ac output voltage, referenced to the primary excitation voltage, stays constant until the centre of the core passes the null point, where the phase angle shifts by 180° to one side and -180° to the opposite side. With the right algorithm or circuitry, this phase shift can be used to determine the direction of the core from the null point [54].

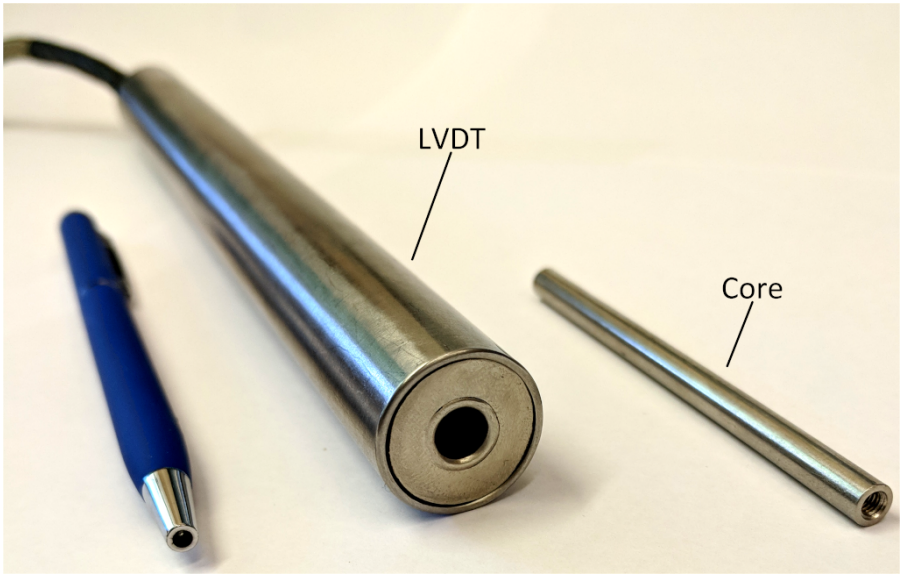

Figure 2.5: A photo of a Linear Variable Differential Transformer (LVDT)

Since the LVDT core does not touch the inside of the coil bobbin, it is defined as a non-contact sensing element since it is friction free [57]. This means that repeated full-stroke cycles can be repeated without wear or degradation of the performance characteristics. Moreover, an LVDT is said to be an infinite-resolution sensor. The only limitations imposed on resolution are due to noise, characteristics of the signal-conditioning electronics, or limitations of the user's signal-receiving circuitry. Higher excitation voltages are used in noisy environments to maintain a high signal/noise ratio. Quantizing error in the receiving electronics may limit resolution due to the analogue-to-digital converter that is often incorporated there by the user. Since the LVDT conditioned output is an analogue signal, an Analogue

to Digital (A/D) converter is needed to present the signal to a digital system such as a controller using a microprocessor. Furthermore, hermetically sealing an LVDT provides a very rugged sensor, which can be used in high-humidity, high-vibration environments and over a wide temperature range. Eventually, if a stainless steel material is used for the housing and end plates, a substantially corrosion resistant sensor is produced.

Therefore, if an ac signal $s(t)$ at frequency f_o is supplied to the LVDT:

$$s(t) = A_p cos(2\pi f_o t) \tag{2.1}$$

it results in two secondary signals dependant on the LVDT sensitivity, core position and winding ratio as follows:

$$\begin{aligned} y_1(t) &= A_1(x) cos(2\pi f_o t + \phi_1) \\ y_2(t) &= A_2(x) cos(2\pi f_o t + \phi_2) \end{aligned} \tag{2.2}$$

The position reading of the LVDT is based on a ratiometric index of the two secondary voltages (A_1 and A_2). The ratio is given by:

$$r(x) = \frac{A_1(x) - A_2(x)}{A_1(x) + A_2(x)} \tag{2.3}$$

The LHC collimator's design guarantees the LVDTs a constant sum for the denominator $S_1(x) + S_2(x)$ over the useful position range of $\pm 40\ mm$. The amplitude demodulation is performed with a sine fit algorithm [58–60] and since the demodulation is asynchronous, it does not suffer from phase error problems. This also implies that filtering or windowing is not required to eliminate the spectral leakage. The high noise immunity and a frequency response of this algorithm, significantly reduces the proximity crosstalk due to different LVDTs.

Despite its advantages, excellent performance along the years and the presence of an enclosing shielding material, it was shown by A.Danisi et al. [42, 56, 61] that the linear variable differential transformers are sensitive to external dc or slowly-varying magnetic fields. This phenomenon was first noticed in the CERN's LHC Collimators application. The magnetic interference on LVDTs was observed as a drift on the sensor's position reading, localised on certain sensors along the

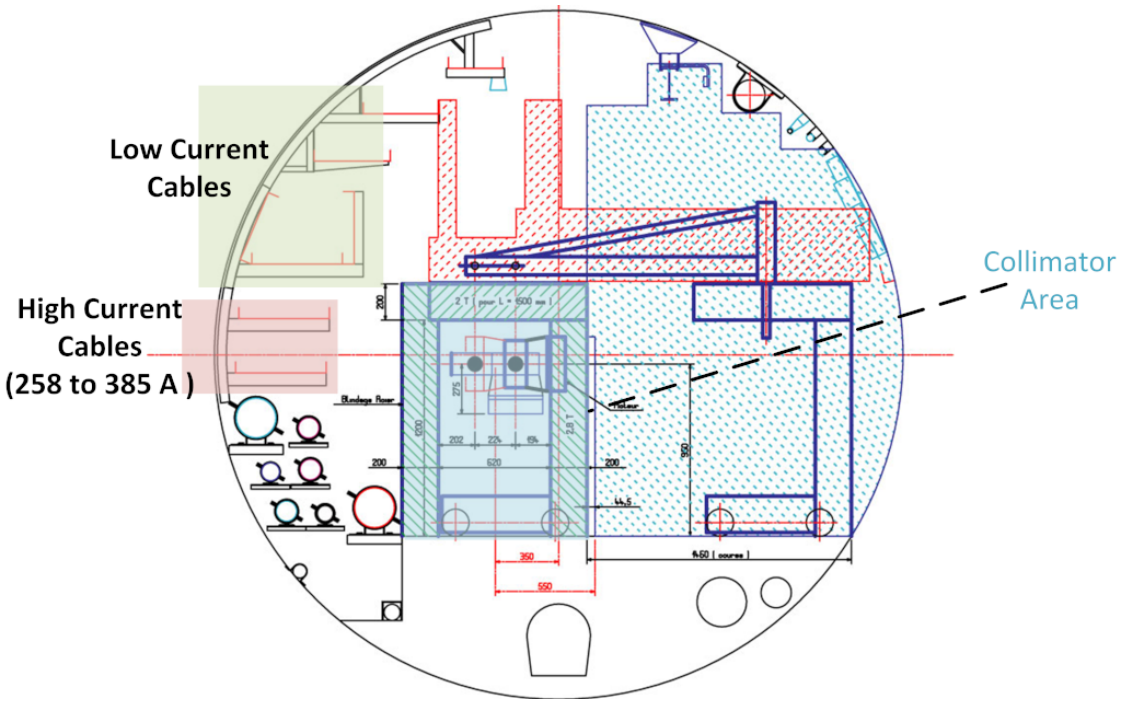

Figure 2.6: Typical cross section of an LHC tunnel [1]

accelerators complex, especially in the transfer lines that connect the beam-lines of different circular machines [39]. After a thorough research in the data sheets, it resulted that some manufactures warned the user about this problem but gave no quantitative information.

Figure 2.6 shows the typical cross section of a transfer line. It is clear that several current cables are placed on planes about one meter away from the collimator area. The top ledges are equipped with cables in which the current is characterised by low peak amplitude. The other ledges are equipped with two series of cables in which the current is constant with a superposed high-amplitude pulsed waveform. According to the SPS extraction cycle, this is a slow varying signal with respect to the sensors and motors signals [62]. Hence, it can be considered as a constant or dc signal. Since the function of these cables is to supply the transfer lines' magnets during their cycle modes [39] the magnitude of these current signals is of some hundreds of Amps.

The dc magnetic field produced by the current of these two cables, is the main source of the magnetic interference recorded on the LVDT positioning sensors of the LHC collimators. This hypothesis is confirmed by the measurements, which have been done on a collimator, shown in Figure 2.7. It was noted that, the current signal of the cables and the position reading of one of the LVDTs is perfectly synchronized.

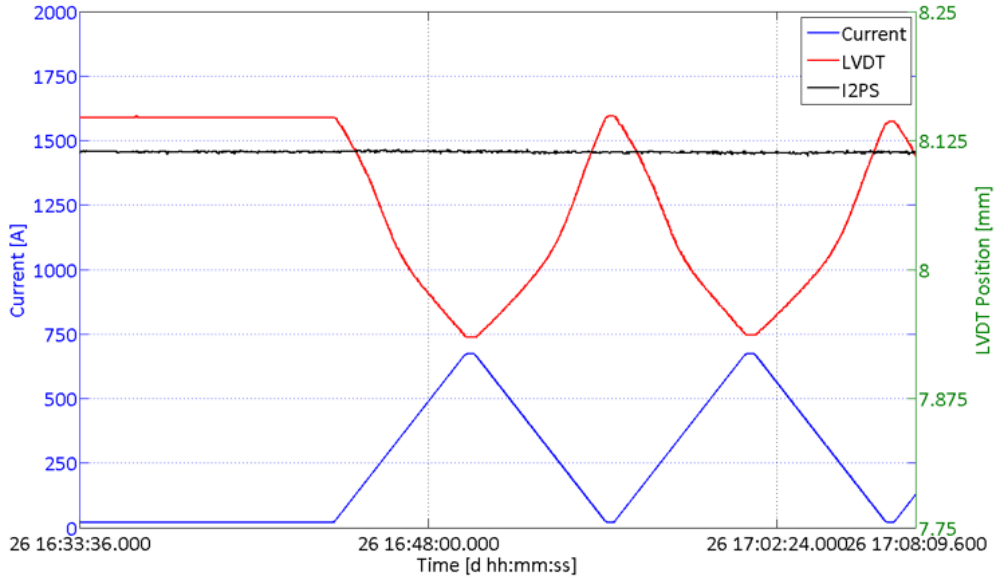

Figure 2.7: Correlation between the I2PS and LVDT position readings with respect to the magnet current cycle, on 26 May 2015, during a span of 35 min of LHC operation. [63]

Furthermore, the magnitude of the position drift can reach 200 μm. Simulations and measurements [39, 64] have been conducted to evaluate the magnetic field strength in the tunnel. The results showed that the maximum magnetic field to expect on the LVDTs placed in the collimators is around 800 A/m, which corresponds to about 1 mT in air. This comes from the fact that the current cables are arranged on the ledges such that the two cables in each pair are carrying two equal-and-opposite currents. Therefore, the magnetic field decreases quite rapidly with the distance from the pair. As a result, this also implies that the huge position drifts, which have been observed, are due to a relatively low-intensity magnetic field and that the LVDT sensor is quite sensitive to external magnetic fields. It was deduced from this study that the slowly varying magnetic field is coupled with the non-linear magnetic material of the LVDT polarizing the materials in a different working point, modulating the secondary voltages accordingly.

2.3 Review of position sensing techniques

LVDTs, are the transducers which dominate the bigger portion of the industry which requires transducers characterised by high precision, contact-less, and radiation hardness. In fact, a lot of research is conducted to enhance this transducer. H.Mandal et al. [65] developed a linear position sensor, which operates similarly to an LVDT. The proposed linear position sensor consists of two identical coils wound on a former made of ferromagnetic material. This acts as the position sensing structure for a specially designed core. Their added advantage is a sensor with a range of motion equivalent to the entire length of the sensor.

J.Maurio et al. [66] patented a novel linear position-sensing device, which makes use of a helically polarised magnet. Their system is oriented in operating in environmental conditions, which are characterised by high temperature and pressure such as nuclear reactors. This sensor includes a magnet which has a number of north and south poles along the circumference of the core in a helical pattern along the linear axis. This defines a very unique magnetic flux variation and hence producing high sensitivity in the sensor. While such sensor designs could be beneficial to the LHC collimator use case, the ferromagnetic material inside the sensor would eventually lead to the same electromagnetic interference as in the conventional LVDT.

A. Danisi [56] reviewed the position sensing techniques [57] with the LHC collimators as the use case. In his work, A. Danisi discussed how contact-type linear position sensors [67] such as resistive sensors are not suited for the requirements of the LHC collimators because of their relatively high uncertainty and low robustness. The major disadvantage of this sensor is the wear of the resistive element leading to performance degradation over time, making the sensor unreliable for continuous operation.

On the topic of resistive position sensors, Y.Kim et al. [68] developed a high performance, high temperature position sensor for control of actuators in aerospace systems. Apart from the high temperature conditions, this sensor needs to handle radiation, thermal/vacuum environment and mechanical loads due to spin [69]. In their work Y. Kim et al. produced a sensor with multi-layer metallisation on a silicon substrate which allowed for high temperature. Furthermore, with passivation layers the scratches caused by the rubbing of the brush on the resistive elements are avoided. While this sensor shows a significant advancement

from traditional resistive linear position sensors, the theoretical output position produced was 40 μm, even though MEMS technology was used to produce it. This precision needs to be at least halved in order to be able to implement this sensor in the LHC collimator.

A. Danisi also eliminated capacitive based linear position sensors [70] due to the ionisation radiation environments the sensor has to work in. E.Dimovasili et al. [71] showed that radiation-induced charge accumulates on the capacitance plates forming the sensor leading to voltage variations. The radiation environments found in the LHC tunnel also eliminated the use of position sensors which make use of the Hall Effect [57]. A. Danisi highlighted that a promising technique would be fiber-based interferometry [72,73] but was later eliminated due to possible degradation of fiber-optic in radiation environments. For the same reason linear optical encoders cannot se used since their electronics and materials suffer degradation due to radiation. Furthermore, since both these sensing techniques are very expensive and since several hundred sensors are required, this solution is found not to be feasible. Finally, inductive displacement sensors [74] which sense the variation of the magnetic field generated by the ferromagnetic materials are also available. These lead to the same issue as the LVDT.

C.Mandel et al. [75] adopted an interesting approach to displacement measurements in harsh environments while still using electromagnetic fields. C.Mandel et al. developed a chip less wireless sensor for two-dimensional displacement, which works on the principle of detuning of a complementary split ring resonator. Their prototype shows displacement detection of a movable part respective to a fixed part in the range of a few millimetres. A split ring resonator is similar to an antenna and a receiver, made out of micro strip lines that when made out of ceramic is able to work in a high temperature environment. While it is possible to use this sort of technology in such environments, it is seen in [76] that radiation effects affect ceramic materials and hence this kind of sensor would also not work in the LHC collimators.

When dealing with a beam whose size (200 μm) is equivalent to a thick hair strand but with a stored energy equivalent to 80 kg of explosive TNT, the precision of the linear position sensors controlling it is required to be roughly equivalent to the size of a large bacterium (20 μm). When such a high precision novel sensor is introduced, is often kept under constant monitoring and optimisation. It often happens that a sensor has not yet been fully characterised and that there are underlying problems that have not been identified. This is simply because certain

operating conditions have not been met. This is one of the main reasons; the I2PS has been under constant monitoring since the first installation. Furthermore, as shall be shown in what follows, various detailed studies have been carried out over the years to evaluate and characterise the sensor.

Indeed, A.Danisi et al. [56, 63, 77] have performed a lot of work in this field with the aim of designing, modelling and characterising this sensor's phenomena. In particular, an electromagnetic model [78] was developed defining the theoretical aspect of the sensor. This model is the starting point of the design of a new sensor since it provides the necessary mathematical functions. It is also critical since it mathematically shows how the sensor can be operated with both a voltage and a current supply. Moreover, the authors provide variations to the model such as a preliminary analysis of how the sensor behaves with temperature change [79] and the high frequency effects [80]. This is followed by 2D numerical analysis with a software called Flux by Cedrat, of the sensor, hence verifying the electromagnetic model [81, 82]. Furthermore, the author shows how his 2D model could be used to design the sensor and optimise it.

As already mentioned, A.Danisi et al. [80] also modelled the high frequency effects of the I2PS. The work through analysis, simulation and experiments showed that the electrical resistance of the coils is the parameter, which experiences the highest change from the high-frequency phenomena. They also showed that the inductance change exhibits very small variations with frequency. This study is very important in cases where the sensors need to be operated at high frequency. A.Masi et al. also developed a new real time high precision reading and temperature compensation algorithm. It was discovered that the standard three-parameter sine fit algorithm used for the LVDT demonstrated a sinusoidal disturbance to the main signal. Their algorithm uses a time windowing function to reject the low and high frequency effects, hence obtaining a higher precision while limiting the impact on the real-time implementation and respecting the constraints specified [53]. Moreover, this algorithm is combined with a method on how to compensate for temperature drift. A novel method of reading the temperature in such sensors is presented and it is noted that through this algorithm a dramatic reduction of the temperature sensitivity is reported.

L. Sabato et al. [83] modelled the I2PS parasitic capacitance with special attention to the moving coil. This study provided the first step in obtaining a parasitic capacitance model. An analytical model taking into account the curvature radii of the conductors and the presence of all the layers was proposed with the aim

of predicting the resonance frequency. Furthermore, S.Troisi et al. [84] aimed at understanding the effects of the shield on the sensor. The standard I2PS model developed by A.Danisi describes the sensor without the conductive enclosure. S.Troisi builds on this work. Through analytical and FEM simulations S.Troisi found out that the shield does influence the sensor. The impact is uniform and hence the effect can be compensated through calibration.

Table 2.1 summarises the position measurement techniques available and the reason why this technology is not suitable for operation in the LHC.

Table 2.1: Summary of existing position sensing techniques and their respective drawbacks from an LHC implementation point of view.

Measurement technique	**Drawbacks**	**Advantages**
Resistive	Wear and tear High uncertainty	Low cost Low tech Easy to use
Capacitive	Radiation induced charge	Low uncertainty Non-contact sensing
Inductive	Susceptibility to electromagnetic Interference due to ferromagnetic Materials present	Contact less Good sensitivity High resolution
Hall Effect transducers	Electronics in radioactive environment	Highly reliable High speed operation Pre-programmable
Magnetostrictive	Electronics in radioactive environment	Contact less High resolution
Magnetoresistive	Expensive High uncertainty	Contact less Good sensitivity
Encoders	Radiation degradation Electronics in radioactive environment Expensive	Improved noise immunity High measurement accuracy Low-latency
Interferometry	Radiation degradation	Low uncertainty

2.4 The Ironless Inductive Position Sensor

Following the shortcomings of the LVDT, the I2PS [56] was proposed to overcome this magnetic interference problem. The I2PS keeps the same inductive coupling based working principle as that of the LVDT. This keeps the main advantages of the typical LVDTs hence qualifying it as a valid alternative to be used in the harsh environments of the LHC collimators. Table 2.2 presents a time line of the I2PS development.

Table 2.2: Progression of I2PS development

I2PS Development Stage	Reaserchers
LVDT analysis and problem development	A.Danisi & G.Spiezia
I2PS conception and design phase	A.Danisi
Electromagnetic modelling	
Finite element modelling	
Testing	
Thermal compensation algorithm	
High frequency phenomena	
Parasitic capacitance study	L.Sabato
Shield impact analysis	S.Troisi
Influence of external objects on the measurement read	A.Grima

2.4.1 Design

The main body of the I2PS houses four out of the five coils of the sensor and is stationary [56, 56]. These four coils are the two supply and two sense coils, which are stationary. These coils are wound on a common 1.5 mm thick plastic bobbin, which is 20 mm in diameter. As presented in Figure 2.8, the sense coils are wound directly on the plastic bobbin. These two coils are wound 1 mm apart from each other. The supply coils are wound exactly on top of the sense coils adhering to the size (80 mm) of the sense coils. The two sense coils are the same. This implies that they have the same wire diameter (0.05 mm) in that they both have three layers of 1600 $turns$. This said, their resistance and inductance is equal. Indeed, when supplied by a current source these two coils are connected in series.

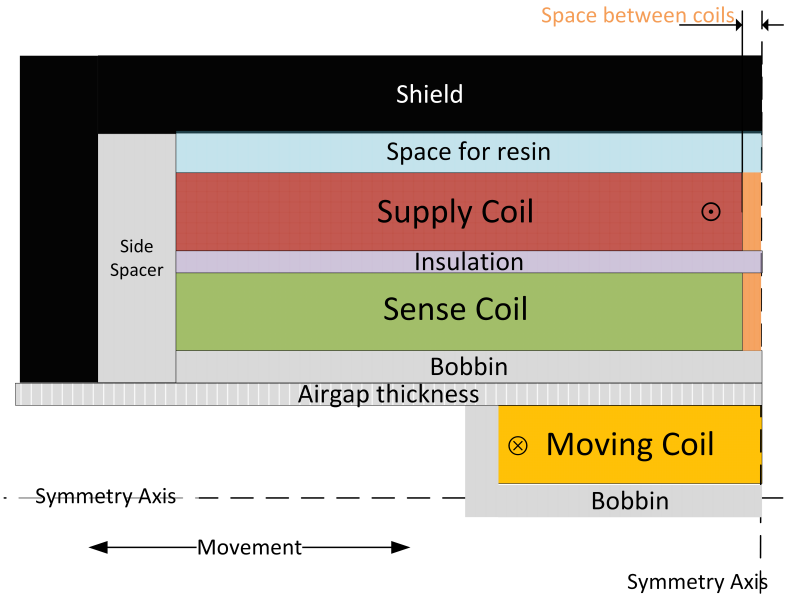

Figure 2.8: I2PS Diagram. A quarter of the I2PS design is presented since the sensor is symmetrical in the x and y domain

Similarly, the supply coils are also almost identical. They are both wound with a 0.2 *mm* wire, both of them have four layers and 400 turns per layer. (The number of turns is worked out by dividing the length of the coil i.e. 80 *mm* with the thickness of the wire, these values are as designed by A. Danisi [56]). Thus, their resistance and inductance are the same. The only difference in the supply coils is that they are wound opposite to each other and so the magnetic field they generate when they are supplied by a sinusoidal signal, is equal but opposite.

The fifth coil constitutes the movable part of the structure and due to this, it is referred to as the moving coil. The latter is wound on its own, 90 *mm* long; 4 *mm* wide, plastic bobbin with a 0.4 *mm* wire, hence generating 3150 turns (225 turns per layer for fourteen layers). The moving coil is short-circuited such that a current is induced when the coil is in a magnetic field. A stainless steel 316 LN shield covers the body of the sensor to provide mechanical protection. The sensor is hermetically sealed with resin and so the sensor is also guaranteed to be radiation hard.

2.4.2 Working principle

When the supply coils are fed with an ac signal a magnetic field is generated inside the sensor. When the moving coil is equidistant from the two sense/supply coils the net induced current in the latter is zero. Moreover, as transformer theory states, a

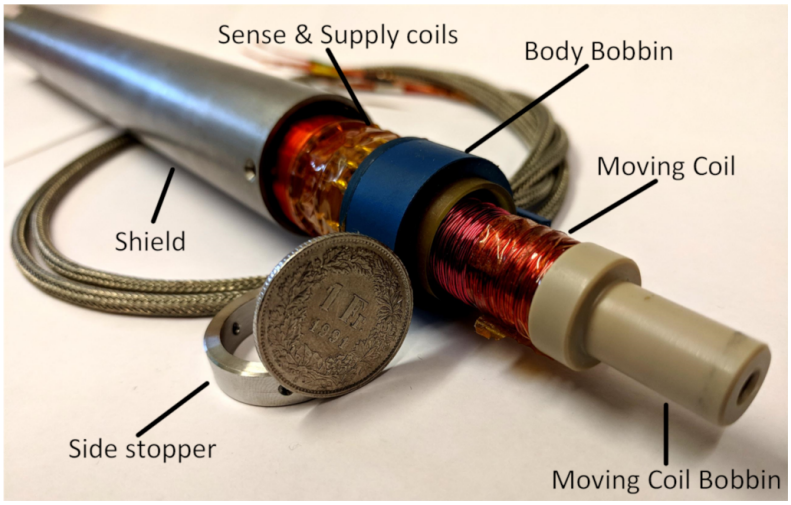

Figure 2.9: A photo of the I2PS pre-assembly

voltage is induced in the sense coils related to the supply coils by the ratio of their number of turns. When the moving coil is at the centre the voltage of the two sense coils, then it is the same. This happens because the mutual inductance between the moving coil and the two sense coils is equal. Indeed, this is the position in which the sensor is in equilibrium condition henceforth referred to as the electrical zero of the sensor.

As the position of the moving coil is changed, this equilibrium condition is broken. A current is induced in the moving coil. The mutual inductance between the moving coil and the sense/supply coils is higher on one side and lower on the other side. The extra magnetic flux on one side generates a higher voltage on one of the sense coils while the other sense coil suffers a voltage drop. For example, when the moving coil is parallel to Sense Coil 1 and hence Supply Coil 1, the magnetic field generated by this coil will decrease the coupling between these coils. On the other hand it will increase the coupling between Supply Coil 2 and Sense Coil 2. Hence, the position of the moving coil with respect to the electrical zero, can be extracted. This provides a sensor with higher sensitivity, with respect to a single supply coil construction like that of the LVDT. It is also independent of the need for a non-linear magnetic core, where the core would always perturb the coupling between supply and sense coils, but by different amounts.

In conclusion, the advantages of contact-less sensing, robustness, infinite resolution, very low position uncertainty and the possibility of having radiation hardness found in a typical off the shelf LVDT, are also brought out by the I2PS. The added-value of the I2PS is its immunity to external magnetic fields, hence making it a more suitable choice in case of environments characterised by harsh magnetic fields.

2.4.3 The electromagnetic and electrical model

As described in [56] the modelling of the I2PS is mostly made up of the calculation of the mutual and self-inductance of the different windings. Starting from the parameters of the windings, the values of self and mutual inductances can be accurately calculated and since the coils are air cored, the mutual inductances will be a function of the winding geometry and their relative position only. This said, the mutual inductance between the sensor's multiple layer windings was calculated by adding up the layer-by-layer mutual inductances. The mutual inductance between two single layers of two different windings have been in turn calculated by adding up the contribution of elementary mutual inductances between two circular coaxial turns, using the filament method [85]. Indeed, the mutual inductance in the latter case can be expressed as:

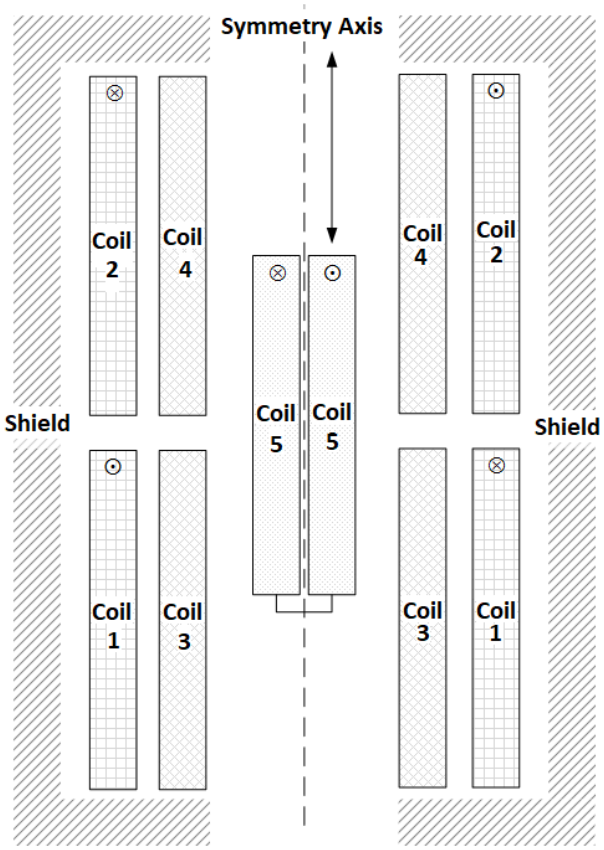

Figure 2.10: Longitudinal cross-section of the ironless inductive position sensor structure. The sensor is symmetric about the y-axis. Coils 1 & 2 are the supply coils. (Note that they are wound opposite to each other.) Coils 3 & 4 are the sense coils. Coil 5 is the moving coil.

$$\begin{aligned} M_l &= \frac{2\mu_0\sqrt{R_pR_s}}{k}\left[\left(1-\frac{k^2}{2}\right)K(k)-E(k)\right] \\ &= \mu_0\sqrt{R_pR_s}\phi(k) \end{aligned} \tag{2.4}$$

where $\mu_0 = 4\pi 10^{-7} H/m$, R_s and R_p are the coil radii and

$$\alpha = \frac{R_s}{R_p} \quad , \quad \beta = \frac{c_0}{R_p} \quad , \quad k^2 = \frac{4\alpha}{(1+\alpha)^2+\beta^2} \quad , \quad \phi(k) = \left(\frac{2}{k}-k\right)K(k) - \frac{2}{k}E(k) \tag{2.5}$$

Also c_0 being the distance between the turns, K and E are the complete elliptic integrals of first and second kind respectively. Therefore, letting N_{lp}, N_{ls} the number of layers of first and second winding and N_p, N_s the number of turns per layer of first and second winding respectively, the overall mutual inductance for the two coils at distance C_0 is:

$$M_\tau(C_0) = \mu_0\sqrt{R_pR_s}\sum_{i=1}^{N_{lp}}\sum_{j=1}^{N_{ls}}\sum_{n=1}^{N_p}\sum_{l=1}^{N_s}\phi_{i,j,n,l}(k_{i,j,n,l}) \tag{2.6}$$

where

$$k_{i,j,n,l} = \sqrt{\frac{4\alpha_{i,j}}{(1+\alpha_{i,j})^2+\beta_{i,n,l}^2}}$$

and the geometrical values defined in 2.5 are a function of the layer and/or of the distance between the single circular turns, as follows:

$$\alpha_{i,j} = \frac{R_{s,j}}{R_{p,i}} \quad , \quad \beta_{i,n,l} = \frac{C_{n,l}}{R_{p,i}}$$

with

$$R_{p,i} = R_p + (i-1)d_p \quad , \quad R_{s,j} = R_s + (j-1)d_s \tag{2.7}$$

$$C_{n,l} = c_0 + (z_n - z_l) \tag{2.8}$$

$$z_n = -a_p + (n-1)d_p \quad , \quad z_l = -a_s + (l-1)d_s \tag{2.9}$$

Where in Equation. 2.9, a_p and a_s represent the semi-length of the first and second

coil respectively, and d_s and d_p are the corresponding wire diameters. Furthermore, z_n and z_l are the z-coordinates corresponding to the n-th and the l-th turn of the first and second winding respectively. Then, when the moving coil is involved in the calculations of the mutual inductance, c_0 will be proportional to the actual moving coil position. Hence, the resulting mutual inductance will be also dependent on this position.

On the other hand the self-inductance can be seen as the superposition of the self-inductances of each layer of the multi-layer winding and the mutual inductances between the layers of the same winding. Therefore the self-inductance of a layer is computed as:

$$L_l = \frac{\mu_0 \pi N^2 R^2}{2s} T(k_l) \tag{2.10}$$

where N is the number of turns, R is the radius of the layer, S is the semi-length of the winding and

$$T(k_l) = \frac{4}{3\pi\beta k_l^3}\left[(2k_l^2 - 1)E(k_l) + (1 - k_l^2)K(k_l) - k_l^3\right]$$
$$k_l^2 = (1 + \beta^2)^{-1} \quad , \quad \beta = \frac{s}{R}$$

It is pertinent to point out that the ironless inductive position sensor can be energised either with a voltage or with a current signal. However, the behaviour of the sensor in these two situations has to be analysed separately, as seen in [56]. Adopting the number labels in Figure 2.10, Equations 2.11 and 2.12 give the general relations in phasor form that link the sense voltage with the supply currents.

$$V_3 = j\omega\left(M_{31}I_1 + M_{32}I_2 - \frac{j\omega M_{35}}{Z_5}M_{51}I_1 - \frac{j\omega M_{35}}{Z_5}M_{52}I_2\right) \tag{2.11}$$

$$V_4 = j\omega\left(M_{42}I_2 + M_{41}I_1 - \frac{j\omega M_{45}}{Z_5}M_{51}I_1 - \frac{j\omega M_{45}}{Z_5}M_{52}I_2\right) \tag{2.12}$$

where ω is the angular frequency, Z_i is the impedance of coil i and M_{ij} is the mutual inductance between coil i and coil j.

Where I_5 is obtained by simply applying the voltage balance on its mesh and

considering all the magnetic fluxes coupled with the coil. This leads to an induced current of:

$$I_5 = -\frac{j\omega}{Z_5}(M_{51}I_1 + M_{52}I_2) \tag{2.13}$$

where $Z_i = R_i + j\omega L_i$ is the winding impedance of the i-th coil (in the case of the moving coil the impedance of the short-circuited coil), M_{ij} is the mutual inductance between windings i and j and I_i is the current in coil i. (Equation 2.13 implicitly assumes that no current is flowing in the sense windings which are connected to the high-input impedance readout system).

Equations 2.11 and 2.12 are valid in any supply condition and neglect the effect of high-frequency phenomena. The position dependence is given by the mutual inductance involving coil 5 i.e. the moving coil.

Choosing the supply type, makes the position dependency on the supply more evident. In current supply, $I_1 = -I_2 = I$. Therefore, the supply currents are position-independent while the voltages are position dependent. In this case, the sense voltages can be represented by equations 2.14 and 2.15:

$$V_3 = j\omega\left(M_{31} - M_{32}\right)I + \omega^2 I\left(\frac{M_{35}M_{51}}{Z_5} - \frac{M_{35}M_{52}}{Z_5}\right) \tag{2.14}$$

$$V_4 = j\omega\left(M_{41} - M_{42}\right)I + \omega^2 I\left(\frac{M_{45}M_{51}}{Z_5} - \frac{M_{45}M_{52}}{Z_5}\right) \tag{2.15}$$

Therefore in the current supply case, the sense voltages become a superposition of a constant term and a variable term which changes according to the value of the mutual inductances involving the moving coil. The complete expression of the separate supply coil voltages is presented as:

$$V_1 = R_1 I + j\omega\left(L_1 - M_{12}\right)I + \frac{\omega^2 M_{15} I(M_{51} + M_{52})}{Z_5} \tag{2.16}$$

$$V_2 = -R_2 I + j\omega\left(M_{21} - L_2\right)I + \frac{\omega^2 M_{25} I(M_{51} + M_{52})}{Z_5} \tag{2.17}$$

Similarly, in the voltage supply case $V_1 = -V_2 = V$, the supply current is position-dependent and the voltages on the supply coils are position-independent. In this case, the sense voltages also depend on the impedance of the supply coils [81]. Equations 2.11 to 2.15 are a low-frequency description of the sensor's electromagnetic behaviours. A high-frequency analysis has been performed in [86], to take into account the skin and proximity effect and in particular their effect on the electrical resistance and inductance. The sampling, reading and filtering techniques implemented for the I2PS is presented in [53, 56] and unless otherwise stated these methods are used in the following experiments.

2.5 Summary

Without doubt, the description of the LHC collimation system serves as a useful introduction to better understand the requirements of specifications for the sensor. The low level control systems describe the function of the linear position sensors in the context of the task they are required to fulfil. Indeed, the specifications of LHC collimators pose a serious challenge to the design and operability of the sensors especially due to the harsh environment that they produce. This chapter has presented the main features and characteristics of the two linear position sensors used in the collimators. Moreover, it can be understood that the quest of obtaining a position sensor which is robust in a harsh environment such as that of space, nuclear power plants or particle accelerators, is still ongoing.

Having said this, this chapter presented some of the latest studies and enhancements done on linear position sensing solutions. Furthermore, the various studies carried out over the years to characterise the ironless inductive position sensor are presented. Different aspects have been investigated and indicate that further characterisation of the sensor is still required to obtain a robust sensor that is operable in any situation.

Chapter 3

Electrical Characterisation of the I2PS with Cable

3.1 Introduction

The use of long cables in ac circuits induce a list of problems varying from impedance, skin effect, to wire insulation. This gives rise to degraded overall performance and noise. Hence, this chapter aims at providing a deeper understanding on the electrical behaviour of the sensor with different lengths of cable. Since the cables in the LHC are secured on racks tribological phenomena is neglected in this study. It provides a metrological characterisation of the sensor in the frequency and time domain. Moreover, it investigates the impact on the performance of the I2PS due to changes in the cable capacitance in long cables. This chapter goes on and provides a unique Simulation Program with Integrated Circuit Emphasis (SPICE) model for the I2PS which is also able to simulate the cable's phenomena. Finally, a countermeasure circuit is designed in this simulation, whilst a prototype is built and tested.

3.1.1 Transfer function with cable

The relationship between the inductance, the input current, the output voltage and the moving coil position is well documented in [56, 78] and summarised in Section 2.4.3. Starting from the sense coils' voltages:

$$\begin{aligned} V_3 &= j\omega(M_{31} - M_{32})I + j\omega M_{35}I_5 \\ V_4 &= j\omega(M_{41} - M_{42})I + j\omega M_{45}I_5 \end{aligned} \tag{3.1}$$

where:

- M_{ij} are the mutual inductances between i^{th} and j^{th} coils;
- V_i = the voltage of the i^{th} coil of the I2PS;
- I is the input current (since the I2PS is using a current supply); and
- I_5 is the current induced in the moving coil.

Since these two equations are very similar and the only difference is the interaction of the different mutual inductances only V_3 will be considered. It is also known from [56] that:

$$\begin{aligned} I_5 &= \frac{V_5}{Z_5} \\ V_5 &= -j\omega(M_{51} - M_{52})I \\ Z_5 &= R_{mc} + j\omega L_{mc} \end{aligned}$$

where:

- R_{mc} is the moving coil resistance and
- L_{mc} is the moving coil inductance.

$$
\begin{aligned}
\therefore\ I_5 &= \frac{-j\omega(M_{51} - M_{52})I}{R_{mc} + j\omega L_{mc}} \\
V_3 &= j\omega M_3 I + j\omega M_{35}\left(\frac{-j\omega(M_5)I}{R_{mc} + j\omega L_{mc}}\right) \\
\frac{V_3}{I} &= j\omega M_3 + \frac{\omega^2 M_{35} M_5}{R_{mc} + j\omega L_{mc}} \\
\frac{V_3}{I} &= \frac{j\omega M_3 R_{mc} + \omega^2(M_{35}M_5 - L_{mc}M_3)}{R_{mc} + j\omega L_{mc}}
\end{aligned}
\tag{3.2}
$$

Taking the Laplace transform of $\frac{V_3(t)}{I(t)}$ the transfer function of the I2PS without cable can be defined as:

$$
\frac{V_3(s)}{I(s)} = \frac{(M_3 R_{mc})s + \omega^2(M_{35}M_5 - L_{mc}M_3)}{R_{mc} + (L_{mc})s} \tag{3.3}
$$

where: $M_3 = M_{31} - M_{32}$ and $M_5 = M_{51} - M_{52}$

The transformer like structure of the sensor is reflected in the derivation of the transfer function with the cables. In this case, the sense and supply coils have to be considered separately as follows.

3.1.2 Supply Coils Transfer Function

The nominal T-model of a medium transmission line is used where the lumped shunt admittance is placed in the middle and the net series impedance is divided into two equal halves, whilst being placed on either side of the shunt admittance. Figure 3.1 shows the T-model linked with the supply coil impedance. Since the two coils are connected together and a floating supply is used, the sensor forms a virtual ground between the two coils. Therefore, only half of the circuit needs to be considered.

Working directly in the S-domain:

$$
\frac{I_{out}}{I_{in}} = \frac{I_{out}}{I_1} \times \frac{I_1}{I_{in}}
$$

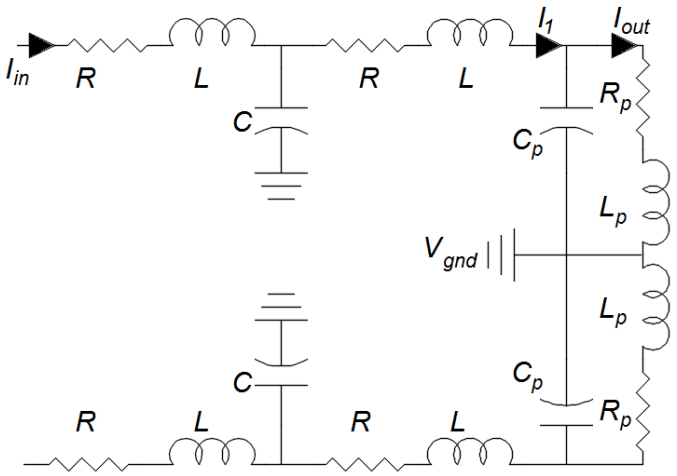

Figure 3.1: Cable model with I2PS supply coil as load

$$\frac{I_{out}}{I_1} = \frac{1}{s^2 C_p L_p + s C_p R_p + 1}$$

Where:

- C_p, L_p, and R_p are the capacitance, inductance and resistance of one supply coil.
- $L = \frac{lh}{2}$, l is the inductance of the cable per km, similarly $R = \frac{rh}{2}$ and $C = \frac{ch}{2}$ are the resistance and capacitance of the cable. R, C, L are the equivalent value in when using the T-model.

$$\frac{I_1}{I_{in}} = \frac{1}{s^2 LC + s(RC + ZC) + 1}$$

where:

$$Z = \frac{sL_p + R_p}{s^2 C_p L_p + s C_p R_p + 1} \tag{3.4}$$

$$\begin{aligned}
\frac{I_1}{I_{in}} &= \frac{1}{s^2 LC + s\left(RC + \left(\frac{sL_p + R_p}{s^2 C_p L_p + s C_p R_p + 1}\right) C\right) + 1} \\
&= \frac{1}{s^2 LC + \left(\frac{s^3 C_p L_p RC + s^2 C_p R_p RC + sRC + s^2 L_p C + sR_p C}{s^2 C_p L_p + s C_p R_p + 1}\right) + 1} \\
&= \frac{1}{\frac{s^4 C_p L_p LC + s^3 C_p R_p LC + s^2 LC + s^3 C_p L_p RC + s^2 C_p R_p RC + sRC + s^2 L_p C + sR_p C + s^2 C_p L_p + s C_p R_p + 1}{s^2 C_p L_p + s C_p R_p + 1}}
\end{aligned}$$

$$\frac{I_1}{I_{in}} = \frac{s^2 C_p L_p + s C_p R_p + 1}{s^4(a) + s^3(b) + s^2(d) + s(e) + 1} \tag{3.5}$$

where: $a = C_p L_p LC$, $b = C_p R_p LC + C_p L_p RC$, $d = LC + C_p R_p RC + L_p C + C_p L_p$, $e = RC + R_p C + C_p R_p$

$$\begin{aligned} \therefore \frac{I_{out}}{I_{in}} &= \frac{1}{s^2 C_p L_p + s C_p R_p + 1} \times \frac{s^2 C_p L_p + s C_p R_p + 1}{s^4(a) + s^3(b) + s^2(d) + s(e) + 1} \\ &= \frac{1}{s^4(a) + s^3(b) + s^2(d) + s(e) + 1} \end{aligned} \tag{3.6}$$

Because the I2PS is usually operated using a current supply, the voltage supply case is omitted from these derivations. It is important to consider that in the case of the use of a voltage supply, the supply coils are connected in parallel to the supply source, where one of them is inverted (to create the opposite induced field).

3.1.3 Sense coil Transfer Function

Figure 3.2 shows the equivalent circuit for the output side. In this case, the sense coil's parasitics need to be taken into consideration at the input end, while the acquisition input impedance needs to be taken as a load. In this case, the load is resistive but there are instances where bias capacitors are also added and hence need to be equated in the load.

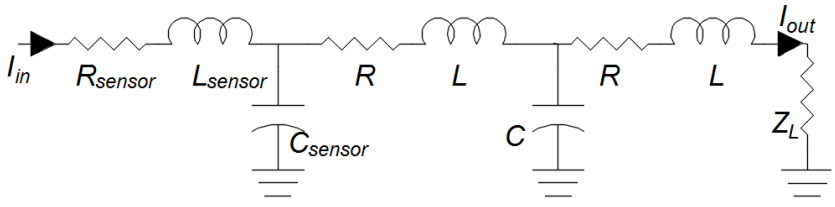

Figure 3.2: Cable model with I2PS sense coil as supply and acquisition bias resistor as load

$$\frac{V_{out}}{V_{in}} = \frac{I_{out}}{I_{in}} \times \frac{I_{in}}{V_{in}} \times \frac{Z}{V_{out}}$$

$$\begin{aligned}\frac{I_{out}}{I_{in}} &= \frac{I_{out}}{I_1} \times \frac{I_1}{I_{in}} \\ &= \frac{1}{[LC]s^2 + [RC + ZC]s + 1} \times \frac{1}{[LC]s^2 + [RC_{sensor} + Z_L C_{sensor}]s + 1}\end{aligned} \tag{3.7}$$

Where: $Z_L = \frac{sL+R+Z}{s[C_{sensor}L]+[ZC_{sensor}+C_{sensor}R]s+1}$

$$\begin{aligned}\frac{I_{in}}{V_{in}} &= \frac{1}{Z_{in}} \\ \frac{1}{Z_{in}} &= \left(R_{sensor} + sL_{sensor} + \left[\frac{1}{sC_{sensor}} \parallel R + sL\left\{\frac{1}{sC} \parallel Z + R + sL\right\}\right]\right)^{-1}\end{aligned}$$

where:

$$\begin{aligned}\left\{\frac{1}{sC} \parallel Z + R + sL\right\} &= \frac{Z + R + s[L]}{[CL]s^2 + [CZ + CR]s + 1} = A \\ R + sL\{A\} &= \frac{[L^2C]s^3 + [2(RCL) + LCZ]s^2 + [RCZ + R^2C + 2L]S + 2R + Z}{[CL]s^2 + [CZ + CR]s + 1}\end{aligned}$$

$$\frac{[L^2C]s^3 + [2(RCL) + LCZ]s^2 + [RCZ + R^2C + 2L]s + 2R + Z}{[L^2C_{sensor}C]s^4 + [2(RCL) + LCZ]s^3 + ([RCZ + R^2C + 2L]C_{sensor} + [CL])s^2 + ([CZ + CR] + [2R + Z]C_{sensor})s + 1}$$

Therefore,

$$Z_{in} = \frac{[L^2C]s^3 + [2(RCL) + LCZ]s^2 + [RCZ + R^2C + 2L]s + 2R + Z}{[L^2C_{sensor}C]s^4 + [B]s^3 + (D]C_{sensor} + [CL])s^2 + (E)s + 1} + R_{sensor} + sL_{sensor}$$

Hence,

$$\frac{1}{Z_{in}} = \frac{P}{[L^2C]s^3 + [B]s^2 + [D]s + 2R + Z + R_{sensor}(P) + sL_{sensor}(P)} \tag{3.8}$$

where:

$$B = 2(RCL) + LCZ$$
$$D = RCZ + R^2C + 2L$$
$$E = [CZ + CR] + [2R + Z]C_{sensor}$$
$$P = [L^2C_{sensor}C]s^4 + [B]s^3 + ([D]C_{sensor} + [CL])s^2 + (E)s + 1$$

Finally multiplying Equations 3.7 and 3.8 with Z gives $\frac{V_{out}}{V_{in}}$.

From the theoretical model, it can be deduced why it is advantageous to operate the I2PS with a current supply. Supplying the sensor with a voltage supply implies that the amplitude of the supply coil voltage will be a function of the cable length. Similarly, the temperature compensation voltage acquired by the Data Acquisition Board (DAQ) from the supply coils is also a function of the cable length.

3.1.4 Result Verification

The theoretical model is tested with a sinusoidal signal and the output voltages of $\pm 9.4\ V$ and $\pm 4.69\ V$ with a 50 mA and 2 $5mA$ peak current supply respectively. This voltage is obtained at a frequency of 1 kHz with the mutual inductances set for the moving coil to be at position 0 mm. The electromagnetic model presented in [56] can be used to generate the mutual inductances at other positions.

A test bench (similar to the one used in [81, 117]) is set-up where the I2PS is supplied by a Keithley 6221 current generator. The amplitude value is chosen in order to match with the model. A high-resolution high-sampling rate DAQ, NI-PCI 6351, is used to acquire the supply coils and the sense coils whose amplitudes are evaluated by applying a sine-fit algorithm on 2000 samples acquired at 250 kS/s. The absolute accuracy at full scale of the DAQ on a 10V range is 0.02% ($1520\mu V$). Then, the ratiometric index value is applied, i.e., the difference of the secondary voltage amplitudes over its sum. Let's take the sensor's operating position range as (-P,+P). Moving the I2PS moving coil from position -P to +P , using a stepper motor and linear slider combination a conversion table is created between the array of position readings p_i and their corresponding ratiometric values r_i. The reference positions p_i are measured by another independent displacement sensor. the absolute reference position is measured by means of the photoelectric

linear encoder Heidenhain LIP 481R, whose uncertainty is $\pm 0.5\ \mu m$. At each position p_i, (N = 50) repeated measurements are done to evaluate uncertainty. Then, the average of u is evaluated. It represents the uncertainty $u_{I2PS+read}$ of the I2PS sensor and the associated reading system. Indeed, the uncertainty of the sensor itself cannot be evaluated without the reading system. Hence, the reading system can be regarded as the transducer of the sensor.

When a 1 km return cable is added to the model there is a 4 V attenuation as can be noted in Table 3.1. There is an average difference of 0.43 V between the experimental values and the theoretical ones, i.e. 7% difference. This difference is acceptable and may be attributed to experimental error and minor physical phenomena both in the I2PS and the cable that are ignored in the analytical model. A.Danisi [56] showed that the I2PS is highly sensitive to coil geometries such as imperfections in the coil and resin. The same readings were repeated with different cable lengths, supply current and frequency giving approximately the same discrepancies.

Table 3.1: Table comparing the sense coil voltages obtained from the experimental test-bench with different cable lengths with respect to those obtained from the model and from the simulation. All the values are obtained with a current supply of 50 mA at 1 kHz at a sampling rate of 250kS/s while using sine fit for signal demodulation as presented in [53, 56]

Cable Length [m]	***Exp[V]***	***Model [V]***	***Diff [%]***
0	*8.5*	*9.4*	*10*
200	*8.3*	*9.1*	*9*
400	*8.1*	*8.4*	*4*
600	*7.5*	*7.3*	*3*
800	*6.7*	*6.3*	*6*
1000	*5.9*	*5.4*	*9*

3.2 I2PS Characterisation at Different Frequencies

3.2.1 Characteristic Curve at different Frequencies

Using the same test bench, the transducer's characteristic curve is obtained for various frequencies. It is noted that with different frequencies and the same supply voltage, the resulting output voltage changes [92]. Therefore, in order to have a good comparison for the characteristic curves, it is important that the sense coil's voltage is similar for all frequencies. Different reference points could be selected that can give a fair comparison. In this case the electrical zero is selected as the common point. Taking this as the starting point, the amplitude of the ac current is set such that the electrical zero position is always around 5 V. The dc current is set at 10 mA. Table 3.2 presents these settings.

Table 3.2: I2PS settings for 5 V at electrical zero and the respective sensitivity and NLE

Frequency [Hz]	I_{ac} **[mA]**	**Gain**	**NLE**
500	*61.67*	-371	2.13
750	*40.9*	-267	1.27
1000	*30.5*	-229	0.8
1250	*24.20*	-212	0.55
1500	*20*	-202	0.4
1750	*16.94*	-195	0.3
2000	*14.65*	-190	0.27
2250	*12.85*	-187	0.28
2500	*11.38*	-183	0.28
2750	*10.18*	-181	0.29

Using these settings, Figure 3.3 presents the characteristic curve of the I2PS at different frequencies while Figure 3.4 presents the ratiometric index for all the curves and the last two columns of Table 3.2 present the gain which is the gradient of the ratiometric index index and NLE of these curves. (Note that the gain value is negative due to the gradient of the ratiometric index as presented in Figure 3.4)

The Non Linearity Error (NLE) is computed as:

$$NLE = 100\frac{max(p' - p^*)}{CPR} \tag{3.9}$$

where $p^*$is the core reference position, p' is the position calculated through linear interpolation of the curve and CPR is the core position range.

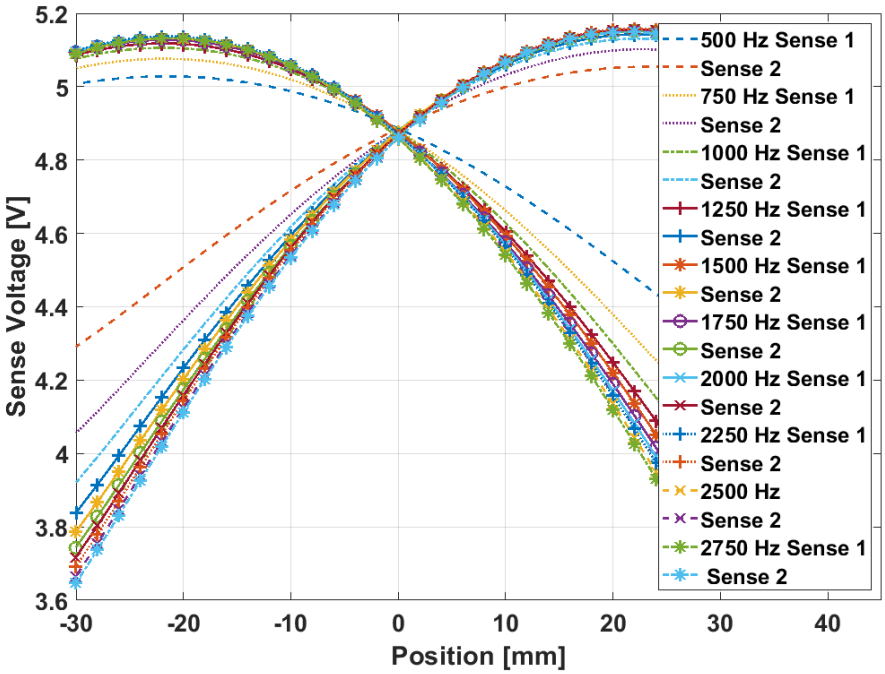

Figure 3.3: I2PS characteristic curve

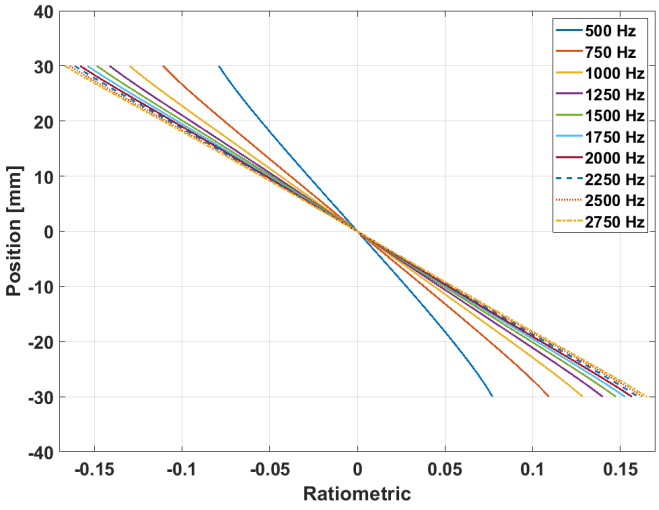

Figure 3.4: I2PS ratiometric index

Figure 3.3 shows that as the frequency increases the voltage swing increases, similarly, Table 3.2 shows that the gain increases as the frequency increases. This increase in voltage swing is also reflected in the NLE which decreases as the frequency increases. Note that as the frequency increases the change in gain and

voltage swing decreases. i.e. the gain changes by 169 between 500 Hz and 1500 Hz, on the other hand it changes by 20 between 1.5 kHz and 2.75 kHz.

3.2.2 Frequency analysis

For a thorough frequency analysis of the sensor with cables, an empirical approach is adopted such that un-modelled parasitic effects are not ignored. A test bench similar to the one described in Section 3.1.4 is set up. The difference in this case is that frequency analysis is the main aim and so a network analyser is used with an active probe. This offers probing with negligible circuit loading due to its low input capacitance. To achieve the frequency response of the I2PS with a long cable at the different cable lengths the different pairs in a 200 m cable were bridging. It was made sure that each 200 m portion is disconnected when not used. This is because it was noted that this affects the results. (The 1 km cable combination, in 200 m steps, was compared with a 1 km cable and showed the same results.)

The frequency response of the I2PS is obtained not only to describe the effect of the cable's length on the sensor but also to obtain a more in-depth understanding of the frequencies of operation of one of the transducers. Figure 3.5 shows the measured I2PS frequency response with and without the cable, with the moving coil at the centre. It is noted that with the moving coil at the centre and without the moving coil, the frequency response of the cable and amplitude remain the same. Without the cable, the I2PS exhibits a response similar to that of a high pass filter. A +20 dB/dec gradient can be noted at low frequencies up to a cut-off frequency of 1.3 kHz, where the sensor achieves a flat response with an average of 1.5 dB gain.

On the other hand, when the cable is attached, the response becomes similar to that of a band pass filter. This graph also shows that an increase in cable length leads to a narrower bandwidth and a lower gain. It is important to note that there is a 5.5 dB difference in gain without cable compared to when the sensor is connected to a 1 km cable as is shown in Figure 3.5. This 5.5 dB difference in gain translates to 275 μm of position change. It is also important to notice that the cable does not have a very drastic impact on the gain at low frequencies up to 900 Hz. For comparison with a peer, the same procedure was repeated for the LVDT. Despite the fact that the LVDT is the basis for the I2PS design, the method of operation and construction differs for the two. This reflects on their frequency response.

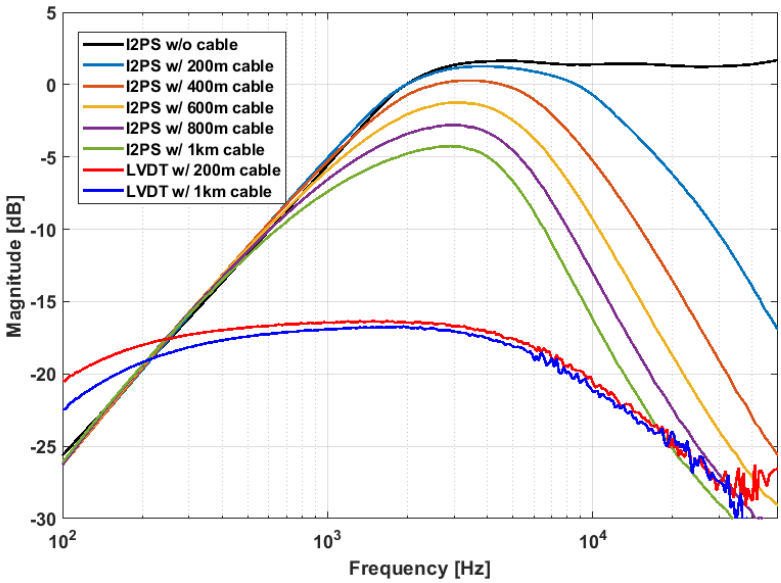

Figure 3.5: Comparison between the effect of the cable on the frequency response of the I2PS and the LVDT, as obtained from test bench

Unlike the I2PS, which is defined by its low frequency gradient, the LVDT has a much lower gain and smoother flat band. Furthermore, a change in the cable length of the LVDT does not change the bandwidth of the sensor. Increasing the cable length attenuates the gain at the lower frequencies.

To understand the origin of the characteristic curves presented in Figure 3.3 the moving coil is moved at 10 mm intervals between ± 30 mm. This test produces the range of frequencies where the sensor still exhibits change in output voltage when the moving coil is moved. Combining this test with the cable length produces a set of results which identifies the limit of operation of the sensor from a combined frequency and cable length point of view. Hence, a guideline can be defined which dictates the frequency range at a particular cable length.

Figures 3.6 and 3.7 show the frequency response when the the moving coil is moved and the cable length is 200 m and 1 km. The other lengths are not presented since they are a repetition of these two but bounded by them (meaning the effect is smaller than in the 200 m case, but greater than in the 1 km case.)

Furthermore, Figures 3.6 and 3.7 show that even though the cable length reduces the bandwidth, the voltage variation due to the moving coil is not altered. It is noted as well that the range of operation of the I2PS is between 500 Hz and 2.5 kHz. Additionally, it can also be observed that a variation in the frequency also varies the amplitude of the sense coils. This change depends also on the cable's length because the flat top is achieved much faster with the 1 km cable as opposed

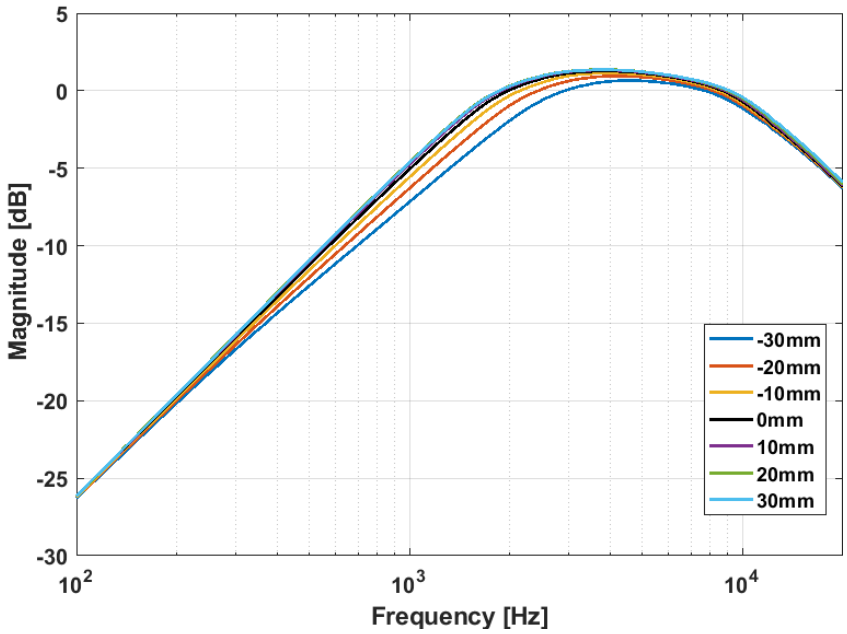

Figure 3.6: Varying the moving coil position with a 200 m cable

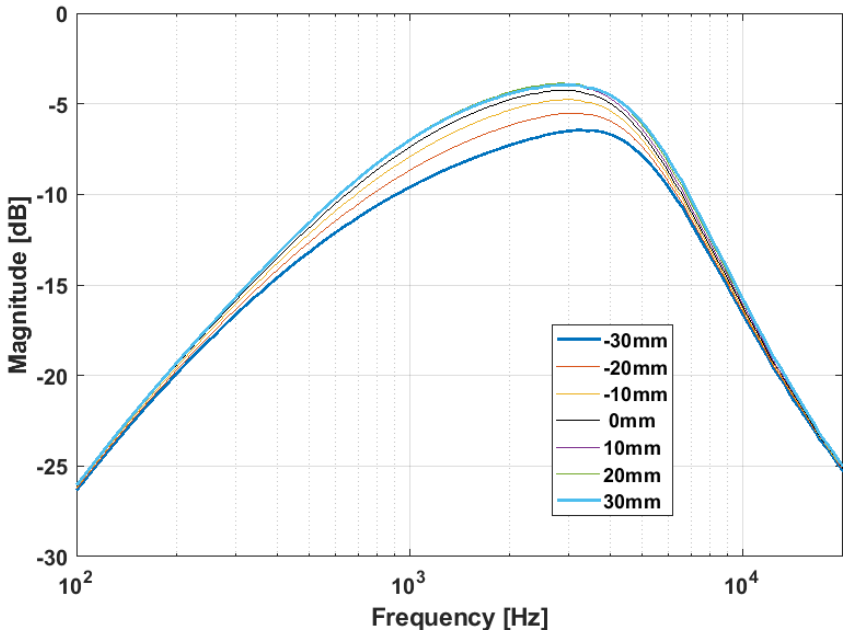

Figure 3.7: Varying the moving coil position with a 1 km cable

to the 200 m one. Correlating these graphs to position, a change between a 200 m cable to a 1 km one at 2 kHz translates to 725 μm and a change of frequency from 1 kHz to 2 kHz translates to 400 μm of change.

As can be noted from Figure 4, this change could be avoided if the frequency of operation selected was on the flat band of the frequency response. This is not possible since at those frequencies the sensor is not sensitive to change, as can be noted from Figure 3.6 and Figure 3.7. It is also important to note that if a new

sensor is designed, which is sensitive in the pass band of the frequency response of Figure 4, it must be ensured that the cable does not attenuate this frequency. This is because in this case the cable's effect is noted mostly at high frequencies. It can therefore be deduced that the best option is to have a sensor whose passband starts from low frequencies.

3.3 Simulation

The necessity of a reliable SPICE model of the I2PS is accentuated by the fact that there is no fast and economic tool to simulate the transducer and other electronics. This is the added advantage over the electromagnetic and finite element models. Since such a model is able to capture the impact of all major non-ideal effects of a practical I2PS and cable, it is capable of modelling the sensor‘s sensitivity to the cable.

LtSpice by Linear Technologies is used to model the I2PS. The discrete equivalent circuit of the I2PS is based on that of a transformer since the I2PS has five cross-coupled coils. SPICE simulators use coupling constants (in LtSpice it is called k-statements) to signal the coupling strength of an inductor with another inductor [144].

The mutual inductance and the self-inductance as obtained from the electromagnetic model are used to calculate the coupling constant k using the equation:

$$k = \frac{M}{\sqrt{L_1 L_2}} \tag{3.10}$$

It is important to note that the coupling constants have to obey the following constraints $0 \leq k_{ij} \leq 1$ (where 1 is perfect coupling) and also:

$$0 \leq \begin{vmatrix} 1 & k_{12} & k_{13} & k_{14} & k_{15} \\ k_{12} & 1 & k_{23} & k_{24} & k_{25} \\ k_{13} & k_{23} & 1 & k_{34} & k_{35} \\ k_{14} & k_{24} & k_{34} & 1 & k_{45} \\ k_{15} & k_{25} & k_{35} & k_{45} & 1 \end{vmatrix} \leq 1 \tag{3.11}$$

The determinant size of equation 3.11 changes depending on the number of coils.

Apart from the inductance, coupling coefficients and the resistance of the coils, there are a number of important parasitic capacitances to be added to the circuit. Namely, the self-capacitance of the coils and the cross-coil capacitance between the supply and sense coils. These capacitance can be calculated by assuming that the last layer of the coils is a cylindrical foil [83] and hence the capacitance is simplified to:

$$C = \frac{2\pi\epsilon_0\epsilon_r l_c}{\ln\left(\frac{R_2}{R_1}\right)} \tag{3.12}$$

On the other hand, the calculation of the self-capacitance of the coils is more complicated since a multilayer coil has to be considered.

This is achieved by first calculating the turn-to-turn capacitance of a thin cabled multi-turn coil using the equation:

$$C_{tt} = \frac{2\epsilon_o\epsilon_r l_t}{\sqrt{\left[2\epsilon_r + \ln\frac{r_o}{r_c}\right]\ln\left(\frac{r_o}{r_c}\right)}} \times \arctan\left(\frac{\sqrt{3}-1}{\sqrt{3}+1}\sqrt{\frac{2\epsilon_r + \ln\left(\frac{r_o}{r_c}\right)}{\ln\left(\frac{r_o}{r_c}\right)}}\right). \tag{3.13}$$

where: ϵ_r is the coating permittivity of PEEK [1], r_c is the inner radius of the

[1]Polyether ether ketone (PEEK) is a colourless organic thermoplastic polymer in the polyaryletherketone (PAEK) family, used in engineering applications.

conductor, r_o is the outer radius of the conductor including the coating, $l_t = 2\pi(r_s + \frac{k_l}{2} r_o)$ is the medium length of the turns, k_l is the number of layers and r_s is the curvature radius of the coil.

It is noted from [86,116] that parasitic capacitance for a three-layered core-less coil converges to:

$$C \approx 0.5733\ C_{tt} \tag{3.14}$$

and similarly, the stray capacitance for a four-layered core-less coil converges to:

$$C \approx 0.754\ C_{tt} \tag{3.15}$$

As explained by L. Sabato [83] there are other parasitic capacitances for this sensor. Additionally, these capacitances cannot be calculated since the classical equations for the capacitance cannot be used, hence the latter are obtained empirically. This implies that this simulation will not be generic for any I2PS or similar sensor and requires a separate procedure to obtain these values. Having said this, using the values obtained from [83] the simulation was tested with and without these capacitances and from the results it can be deduced that they can be omitted since they are very small and will only effect the sensor at very high frequencies.

Table 3.3 presents the electrical properties of the supply and sense coils as well as the electrical properties of the long cable used.

Table 3.3: Electrical properties of an I2PS and cable parameters as measured by LCR meter with 0.01% accuracy

I2PS			
	Supply Coil	***Sense Coil***	***Cable***
Resistance [Ω]	*55*	*3.3*	37.5 [Ω/km]
Capacitance [pF]	*5.91*	*2.24*	<75 nF/km
Inductance [mH]	*11.9*	*94.7*	650 μH/km
LVDT			
	Primary Coil		***Secondary Coil***
Resistance [Ω]	*61.2*		*332.9*
Inductance [mH]	*3.86*		*4.82*

As it can be observed from the block diagram presented in Figure 3.8, the circuit is supplied through a floating current supply. This produces a sinusoidal current which is not with respect to ground or a reference. In order for the temperature compensation to work, a dc current circuit (10 mA) is added to the signal. A.Danisi [79] showed that with this dc current amplitude, the self heating of the sensor is negligible. The inductor model incorporates the parasitic capacitances and resistance of the coils. The parasitic capacitance, C_{ss}, links the supply and sense coils. At the end of the circuit, as explained at the beginning of this section, there is the decoupling capacitors and resistors required for the DAQ as specified by National Instruments (NI) [118]. Finally, as explained in Section 2.4.3 the moving coil is short-circuited such that a current is induced. Since, the simulator does not allow short circuits and non-grounded circuits a 0 Ω resistance and a ground connected through a 100 $k\Omega$ resistance are used. The latter satisfies both the simulator requirements and ensures correct operation.

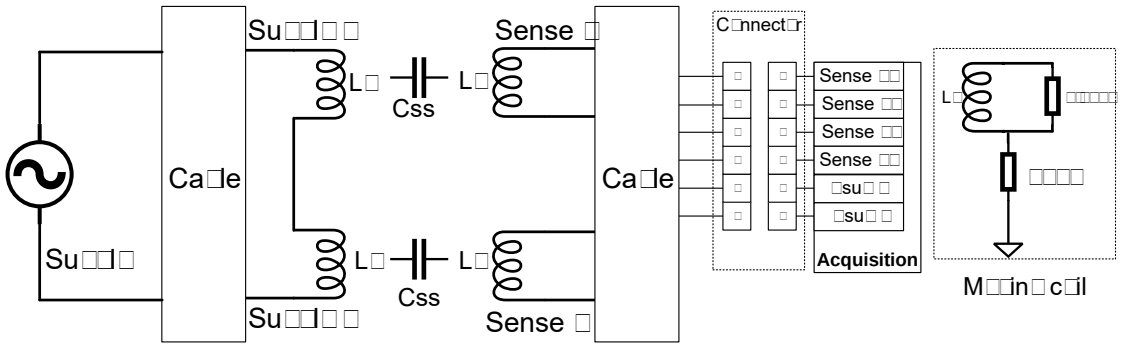

Figure 3.8: Block diagram of the simulation circuit

3.3.1 Simulation Results

The I2PS is first simulated without the cable or additional circuitry. Figure 3.9 presents a comparison between the characteristic curve of the I2PS obtained from the simulation and from the test-bench. The graph describes the same non-linear symmetric dependence of the first harmonics with respect to the moving coil position as that of the experiment with a maximum discrepancy of only 3%.

Furthermore, the output voltage is attenuated by 3 V when the 1 km return cable is added to the simulation as presented in Table 3.4. The difference between the experimental voltages and the simulated ones reaches a maximum of 2.5%, which is acceptable. Moreover, although the mutual inductance values are obtained from the electromagnetic model, the initial voltage is closer to the test bench voltage

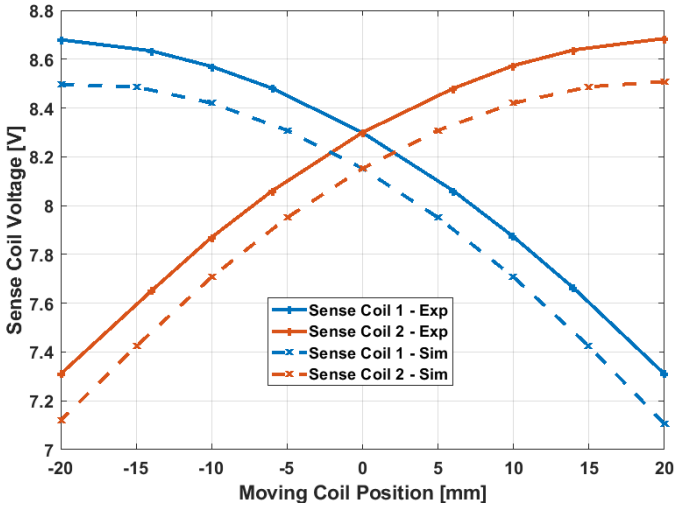

Figure 3.9: Comparison of the I2PS sense voltages at different positions from the test-bench with the simulation. Obtained at 50 mA at 1 kHz.

than the electromagnetic model. This is mostly because the simulation models the whole network of discrete components. The same values are reproduced when the same readings were repeated with different cable lengths, supply currents and frequencies.

Table 3.4: Comparison of the sense coil voltages obtained from the experimental test-bench with respect to those obtained from the simulation. The table also provides the percentage difference between simulation and experiment.

Sense coil's voltage			
Cable Length [m]	***Experiment [V]***	***Simulation [V]***	***Difference [%]***
0	*8.5*	*8.3*	*2.4*
200	*8.3*	*8.2*	*1.2*
400	*8.1*	*8*	*1.3*
600	*7.5*	*7.4*	*2*
800	*6.7*	*6.5*	*97.6*
1000	*5.9*	*5.6*	*2.4*

The frequency response of the sensor attached to the supply circuitry, cable and acquisition as obtained from the test-bench are compared with the simulation results in Figure 3.10. The latter compares the simulation with the experimental measurements for three different cable lengths with the moving coil set in the centre. The frequency response of the simulation is similar in shape to that obtained from the experimental test bench. The behaviour, meaning the way the gain and bandwidth decrease when the cable length is increased, is also comparable.

Without the cable, the frequency response is very similar. The magnitude raises

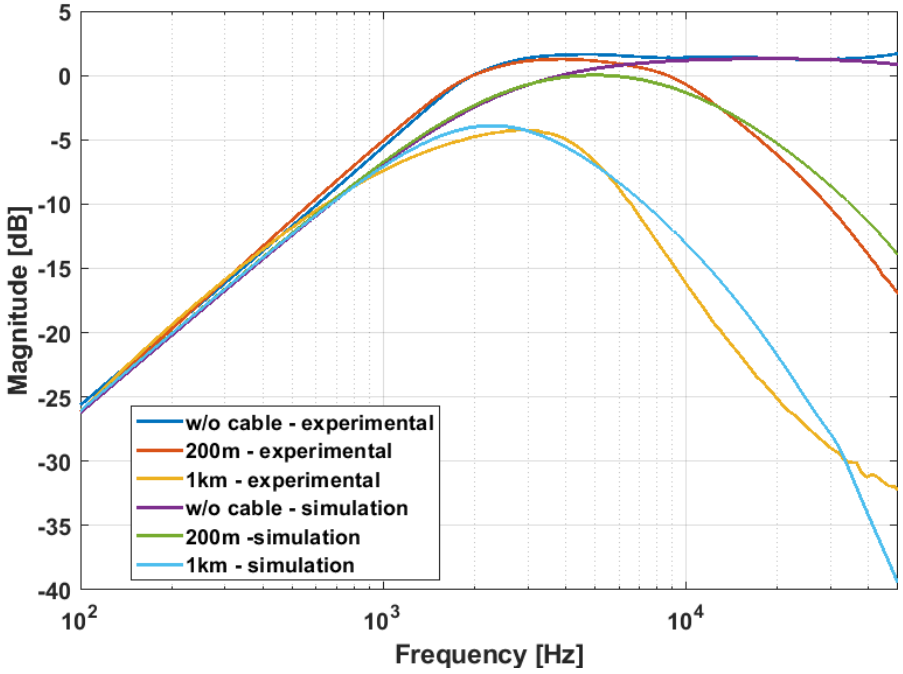

Figure 3.10: Effect of cable on the frequency response with different cable lengths with comparison to simulation

with the same gradient to approximately 1 kHz, where it starts a much slower decrease towards the plateau than the test-bench one. Similar to the latter, the simulation converges towards 1.5 dB and continues towards higher frequencies which are not important for this study. The frequency response with the 200 m cable behaves very similar to the one without cable, with the difference that a roll-off happens around 10 kHz for the test-bench. The frequency response of the simulation with the 200 m cable repeats this performance while matching the frequency response of the simulated short cable. Similar to the test bench it then conversely starts a roll-off at around 10 kHz. Finally, the response of the sensor with a kilometre of cable exhibits a degraded amplitude and bandwidth.

This behaviour is repeated in the simulation. As can be noted from Figure 3.10 the only difference is the shape where the simulated one is much smoother and symmetrical with respect to the experimental one.

As explained in previous sections, this difference is due a number of factors that cannot be taken into account in the simulation. This includes imperfections in the winding's multi-layers and in the shield. Moreover, the lack of homogeneity of the electrical conductivity in the shield and the imperfections of the sealant used to seal the sensor, influence significantly the parasitic components of the sensor at high frequency. Furthermore, the sensor has a strong sensitivity with respect to the winding's imperfection, especially on the moving coil [56]. Since

the simulation is strongly dependent on ideal geometrical values, it can lead to big changes. Having noted this, the overall simulation, meaning both the time domain and the frequency domain results, produce comparable measurements as that of the test bench measurements. It can therefore be concluded that within this parametric space, the simulations can be used when variations to the sensor's electronics are required.

3.4 Sensitivity to Change in Cable Parasitic Capacitance

A water flood of a small section of the tunnel which wet the cables showed strange position drifts in the position reading of the I2PS. This launched an investigation in the cables used for the standard I2PS operation in the LHC tunnels. It is noted that the latter are not immune to defects. In fact, these cables may have protrusions, voids, cracks, de-laminations, conductor shield interruptions, water trees and electrical trees [121]. The polymeric insulation is also prone to ageing, degradation and other breakdown mechanisms which are statistical in nature [119, 122, 123]. A change in the dielectric of the cable or of the space in between the cables leads to a change in the cable capacitance.

Indeed, three possible capacitance combinations can be identified in a multi-pair cable as seen in Figure 3.11:

- The capacitance between the two cables of one twisted pair - henceforth referred to as *mutual capacitance* - MC;
- The capacitance between one cable of a twisted pair and another cable of another twisted pair - henceforth referred to as *cross-cable capacitance* - CC; and
- The capacitance between one cable of a twisted pair and the shielding foil - henceforth referred to as the *cable-to-shield capacitance* - CS.

Referring to Figure 3.8, the notation adopted to present the following results numbers the cables using the number assigned to the latter in the connectors. For

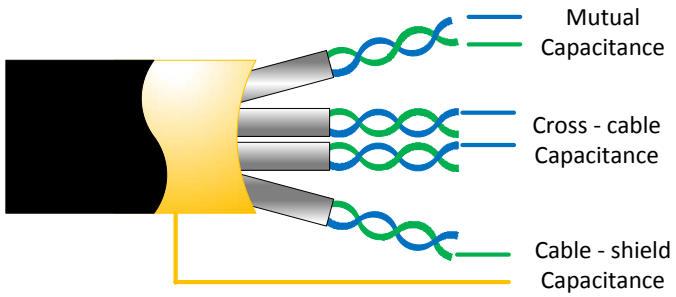

Figure 3.11: Existent capacitances between cables in a multi-shielded-twisted pair cable

example, a change in the mutual capacitance of the twisted pair cable connected to the sense 2 coil is referred to as 3-4, since it is the capacitance between cable 3 and 4. The same pair's cable-to-shield capacitance is referred to as G-3 and G-4. Similarly, for the cross-cable capacitance it is referred to as 1-3, 1-4, 3-5, 3-6. Therefore, the capacitance change between cable X and cable Y is named X-Y. The cables copper sheath is referred to as "G".

The setup described in Section 3.1.4 is used with some small changes. The investigative method adopted for the capacitance sensitivity measurements is as follows:

1. To satisfy the warm up time recommended (fifteen minutes) by NI for the DAQ [142] the sensor is turned on, and left working for thirty minutes;
2. The electrical zero of the I2PS is then found. This is done by moving the moving coil until both sense coil voltages are equal hence the ratiometric index is very close to zero. This marks the centre of the sensor and hence the linear encoder is reset to 0 mm;
3. The moving coil is then moved to the positions required, in this experiment the positions: $\pm 20\ mm, \pm 10\ mm, \pm 5\ mm, \pm 2.5\ mm$ are selected;
4. For every measurement, the position of the I2PS is recorded first with the capacitance box disconnected and then the capacitance box is connected and a sweep starting from 50 pF to 10 nF is performed.

Since the I2PS is built as a valid alternative to the LVDT, the same procedure is also repeated on the LVDT, to verify if the same phenomenon is also present in this linear position sensor.

3.4.1 Test-bench Results

The setup results show that for all capacitance combinations a change in the latter corresponds to a change in position. However, they exhibit two small differences: the impact is not always of the same magnitude and the impact is not always linear [146]. These averages are summed up in Table 3.5.

Table 3.5: Comparison of the average sensitivity for the I2PS and LVDT as obtained from the test-bench

Δ c between:		**Sensitivity** $[\mu m/nF]$	
		I2PS	***LVDT***
Mutual capacitance	***1-2***	*-448*	*-10*
	3-4	*440*	*11*
Cable-shield capacitance	***G-1***	*-91*	*-1*
	G-2	*-105*	*-1.2*
	G-3	*96*	*1*
	G-4	*95*	*0.62*
Cross-cable capacitance	***1-3***	*-1.92*	*1*
	1-4	*1.65*	*-0.03*
	1-5	*-363*	*0.06*
	1-6	*132*	*2.6*
	2-3	*-8.56*	*0.01*
	2-4	*1.25*	*-1.4*
	2-5	*135*	*1.1*
	2-6	*-350*	*1.6*
	3-5	*-149*	*-1.4*
	3-6	*351*	*-1.8*
	4-5	*365*	*-0.07*
	4-6	*-160*	*-2.6*

From this table it can be observed that the mutual capacitances contribute to the highest sensitivities. As expected, fitting a linear line on the graph presented in Figure 3.12 approximates the sensitivity to be $\pm 445\ \mu m/nF$. Figure 3.12 presents a general summary of the capacitance effects on position result. Thus only a few combinations are presented.The most dominant effect of cable capacitance change on the I2PS is on the mutual capacitance, followed by the cross-cable capacitance. Furthermore, it can be concluded that, a capacitance change of the mutual capacitance is very dangerous since it directly increases the capacitance of

the sense coils. Coil theory models a non-ideal coil as an inductor and resistor in series, with a capacitance in parallel to the two. Hence, a change in the mutual capacitance of the cable changes the overall impedance model of the coil in question by adding (since it is parallel) to its self-capacitance. In theory, a small change in the self-capacitance of a coil should not have these drastic implications but since the I2PS is a perfectly balanced bridge circuit, a slight change in one of these capacitances directly leads to an imbalance leading to a position change.

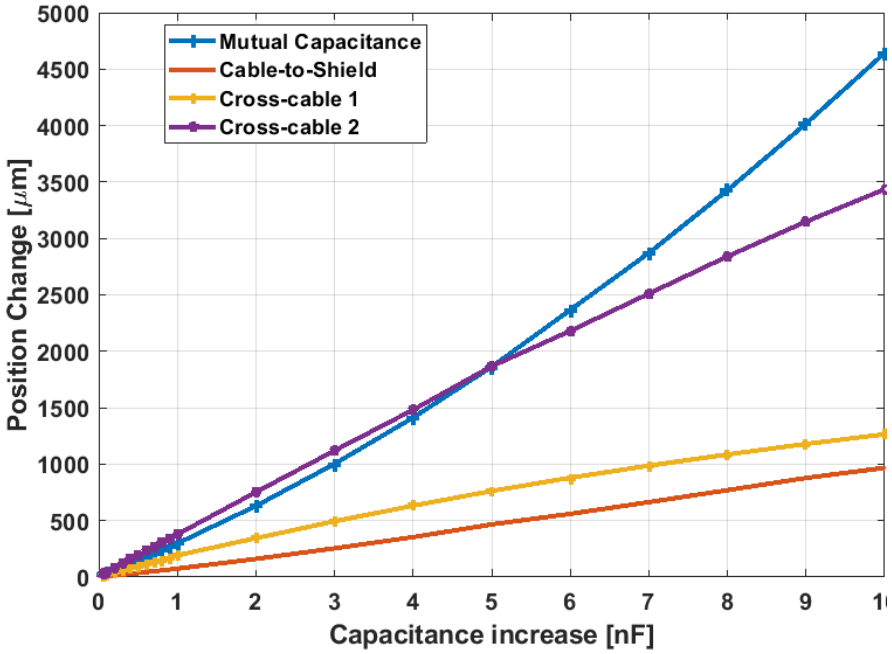

Figure 3.12: I2PS position change due to a change in cable capacitance, as obtained from the test bench.

Table 3.5 and Figure 3.13 show that a symmetrical sensitivity exists for each position change of each combination. This implies that if the capacitance changes equally on all cables, which is highly unlikely, all the effects would cancel since the balance of the bridge would be kept. Moreover, what is noteworthy about the results is that although the sensitivity is symmetrical about the x-axis, it is not identical. This can be attributed to small imperfections along the sensor or the cable. Furthermore, the same procedure is repeated on different moving coil positions and it is noted that the position change is constant for all moving coil positions. This is the reason why although in theory an equal change in capacitance on all cables should cancel out, in practice it cannot. Table 3.5 also compares the position change of the I2PS with that of the LVDT. The profile of the latter is also presented in Figure 3.14. Observe the lower sensitivity, approximately $\pm 11\ \mu m/nF$, of the LVDT. Similar to the frequency response, the behaviour of the LVDT is very different from that of the I2PS. In this case, this is because the LVDT does not depend heavily on the self and mutual inductance of the coils, but it depends

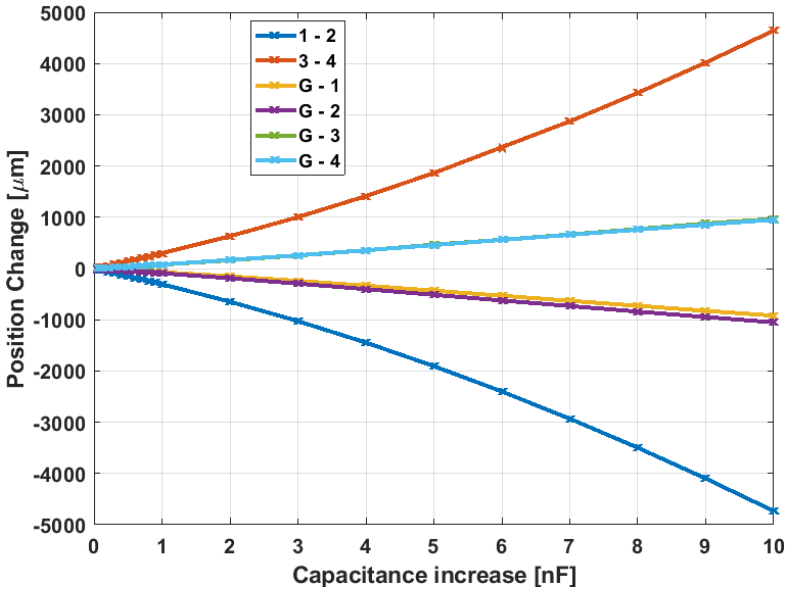

Figure 3.13: All mutual and cable-to-shield capacitances

heavily on the magnetic core.

Figures 3.13 and 3.12 also present the cable-to-shield capacitance. The behaviour for the cable-to-shield capacitance is linear with respect to capacitance change. From Table 3.5 it can be observed that the sensitivity drops to $\pm 100\ \mu m/nF$. This capacitance is pulling the common mode signal to ground, since in the cable the shield is grounded. The grounding effect depends on the size of the capacitance.

Following the mutual capacitance, some of the cross-cable capacitance also exhibits a very high position change. The highest cross-cable capacitance sensitivity is presented in Figure 3.12. Table 3.5 presents the sensitivity of every combination. For the cross-cable capacitance, the sensitivity depends heavily on which cable is linked to which other cable. The biggest impact in this case happens when cables 1-4 i.e. the sense coils cables, are connected to cables 5-8 i.e. the supply coil cables. The supply coil, as explained in previous sections, is supplied with a current source. Consequently when tested the mutual and cable-to-shield capacitance do not impact the position if applied to cables 5 to 8. On the other hand, in this case it affects the sense coils because the supply coil's voltage, needed for the temperature compensation, is also an ac voltage signal of approximately the same amplitude as the sense coils with a dc offset. The dc part is not affected by the added capacitance and hence the temperature compensation still works correctly. The primary ac signal, which is not used, influences the sense coil voltages when linked to them by adding an unbalanced common mode noise, which the differential receivers cannot reject.

Receivers used with such cables acquire differential signals, while essentially rejecting common mode signals [120]. However, there are sources of differential noise, even in a well-balanced twisted pair transmission line. Because of coupling, asymmetrical parasitic reactance is a main cause of differential noise. In the body of a multi-pair cable, each wire of each pair is affected considerably equally by adjoining wires because the pair is twisted. Nonetheless, there are scenarios that give rise to coupling between adjacent wires from different pairs. This leads to an interfering signal injected into one wire of a pair, but not into the other i.e. differential noise.

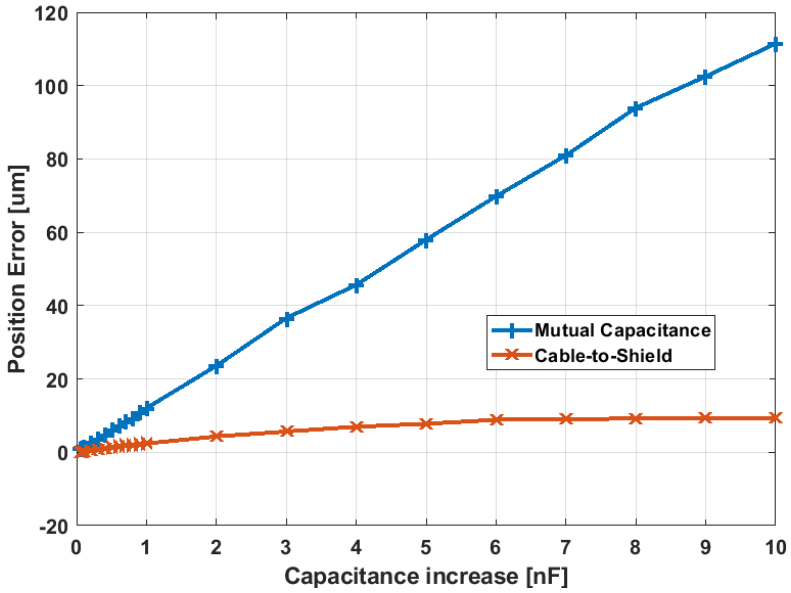

Figure 3.14: LVDT position change due to an increase in the mutual and cable-shield capacitance, as obtained from the test bench.

Once the problem of high sensitivity to capacitance change is demonstrated in the tests, the same effect is re-created in the SPICE simulation presented previously. Additionally, this task was also performed to have a platform on which a possible countermeasure can be developed. The simulation presented in Section 3.3 is modified to add the cable properties as measured from the test-bench and obtain a result similar to the test-bench. This modification is presented in Figure 3.5.1.

Figure 3.15 compares the results obtained from the simulation to that of the test-bench. Note from this figure that the general shape and magnitude for the simulation corresponds with that of the test-bench. As the capacitance change increases, the difference between the latter increases. A 94% match with the test-bench is observed for the mutual capacitance. Similarly, the results of the rest of the capacitance combinations are comparable to the test-bench results. Figure 3.15, presents some of the cable-to-shield and cross-cable capacitance results. The cable-to-shield capacitance simulation presents a minimum of 92% match to

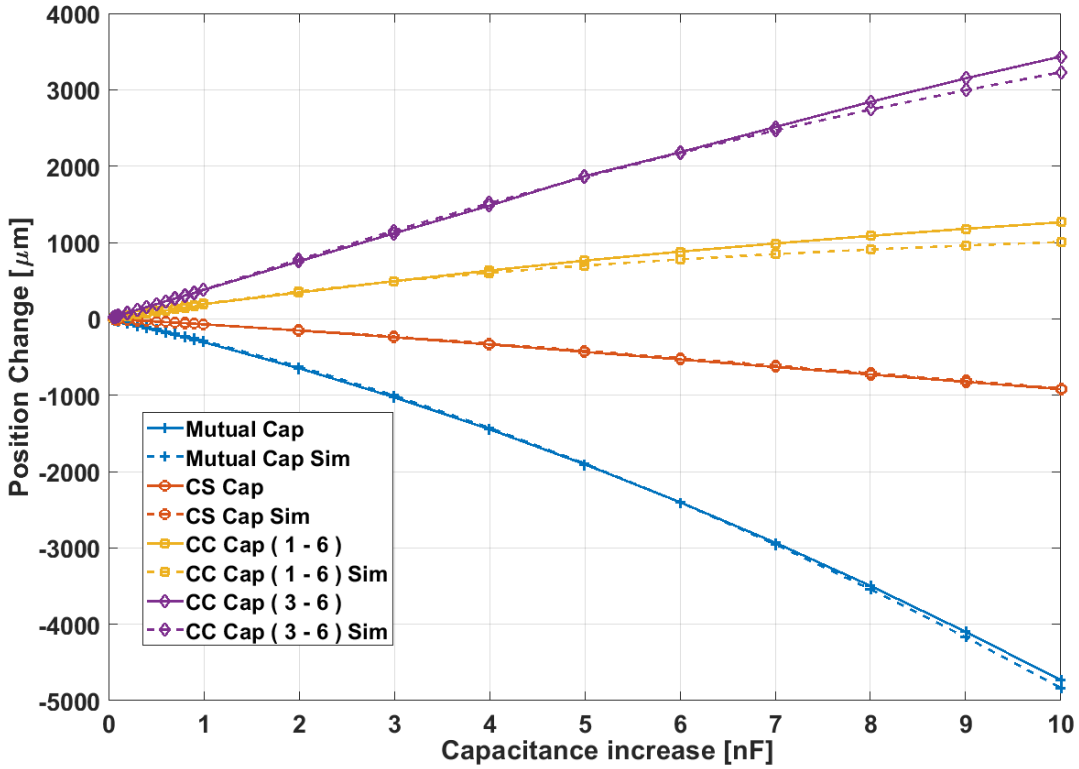

Figure 3.15: Comparison between some of the test-bench and simulation results for the mutual capacitance change

the test-bench results i.e. 85 μm of difference with respect to a position change of 1000 μm. The cross-cable capacitance variation presents a maximum difference between experiment and simulation of 400 μm with respect to a 4000 μm of position error.

As explained previously in Section 3.3, the simulation is based on the theoretical capacitances and inductances. As it was stated in [83], it is very difficult to measure these values for this kind of sensor since when sealed it becomes a complicated network of inductances and capacitances and every imperfection and in-homogeneity adds to the nodes of this sensor. Having said this, the general shape, the magnitude of the position change, and its behaviour is comparable. The overall difference between the simulation and experiment with respect to the position change is small enough to accept the simulation and hence use it to find a way to reduce this sensitivity.

3.5 Capacitance Sensitivity Correction

Unlike the temperature, this correction must be fulfilled without a capacitance measurement. This is why rather than a compensation method it is more a countermeasure. A compensation based on the measurement of the capacitance cannot be implemented since all such measurement techniques require the sensor to be turned off during operation, which is not possible. Furthermore, reading all the capacitance combinations of the cable would entail an enormous task. A technique that allows the sensor to 'ignore' the change in capacitance and hence not affecting the bridge, is developed [146]. The solution developed to counter the I2PS cable capacitance sensitivity is divided in two parts:

1. The capacitance that is related to the sense coils.
2. The capacitance that is only related to the primary coil.

Different techniques and circuits were developed in simulation to cancel this capacitance. The best technique found in simulation is to add a filter across the differential channel, which attenuates the ac part of the signal enough to cancel the effects while still high enough to be accurately resolved using the sine-fit algorithm. This was later discarded since it was easier to connect all supply and temperature reading cables (which carry the same amplitudes) to a new multi-pair cable. This is because for seven I2PS the number of cable pairs required is not enough in one cable. This allows the minimisation of interference being generated in the sense coils cables. For the former, the following approach is adopted.

3.5.1 Countermeasure design and simulation results

In order to maintain the correct position measurement, a countermeasure circuit is developed to cancel out the change in capacitance of the sense coils. The aim is therefore to add an inductance, in parallel to the mutual capacitance i.e. across the sense coils, big enough to cancel the added capacitance and hence stabilising the inductance of the sense coil in the process. The handicap of such a solution is that a discrete component corrects with the same amount for all capacitance

combinations. Additionally, since this inductance is connected on either side of the differential signal, the input voltage from each side should be equal and opposite.

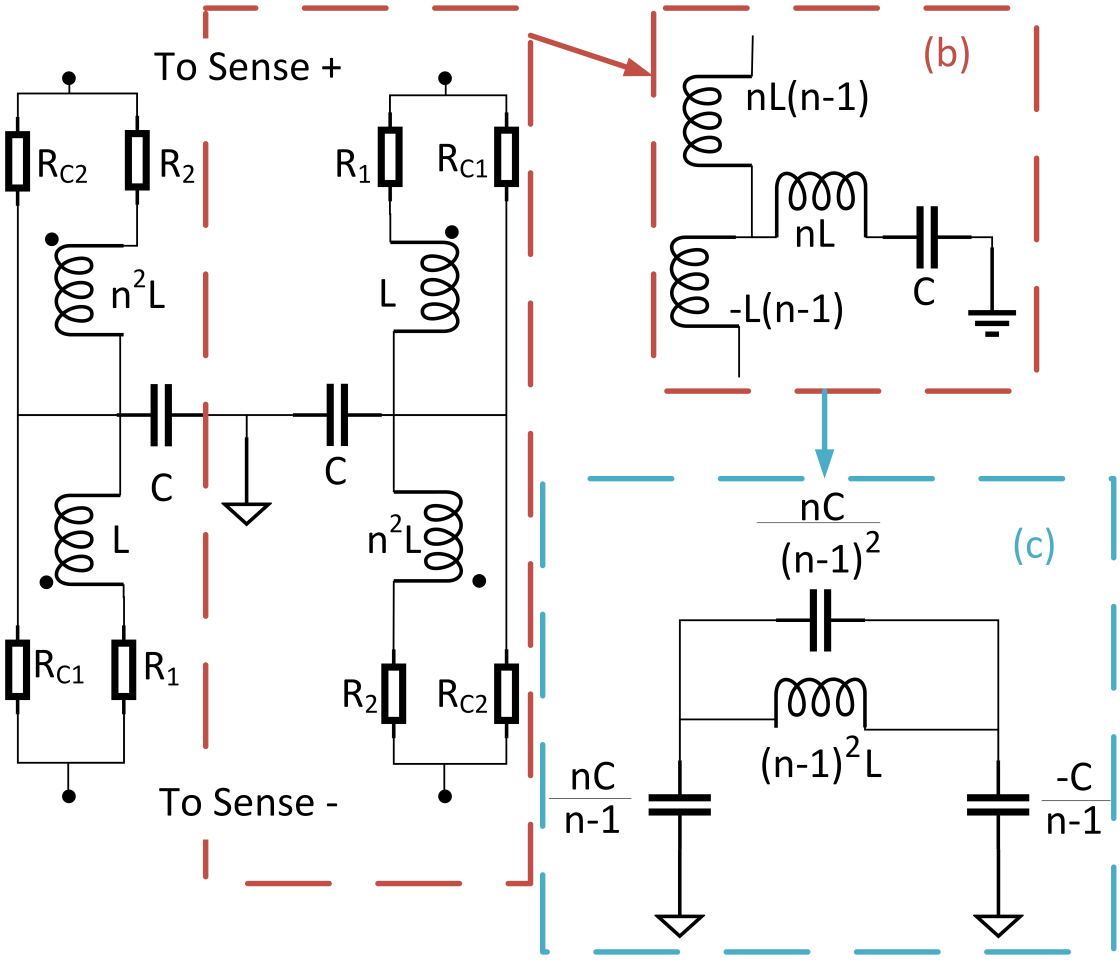

Figure 3.16: The countermeasure circuit simulated and added at the end of the long cable. Circuit (b) is the equivalent circuit of the highlighted circuit.

The circuit is presented in Figure 3.16, and is adopted from the negative capacitance circuits disclosed in [124] but used in a different way. The highlight of the circuit is two inductors with inductances L and n^2L which are directly coupled on one core. n is the turn ratio between the two inductors, while, n^2 is the inductance ratio of the two inductors. The two ends of the inductors are connected to the sense coils while the other two ends are joined together with a grounded capacitor C. These two inductors are connected opposite to each other to create the equivalent circuit presented in Figure 3.16(b). The opposite inductance again introduces a phase shift of 180° is introduced by the opposite inductance hence, placing the voltage at the centre equal to either way of the differential signal. When both voltages are identical in magnitude, there is no current flowing through the circuit. This is an important feature of this circuit since it turns off the circuit when there is no added capacitance. When the cable capacitance changes, the differential voltage is not the same any more, this generates a current flow and therefore mutual inductance.

If a perfect coupling coefficient is assumed (i.e. k = 1), with the help of a $Y - \Delta$ network transformation, the π network of the circuit can be derived as shown in Figure 3.16. A negative capacitance is derived on the side of the inductor, which has the greater number of turns. The turn ratio n, can never be 1 since it would cancel the total inductance. As shown in [124], a high n is desirable for parasitic capacitance cancellation, as is the case for this circuit. Furthermore, as all the components are a function of the mutual inductance and this depends on the current passing through each coil, their values vary with the difference between the differential voltages. A second identical, but inverted circuit creates the same circuit but on opposite ends. This therefore balances the differential signals.

Finally, the remaining component is the inductance located between the two differential sense voltages. The latter acts as a cancellation component to the added capacitance. The size of the resulting inductance, and hence the cancellation, can be controlled using the capacitance in parallel to the inductor which is dependent on the capacitor size selected. The bigger the capacitance the smaller the size of the inductance. The parasitic resistances of the coils are modelled by R_1 and R_2 and R_{c1} and R_{c2} are resistances placed in parallel to the coils such that the resistance of the coil is attenuated. The self-capacitance of the transformers will be in parallel to the inductance, hence in series together and in turn parallel to the mutual capacitance. Furthermore, this self-capacitance will be balanced on both sense coils. From experiments, it is noted that the position change due to a balanced mutual capacitance change is negligible.

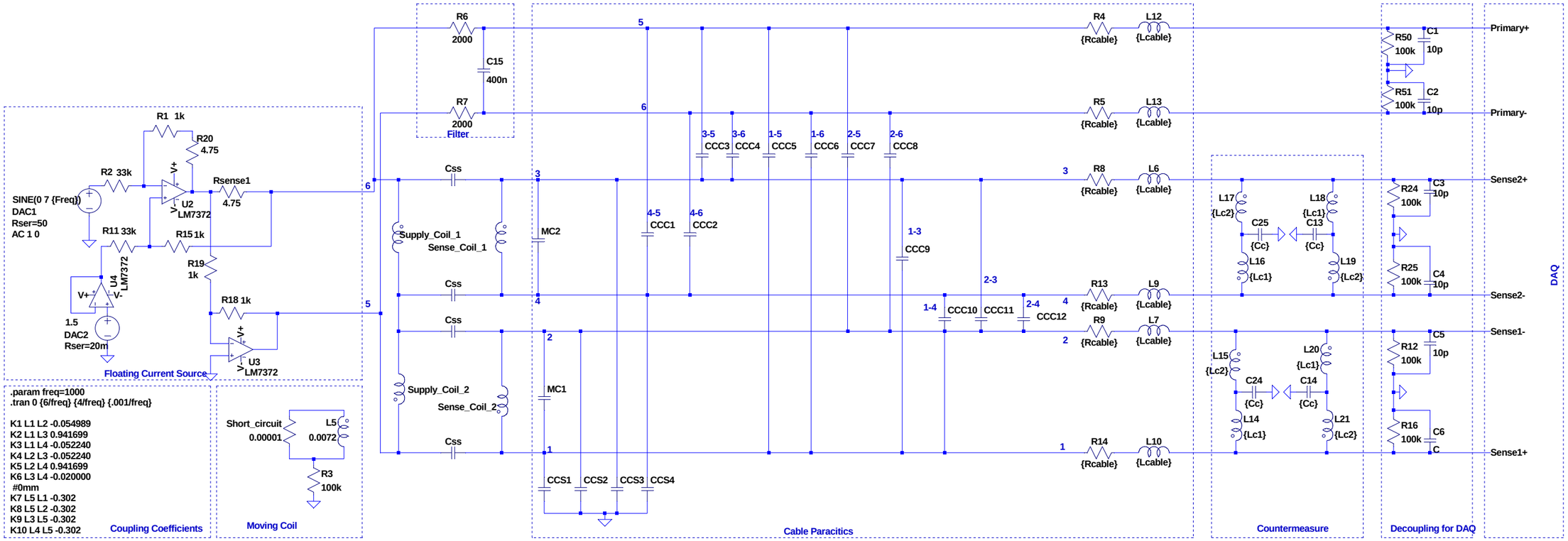

Fi□ure □□□□□T□e final simulated circuit

The circuit presented in Figure 3.5.1 is the final simulated circuit for the correction of position change due to capacitance change in the cable. Divided in sections it shows the :

- floating current source which generates the differential ac + dc current supply;
- coupling coefficients for the moving coil position at the electrical zero and the moving coil next to it;
- sensor sense and supply coils with the cross-coil capacitance connecting them;
- detailed cable capacitance model;
- counter measure circuit; and
- decoupling resistors and capacitances as required by the DAQ manufacturer for differential reading.

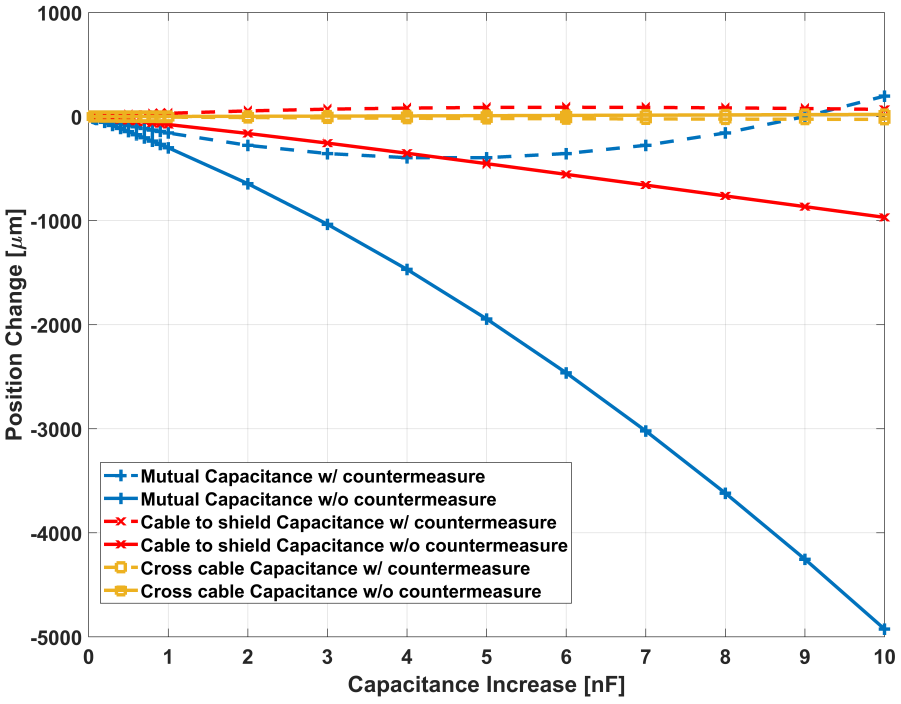

Figure 3.17: Comparison between the simulated I2PS position change due to a change in cable capacitance with and without the countermeasure

The simulation results of the sensor position with and without the countermeasure are presented in Figure 3.17. Several things can be noted from this figure:

1. All capacitance combinations exhibit a strong decrease in the position change.
2. The mutual capacitance position error is not linear.

3. The mutual capacitance position error exhibits the biggest correction.
    - With a 10 nF capacitance change, the position change is reduced to 197 μm from 4971 μm.
    - At 5 nF, it is reduced to to 400 μm from 2000 μm.
4. The position error for the cable-to-shield is linear and for 10 nF capacitance added, the position change is reduced from 1000 μm to less than 200 μm.

These corrections are considered good enough to develop the countermeasure circuit and employ any further optimisations to the hardware circuit

3.5.2 Test-bench Results

To produce the high n four audio transformers with a winding ratio of 1 : 6.45 are used. The transformers are characterised and it is found that the ac resistance and inductance at 1 kHz are tabulated in Table 3.6. (The parasitics of the transformer coils are measured over a sample of similar transformers and since the variation between them is very small, it is considered to be negligible.) The capacitance value is set to be 5 pF and the R_{c1} and R_{c2} are set to 300 Ω and 3 $k\Omega$ respectively. The circuit is built and tested on the same test bench used in Section 3.4.

Table 3.6: Measured audio transformer values

	Primary Coil	**Secondary Coil**
Resistance [$k\Omega$]	*1.37*	*37.5*
Inductance [**H**]	*0.22*	*9*

The circuit with these components in place produces the position change presented in Figure 3.18 when the cable capacitance is changed. Furthermore, a comparison between the position change exhibited by the sensor position with and without countermeasure circuit for a capacitance change is presented in Figure 3.19. Several differences are noticed with respect to the simulation. In this case, all position changes are non-linear, implying that some non idealities are added to the circuit from the transformer circuits. While the position change due the mutual capacitance is still non-linear with the optimised final circuit it is monotonically increasing. The biggest and most dangerous position change noted is from the mutual capacitance. With the countermeasure, this sensitivity (the gradient of the

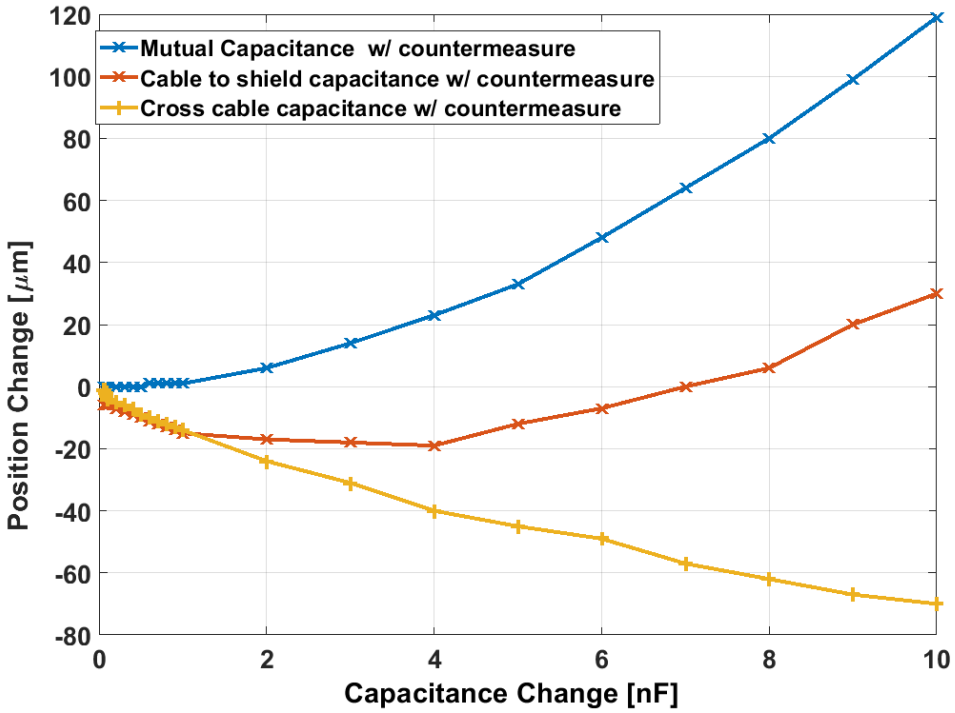

Figure 3.18: I2PS position change due to a change in cable capacitance with the countermeasure, as obtained from the test bench.

fit line) is reduced from 448 $\mu m/nF$ to 10.7 $\mu m/nF$. This is an improvement of over 97%. At 10 nF the position change decreases from 4971 μm to 120 μm. Another improvement is observed on the cable-to-shield capacitance where a linear fit yields a mean sensitivity of 2.4 $\mu m/nF$. This roughly translates to a 96% improvement. At 10 nF the position change decreases from 1000 μm to 30 μm. The cross-cable capacitance in this case represents the remaining capacitance combinations that link the sense coils together without the supply and primary cables. The sensitivity in this case changes from 7.2 $\mu m/nF$ from 8.56 $\mu m/nF$ but since this is already low, an improvement is not expected.

Comparing these results to the LVDT results in Table 3.5, the mutual capacitance sensitivity of the LVDT is found to be 11 $\mu m/nF$ while the I2PS sensitivity now is now 10.7 $\mu m/nF$. On the other hand, while the cable-to-shield capacitance showed an improvement of 96%, it is still 1.2 $\mu m/nF$ higher than that of the LVDT. Nonetheless, with the countermeasure in place, the drift at 10 nF is still well within the ± 200 μm allowed maximum limit.

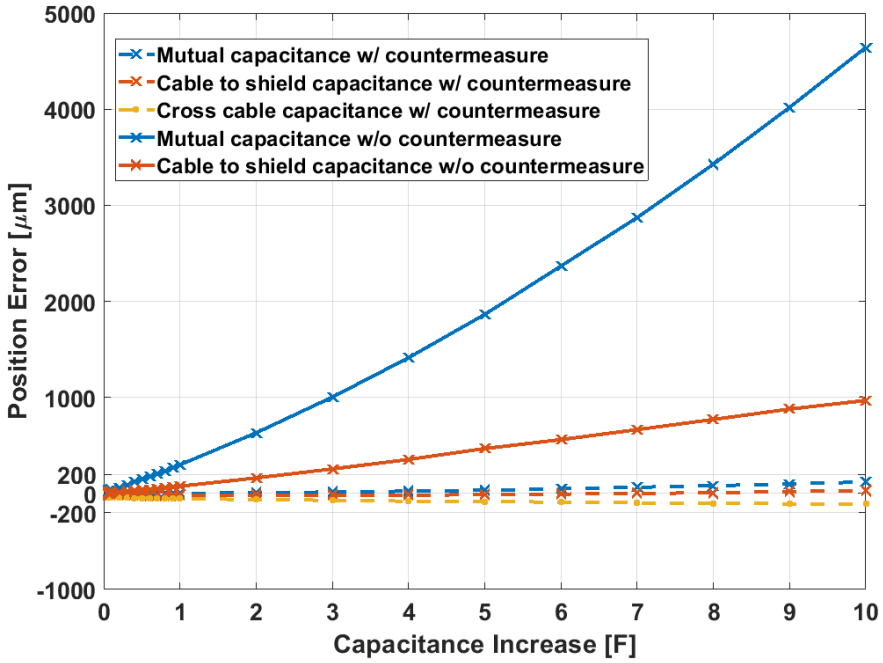

Figure 3.19: Comparison between the I2PS position change due to a change in cable capacitance with and without the countermeasure, as obtained from the test bench.

3.6 Summary

The LHC collimation environment forces the I2PS to operate with cables that span hundreds of meters. The position sensitivity and reliability are two aspects of this transducer that cannot be compromised during operation.

This chapter provides a detailed understanding of the transducer's behaviour with the cable. It shows that the I2PS is indeed affected by the cable parameters. The frequency response of the sensor with the cable produces empirical data on the frequency range of the sensor to be operated in. Furthermore, the latter, with the cable lengths noted, are to be used as a guideline when installing new collimators housing I2PS. Additionally, the frequency response showed that the transducer's frequency response should be designed or manipulated to be flatter.

This chapter also investigates the case study regarding the impact of cable capacitance change on the I2PS position. The results show that the I2PS is highly sensitive to this phenomena unlike the LVDT which is immune to this effect. A SPICE simulation that is able to model the electromagnetic and parasitic effects of the transducer with the cable is proposed. The simulation presented offers a good match with the results obtained empirically. Indeed, such simulations

help understand the physical phenomena better and are a crucial step for the design of a countermeasure circuit to eliminate these unwanted effects. Finally, a countermeasure is designed in simulation, built, and tested. Consequently, the empirical results show that the countermeasure circuit drastically reduces the I2PS sensitivity to cable capacitance change by 97% and yields a performance which is comparable to that of the LVDT.

Chapter 4

Thermal and Compensation Algorithm Characterisation

4.1 Introduction

While climate control keeps the LHC tunnel at a steady temperature, it still changes by a few degrees. Furthermore, local temperature spots can occur along the length of the tunnel due to heat generation from various objects, which lead to an increase in local temperatures. From literature and from operation it is noted that the I2PS is quite sensitive to temperature change. Until now, it is assumed that an ambient change in temperature affects only the moving coil and all sensors (operated differently) in the same way [87]. To understand better the aim of this chapter, Figure 4.1 presents the position and the dc voltage from one of the sensors installed in the collimators for the 2018 run. This is one of the many similar examples which point to the same problems. Indeed, Plot a and Plot c represent the same data but plot c presents the missing part of plot a. Plot b presents the dc voltage as obtained from the I2PS.

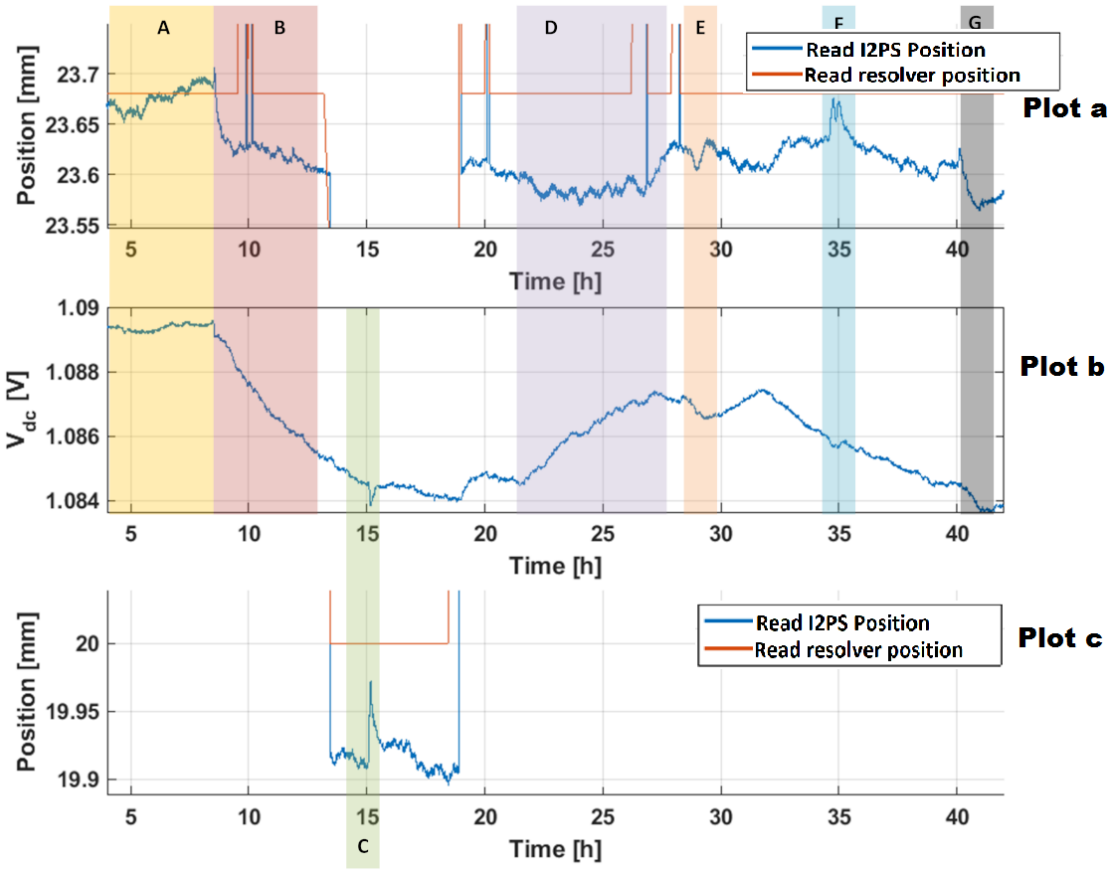

Figure 4.1: Comparison between the position measured by the I2PS in a collimator and the I2PS dc voltage from 2018 run. The sensor position is the position of the jaw as measured by the I2PS while the reference position is the position as measured by the resolver in the collimator setup. V_{dc} is the measured primary voltage of the I2PS which represents the temperature of the sensor. As explained in Chapter 1.

4.1.1 Problem Definition

The figure, which presents the as measured resolver position and as the measured I2PS position, is divided seven windows. Window A shows a stable temperature and a stable position, which is less than 50 μm. The sensor has been in this condition for a long time. The position then suffers a large decrease. In fact, it decreases by 100 μm in 3 hours and settles down in 7 hours (window b). If only the measured I2PS position is considered, this change leads to an ambiguity of this position change is due to actual moment or not. In this case it is a position drift by the I2PS since the reference i.e. the read resolver position did not change i.e. the jaw is actually not moved. On the other hand the dc voltage which represents the temperature takes 11 hours to stabilise at an offset of 80 μm. Window D shows a change in V_{dc} while no change in position hence remaining with the offset instead of following the temperature and returning back. Windows C and D show changes in V_{dc} which are also noted in position while window F shows a spike in

position which is not represented in V_{dc}. The position in this figure continues to drift until it eventually reaches 150 μm of position drift while the V_{dc} remains at an average value of 1.083 V. Similar problems are also shown in Figure 4.2 where there is a high position change when there is motion, which seems to originate from temperature but it is not understandable why this is happening. Furthermore, as can be noted from Figure 4.2, windows 2 and 4 there are drifts of similar magnitude with very different V_{dc} changes.

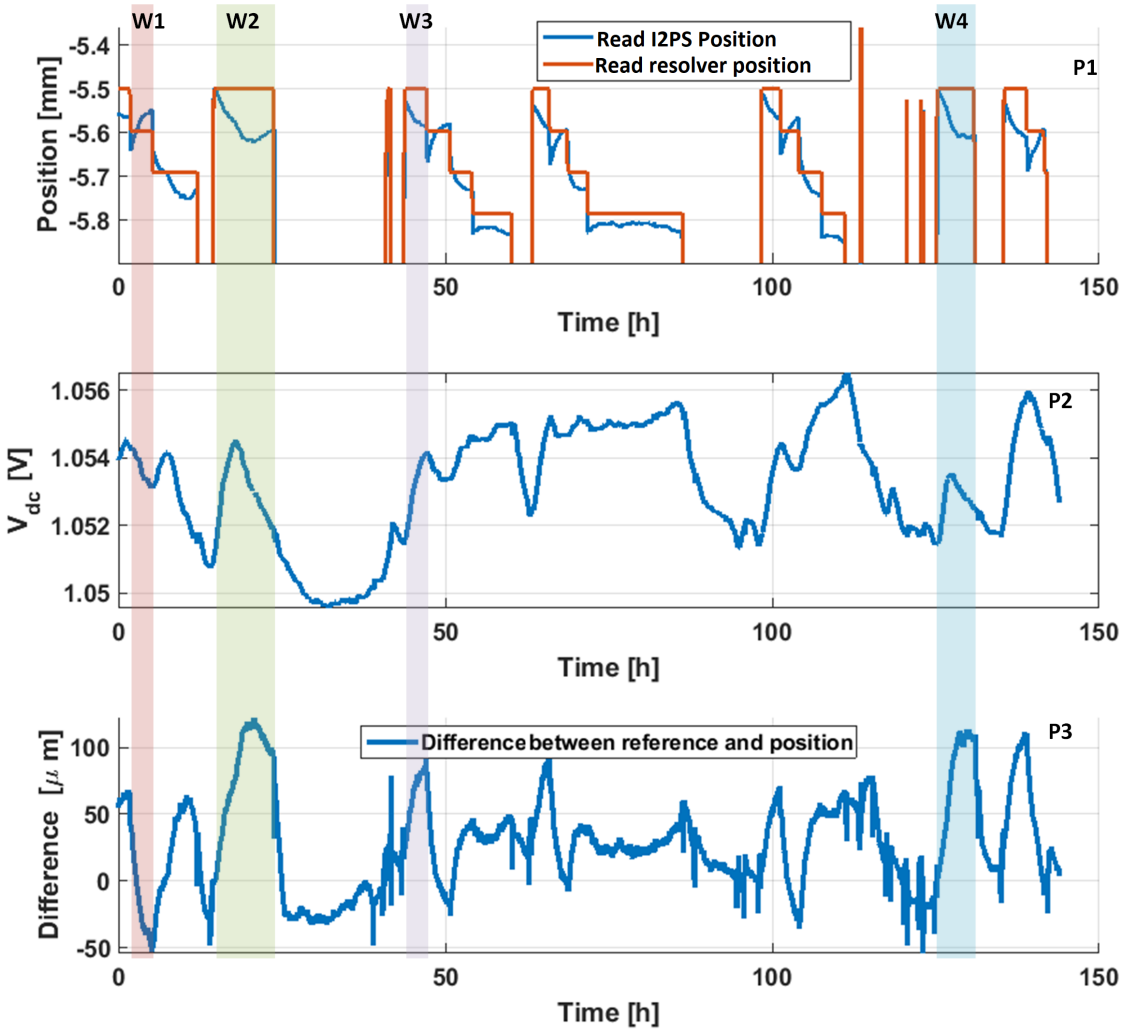

Figure 4.2: Comparison between the position measured by the I2PS in a collimator and the I2PS dc voltage from 2017 run. The sensor position is the position of the jaw as measured by the I2PS while the reference position is the position as measured by the resolver. As explained in Chapter 1. Therefore the calculated difference presented is between the as read resolver position and the I2PS.

It is important to add that at CERN's control room, two limits are defined during commissioning. During calibration of the collimator with the beam, the position read from the linear position sensor, being an LVDT or an I2PS, and the read resolver position must be within a maximum of 50μm from each other at beam

position. Two limits are then placed on this position. The first limit is within a minimum of $200\mu m$ of the position read during calibration of the collimator with the beam. This is a warning limit where only a warning is issued that the position has changed by $200\mu m$ from the calibrated position. The second is within a minimum of $400\mu m$ of the calibrated position and this is connected to the beam dump interlock. This implies that if the read position of the position sensor exceeds $400\mu m$ of the calibrated position it dumps the beam of particles. In these cases the maximum position change from initial position is of 150 μm which means it is operating $50\mu m$ of the warning limit. This is not optimal and needs to be fixed.

This chapter therefore aims at understanding why the position change happens much faster than the change in V_{dc}. Moreover, it focuses on investigating why spikes, such as the one in window c, come to decrease the offset, while according to the trend it should increase it. Furthermore, an analysis on how the temperate change is reflected so fast in the position while other windows are not, is to also be unveiled. Also, this chapter delves into understanding why the position does not return to the previous position when the temperature does. Hence, it aims to show the relationship between the position and the V_{dc}. Additionally, an investigation will be carried out, showing if there is a relationship with the moving coil position. Ultimately, this work will also deal with the variation and behaviour of the V_{dc}. Finally, an understanding as to why on the same machine some sensors suffer a higher position drift than others, shall be considered. Since it is difficult to find an answer to these questions from only the operational data, tests are indeed devised in the lab.

Therefore, this chapter presents a deep empirical analysis conducted for the I2PS in the context of thermal sensitivity. First, the transducer's parameters are broken down in basic components and each analysed individually. Then the position read with respect to the temperature change is investigated. Finally, the temperature compensation is also analysed.

4.2 Test-bench Setup

In order to study the relationship between general environmental changes in temperature and the position read by the sensor, a situation where the sensor is at constant thermal conditions has to be obtained. The sensor is placed inside a

climatic chamber with air vents closed and heaters off. It is kept in this condition such that thermal equilibrium is achieved. This procedure is repeated each time the sensor is taken out of the chamber or the chamber is opened to move the moving coil. This is done so that the initial control measurement is obtained at constant temperature. Hence, it is used as the initial position.

The chamber is then set to go from room temperature to 40°C in 2 hours. It is left at 40°C for 30 minutes. The readings are stopped once the climatic chamber starts to cool off. The supply and sense voltages are acquired using an NI PCI-6143 DAQ [88] and hence the position is calculated through a ratiometric reading. The temperature of the chamber is also logged. This procedure is repeated for different moving coil positions, frequencies and cable length. The same procedure is repeated with a Keysight Vector Network Analyser (VNA) in conjunction with BenchView to acquire and log the resistance and inductance of the coils as the temperature changes with different moving coil positions.

4.3 Acquired Voltage Drift due to Temperature Change

To analyse the temperature impact on the position the raw voltages are acquired and analysed first. The acquired voltages are the sense and supply coil's ac and dc voltages.

4.3.1 The Sense Voltages

The two sense voltages are acquired separately. It is assumed [56] that there is negligible current in these coils. Henceforth, the voltage of sense coil 1 will be referred to as V_{Sense1} and the voltage of sense coil 2 will be V_{Sense2}. Indeed, the behaviour of the sense coil's voltage is what impacts the raw, uncompensated position read by the sensor. The sense coils' voltage can drift in three manners:

1. One sense coil increases while the other decreases or vice-versa.
2. Both sense coils' voltage increase/decrease at the same rate.

3. Both sense coils' voltage increase/decrease at the different rates.

It is noted from numerous experiments that all three ways are noted in the I2PS at some point. Starting at 1 kHz at the centre of the sensor i.e. the electrical zero, the two sense voltages drift by the same amount in the same direction, as is noted in Figure 4.3a. As the moving coil position starts moving away from the electrical zero, as seen in Figure 4.3b, the drift starts to happen at the same rate and then it increases until both are changing at different rates. At 15 mm, the sense coils voltages immediately start drifting at a different rate, as seen in Figure 4.3c, and finally close to the end of the sensor. Ultimately, the sense coils voltage go into two different directions, as identified in Figure 4.3d.

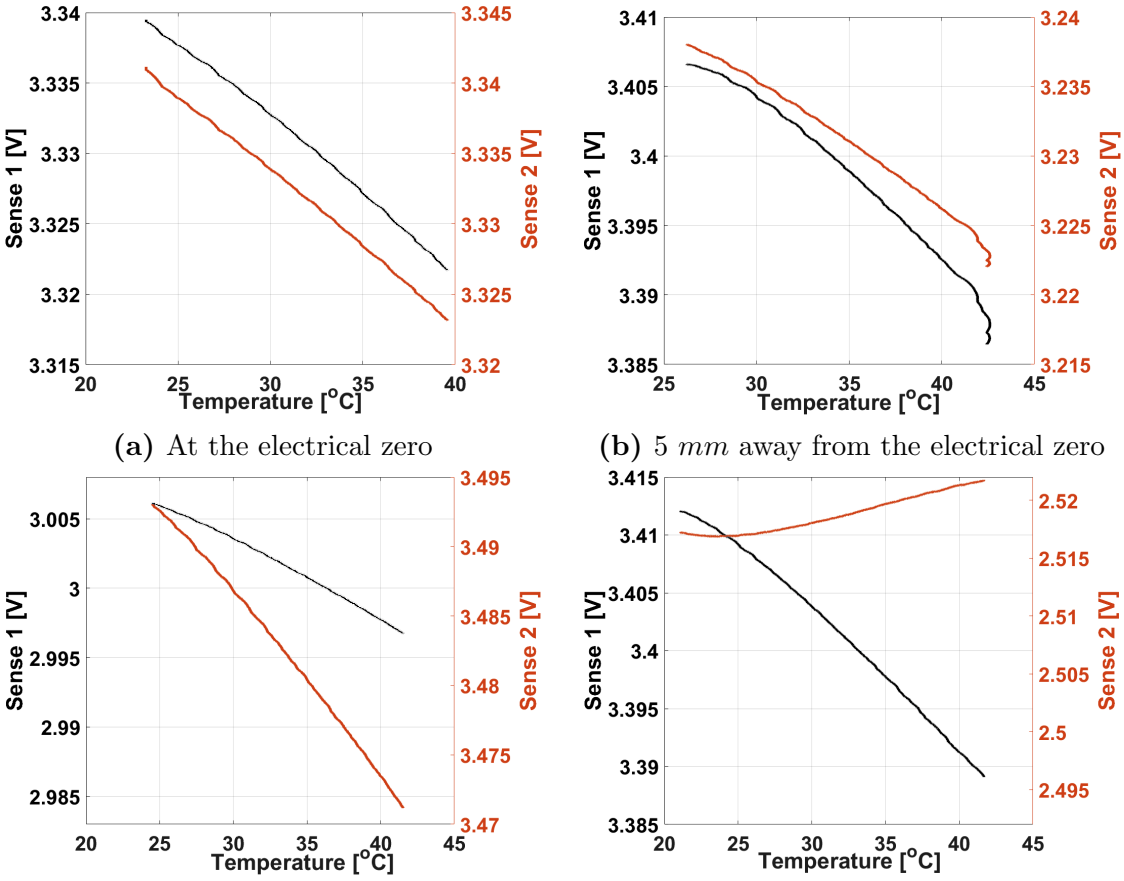

(a) At the electrical zero

(b) 5 mm away from the electrical zero

(c) 15 mm away from the electrical zero

(d) 30 mm away from the electrical zero

Figure 4.3: Sense coils voltage

Moreover, as the amplitude of the supply signal is changed the amount of drift is also changed, for e.g. if the $I_{ac} = 10\ mA$ the change in the sense coils at 15 mm is max 0.014 V. If $I_{ac} = 45\ mA$ the change in the sense coils at 15 mm is max 0.042 V. Furthermore, it is noted from Figure 4.3 that one of the sense coils changes by the same amount. From Figure 4.3a note that both sense voltages change by the same amount. For example consider the change in temperature from 30^oC to

40^oC the change in voltage is approximately 0.011 V. Then consider the voltage change at 30 mm. One sense voltage changes by approximately 0.011 V (for a temperature change of 10°C) while the other one changes by a very small amount. To summarise, at any moving coil position, at least one of the coils' voltage changes by 0.011 V for a 10°C change.

4.3.2 The Supply dc Voltage

In order to compensate for temperature change, a temperature reading is required. The mean temperature of the sensor is obtained by superimposing a dc offset I_{dc} to the ac supply current [56]. In this way, the dc part of the consequent supply voltage, V_{dc}, will be directly proportional to the mean temperature along the sensor. This is because it will be proportional to the supply coils' resistance, which is affected by the temperature according to a relation similar to

$$R = R^0(1 + \gamma\Delta T) \tag{4.1}$$

giving

$$V_{dc} = R_s I_{dc} = R_s^0(1 + \gamma\Delta T)I_{dc} = \ V_{dc}^0 + g_{dc}\Delta T \tag{4.2}$$

where g_{dc} is constant of proportionality between the primary DC voltage and the ambient temperature.

From the experiments it is noted that:

1. The dc voltage is stable for different sensor and cable conditions as is noted in Figure 4.4;

2. As I_{dc} is increased the amplitude and the voltage swing for the same temperature change is also increased. Figure 4.5 presents a variation of I_{dc}.

   The voltage change for these two is 0.0444 V when $I_{dc} = 5\ mA$ and 0.303 V when $I_{dc} = 40\ mA$. This is expected since this voltage follows $V = IR$. As I remains constant as R increases, V increases as well.

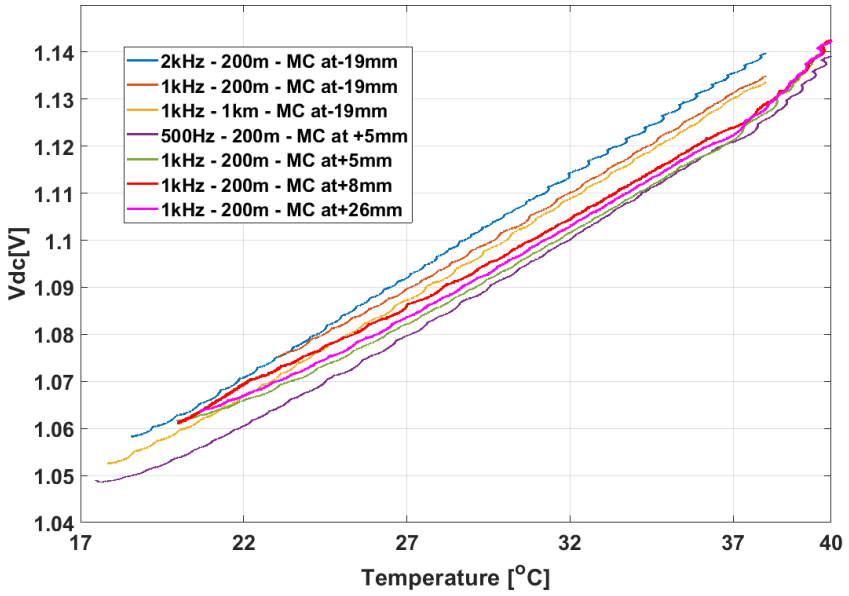

Figure 4.4: V_{dc} for different sensor and cable conditions at $I_{dc} = 10\ mA$

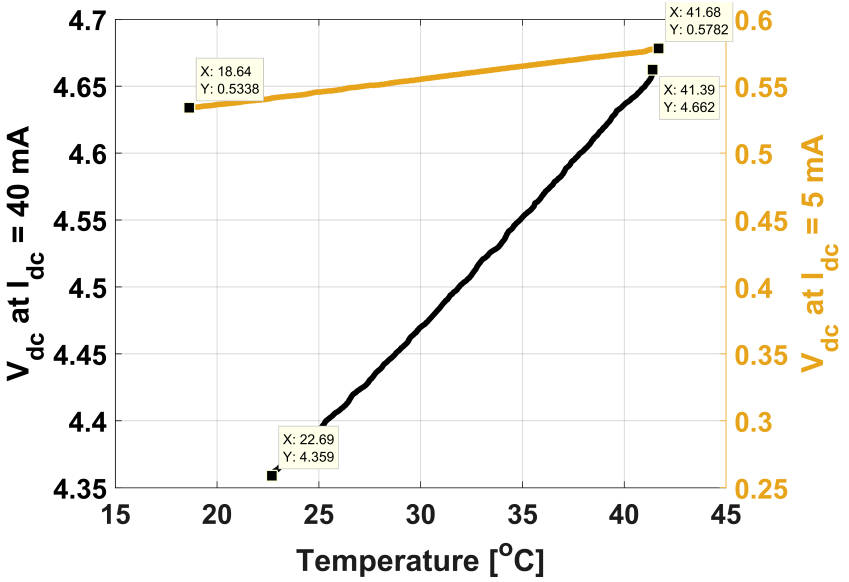

Figure 4.5: V_{dc} at different I_{dc} for the same moving coil position

4.3.3 The Supply ac Voltage

As expected, the supply ac voltage exhibits the same behaviour as that of V_{dc}. V_{ac}. This also changes due to the relationship of $V = IR$. The change of V_{ac} is very small as is noted in Figure 4.6.

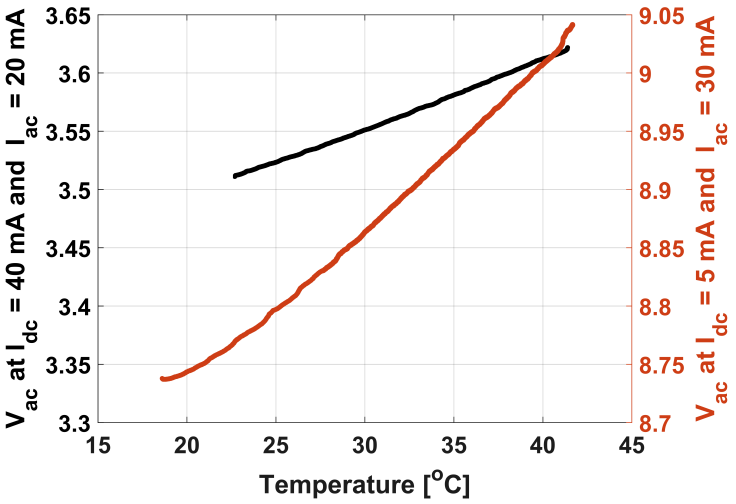

Figure 4.6: V_{ac} at different I_{dc} and I_{ac}

The voltage change for these two is 0.11 V when $I_{ac} = 20\ mA$ and 0.304 V when $I_{ac} = 30\ mA$. Although one may argue that V_{ac} can substitute V_{dc}, hence simplifying the supply circuitry, V_{ac} is also dependent on the position, as presented in Figure 4.7.

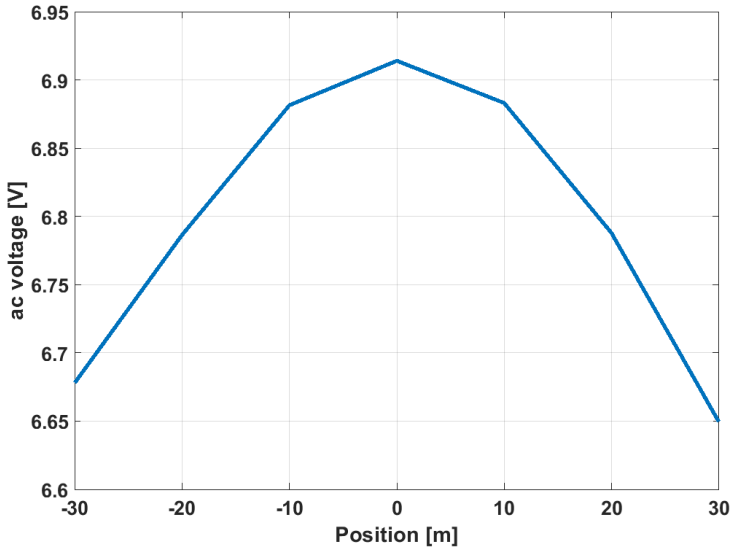

Figure 4.7: V_{ac} at different moving coil positions

As introduced in equations 2.16 & 2.17 the voltages of the separate coils are a function of the position. The two coils are connected in series and so their total ac voltage is:

$$V_{ac} = V_1 + V_2 \tag{4.3}$$

$$V_{ac} = (R_1 - R_2)I + j\omega I(L_1 - L_2) + \omega^2 I \frac{(M_{51} + M_{52})(M_{15} + M_{25})}{Z_5} \tag{4.4}$$

An experiment is set up which uses the same setup as before but instead of reading the sense coil's voltages with the DAQ, the resistance and inductance of each coil is measured with a VNA. The VNA is set to acquire automatically every minute the resistance and inductance in the frequency range of 250 Hz and 3 kHz.

4.3.4 The Supply Coils

The overall resistance of the supply coils, henceforth referred to as R_p, is the dc + ac resistance (the added resistance due to skin effect) is shown in Figure 4.8a. (Note that the supply coils are wound one opposite to the other and connected in series. Therefore, the impedance in this case is the total of both. Furthermore, although the sense coils were grounded such that the inductance is removed, the inductance measured is still the combination of all other effects found in the sealed sensor.)

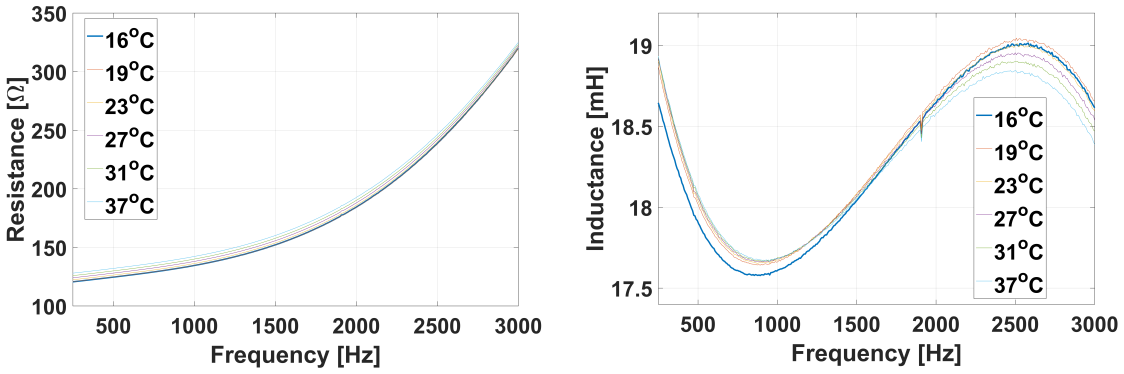

(a) Resistance **(b)** Inductance

Figure 4.8: Supply Coil

The resistance increases as the frequency increases and as the temperature increases. This response is due to the ac parasitics such as the skin effect. This resistance relationship with temperature is what is seen in the ac voltage V_{ac}. The inductance, L_p on the other hand, is different. Up to 1.5 kHz the inductance increases as the temperature increases. After 1.5 kHz the inductance first increases

and then decreases as the temperature increases. There is a point of inversion at approximately 1.5 kHz. The change is bigger as the frequency increases i.e. having higher dependence with temperature change.

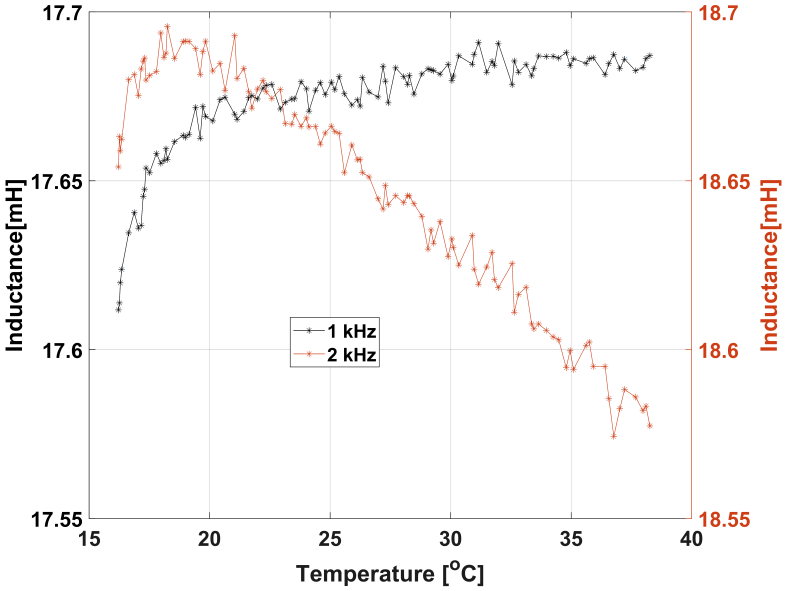

Figure 4.9: Supply coil inductance at 1 kHz and at 2 kHz with respect to temperature

The resistance change due to temperature at 1 kHz is of approximately 10 Ω and is similar up to 2.5 kHz. Figure 4.9 presents the inductance at 1 kHz and at 2 kHz. At 1 kHz the inductance increases but then stabilises. This implies that at lower temperatures, from 15°C to 20°C, it will change faster than at higher temperature. For 2 kHz the response is different for the inductance change as temperature increases the inductance decreases.

4.3.5 The Sense Coils

The resistance of the sense coils, R_s as can be noted in Figure 4.10a increases as temperature increases. The resistance change at lower frequency $\Delta R_s^{1kHz} \approx 200\ \Omega$ is lower than that at higher frequencies $\Delta R_s^{3kHz} \approx 100\ \Omega$. On the other hand the inductance change is of $\Delta L_s = 12\ mH$ and changes by the same amount for all frequencies, as can be noted in Figures 4.10b and 4.11.

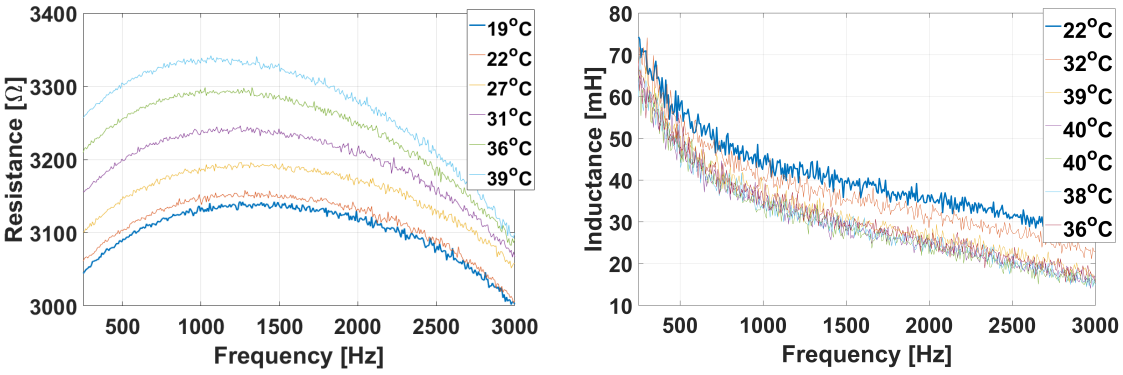

(a) Resistance **(b)** Inductance

Figure 4.10: Sense Coil

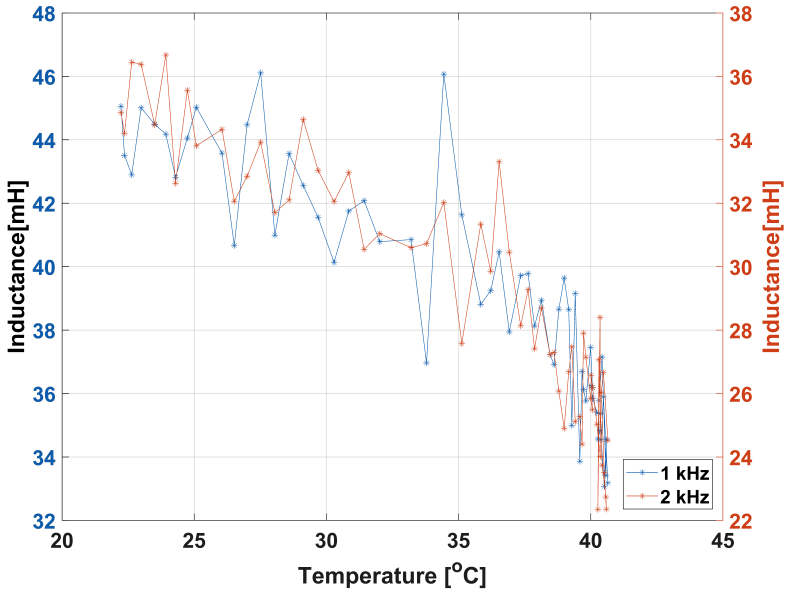

Figure 4.11: Sense coil inductance at 1 kHz and at 2 kHz with respect to temperature

4.3.6 The Moving Coil

The resistance of the moving coil changes uniformly with temperature while the inductance change is almost negligible as can be noted from Figure 4.13. Indeed, the inductance of the moving coil changes mostly with frequency, as noted in Figure 4.12b

As explained in [89, 90], the ac resistance of a coil is very complicated and a lot of factors can influence this value with respect to frequency. In [89] it was explained how the ac resistance varies from the inner layer to the outer layer for a long solenoid. In the case for the I2PS, the complication increases since for the supply coil there is a shield outside the outer layer and another coil inside the inner layer.

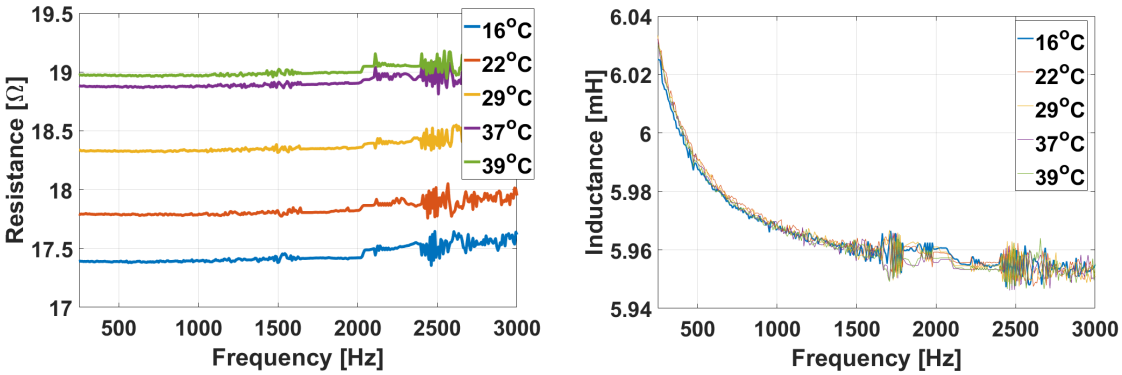

(a) Resistance **(b)** Inductance

Figure 4.12: Moving Coil

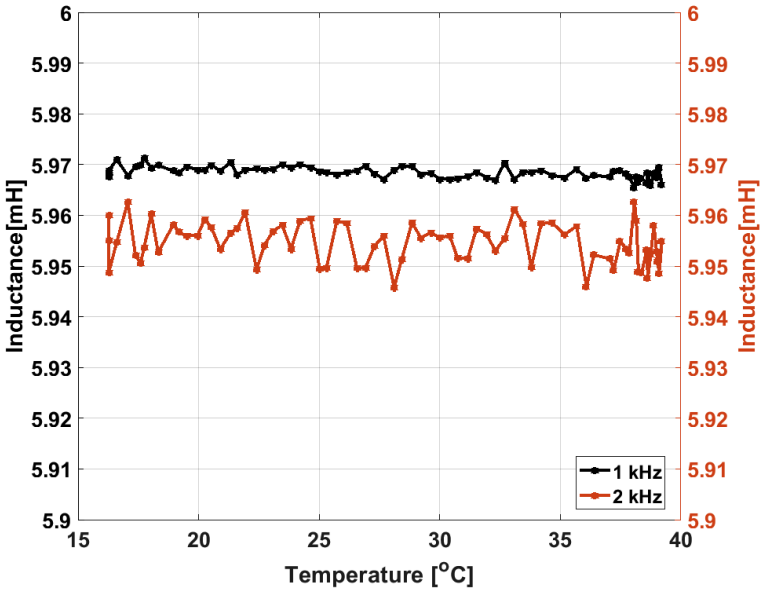

Figure 4.13: Moving coil inductance at 1 kHz and at 2 kHz with respect to temperature

On the other hand, there is a coil both inside and outside the sense coil. Both papers explain how the current distribution in a coil is a complex phenomenon to model theoretically. Furthermore, [90] explains that for the tesla coils which the author is working with and similar complex wound coils it is difficult to get very precise lumped or distributed model components for each coil. This is because multiple effects are being dealt with at the same time. Nonetheless, for these experiments the ac resistance is not the main aim. The main aim is to understand how the main lumped components behave with temperature.

Figure 4.14 presents a comparison between the calculated resistance change (according to the linear function $R = R_{ref}(1 + \alpha(T - T_{ref}))$) and the measured resistance change with temperature. Note that the gradient is lower for the supply and sense coils. It may be the case that the supply and sense coil's temperature for different coil layers are not changing at the same rate and this leads to a

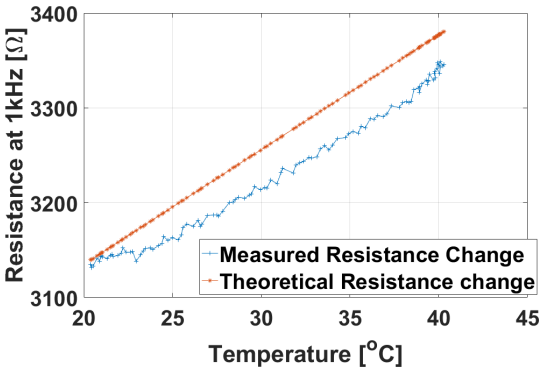

(a) Sense coil

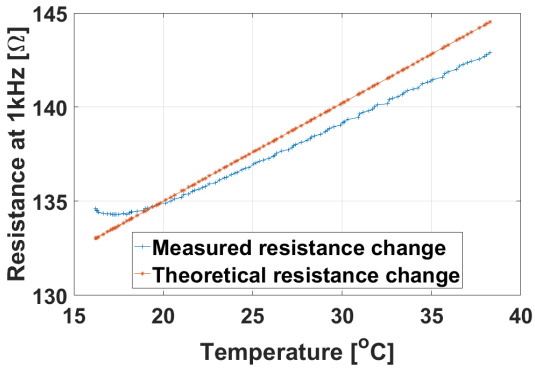

(b) Supply Coil

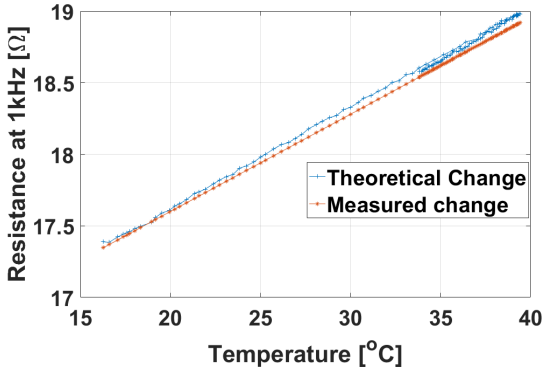

(c) Moving coil

Figure 4.14: Comparison between theoretical resistance change and experimental resistance change

slower resistance change or there are other non-linear effects in conjunction to the resistance. Overall the change is similar. On the other hand, the moving coil has a much bigger cable diameter and exhibits a linear response and the same gradient, as the theoretical one. Additionally, the moving coil's winding is exposed to the temperature change directly, because it is not insulated. From [56] the temperature dependence of the position reading of the I2PS was expressed as:

$$V_3 = j\omega \left(M_{31} - M_{32}\right) I + \omega^2 I \left(\frac{M_{35}M_{51}}{Z_5(T)} - \frac{M_{35}M_{52}}{Z_5(T)}\right) \tag{4.5}$$

where the dependence of the moving coil resistance with the temperature is linear, as follows:

$$R_5 = R_5^0(1 + \gamma \Delta T) \tag{4.6}$$

where R_5^0 is the resistance of the winding at room temperature, γ is the temperature coefficient and ΔT is the temperature deviation.

Therefore, to complete the expressions presented in [56] with the results obtained from these tests, the resistances of the supply coils are set to change with temperature. Hence, the complete equations of the separate supply coil voltages can be expressed as:

$$V_1(T) = R_1(\mathbf{T})I + j\omega\left(L_1 - M_{12}\right)I + \omega^2 I\frac{M_{15}(M_{51} + M_{52})}{Z_5(T)} \tag{4.7}$$

$$V_2(T) = -R_2(\mathbf{T})I + j\omega\left(M_{21} - L_2\right)I + \omega^2 I\frac{M_{25}(M_{51} + M_{52})}{Z_5(T)} \tag{4.8}$$

while the temperature dependence of the sense coils remains unchanged as equation 4.5, where the dependence of the moving coil resistance is the only resistance that affects the sense coil's voltages.

However, by writing the equations in this from, the self inductance change due to temperature noted in these results, is ignored. This said, from these results it is noted that L_1, L_2, L_3 and L_4 are dependent on temperature as well as on frequency. Furthermore, from literature it is known that the mutual inductance is generally given by:

$$M_{ij} = k\sqrt{L_i L_j}, \qquad 0 \leqslant k \leqslant 1 \tag{4.9}$$

where k is the coupling coefficient i.e. a value of how much of the magnetic flux produced by one coil passes through the other coil. Let's assume for now that k is 1 since the coils in the I2PS are tightly wound and close to each other. According to this equation, if either L_i or L_j or both change with temperature, then M_{ij} is also a function of temperature. Hence,

$$M_{ij}(\mathbf{T}) = k\sqrt{L_i(\mathbf{T})L_j(\mathbf{T})}, \qquad 0 \leqslant k \leqslant 1 \tag{4.10}$$

Adding equation 4.10 to equation 4.7 shows that the sensor is dependent also on temperature even though the moving coil is independent to inductance to temperature change. This implies:

$$V_1(T) = R_1(T)I + j\omega\left(L_1(\mathbf{T}) - M_{12}(\mathbf{T})\right)I + \omega^2 I\frac{M_{15}(\mathbf{T})(M_{51}(\mathbf{T}) + M_{52}(\mathbf{T}))}{Z_5(T)} \tag{4.11}$$

$$V_2(T) = -R_2(T)I + j\omega\left(M_{21}(\mathbf{T}) - L_2(\mathbf{T})\right)I + \omega^2 I\frac{M_{25}(\mathbf{T})(M_{51}(\mathbf{T}) + M_{52}(\mathbf{T}))}{Z_5(T)} \tag{4.12}$$

while the temperature dependence of the position reading of the I2PS remain as:

$$V_3(T) = j\omega\left(M_{31}(\mathbf{T}) - M_{32}(\mathbf{T})\right)I + \omega^2 I\left(\frac{M_{35}(\mathbf{T})M_{51}(\mathbf{T})}{Z_5(T)} - \frac{M_{35}(\mathbf{T})M_{52}(\mathbf{T})}{Z_5(T)}\right) \tag{4.13}$$

$$V_4(T) = j\omega\left(M_{41}(\mathbf{T}) - M_{42}(\mathbf{T})\right)I + \omega^2 I\left(\frac{M_{45}(\mathbf{T})M_{51}(\mathbf{T})}{Z_5(T)} - \frac{M_{45}(\mathbf{T})M_{52}(\mathbf{T})}{Z_5(T)}\right) \tag{4.14}$$

If the thermal expansion of the material of the winding is considered, which is given by its coefficient of linear expansion, then it is possible to express it by the formula [91]:

$$L = L_0(1 + \beta\Delta T) \tag{4.15}$$

where β is the coefficient of linear expansion of copper $(16.8 \times 10^{-6} m/(mK))$

Groszkowski in [91] concludes that there are four factors that influence the temperature coefficient of inductance: thermal expansion, the skin effect, eddy currents and the self-capacitance of the coil. The last three are also a function of frequency. He also concludes that in a multilayer coil, the eddy currents and the capacitance effects prevail over the skin effect.

In the case of the I2PS, since the self-capacitance is calculated to be in the pF range and the frequency is less than 3 kHz, the equation provided in [91] of $\lambda' = \lambda(1 + CL\omega^2)$ where C is the self-capacitance and L is the inductance of the coil, is negligible.

However, the theoretical inductance change for the supply coil due to thermal expansion according to the equation in 4.15 at 1 kHz leads to a linear increase of :

$$L = L_0(1 + \beta\Delta T) = 17.68(1 + (16.8e - 8)(20)) = 17.6859\ mH$$

which is the same as the measured one, as noted in Figures 4.8b. The problem arises when calculating the change in inductance at 2 kHz and for the sense coil. In both these cases there is a decrease in inductance with an increase in temperature. Since the I2PS is made up of a complex combination of coils so close to each other, it is very difficult to understand if the ac components values are self-generated or if they are a combination. For example the sense coil's inductance at 1 kHz is due to the thermal expansion of the coil while at 2 kHz it changes because the parasitics of one coil become more dominant than the other.

4.3.7 Manual Change of Parameters

Since the I2PS's final reading is position, it is important to understand what this change in inductance and resistance translate to in position. A variable resistor and an inductor are connected in series to the coils such that the manually changed lumped circuit component values are translated to a read position change. Unless otherwise stated all position change presented in the following text is the difference between the position read from the I2PS with respect to a reference position as obtained from the Heindehin encoder. The latter measures the actual position of the moving coil with respect to the electrical zero with a ± 1 μm uncertainty.

The position change for a resistance sweep of the supply coil is presented in Figure 4.15a. It shows that a resistance change of 60 Ω results in a 72 μm of position change. Hence the sensitivity can be found to be: $1.5\mu m/\Omega$. The inductance on the other hand induced a non-linear position change of maximum 140 μm with an inductance of 4.8 mH. As can be noted from Figure 4.15b the increase is linear and monotonic until 3.8 mH and leads to just 35 μm of position change for 1 kHz. For 2 kHz, up to 3.8 mH, it is monotonically decreasing and then it increases. The resistance change leads to the same position change at all moving coil positions and it decreases by approximately 20 μm.

Since the sense coils are the reading part of the sensor and they require to be identical such that a balanced bridge is achieved as long as there is an equal and balanced resistance and inductance change on both coils, there is no position change. On the other hand, there are drastic effects if the bridge is unbalanced. Figure 4.16a presents the position change for an unbalanced resistance sweep for the sense coils. It shows that a resistance change of 400 Ω results in a 1000 μm of position change. Hence, the sensitivity can be found to be: $2.5\mu m/\Omega$. The

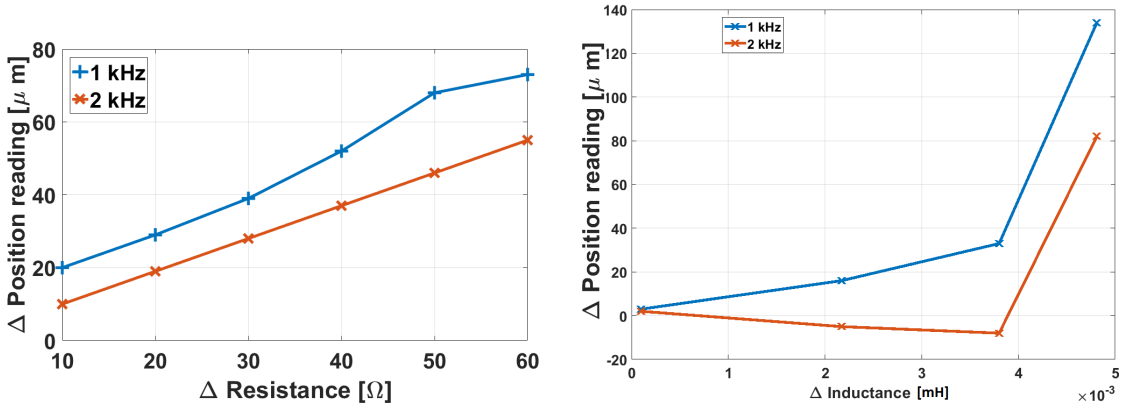

(a) Resistance **(b)** Inductance

Figure 4.15: Manual change in Supply coils

inductance on the other hand induced a non-linear position change. Similar to the supply coil case up to 3.87 mH, the position change is constant when the supply is at 1 kHz and monotonically decreasing for the 2 kHz case. In fact, when an inductance of 1.8 mH is introduced, it increases.

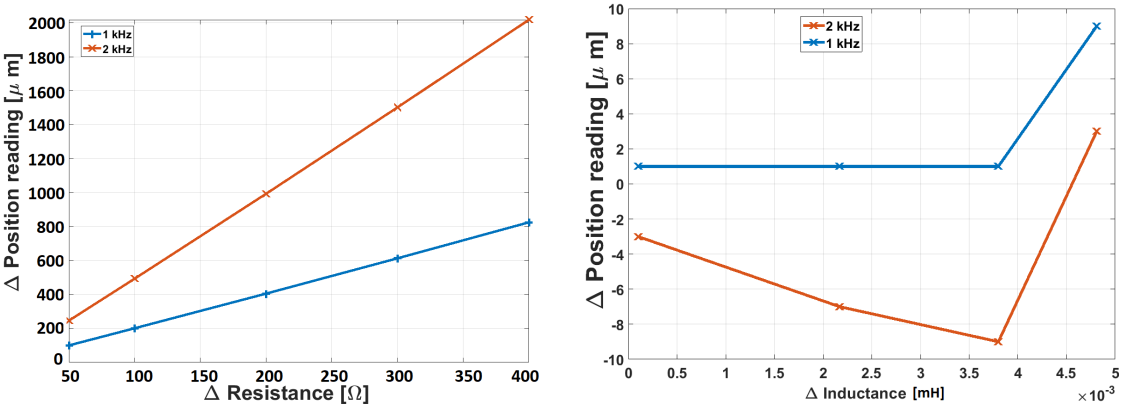

(a) Resistance **(b)** Inductance

Figure 4.16: Manual change in Sense coils

Figure 4.17 presents the position change at different frequencies and positions of the moving coil. The solder joint shorting the moving coil in this case is de-soldered and the resistance box is added in series. This changes the resistance of the coil while keeping the moving coil short circuit as described in Chapter 2. At 5 mm as resistance increased, the change in position increased. At the same moving coil position as the frequency increased, the change in position decreased. The position change in this case leads to a maximum of 1000 μm of position change at 500 Hz. Similarly, at 20 mm, as the resistance increased and frequency increased, the change in position decreased. The position change in this case leads to maximum of 3000 μm of position change at 500 Hz. Figure 4.13 shows a resistance change of approximately 2 Ω for a 20°C temperature change. With the

moving coil positioned at 20 mm, this resistance would lead to a position change of 1200 μm at 500 Hz, 700 μm at 1 kHz and 100 μm at 2.5 kHz. This concludes that for the moving coil it is more beneficial, from the resistance point of view, to operate the sensor at a higher frequency. This is due to the fact that this leads to the smallest position change. Furthermore, since there is no change in the inductance of the moving coil, this test is skipped.

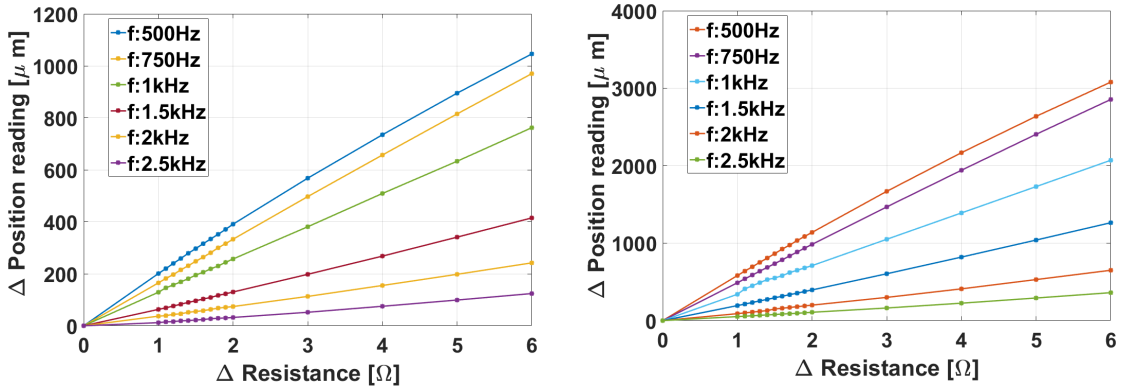

(a) Resistance change at 5 mm **(b)** Resistance change at 20 mm

Figure 4.17: Manual Resistance change in Moving coil at different frequencies and position

For the sense coils, as long as the thermal change is uniform along the sensor, there would be no position drift. In the current state of operation of the I2PS in the LHC, it is assumed that the temperature change of the surrounding environment is uniform and slow. This implies that the sensor's temperature is changing gradually and uniformly along the sensor. This assumption defines the settings used in the climatic chamber for all the tests. It is also assumed that since the dc resistance is the same and they are wound uniformly and directly on the plastic bobbin, with an insulator between the sense coils and the supply coil, the resistance and inductance of the two changes by the same amount, if a uniform temperature change is exhibited. As noted in Figure 4.8a, the resistance change in the supply coils is of 10 Ω. This leads to a change of position of 10 μm, which is negligible.

4.4 Position Change due to Temperature Change

The previous sections considered the raw components of the sensor. The following sections test and analyse the position change for the sensor. From the previous sections it is expected that the position change depends on the moving coil position and frequency.

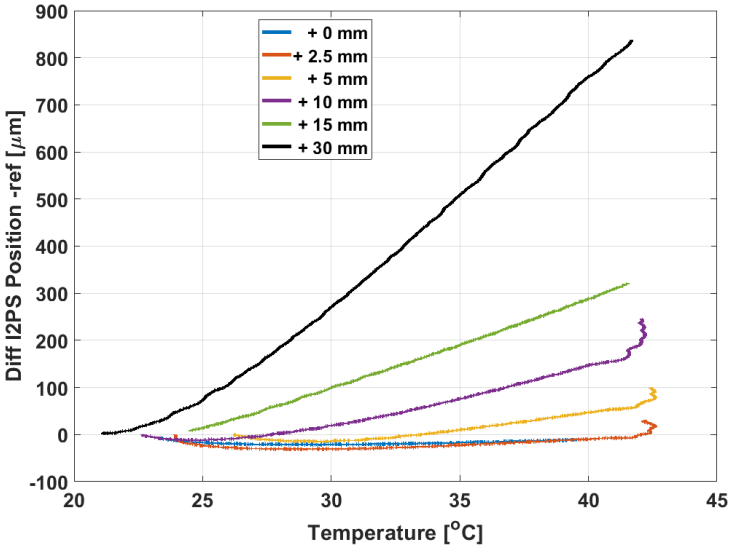

Figure 4.18: Position change for different moving coil positions at 1 kHz

Starting with an operating frequency of 1 kHz and 200 m cable, the read position change at various positions is tested for a temperature change of approximately 20°C. Figure 4.18 shows that as the moving coil moves away from the centre, the read position drift increases up to 800 μm. Note that at the centre, the read position change is negligible. It can be deduced from the results presented in Figure 4.3 that since at the centre of the coil the sense voltages change by the same amount the change in the read position is negligible. The small change that happens is due to the small difference that can exist in between the coils or any time delays in the calculation of the two sense coils voltages. On the other hand, it can also be understood that since at 30 mm one of the sense coils voltage changed by a different amount than the other one, the read position is now different since it depends on the ratio between the difference and the sum of the two sense voltages. Conversely, the opposite behaviour is noted when the sensor is operated at 2 kHz as presented in Figure 4.19. As the moving coil moves away from the centre the read position change is smaller.

Figure 4.20a shows the same results as that of 1 kHz and similarly, it is noted that for 1.5 kHz, as the moving coil moves away from the centre, the position change increases but at a rate of four times lower.

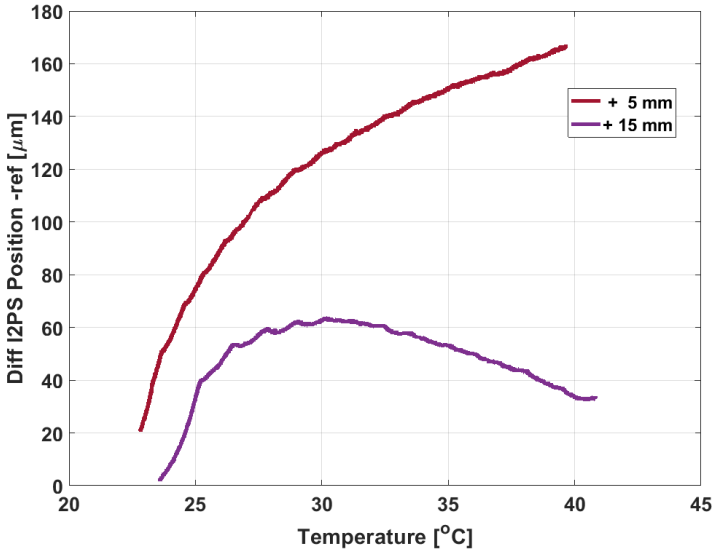

Figure 4.19: Position change for different moving coil positions at 2 kHz

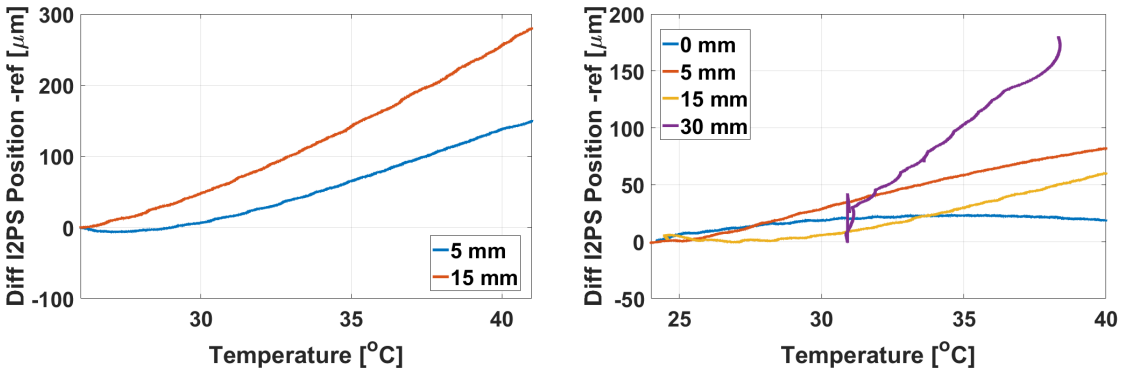

(a) Position change for different moving coil positions at 750 Hz

(b) Position change for different moving coil positions at 1.5 kHz

Figure 4.20: Comparing the position change due to change in temperature at different moving coil positions and operating frequencies

4.4.1 State-of-the-art of the Compensation Algorithm

As explained in Section 4.3.2, the mean temperature of the sensor is obtained by superposing a dc offset to the ac supply current [56]. In this way, the dc part of the consequent supply voltage will be directly proportional to the mean temperature along the sensor. This is because it will be proportional to the supply coils' resistance. The compensation equation is defined to fix the ratiometric value which is a function of the ambient temperature, r(T), by the amount with which V_{dc} changes with respect to a reference value using the following equation:

$$r_o = \frac{r(T)}{1 + \zeta \Delta\ V_{dc}(T)} \tag{4.16}$$

In this case as V_{dc}^{0}, r_o is the value of the ratiometric index at room temperature. In practice, these are the ratiometric index and dc voltage during calibration. Furthermore, ζ is the correction factor defined as:

$$\zeta = \frac{\alpha_r}{g_{dc}} = \frac{\frac{\Delta r}{r_o \Delta T}}{g_{dc}}$$

From experiments we noted that with an I_{dc} of 10 mA the V_{dc} varies between 1.05 V and 1.15 V. Taking the reference at 21°C this leads to a $\Delta\ V_{dc} = 0.1\ V$.

4.4.2 Thermal Characterisation and Review

The V_{dc}^{ref} and ζ have been set in the past to 1.14 V and 0.3 respectively. Since in the previous results it is noted that this dc voltage represents a temperature which is too high for these measurements, the reference dc voltage is set at the beginning of the measurement as the value at that time and temperature. It is noted from multiple measurements that sometimes these settings are too high and the compensation, as shown in Figure 4.21, overcompensates. It is also noted that sometimes manually selecting a ζ, which is smaller or bigger, corrects properly for some time and then the position reading starts to drift again away from the reference position.

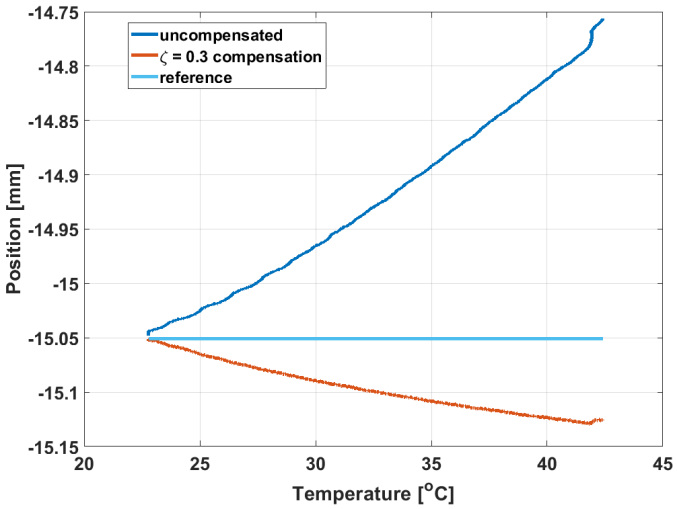

Figure 4.21: Comparing compensated position readout with $\zeta = 0.3$ to that of the uncompensated position readout at $I_{dc} = 10\ mA$

The I2PS has a position change which is of approximately 10 μm. Note that if

ζ is under-compensating, the position drift would be between the uncompensated value and the reference position. In this case it is beyond the reference position and therefore it is overcompensating. Nonetheless, an overcompensation which leads to a position change of 10 μm is acceptable in the LHC collimator environment but it does not match what is noted in operation. On the other hand, it would be beneficial if the values are honed to the point where this drift is completely removed.

Therefore, to understand why the ζ is overcompensating, the parts that make the ratiometric index i.e. the sense coils voltage and the ratiometric index itself are analysed individually. Figures 4.22 & 4.23 present a linear fit to the sense voltages, the ratiometric index, and the change in V_{dc}. From these figures it is shown that the gradient of the V_{dc} is two orders of magnitude higher than that of the ratiometric index. This means that if the V_{dc} change is not attenuated, it would compensate at a rate of two orders of magnitude more than required for the ratiometric index.

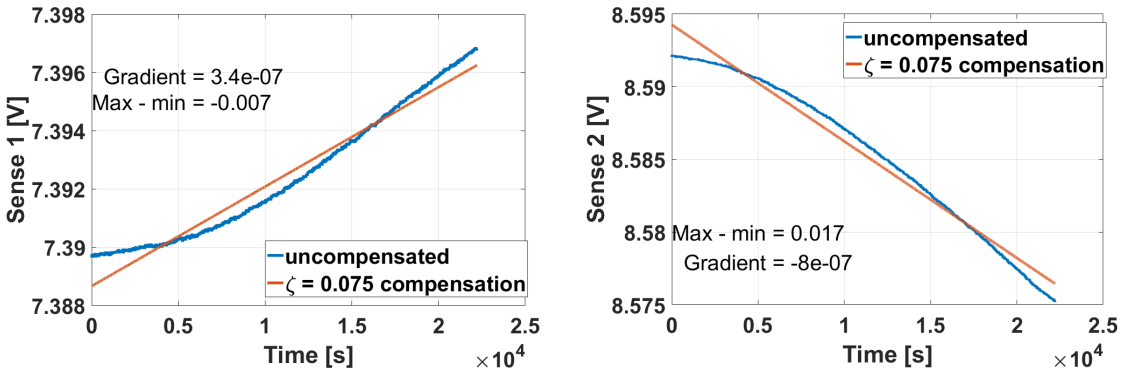

(a) Sense 1 **(b)** Sense 2

Figure 4.22: Comparing the maximum change of sense 1 and sense 2 with the change in V_{dc}

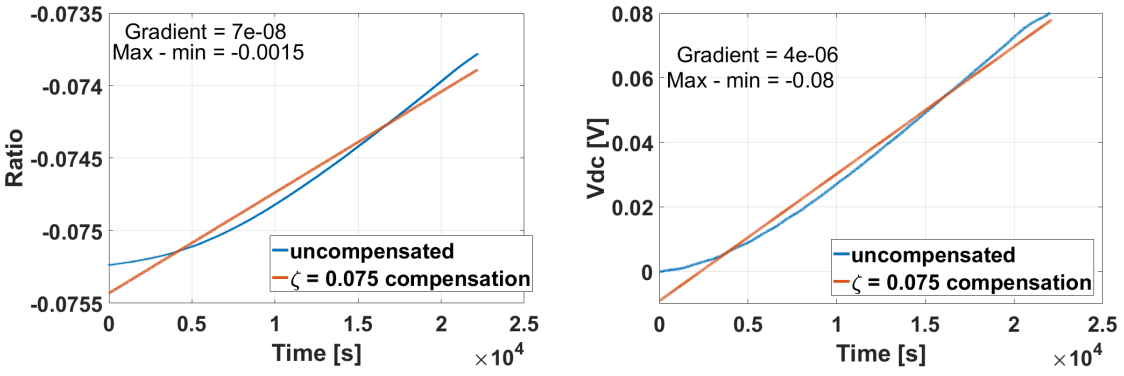

(a) ratiometric index **(b)** The change in V_{dc}

Figure 4.23: Comparing the maximum change of the ratiometric index with the change in V_{dc}

It is understandable that an experiment is needed that sheds light on the magnitude of ζ which is required to keep the read position at a reference (preset) position.

Furthermore, it is also interesting to understand if the magnitude of the I_{dc} has a strong impact on the ζ required. The former is achieved by implementing a simple addition to the LabView code. The start position is set as the reference position. As explained before the reference position is usually the position in which the sensor is left to settle. The difference is calculated and based on that difference where the ζ is increased/decreased in increments of 0.0001. This rate of change is selected to be this small such that it has time to settle and avoid overshoots. The user is allowed to intervene and change this increment value at any time. When it is left on its own with a large value, it sometimes oscillates around the reference position (as has happened in Figure 4.24b). While the exact value required cannot be obtained immediately, the trend and mean value is still achievable. Indeed, this test is also repeated multiple times with different I_{dc}.

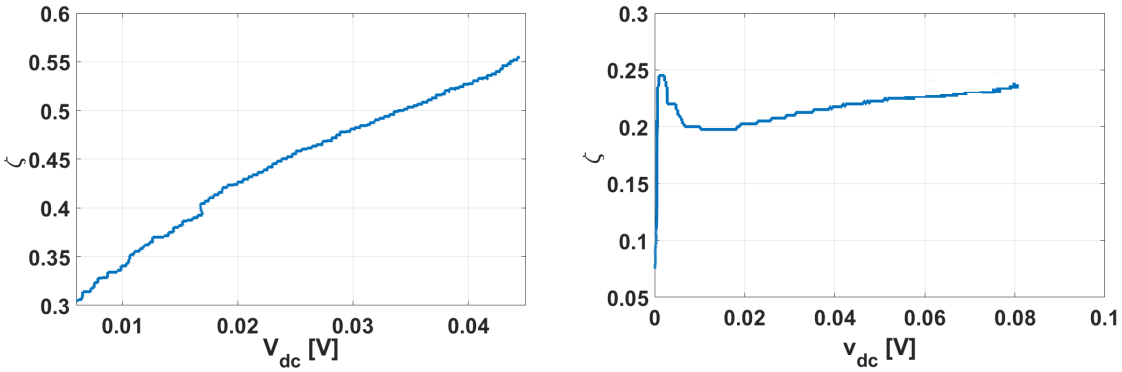

(a) with 5 mA **(b)** with 10 mA

Figure 4.24: V_{dc} with different input currents

Figure 4.24 shows two different ζ required for two different I_{dc} conditions. In Figure 4.24a the moving coil position is set to 15 mm and the I_{dc} is set to 5 mA. In this case one is to note the large ζ variation required for that particular $\Delta\ V_{dc}$. On the other hand, Figure 4.24b shows the ζ variation required for the sensor to keep the same reference position of 15 mm. In this case the current is set to 10 mA. Note how in this case the change in the ζ required is much smaller. Furthermore, note the smaller ζ swing/variation required. One can say that the ζ required is more stable. Finally, Figure 4.25b shows the ζ variation in the case where the moving coil position is at 15 mm with the I_{dc} set to 40 mA. Here, noteworthy is how small the ζ variation is. This implies that as the I_{dc} increases at 1 kHz, the required magnitude and ζ swing for good compensation decreases. Additionally, this also shows that the ζ change also stabilises as the current increases.

Figure 4.25a shows the position and the relationship between the $\Delta\ V_{dc}$ and ζ required to keep the position close to the reference position by 1 μm. These figures are obtained with an $I_{dc} = 40\ mA\ and\ I_{ac} = 20\ mA$. A linear and cubic fit are

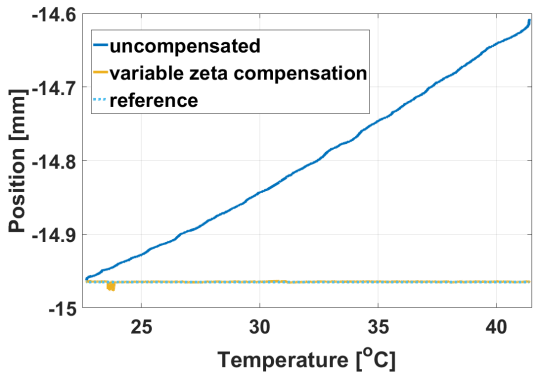

(a) Comparison between uncompensated and variable ζ required to get reference position

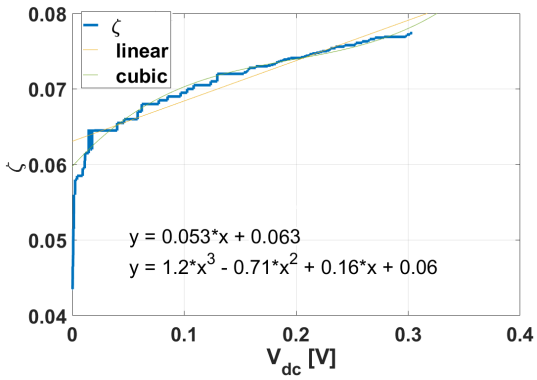

(b) The change in ζ to get the reference position with an $I_{dc} = 40\ mA$

Figure 4.25: Variable compensation algorithm

obtained for this relationship as presented in Figure 4.25b such that it could be implemented in the code.

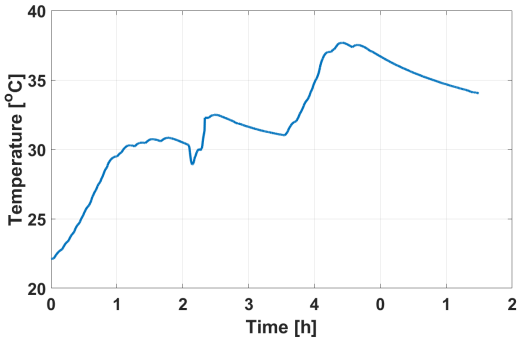

(a) Temperature profile followed

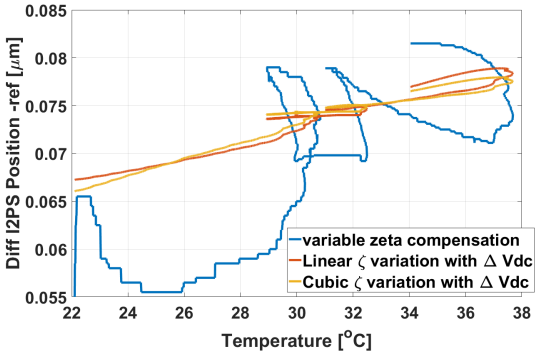

(b) Comparison between the ζ required and the calculated one from the previous experiment

Figure 4.26: Temperature and ζ readings during the long temperature profile

To test the possibility of implementing a variable ζ system and test the high I_{dc}, the following test is conducted. The variable ζ, as obtained from Figure 4.25b, is used on a long various temperature variation, done to mimic but exaggerate a day change in operation. The temperature variation is presented in Figure 4.26a, unlike the other temperature profiles the change is much more dynamic. The position correction presented in Figure 4.27 shows how the $\zeta = 0.3$ correction is overcompensating. On the other hand, a fixed average $\zeta = 0.075$ and the cubic and linear variations show a good correction. Finally, the ζ required (as in the previous test) is presented in Figure 4.26b. Here a comparison shows that while the cubic and linear variation is smaller, when compared to the variation required, it is similar to a best fit. As a result, a good correction is still obtained.

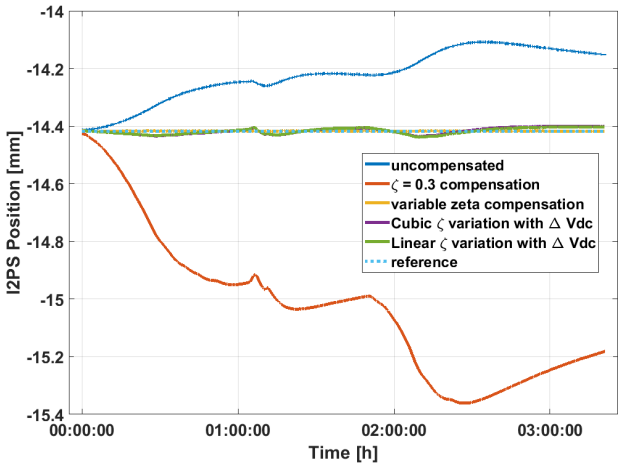

Figure 4.27: Position change for a long temperature profile at 1 kHz with high I_{dc}. The uncompensated position is compared to the normal compensation settings and to the cubic and linear adaptation.

To summarise these findings, a smaller ζ variation with temperature is preferred with respect to a very big variation, since in reality a more accurate approximate value could be obtained. Indeed, in this test a fixed ζ of 0.075 could compensate for the whole temperature swing.

Since no work has been previously conducted on this issue, it is important to characterise and compare the variation of position and ζ with temperature when a dc current of 10 mA and 40 mA are used. Furthermore, it will also be beneficial to obtain this characterisation at different moving coil positions and different frequencies. Starting from the 1 kHz case, the position is varied from 0 mm to 30 mm. Indeed, the position change is similar to that of Figure 4.18. The ζ required however is presented in Figure 4.28.

It can be observed that at the centre the compensation does not work unless a very high ζ is set. This may be due to the fact that the ratiometric index is very small and hence very close to zero. Undeniably, as the position starts to increase, the position of the ζ required becomes negative. This is due to the fact that the position change at the beginning does not go towards the electrical zero but instead goes away from the zero position and then changes direction, as shown in Figure 4.18. The direction change of the drift in these results is accompanied by a required ζ of 0 and then a positive ζ. While it may seem that none of the settings obtained in Figure 4.25b are able to compensate properly for this position change, it must be kept into consideration that the compensation required is for moving coil positions which are greater than 10 mm (or smaller than -10 mm). The position change between -10 mm and 10 mm is less than 100 μm at 1 kHz and hence a compensation is not strictly required. On the other hand, it is important that

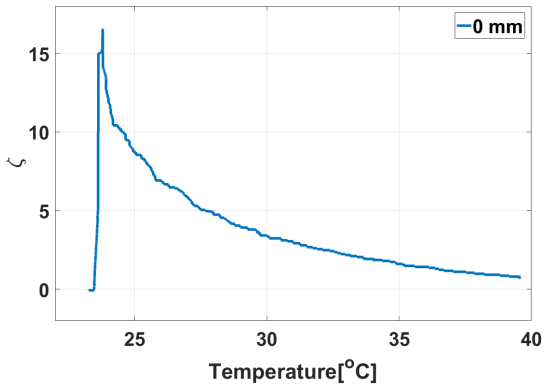

(a) ζ required when the moving coil position is at 0 mm

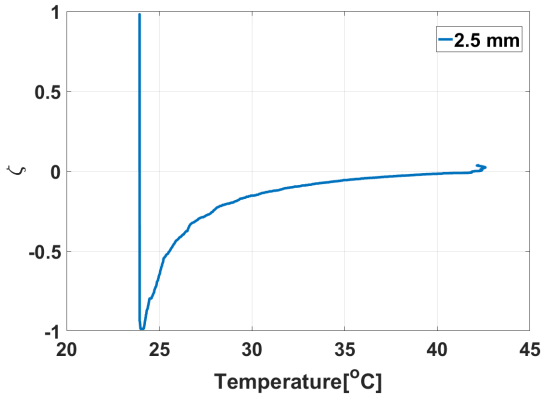

(b) ζ required when the moving coil position is at 2.5 mm

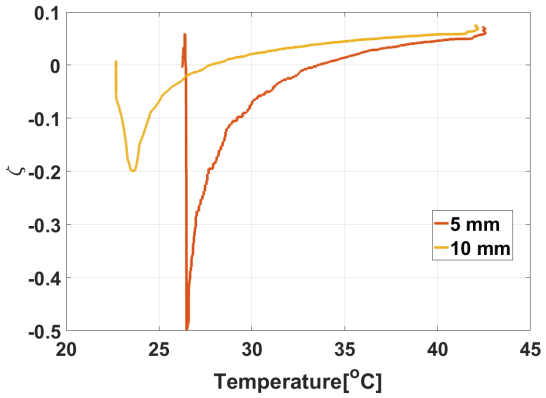

(c) ζ required when the moving coil position is at 5 mm and 10 mm

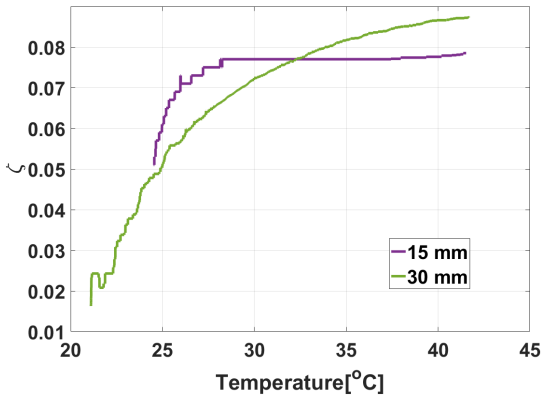

(d) ζ required when the moving coil position is at 15 mm and 30 mm

Figure 4.28: Different ζ requirements for different moving coil positions at 1 kHz with same cable length 200 m and supply $I_{ac} = 20\ mA$ $I_{dc} = 40\ mA$

the compensation does not overcompensate and hence becomes the source of error. Beyond the moving coil position of $\pm 10\ mm$, the compensation works as required.

As led to expect from Section 4.4, changing the frequency changes the way the position changes and hence the ζ required to compensate. While at 1 kHz the position drift is always towards the electrical zero, at 2 kHz the position change is away from the electrical zero. For example if the initial position is at 15 mm, at 1 kHz the position will drift to 14 mm. On the other hand at 2 kHz the same initial position of 15 mm will drift to 16 mm. This can be better appreciated in Figure 4.29a. This means that in order to compensate for the position drift, the compensation algorithm now requires a negative ζ for the majority of the sweep. Note that at 36°C in Figure 4.29b the position changes direction and starts going towards the electrical zero. At the same time the ζ required in Figure 4.29c changes from negative to positive. Similarly, the position change at the electrical zero, presented in Figure 4.29a, is away from the electrical zero, and therefore requires a negative ζ throughout the whole temperature sweep.

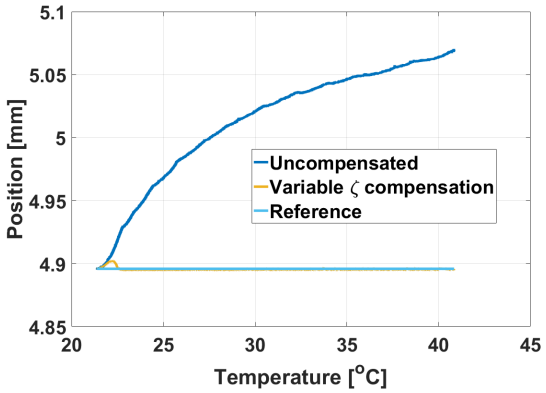

(a) Position readout change when the moving coil position is at 0 mm

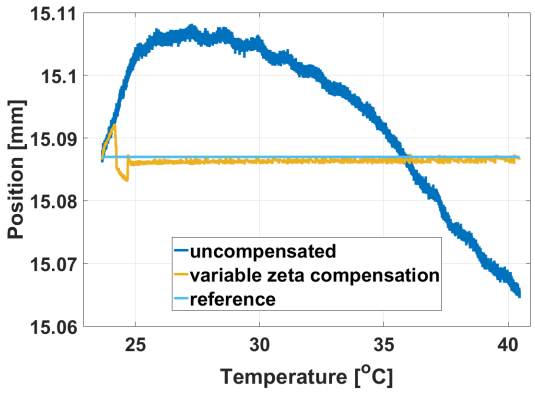

(b) Position readout change when the moving coil position is at 15 mm

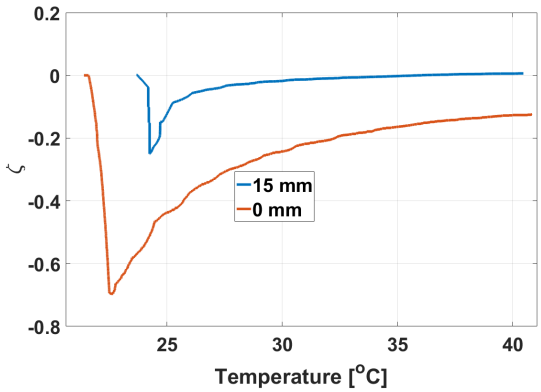

(c) ζ required when the moving coil position is at 0 mm and 15 mm

Figure 4.29: Position readout change and ζ required when the operating frequency is set at 2 kHz with same cable length 200 m and supply $I_{ac} = 20\ mA$ $I_{dc} = 40\ mA$

It is important to point out that this experiment is repeated for different frequencies, in order to understand better how the position changes with respect to ambient temperature change at different frequencies. Moreover, it is repeated to understand the magnitude and stability of ζ. From the following experiments it can be summarised that the position change is different for different frequencies at the same position for the same temperature profile. Not all plots are presented since there are a lot of repetitions. On the other hand, a summary for each frequency is presented. To compare the $I_{ac} = 40\ mA$ $I_{dc} = 10\ mA$ readings are taken also at 1.5 kHz and 2.5 kHz. The same reading is repeated at $I_{ac} = 18\ mA$ $I_{dc} = 40\ mA$ at 1.5 kHz and $I_{ac} = 10\ mA$ $I_{dc} = 40\ mA$ at 2.5 kHz. This helps in understanding the magnitude of the I_{dc} and the respective ζ required at 500 Hz intervals.

For 750 Hz, at 5 mm, $I_{dc} = 10\ mA$, ζ goes from 0 to 0.6 over 20°C hence a total change of 0.5. The 40 mA counterpart goes from 0 to 0.16. At 15 mm, $I_{dc} = 10\ mA$ ζ first goes into negative by 0.2, the position first distances itself from the electrical zero and then approaches it. Then it goes into positive by 0.4. At $I_{dc} =$

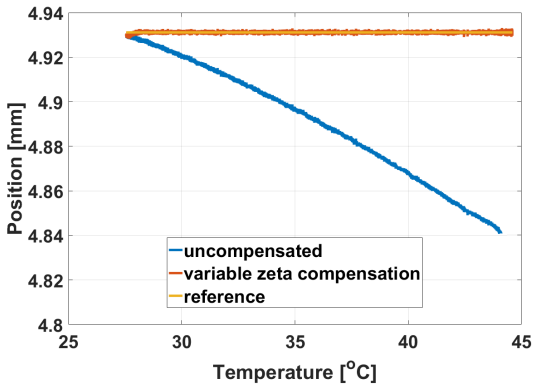

(a) Position w.r.t Temperature for I_{dc} :10 mA, f = 1250 Hz, MC pos: 5 mm

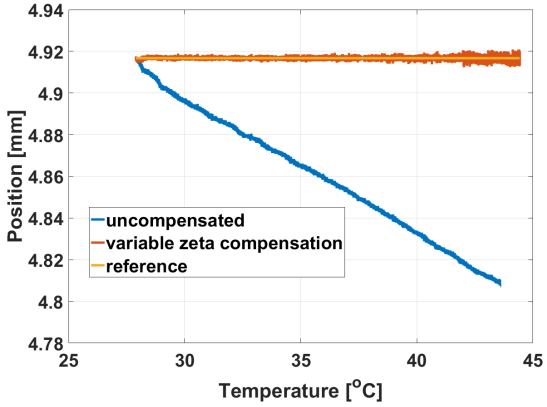

(b) Position w.r.t Temperature for I_{dc} : 40 mA, f = 1250 Hz, MC pos: 5 mm

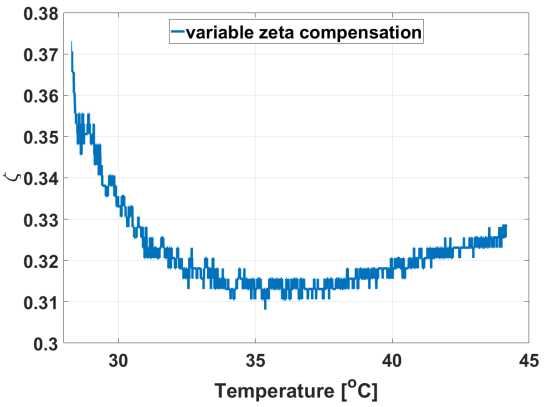

(c) ζ w.r.t Temperature for I_{dc} : 10 mA, f = 1250 Hz, MC pos: 5 mm

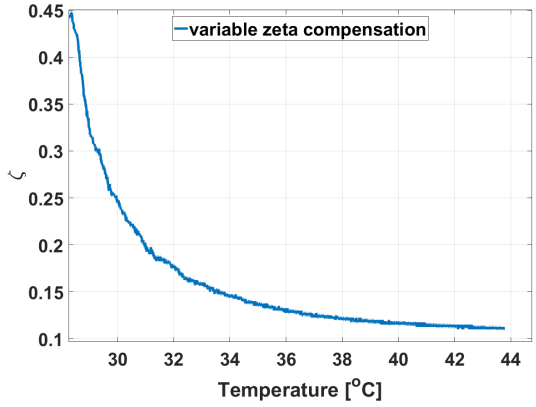

(d) ζ w.r.t Temperature for I_{dc} : 40 mA, f = 1250 Hz, MC pos: 5 mm

Figure 4.30: Position readout change and ζ required when the operating frequency is set at 1250 Hz with same cable length 200 m and but different dc supply

40 mA, ζ goes from 0.02 to 0.1.

For 1250 Hz, Figure 4.30 and 4.31, the ζ required at 5 mm is stable around 0.3 at 5 mm and 0.25 at 15 mm. This is the only frequency which a $\zeta = 0.3$ is the right value when $_{dc} = 10\ mA$ is used. At 5 mm $I_{dc} = 40\ mA$, ζ goes from 0.45 to 0.1, settling for the majority of ΔT at approx 0.13. Similarly, at 15 mm, ζ decreases from the initial value of 0.3 to 0.09 rapidly and then stabilises around this value.

At 5 mm, 1 kHz the position variation is not linear. In fact it first increases and then it decreases. At 1.5 kHz, the position immediately starts to decrease, Figure 4.32a. The final position change is approximately the same. Conversely, the ζ required , Figure 4.32b, to keep the reference position is positive. At 15 mm, Figure 4.32c the position only changes by a max of 100 μm. From 25°C to 33°C the position change is that of only 20 μm. Unlike the 2 kHz where it first increased and then decreased and reached a maximum of 100 μm, or the 1 kHz where it goes

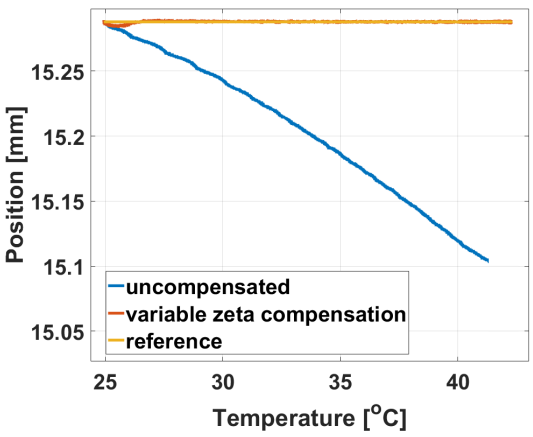

(a) Position w.r.t Temperature for I_{dc} : 10 mA, f = 1250 Hz, MC pos: 15 mm

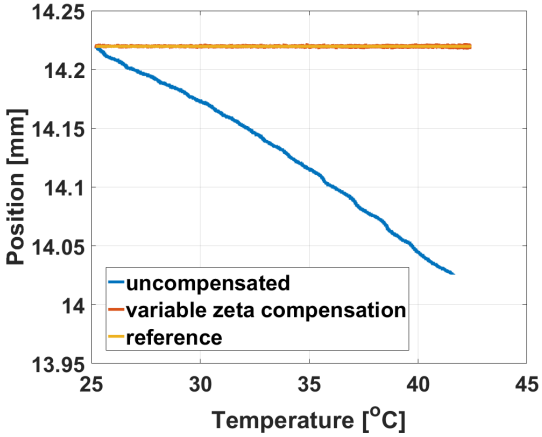

(b) Position w.r.t Temperature for I_{dc} : 40 mA, f = 1250 Hz, MC pos: 15 mm

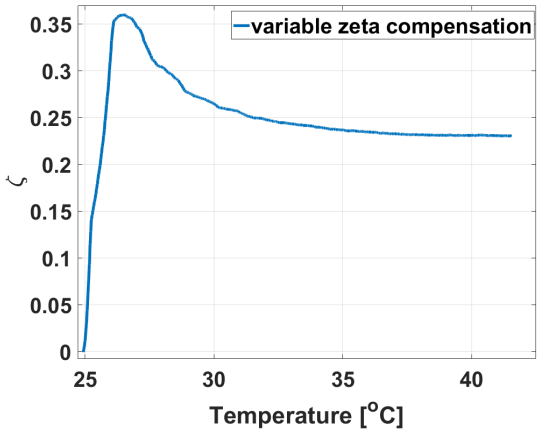

(c) ζ w.r.t Temperature for I_{dc} : 10 mA, f = 1250 Hz, MC pos: 15 mm

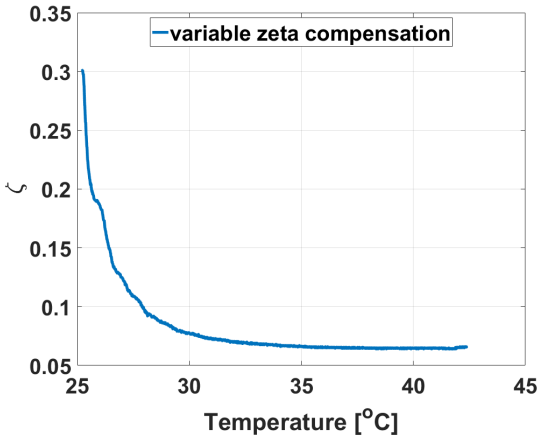

(d) ζ w.r.t Temperature for I_{dc} : 40 mA, f = 1250 Hz, MC pos: 15 mm

Figure 4.31: Position readout change and ζ required when the operating frequency is set at 1250 Hz with same cable length 200 m and but different dc supply

to 350 μm. The difference with respect to the 1 kHz one is that the required ζ, Figure 4.32d is always positive since the position never goes away from the electrical zero.

At the electrical zero, a max 35 μm of position drift is noticed. It requires a very high ζ to compensate. Basically at the centre of the sensor the ζ required is much greater than 1. In this case, at 35°C a ζ of 8 is required. The problem is that while the position change is small, 20 μm over 10° a ζ lower than 1 is incapable of compensating for it. This is also noticed in the 1 kHz case.

From all measurements and experiments it is noted that for the same frequency (1.5 kHz) as the supply current increases the position change decreases. At 15 mm the ζ goes from 0 to 0.1 when $I_{dc} = 10\ mA$. When $I_{dc} = 40\ mA$ it reaches steady state of $\zeta = 0.05$ much faster. The $\Delta\zeta$ is approximately three times

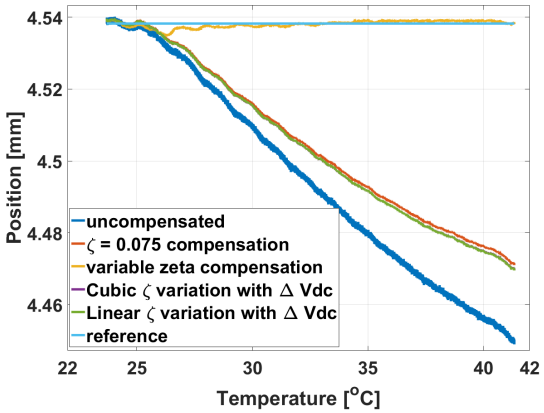

(a) Position change when the moving coil position is at 5 mm

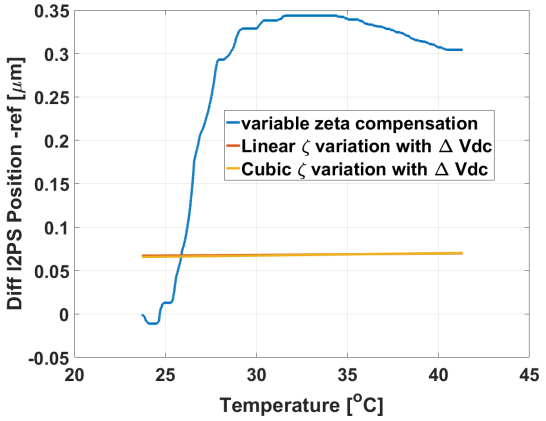

(b) ζ required when the moving coil position is at 5 mm

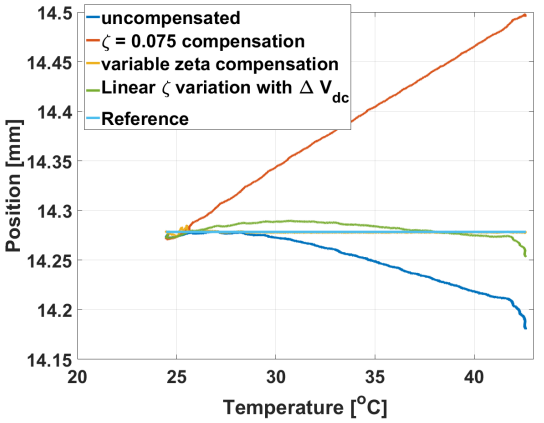

(c) Position change when the moving coil position is at 15 mm

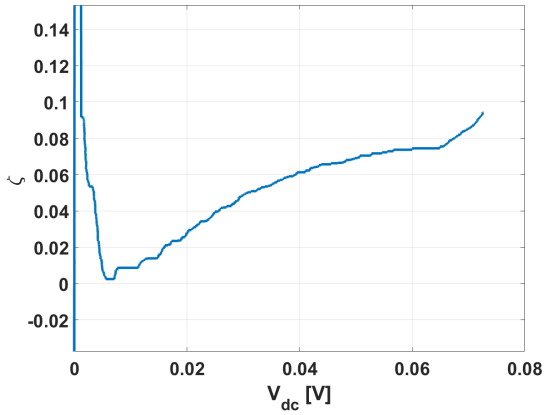

(d) ζ required when the moving coil position is at 15 mm

Figure 4.32: Position readout change and ζ required when the operating frequency is set at 1.5 kHz with same cable length 200 m and supply $I_{ac} = 40\ mA$ $I_{dc} = 10\ mA$

smaller. The position change at 1.5 kHz is smaller in the middle of the coil. When uncompensated, it goes to 50 μm. Then there is compensation with a $\zeta = 0.075$ or the linear fit / cubic fit of the ζ vs Vdc same as that at 1 kHz works well leaving a 10 μm position change.

At 1750 Hz, Figures 4.34 and 4.35, the average ζ required when $I_{dc} = 10\ mA$ and the moving coil position is 5 mm is 0.65 for a balanced compensation since the ζ changes from 0.5 to 0.85. In this case a $\zeta = 0.3$ would for example be under compensating. The position change for the two positions is the same. 1750 Hz is the only frequency at which the I2PS has the same position change at all moving coil positions. On the other hand at 15 mm the change in ζ is 0.2 when $I_{dc} = 10\ mA$ while it is 0.1 at 40 mA. The change in this case is not so big. At 15 mm a $\zeta = 0.075$ as deduced at 1 kHz may be enough to compensate but at 5 mm it would not be.

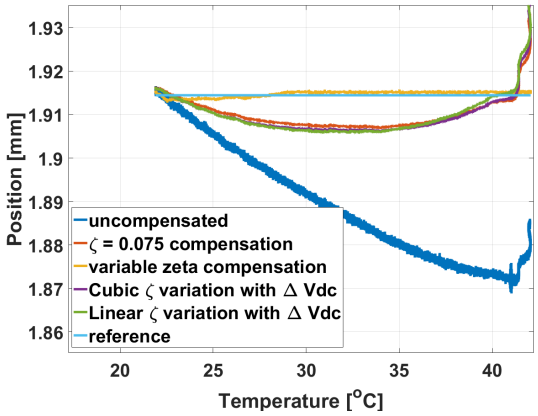

(a) Position change when the moving coil position is at 2 mm

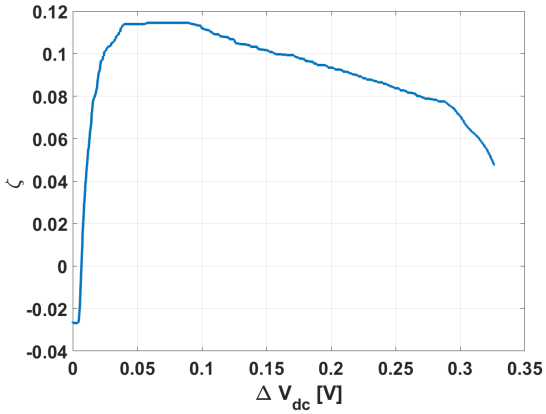

(b) ζ required when the moving coil position is at 2 mm

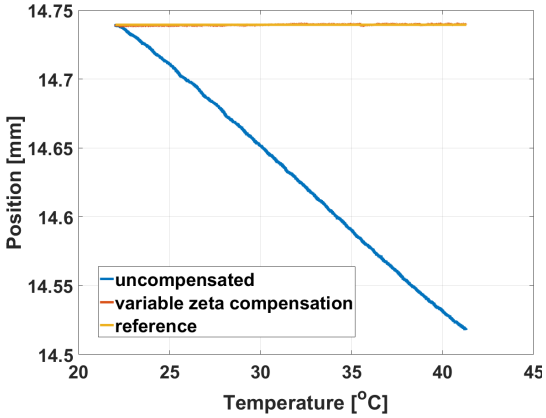

(c) Position change when the moving coil position is at 15 mm

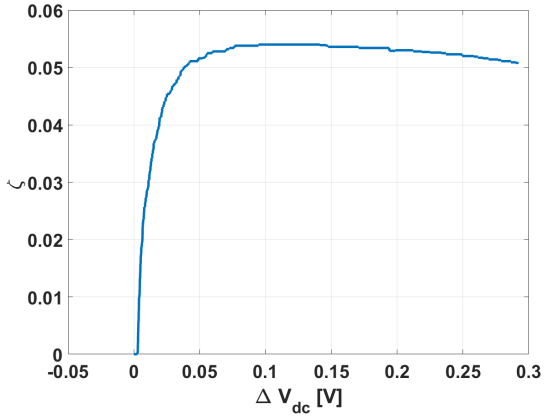

(d) ζ required when the moving coil position is at 15 mm

Figure 4.33: Position readout change and ζ required when the operating frequency is set at 1.5 kHz with same cable length 200 m and supply $I_{ac} = 18\ mA$ $I_{dc} = 40$ mA

At 2.25 kHz, the ζ required at 5 mm starts with a very large value and then stabilises at 0.4 for a temperature change of approx 8°C. On the other hand with $I_{dc} = 40\ mA$ the ζ required is at a stable 0.16. At this point the compensation will be enough for the temperature change. At 15 mm the ζ changes from 0.28 to 0.4. For $I_{dc} = 40\ mA$, MC pos: 15 mm, ζ decreases rapidly from the initial position of 0.3 and sets to approximately 0.2. At this point it decreases with temperature to around 0.1 at a slower rate.

The first important thing to notice is that the position change at 2.5 kHz, 1 mm goes towards the electrical zero unlike the 2 kHz case, and as expected from previous results. Second thing to note is that the change in position at the centre is smaller than at 15 mm. Finally, the ζ required is strange but the profile is repeatable. Up to 2 kHz the ζ required will change and then stabilise at some value. In this case the ζ first increases then decreases, as if there is a negative position change. Afterwards, there is a positive position change as noted with the

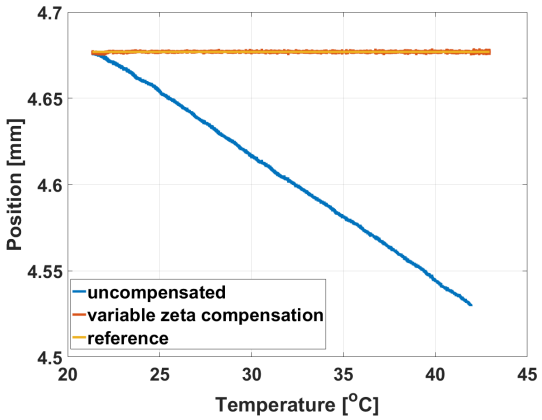

(a) Position w.r.t Temperature for I_{dc} : 10 mA, f = 1750 Hz, MC pos: 5 mm

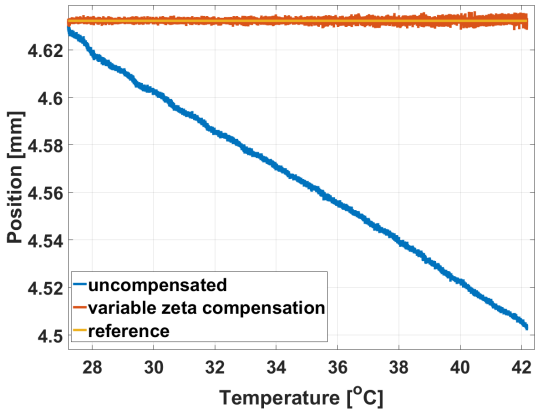

(b) Position w.r.t Temperature for I_{dc} : 40 mA, f = 1750 Hz, MC pos: 5 mm

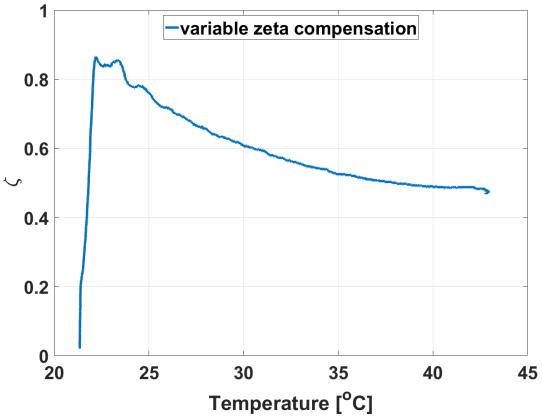

(c) ζ w.r.t Temperature for I_{dc} : 10 mA, f = 1750 Hz, MC pos: 5 mm

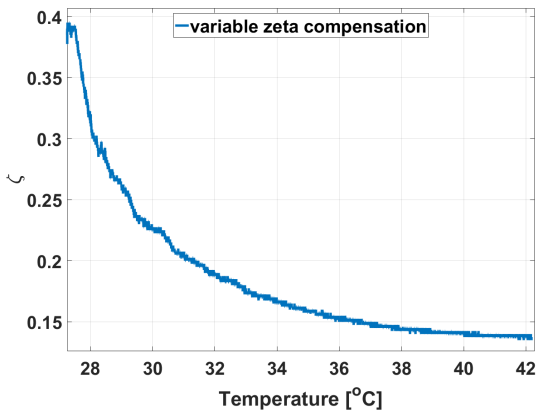

(d) ζ w.r.t Temperature for I_{dc} : 40 mA, f = 1750 Hz, MC pos: 5 mm

Figure 4.34: Position readout change and ζ required when the operating frequency is set at 1750 Hz with same cable length 200 m and but different dc supply

1.5 kHz case. This is unlike the 1.5 kHz case there is no justification to this behaviour because the position change is always the same. Ultimately, it continues to change without reaching a steady state.

Finally, at 2.75 kHz, I_{dc} = 10 mA, MC pos: 5 mm, ζ starts from 4 and decreases with temperature to approximately 1.3. This leads to a total swing of approximately 3.5 over a temperature change of 10°C. With I_{dc} = 40 mA, ζ changes from 2.5 to 0.5, hence a total swing of 2. At I_{dc} = 10 mA, MC pos: 5 mm, ζ is stable around 0.3, while at I_{dc} = 40 mA, it first increases rapidly to 0.9 such that it is able to compensate at low ΔV_{dc} and then it decreases to around 0.4. One can conclude that at this frequency the I_{dc} change from 10 mA to 40 mA offers no special benefits since it does not behave in the same way as the other frequencies.

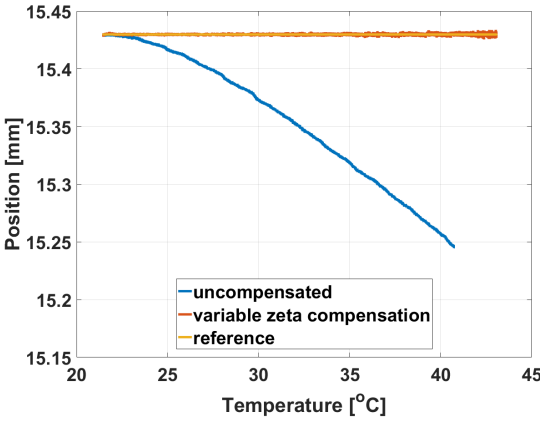

(a) Position w.r.t Temperature for I_{dc} : 10 mA, f = 1750 Hz, MC pos: 15 mm

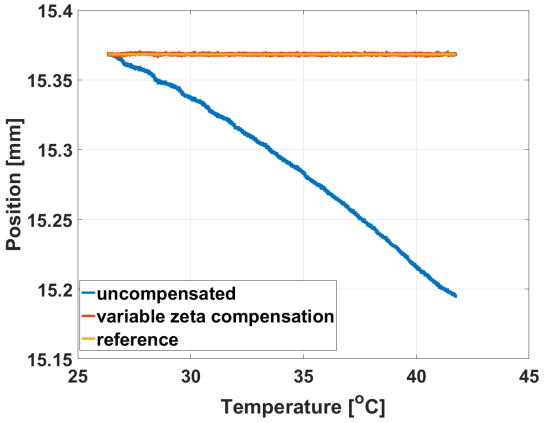

(b) Position w.r.t Temperature for I_{dc} : 40 mA, f = 1750 Hz, MC pos: 15 mm

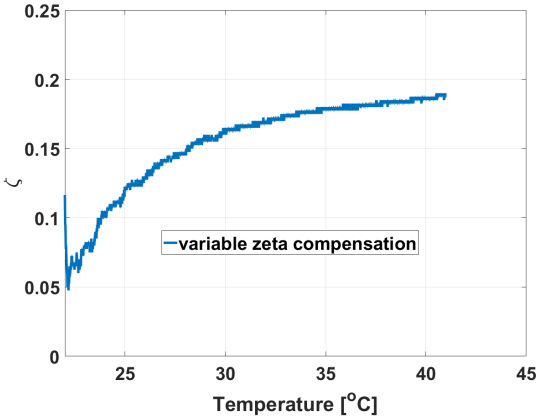

(c) ζ w.r.t Temperature for I_{dc} : 10 mA, f = 1750 Hz, MC pos: 15 mm

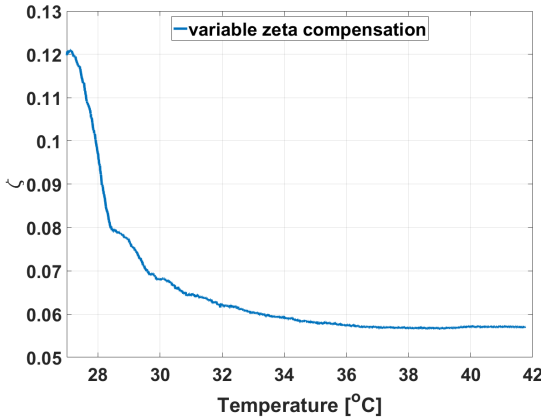

(d) ζ w.r.t Temperature for I_{dc} : 40 mA, f = 1750 Hz, MC pos: 15 mm

Figure 4.35: Position readout change and ζ required when the operating frequency is set at 1750 Hz with same cable length 200 m and but different dc supply

4.5 Summary

From these results it is evident that the behaviour of the I2PS, when the ambient temperature is changed, depends on the frequency and moving coil position. To summarise, the change in position at all frequencies except at 2 kHz is similar. This means:

- As the moving coil goes away from the electrical zero the change in position increases;
- The max change in position for approx 20°C is approximately the same; and
- The read position change is towards the electrical zero

Indeed, there are some differences between the different frequencies

- At 2 kHz the read position change at the electrical zero is bigger than that at the end of the sensor;
- At 2 kHz the read position change is away from the electrical zero; and
- At 1.75 kHz the read position change at 15 mm is similar in magnitude as that at 5 mm.

The ζ required, if the current I2PS settings are kept i.e. operating at I_{dc} of 10 mA, it varies from one scenario to the other. Conversely, these results show that if the I_{dc} is set to 40 mA the ζ required varies less and it is found to be between 0.075 to 0.1. On the other hand, this still does not ensure that there will be perfect compensation. However, since the temperature change in the LHC tunnel will vary by a few degrees and the ζ swing is reduced considerably in most cases, it should ensure a good compensation.

This study has also showed that three frequencies can be set where the position change can be very small. These combinations are:

- 1.25 kHz with $I_{dc} = 10\ mA\ and\ \zeta = 0.3$;
- 1.5 kHz with $I_{dc} = 40\ mA\ and\ \zeta = 0.08$; and
- 1.75 kHz with $I_{dc} = 40\ mA\ and\ \zeta = 0.1$.

This leads to a problem since when installed on a collimator, all seven I2PS installed are set to operate at a different frequencies. This is done since there could be electromagnetic interference when the sensors are close to each other. Hence, three investigations are required at this point, the first aimed at understanding if there are possible modifications to be done to the sensor to enhance the immunity of the sensor to thermal drift. This is presented in Section 5.3. The second aimed at investigating the effect on the position read by an I2PS which is placed in close proximity to another I2PS and which is operating at the same frequency as presented in Section 5.2.

It is also evident from this chapter that if the temperature of the sensor increases gradually and uniformly, the temperature compensation (if configured properly)

can indeed compensate for some of the spurious position reading change and hence limit to a few tens of microns. Therefore, while a deeper understanding of the sensor and the compensation algorithm is successfully achieved in this chapter, further investigation needs to be conducted to understand the position change as noted in operation. This indeed is the third investigation.

To conclude, using the knowledge gained from the research presented in this chapter, the aforementioned investigations shall be presented in the next chapter.

Chapter 5

Design Modifications

5.1 Introduction

As outlined in the previous chapter, this chapter presents further analysis in the development of an enhanced thermal response. This chapter studies the electromagnetic susceptibility and propagation when several I2PS are operated at the same frequency and close to each other. Additionally, the simulation and experimental results of two moving core design changes are presented where the coil is changed to a solid core and the material is changed from copper to brass. These modifications are indeed tested in order to gain higher structural integrity, reduction in manufacturing time and hence in costs, a better linearity response and since brass has a lower thermal coefficient, it exhibits a smaller change in its resistance due to temperature. Finally, this chapter aims at presenting the final modifications implemented on a test collimator showcasing the added stability.

5.2 Behaviour of I2PS in Close Proximity to Each Other

The I2PS was designed on the premise of being immune to slowly varying or static magnetic fields. The sensor's tolerance to high frequency electromagnetic interference was never tested. On the other hand, as a precaution, if multiple sensors are operated at the same time, their operating frequency is varied. This ensured no cross-talk in the cables as well as no cross-talk between sensors in close vicinity. From Chapter 4 it is understood that it is important to understand if operating the I2PS at the same frequency poses any position variation [92]. The magnetic field of two sensors is therefore simulated to understand how the magnetic field behaves outside the transducer, especially at the edges of and in between the two I2PS. Furthermore, the simulation will provide a scale of the magnitude and the distance which the magnetic field propagates from the sensor.

5.2.1 Sensor's Finite Element Model

The Finite Element Model (FEM) [93,94] of the I2PS is developed in the simulator FLUX® by Altair. This simulator offers both modelling in 2D and in 3D. In 2D only the cross-section is modelled and the simulator either extends this in the z-axis (adds depth), if modelled in the x - y axis or rotates the cross-section around an axis. Since the I2PS is axisymmetric, a 2D simulation can be used as long as this condition is maintained. The main advantage of a 2D model is the reduced complexity when modelling the sensor. This leads to a reduction in the computational resources required and faster execution time. In the past [40], the results in 2-Dimensional (2D) showed a 98% match with the 3D simulation. Therefore, for a 2D simulation, as long as the change in the I2PS' position happens only in the y-axis (refer to Figure 5.1) a 2D simulation can be performed. On the other hand, the addition of a second transducer in the x direction, as shown in Figure 5.2 violates the domain axisymmetric requirements and hence a transient-magnetic 3D simulation needs to be performed. Two sensors will be taken in consideration henceforth, as presented in Figure 5.1, which will be referred to as $I2PS_{S1}$ and $I2PS_{S2}$. A transient magnetic application can be defined in both the 2D and 3D simulations which allows the study of the phenomena created by a time variable magnetic field. In fact, with this type of application the magnetic field is

related to the presence of variable currents. Therefore, the simulator requires an electric circuit to execute. A mixture of meshed and non-meshed coils are used to build the 3D scenario. Non-meshed coils make use of the available mesh and so does not rely on it. The main advantage of non-meshed coils is a substantial reduction of the number of nodes. To be able to make simulations, a mesh, consisting of up to millions of small elements that together form the shape of the structure needs to be created.

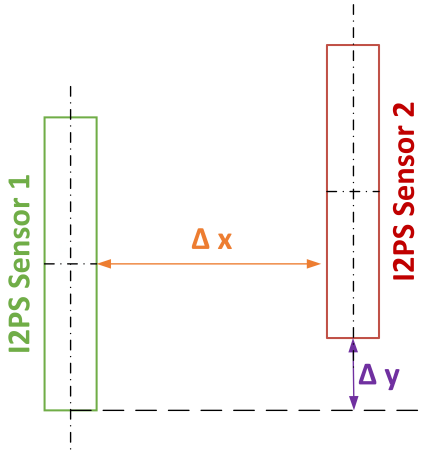

Figure 5.1: A diagram showing the positioning of the I2PS with respect to each other.

In Figure 5.2 the mesh is the small triangles making up the blocks, the elements or nodes are the corners of these triangles. Calculations are made for every single element. Combining the individual results gives us the final result of the structure. Hence, the finer the mesh or the higher the number of nodes the more accurate the result. Moreover, the better the fit of these elements together constitutes the quality of the mesh. Finally, the higher the number of nodes implies a higher individual calculations. This implies that the computational resources required and the time to execute are also increased. A mesh convergence analysis was conducted in [92] and hence the following mesh properties were used for this sensor.

As can be noted from Table 5.1, the thinnest coil of the structure is the sense coil $\approx 0.3\ mm$ and hence, the sense coil is meshed while the supply and moving coils are set to non-meshed coils. Consequently, the sense coil is set to a mesh with $0.15\ mm$ tetrahedrons. This places the non-meshed coils inside the area meshed with elements ranging from $0.15\ mm$ to $1.5\ mm$, as can be noted in Figure 5.2. Therefore, the non-meshed coils are solved with a fine mesh as well. Since, the supply coil is thicker than the sense coil and it is only $0.05\ mm$ away from the sense coil, the mesh relaxation does not affect the simulation accuracy. Furthermore, the moving coil has a bigger diameter and hence a bigger mesh can be used. The outer line of the shield is set to a meshed solid and meshed with $5\ mm$ elements.

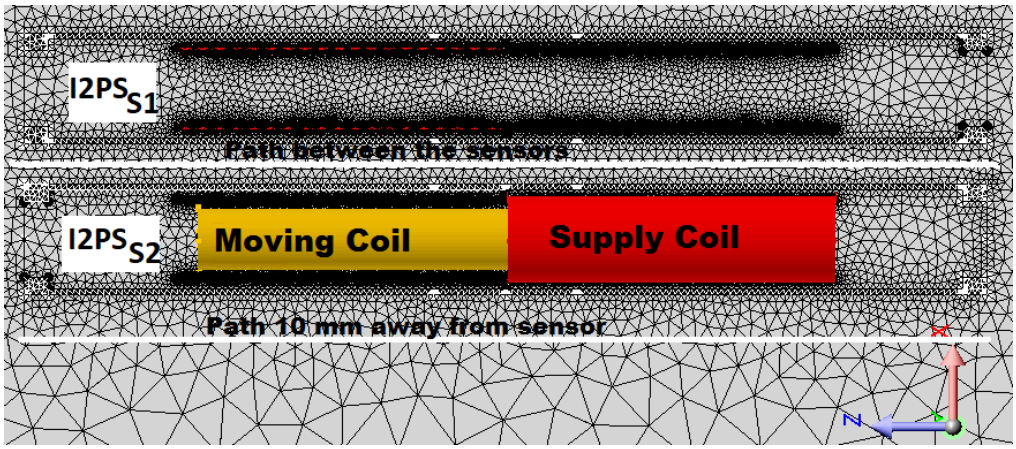

Figure 5.2: FEM meshing scenario highlighting a crossection of the coils and the paths, as in the 3D scenario, used for the graphs.

Table 5.1: Physical characteristics of the sensor

Physical parameter	Value
Sensor's Length	235 [mm]
Sensor's Diameter	13.4506 [mm]
Bobbin diameter of the Sense - Supply coil	19.2 [mm]
Bobbin diameter of the Moving coil	4 [mm]
Sense/Supply coils' length	80 [mm]
Moving coil's length	90 [mm]
Moving coil's number of turns	3150
Supply coil's number of turns	4500
Sense coil's number of turns	1388
Moving coil's wire diameter	0.4 [mm]
Sense coil's wire diameter	0.2 [mm]
Supply coil's wire diameter	0.05 [mm]

Since a transient magnetic application is used, a circuit describing the geometry is defined. Two current supplies are set to generate opposite 50 $mA - peak$ with a frequency of 1 kHz. These are connected to coil conductor elements such that the supply coils are defined. Coil conductors are used to link the coils in the geometry with the one in the electrical network. In the electrical model the supply coil's resistance is set to 55 Ω. The resistance of the sense coils is set to 2.5 $k\Omega$. Since, a very high impedance readout system is used to read the signal from the sense coils, a resistor of 1 $M\Omega$ is placed in parallel. The moving coil resistance is set to 17.9 $m\Omega$ and a resistor of 1 $m\Omega$ is set in parallel to it to simulate the short.

5.2.2 Numerical Simulation Results

The simulation shows the magnitude of the magnetic field that propagates from the I2PS. The results simulate two parallel placed I2PS, 1 cm apart from each other. These results also present the scenario where the moving coils are at the same position and with the same supply phase. This state is presented since it is the circumstance that creates the highest interference between the two. It is noticed that the magnetic field oscillates, as expected, with the frequency of the sensor. In fact, Figures 5.3 and 5.5 present the field lines for the sensor at the crest and at the zero crossing of the amplitude. Furthermore, Figures 5.3 and 5.5 show the magnetic field outside the sensor and hence the field strength escaping the sensor. To put the magnetic field values in context 170 A/m transposes to 213 μT. 58 μT is the strength of earth's magnetic field at 50° latitude and 5 mT is the strength of a typical refrigerator magnet [95].

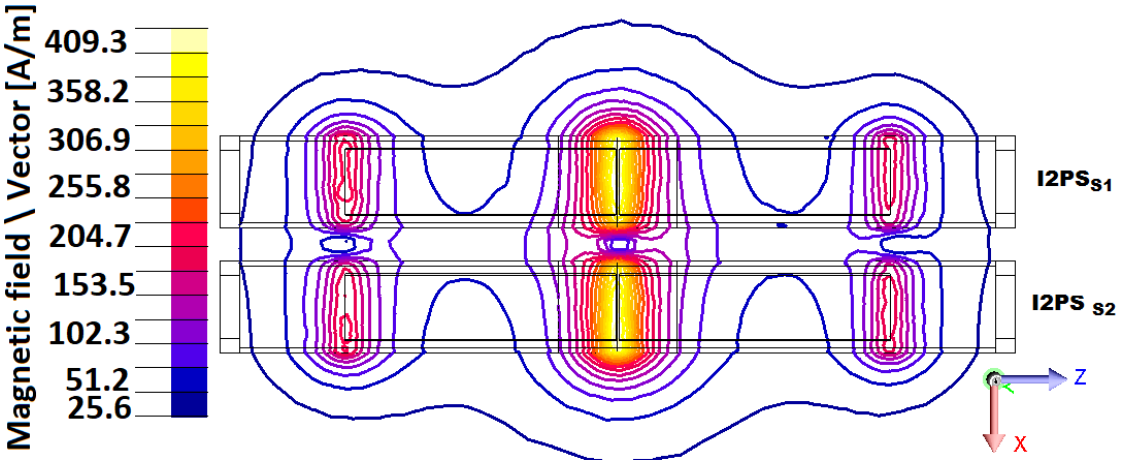

Figure 5.3: A detailed representation magnetic field escaping the sensor at the peak of the supply.

Figure 5.4 shows the magnetic field alongside the sensor at different points. In Flux®, path lines can be defined to take a cutaway of the amplitude of a parameter, in this case magnetic field. The latter are illustrated in Figure 5.2. To understand better the curves presented, the position of the coils along the sensor length are marked in lines at the top of the graph. Five paths are taken into consideration; a path between the two sensors and paths at 5 mm, 10 mm, 20 mm and 100 mm away from the sensor.

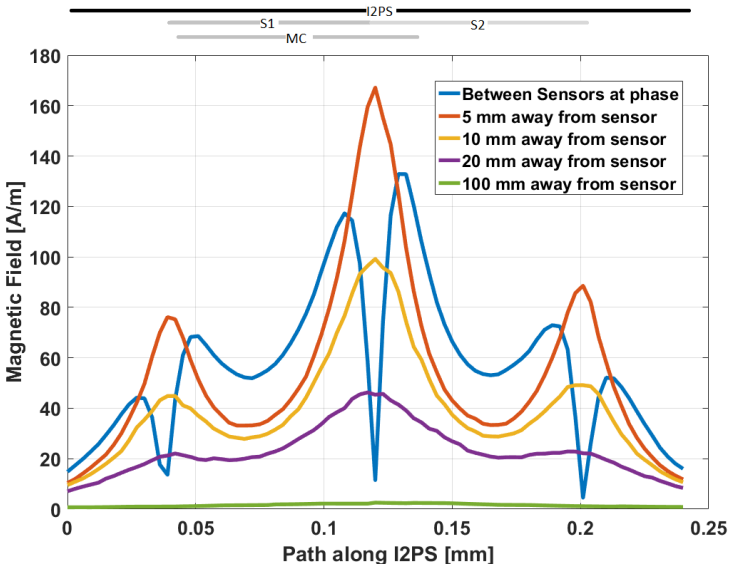

Figure 5.4: Magnetic field at increasing distances from the sensor at the peak of the supply voltage

Starting from the path, which is 5 mm away from the transducer, the magnetic field has three peaks along $I2PS_{S2}$. These are roughly located at the ends of the sense/supply coils and at the gap between the coils at the centre of the sensor. This 1 mm gap between the two sense and supply coils comes from the manufacturing process and cannot be removed. This point can be identified in Figure 5.3 as the spot with the highest density of field lines. Moving away from the centre, two more peaks can be observed at the end of the sense or supply coils. Note that these curves are logged outside any of the sensors and hence only the magnetic field of one sensor is observed. It is also noted that the peak that corresponds with the start of the moving coil (MC) is smaller by 12 A/m than the one on the opposite end. Since the moving coil generates a field opposite to that generated by supply coils (as explained in Section II) the overall magnetic field is attenuated. As the path is moved further away from the sensor, the magnetic field decreases. The shape of the curve taken 10 mm away from the sensor is comparable to that taken 5 mm away but with a smaller amplitude. Finally, the path between the two sensors, which is set 5 mm away from each sensor, is similar to the 5 mm case. In this case, the curve shows multiple peaks forming close to the beginning and ends of the coils. A sharp decrease in the magnetic field is noted at the air-gap between S1 and S2 while the biggest peak is observed at one end of the MC. Furthermore, it can be noted that the shape of the curve corresponds to that of the 5 mm and 10 mm paths. It can be understood that the magnetic field drops because of the interaction of the two magnetic fields coming from the two I2PS.

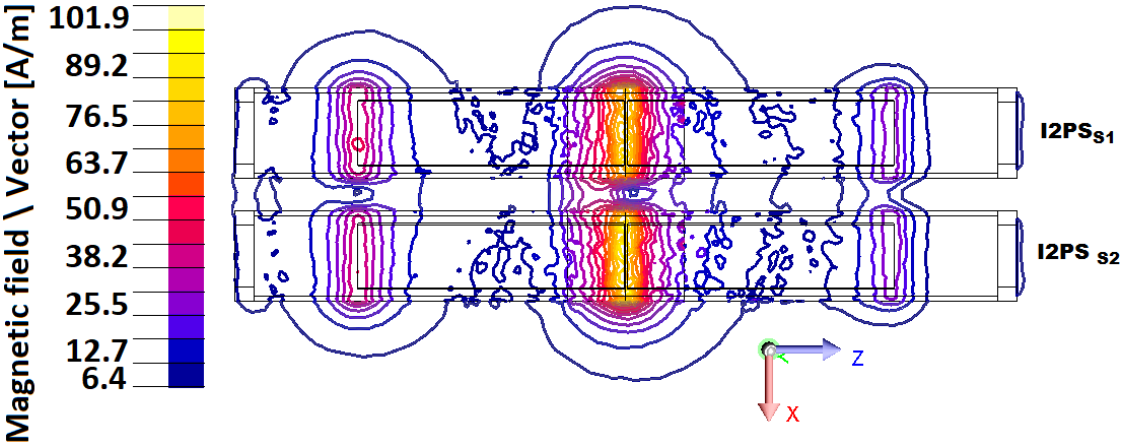

Figure 5.5: Presents a more detailed representation magnetic field escaping the sensor.

When the the supply of the sensor is at the zero crossing, a much lower magnitude is noted. The field lines presented in Figure 5.5 portray a very feeble interaction outside the sensor. From Figure 5.6, it is noted that the field has lower magnitude peaks outside the sensor, with a peak value of 30 A/m. Similarly, the field between the sensors reaches a peak value of 35 A/m with two sharp spikes towards zero at the ends of the moving coils. It is also noted that at 5 mm the difference between the two side peaks is still of approximately 10 A/m, like in the previous case. This means that the interference of the moving coil remains the same. This is expected since the moving coil is not moved.

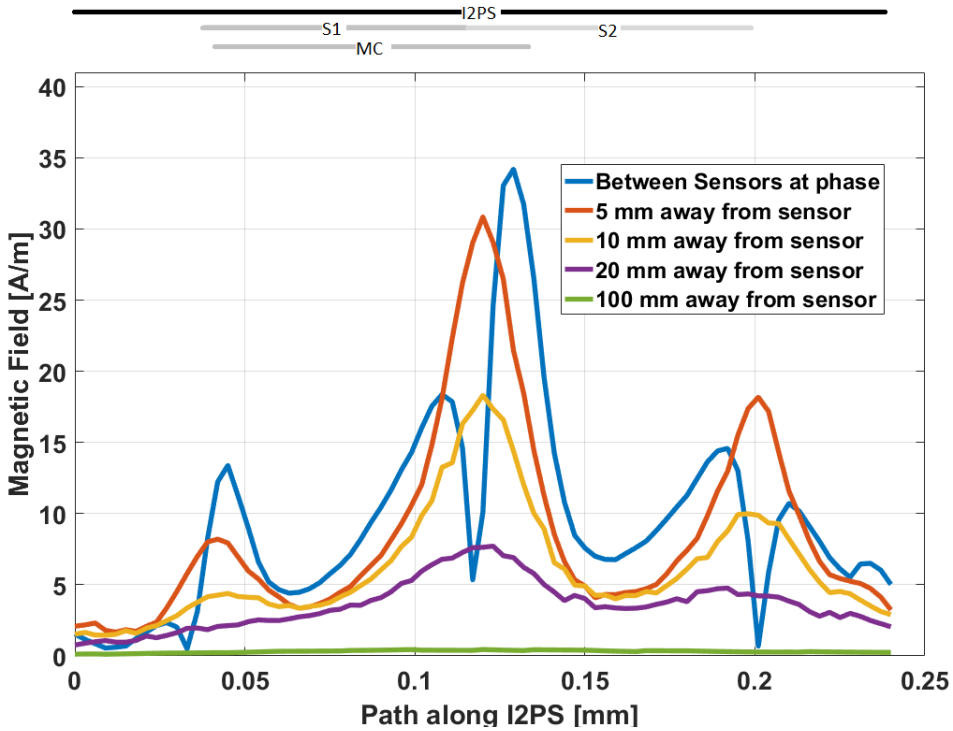

Figure 5.6: A detailed representation magnetic field escaping the sensor at the zero crossing of the supply.

Now, consider the case where $I2PS_{S1}$ is adjacent to $I2PS_{S2}$ as presented in Figure 5.7. The magnetic field, 5 mm away from the sensor is observed in Figure 5.8a. The behaviour is comparable to that experienced when the sensors are parallel. The calculated speculation that the moving coil causes the disproportion in the side peaks as presented in Figure 5.4 & 5.6 is proven in Figure 5.8a. The two side peaks have the same amplitude since the moving coils are placed in the middle of the sensor. Moreover, the amplitude of the magnetic field between the sensors is reduced to approximately 10 A/m. The magnetic field between the two sensors is presented in Figure 5.8b. As observed in Figure 5.7, at the centre, the magnitude falls to zero. At this point, the magnetic field from both sensors cancels out. Figure 5.7 also presents the magnetic field 5 mm away from one sensor end and shows an increase in the middle.

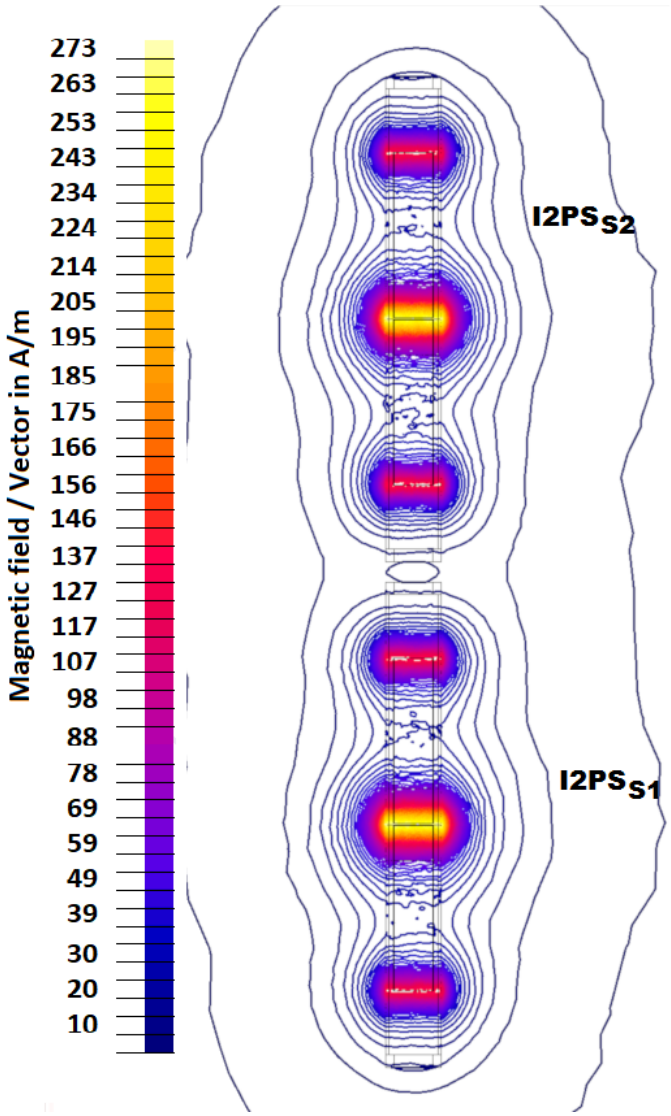

Figure 5.7: The magnetic field at peak amplitude outside when the sensors are adjacent to each other

The simulation results show that there is a resulting magnetic field outside the sensor which exhibits a rapid decline in the magnitude as the sensors are further away from each other. It also shows that in between the sensors there is an interaction between the two sensors. Furthermore, since the magnetic field oscillates, the resulting impact on the I2PS position will also be varying with time. Finally, the results show that at a distance of 100 mm the magnetic field has decreased considerably.

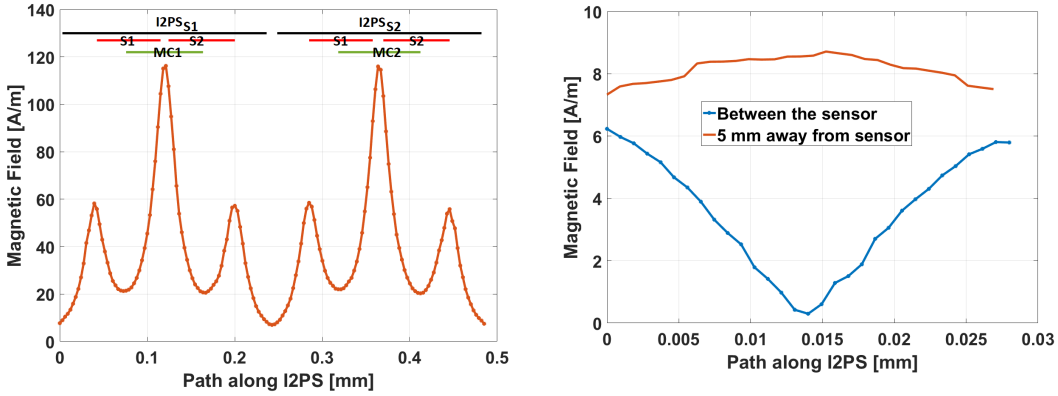

(a) Magnetic field along the sensors **(b)** Magnetic field between the sensors

Figure 5.8: Magnetic field around the transducers when the I2PS are on top of each other

5.2.3 Test-bench Results

A simple test bench is set up where two separate current supplies are used to power the sensors at the same frequency and all coils are acquired by means of a DAQ. The sensor's cables are shielded and grounded. The investigative method adopted is as follows: the sensor is turned on and left working for thirty minutes. This is done to satisfy the recommended warm up time of the DAQ, which is fifteen minutes, [88]. One sensor is fixed at the origin, Figure 5.9, such that the moving coil position is not changed by mistake since in the following measurements, the moving coil is centred but left free to move. On the other hand, the second sensor is moved to a measured position away from the I2PS$_{S1}$. When the I2PS$_{S2}$ is in the required position, the signal acquisition for the I2PS$_{S1}$ is initiated. After a benchmark is obtained, the supply for $I2PS_{S2}$ is turned on.

The magnitude of the sense coils' voltage when the $\Delta x = 10\ mm$ is presented in Figure 5.10. $I2PS_{S2}$ is powered after a waiting time of two seconds (the benchmark window). It can be observed that there is no change in voltage during the benchmark. When $I2PS_{S2}$ is powered there is an immediate voltage drop of

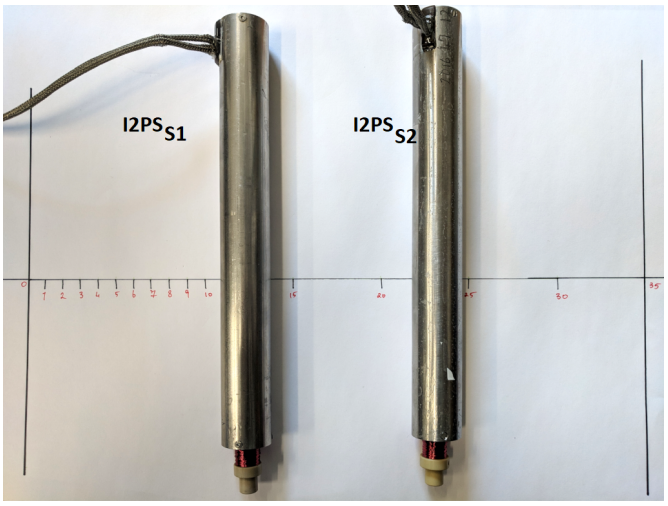

Figure 5.9: Picture showing the parallel I2PS used for the experiment. $I2PS_{S1}$ is moved to the origin of the drawn ruler and $I2PS_{S2}$ is moved away from the former. The moving coils shown outside the sensor are placed inside.

0.1 V and then it starts oscillating with a max Δ V of 0.2 V at a very slow rate of 0.03 Hz.

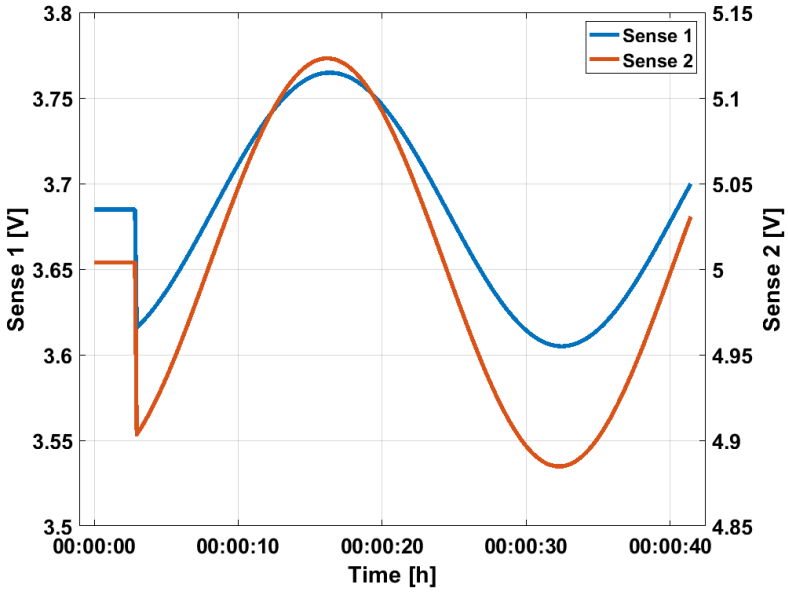

Figure 5.10: The sense coils' voltage with interference when $\Delta x = 1$ cm. Note that for the first two seconds the second I2PS is un-powered and hence there is no interference.

This results in a ± 250 μm of position drift as shown in Figure 5.11a. As $I2PS_{S2}$ is moved further away from the sensor, the position change decreases while the period of the eventual sinusoidal signal remains the same. In fact, the magnitude of the position change reduces to the point that on the scale of Figure 5.11a the position drift is not obvious any more when the sensor is 300 mm apart.

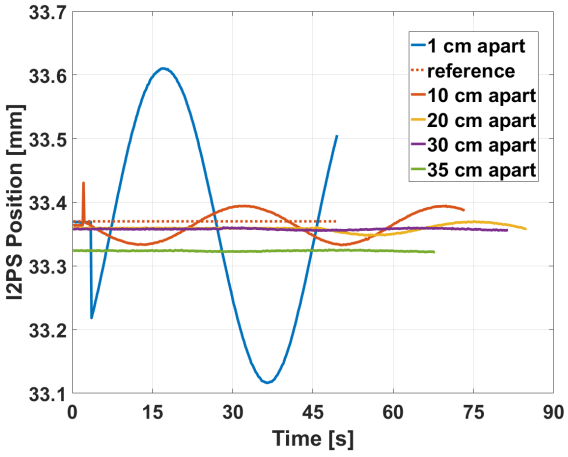

(a) Comparison of the interference magnitude on the position reading at different Δx distances between the two I2PS

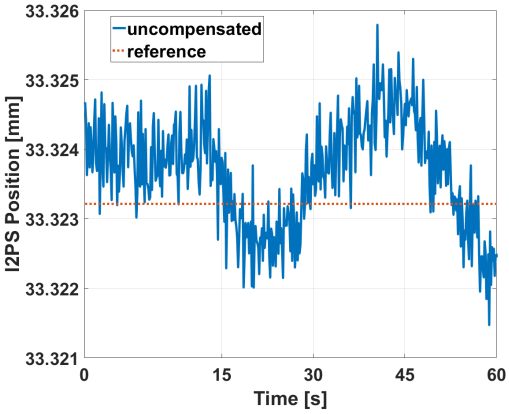

(b) The position change when the gap between the two I2PS is $\Delta x = 35$ cm

Figure 5.11: Interference magnitude on the position reading at different Δx

Figure 5.11b presents the position change when the Δx is 350 mm away. With this gap while there is still interference, it has decreased to approximately 1 μm and hence can be considered negligible. The same procedure is repeated such that $I2PS_{S2}$ is moved in both the x and y-plane. Figure 5.12 presents the position change when the Δx is kept at a constant 150 mm and the sensor is moved in the y direction. In this scenario, as the sensor is moved in the y-axis there is no change in the level of interference between the two.

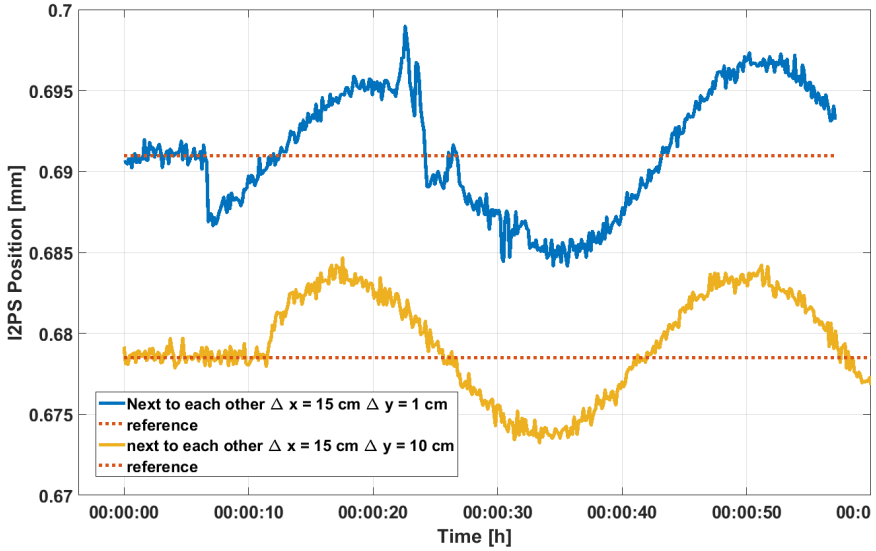

Figure 5.12: Comparison of the position reading with interference at different distances between the two I2PS

These results imply that the I2PS is immune to electromagnetic interference as originally designed, if another sensor is operated more than 350 mm away from it at the same frequency. Any other frequency does not affect the sensor.

5.3 Design Modifications of the I2PS

From the conducted experiments, it is noted that the biggest contributor to thermal drift in the I2PS is the moving coil. The idea behind the following set of experiments is to modify the I2PS such that the temperature dependence is reduced [96]. The aim of this task is to reduce the I2PS sensitivity to temperature by:

1. Choosing a moving coil wire material that is physically less susceptible to temperature change.
2. Resining the moving coil such that it is insulated from temperature change.

These changes are presented in Figure 5.13 where Coil 1 is a normal, copper-wound moving coil, which in this study, is used as the benchmark. The second coil shows a brass-wound moving coil. Brass has a lower thermal coefficient than copper as explained in Section 5.3.1. This implies that the resistivity of the material changes less when the temperature is changed. Coil 3 presents a resined moving coil which is the same as the copper-wound coil with the difference that the coil is encased by an insulator. This should, in theory, also reduce the position change due to temperature change. Finally, modification 4 shows the brass moving core which should provide a more linear voltage versus position response and since it is made out of brass, it should also have similar advantages to that of the brass-moving coil.

Figure 5.13: Comparison of the normal moving coil (Coil 1), the new coil made out of brass cable (Coil 2), a normal moving coil which is encased in resined (Coil 3) and a brass core (4).

5.3.1 Substituting the Moving Coil Copper Winding with Brass

From literature [57] it is found that alloys such as Manganin are sometimes used in LVDTs to stabilise their thermal behaviour. Such alloys have a very low temperature coefficient, as can be noted in Table 5.2, leading to small changes in their electrical resistivity when their operating temperature is changed.

Table 5.2: Table of materials and their respective temperature coefficient and resistivity.

Material	Temperature coefficient of resistance /°C (at 20°C)	Resistivity 1e-8 Ωm at 20°C
Manganin	0.000002	42
Constantan	0.00003	49
Nichrome	0.0004	100
Brass	*0.0015*	*6*
Tantalum	0.0033	13
Gold	0.0034	2.44
Zinc	0.0037	6.3
Silver	0.0038	1.6
Copper	*0.00386*	*1.72*
Platinum	0.003927	10.6
Aluminum	0.00429	2.82

On the other hand, such alloys have several disadvantages e.g. Manganin is magnetic and has a very high resistivity. Choosing this material would lead to the same electromagnetic phenomenon that affects the LVDT. A suitable material for the I2PS that could substitute copper would be brass which is non-magnetic and has a 3.5 times the resistivity of copper and 2.6 times less temperature coefficient. This also means that in order to use brass a thicker wire is needed to keep similar resistance. The resistance is important since it is the value that changes the amount of induced current in the moving coil. Thicker cable also means that the number of turns will decrease and therefore the sensitivity will be reduced. The design parameters presented in Table 5.3 are the values configured for a prototype. The same supply and sense coils are kept and the same moving coil bobbin is used.

Apart from verifying the specifications of the new coil with the electromagnetic model, an FEM [40, 93, 94] as the one in Section 5.2.1 is built in 2D using the simulator FLUX® developed by CEDRAT. Since the sensor is symmetric about an

Table 5.3: Sensor design with brass winding

	Copper	Brass
Inner Radius [mm]	2	2
Outer Radius [mm]	7.33	8.56
Number of turns	250	175
Number of layers	14	11
Wire diameter [mm]	0.335	0.457
Resistance [Ω]	19	21

axes (axisymmetric), it can be modelled in a 2D simulation. The latter is preferred over the 3D one since as explained in Section 5.2.1 it is less computationally intensive. The electrical circuit of the sensor required by the transient magnetic model is as explained in Section 5.2.1. The moving coil parameters are changed depending on the test. The resistance presented in Table 5.3 is used for the brass coil test (coil 2). The resistance of the material is used for the core tests since in this case the moving coil is removed from the electrical circuit.

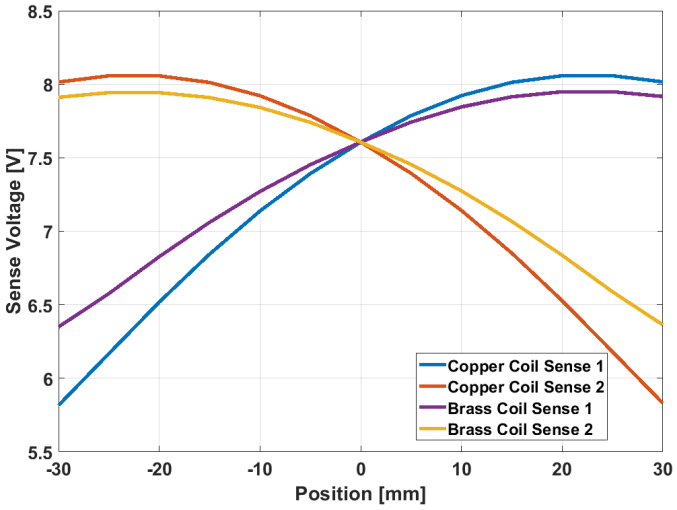

Figure 5.14: A comparison between the simulated characteristic curve of a copper wound moving coil and a simulated brass wound moving coil.

The brass coil, as expected, exhibits very similar results to that of the normal coil with the different wire diameter and number of turns. As noted in Figure 5.14, both curves illustrate a non-linear symmetric dependence of the first harmonic with respect to the moving coil position. While the voltage swing of the copper coil is 2.2 V, the simulated brass coil exhibits a voltage swing of 1.6 V. This implies that there is a 29 % attenuation. Having said this and recognising the fact [56] that the I2PS is very responsive to coil properties, the brass coil can be further optimised to obtain a higher voltage swing. On the other hand, for the function of this test,

it is enough to prove that the sensor works relatively well with a brass coil and hence the thermal test can be conducted.

On the test-bench used in Section 3.1.4, the characteristic curve of the I2PS with a brass moving coil is obtained. This is done such that the gain of the sensor is known and hence the moving coil is placed at the same position as in the previous thermal tests. Furthermore, since the moving coil uses thicker wire and has a high number of turns, the manufacturer randomly winds the moving coil. This means that the distribution of the coil's windings and the number of layers and turns cannot be controlled as precisely as in the supply and sense coils. This can also be noted from Figure 5.13. Therefore, three coils are produced, two with a total of 1852 turns, henceforth referred to as MC1 and MC2. The third, henceforth referred to MC3, has a total of 1950 turns but it is thicker on one side with respect to the other.

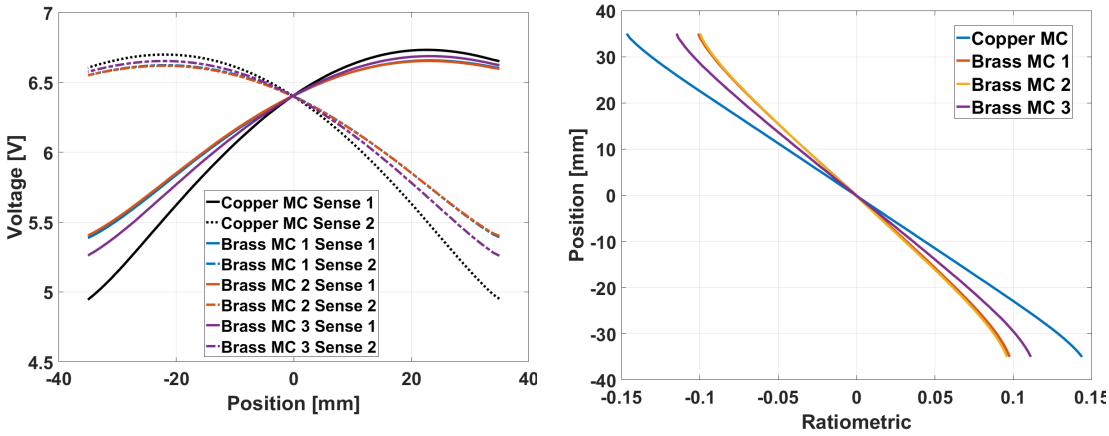

(a) A comparison between the sense coil's voltage of the 3 different brass wound moving coils

(b) Comparison of the different moving coils' ratiometric

Figure 5.15: Characteristic curves and ratiometric of the 3 new brass wound moving coils. MC 1 and 2 are composed of 18 winding layers of 0.457 mm brass magnet wire adding to a total of 1852 turns and MC 3 is composed of 18 layers but with a total of 1950 turns.

Figure 5.15a provides an excellent example showcasing the sensitivity of the sensor to the moving coil parameters. MC1 and MC2 both have the same number of turns and the manufacturer guaranteed a uniform coil thickness. This is reflected in the characteristic curve and ratiometric since MC1 and MC2 are on top of each other. In fact there a 99% match between the two sense coils voltages and a minimum of 95% match between the two ratiometric. On the other hand, a 100 turn increase provides voltage increase presented by MC3. Furthermore, the characteristic curve is comparable to the normal copper-wound moving coil, both in shape and in voltage swing. This small experiment shows how the lower number of turns and higher resistivity of the moving coil affects the sensor since a higher

current is induced in the moving coil. The latter's behaviour is also similar to the simulation. It is important to acknowledge the fact that there will always be small inconsistencies between the simulation and the test-bench. This is due to the factors that could not be taken into consideration in the simulation, namely:

- the windings' defects due to the multi-layers,
- the mechanical flaws of the shield,
- the lack of uniformity of the electrical conductivity in the shield, and,
- the lack of consistency of the sealant used to seal the sensor.

All of these influence substantially the parasitic elements of the sensor. Since the simulation is strongly dependent on uniform and symmetric geometry, it can lead to big difference with respect to the test-bench. Nonetheless, the main goal of this test is not only to compare a bass coil with a copper one but to enquire if the brass coil exhibits a lower sensitivity to temperature change. To ensure a uniform temperature change in the moving coil MC1 is selected since it is one of the coils which is wound uniformly.

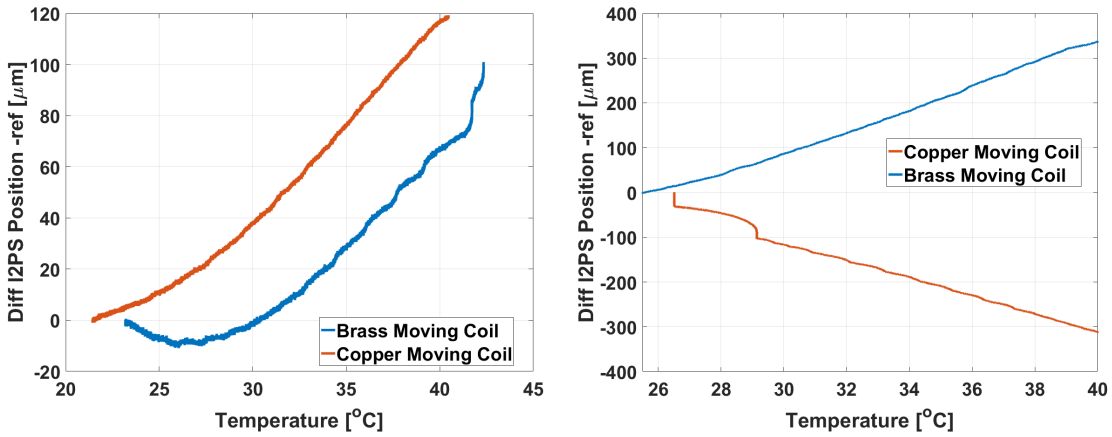

(a) Position change experienced when the temperature is changed. The moving coil is set at 5 mm

(b) Position change experienced when the temperature is changed. The moving coil is set at 15 mm

Figure 5.16: Thermal test comparison between the copper and the brass wound moving coils.

Finally, the same test as presented in Section 4.2 is used to characterise the thermal response. The thermal results, presented in Figure 5.16, show that the position change at 5 *mm* and at 15 *mm* with a brass magnetic wire is similar to that of a copper wound moving coil meaning that unfortunately, there is little to no improvement. A possible explanation may be that, while it is true that

the thermal coefficient is less, it is not equal to or close to zero, like that of manganin. This implies that a change in resistance due to a drift in temperature still happens. Moreover, while the change in resistance due to temperature is smaller, the resistivity of brass is higher than that of copper. Therefore, only a small change is required to change the overall resistance by a significant amount.

5.3.2 Substituting the Moving Coil with a Solid Brass Core

In literature [97] it is also found out that there are similar induction-based transducers with a conductive core instead of a coil such as the LVDT. The benefits from the manufacturing perspective are obvious in this case. Indeed, it is faster and cheaper to manufacture a solid core instead of a coil. If a conducting target is placed inside an ac magnetic field, which in this case is created by the sensor coil fed by an ac supply, the eddy currents mostly found on the solid's surface create a secondary magnetic field. The latter decreases the coil's flux and consequently the effective coil inductance. The sensor sensitivity depends on the solid's resistivity. In the case of the LVDT, which has a ferromagnetic target, the situation complicates itself since the coil inductance is simultaneously increased by the target permeability. As seen in Section 2.2 with the LVDT, a ferromagnetic core leads to electromagnetic interference in the transducer and hence it must not be used for the I2PS. Hence in the case of the I2PS a conductive core which is not magnetic can be tested. Brass is selected in this case as well to investigate possible thermal advancements due to the material properties.

As with the brass coil, the brass core is first simulated, characterised and then the thermal response is tested. In the simulation, the same scenario is used but in this case the moving coil changed from a coil to a solid conductor with the material set to brass while the sense and supply coils are left as the coil conductor regions. The FEM model produces the characteristic curve presented in Figure 5.17a. When a solid core is used, the characteristic curve (left axis in black) is more linear with respect to when a coil is used (right axis in yellow) as shown in Figure 5.17b. The former exhibits a small non-linearity towards the edges. An increase in the voltage swing is noted when a copper core is simulated. Since resistance of the material is lower, a higher current is induced in the surface of the core. Finally, it is important to note that the cores are simulated with a small notch of smaller diameter at one end of the sensor, as presented in Figure 5.13. This notch is used to connect the core to the movable link of the device with an M4 tread and hence

it is also required in the solid core. This added material leads to a non-symmetric characteristic curve as presented in Figure 5.17a. This enforces the description provided in [56] describing the strong sensitivity dependency on the geometry of the sensor and its high requirement for symmetry. Nonetheless, in this case the difference is small enough to be removed in calibration and in theory it can be removed or made symmetric such that this problem is solved. At this point the simulation proved that the I2PS is able to operate with a solid core hence a brass core is manufactured and tested on the same test-bench used for the brass coil.

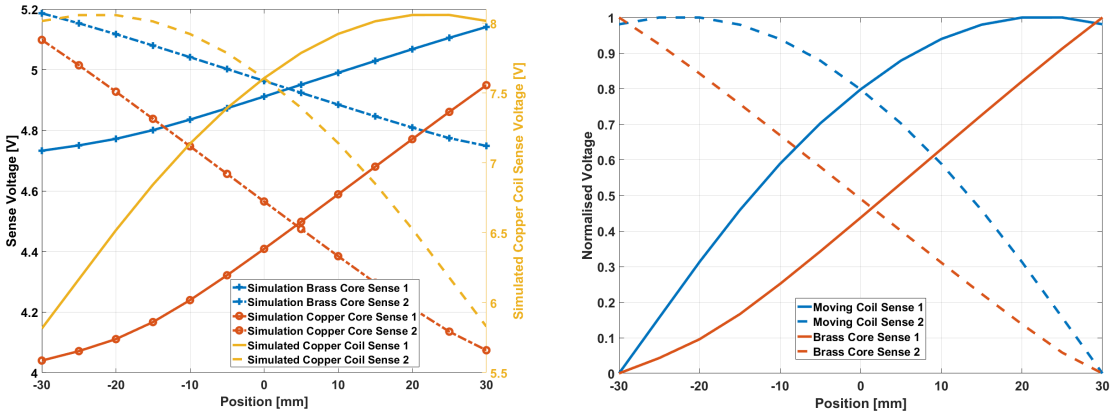

(a) Comparison between the sense voltage of a copper coil, a copper core and a brass core

(b) Normalised plot comparing the sense voltages of the copper coil and a solid brass core

Figure 5.17: Characteristic curves of the solid cores, as obtained from the FEM simulation

The brass core was tested in the frequency range of 500 Hz to 5 kHz to investigate if the latter offers any added advantage over the normal copper wound moving coil's frequency range of operation. It was found that the nominal frequency range of the I2PS with a copper wound moving coil is from 500 Hz to 2 kHz. Hence in order to simplify the comparison, the electrical zero is used as the reference point. Consequently, the current supply is varied for each frequency such that the voltage at the electrical zero is always approximately 5 V. Figure 5.18a shows that the voltage swing for the brass moving core increases from 1.1 V to 3.5 V as the frequency increases. Unlike the normal moving coil the voltage swing change is higher as the frequency increases. On the other hand, the linearity of the output voltage, with respect to position, decreases as frequency is increased. This phenomena is due to the increase in the ac resistance of the core as the frequency increases. As the resistance increases more current is induced and hence a the higher voltage change happens on the sense coil's voltages. Comparing the shape of the characteristic curve of the core at 5 kHz to the curve produced by the copper-wound moving coil at 1 kHz (Figure 5.19a), one can notice that the former is inverted and more linear.

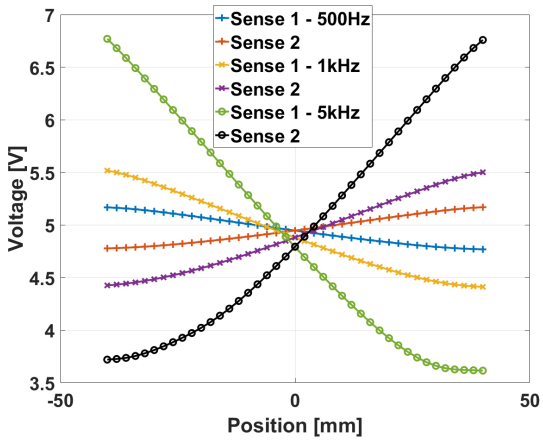

(a) Sense coil voltages at different frequencies

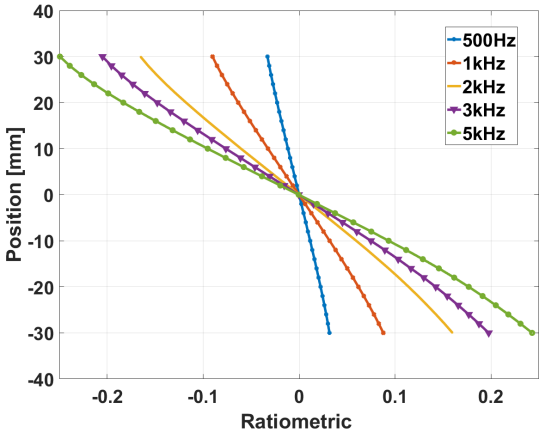

(b) Ratiometric at different frequencies

Figure 5.18: Characterisation of a solid brass core at different frequencies

In fact, at 5 kHz, the voltage of sense coil 1 with respect to position is linear from -40 mm to 20 mm while from 20 mm to 40 mm it curves. Furthermore, the voltage swing at 5 kHz is approximately 3 V. Note that approximately 75 % of the voltage swing happens between -40 mm to 20 mm. The voltage change when the moving core is between 20 mm and 40 mm decreases drastically. Indeed, calculating the NLE of the sense coil voltage with respect to position shows an increase of 1.5% in the non linearity between the 500 Hz and the 5 kHz. This non-linearity is also observed from the ratiometric presented in Figure 5.18b.

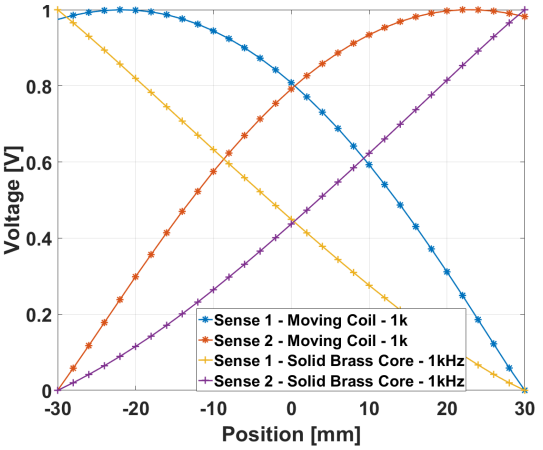

(a) Normalised sense coils' output voltage

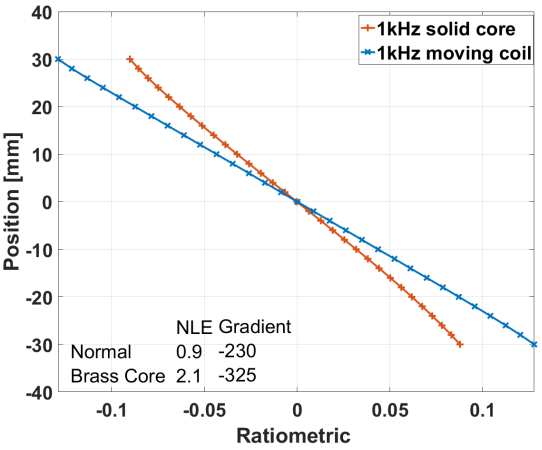

(b) Comparison of the ratio

Figure 5.19: Comparison of the normal moving coil with a solid brass core. The same sense and supply coils are used for the test.

The normalised sense coils' voltage with respect to position at 1 kHz is presented in Figure 5.19a for both the I2PS with the normal moving coil and the brass copper core. It is important to note the difference between the two curves. The brass core's output is much more linear and the centre is closer to the middle of the

voltage swing. In fact there is an 88% increase in linearity. On the other hand, the ratiometric presented in Figure 5.18b and Figure 5.19b show that while the gain is similar to that of the copper wound moving coil and acceptable at this value, the non-linearity of the core is at the acceptability threshold of 2 % [56]. Moreover, the sensitivity of the brass core is higher than that of the I2PS. This is advantageous since it allows for a better, more separate distinction between the voltages of different positions.

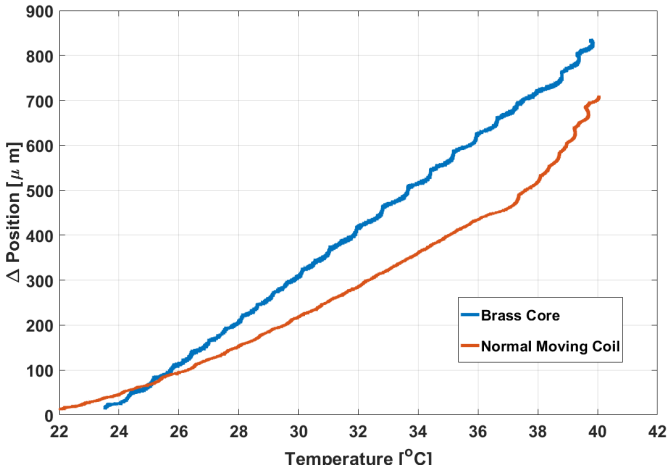

Figure 5.20: Thermal test with the solid brass core

Finally, a comparison of the thermal response of the copper wound moving coil with that of the brass core indicates that the position change due to temperature change is worse. This is presented in Figure 5.20. Indeed, for a temperature change of 16°C, the brass core changes by 820 μm and the copper coil drifts by 660 μm. There is a considerable difference between the thermal expansion and heat distribution of the sold core with respect to that of the coil. While the core is made out of one material the moving coil is composed of multiple materials, two of which are insulators. This implies that the core will expand uniformly since it is a solid block and hence the distance between the core and the sensor's body, i.e. the coils, is reduced. This increases the inductance of the current in the core. Furthermore, as for the brass moving coil the resistance of brass will change less with temperature but at the same for a small change in temperature the resistance change is higher than that of copper.

5.3.3 Resining the Moving Coil

Resining the moving coil means sealing the coil part in a solid coat of plastic. While the electromagnetic behaviour is not degraded, the extra layer can in theory

add a latency effect to the thermal change. Indeed, since there is no change in the characteristic curve, it is not presented. As noted in Figure 5.21, while the position change is somewhat slower, the magnitude of the position change is the same. It can therefore be concluded that apart from the extra protection to the coil and the mechanical strength the resin contributes no added advantage.

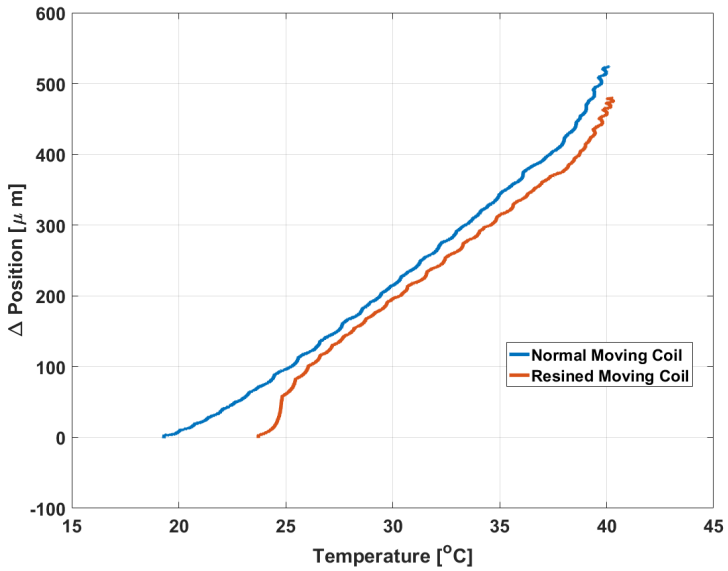

Figure 5.21: Thermal test with a resined moving coil

5.4 Tests on the collimator test system

The engineering department at CERN keeps multiple copies of the collimator set up outside the LHC. This setup is used mainly for compliance testing of the systems and collimators as well as spares for the LHC. A test collimator equipped with only the movement set up, i.e. without the vacuum tank, is modified to accept the I2PS, as can be seen in Figure 5.22. (Note the similarity between the test setup in Figure 5.22 and the collimator design in Figure 2.2.) This setup is used to test both the I2PS under varying temperature and to test the interference conclusion.

5.4.1 Testing same frequency operation

The latter is tested by setting four I2PS to operate at 1 kHz and these vary in distance from each other since they are mounted on the collimator. As presented

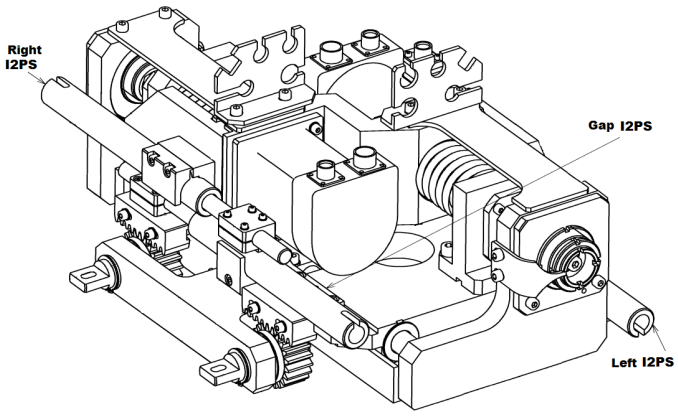

Figure 5.22: A diagram of the collimator setup accommodating three of six I2PS installed for testing. Two such blocks are required. One for the upstream and another for the downstream. [1]

in Figure 5.23 there is no position change as is noted in the lab results presented in Figure 5.12. In reality, as can be noted in Figure 5.22, the Gap sensors are the only sensors which are close to one axis. The rest of the I2PS are located more than 350 mm from each other. Furthermore, they are separated by the body of the collimator. Finally, in a real collimator these are also separated by the tank.

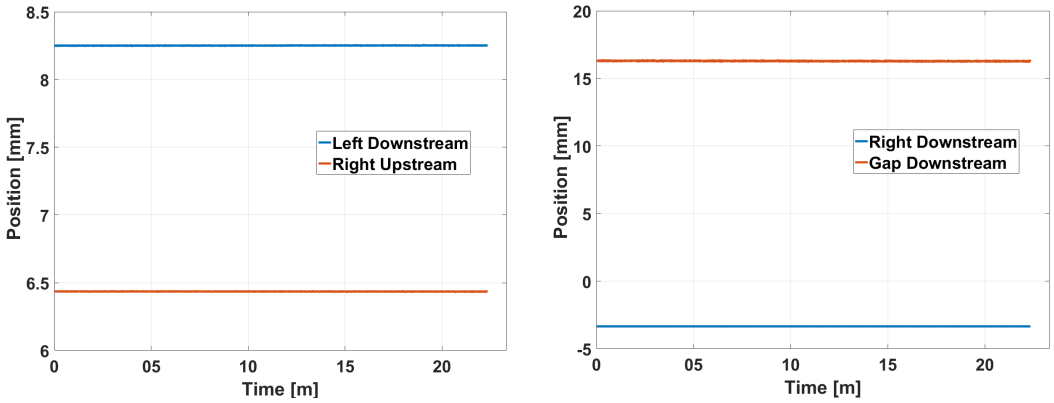

(a) The position of sensors installed in Left Downstream and Right upstream

(b) The position of sensors installed in Right Downstream and Gap Downstream

Figure 5.23: Position reading of the I2PS installed on test collimator

5.4.2 Thermal analysis in collimator environment

The room temperature is monitored as well as the compensated position is read by the sensor. This said, it is important to note that the frequencies of the sensors are from 1 kHz to 2.25 kHz. From Chapter 3 it is known that the most stable frequencies are 1.25 kHz and 1.5 kHz while the most unstable frequencies are 2 kHz and 2.25 kHz [92]. Figure 5.24 shows that the room temperature started

at *24˚C* and it slowly decreased during the night to *19˚C*. The door is then opened and there is a temperature drop to *16.5˚C*.

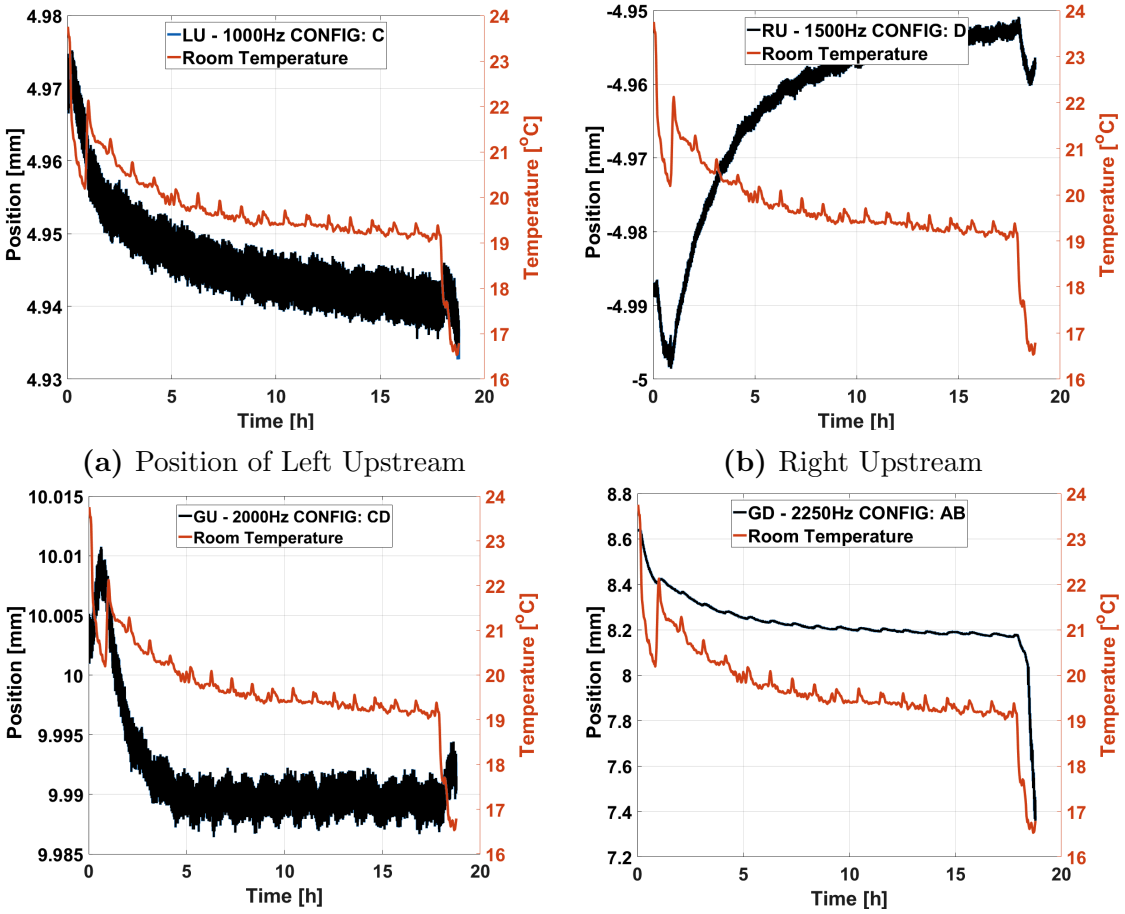

(a) Position of Left Upstream

(b) Right Upstream

(c) Gap Upstream

(d) Gap Downstream

Figure 5.24: A test where the room temperature was varied very slowly with the sensors at outer position.

Figures 5.24a to 5.24d show the position as read by the I2PS during this time. The position is stable for the majority of the sensors except Gap Downstream (GD). While in all sensors there was a maximum of 40 μm of position change GD suffered a 400 μm position change. The position in this case followed the temperature for all sensors except for some initial changes, GD included. Note also how GD suffered a further 900 μm when the temperature dropped. The big change in GD is a combination of effects. The sensor in this position is very close to a motor as observed in Figure 5.27. This has to be coupled with the fact that the sensor is operated at 2.25 kHz. This makes it also more susceptible to thermal change, as noted in Chapter 3. Another odd phenomenon to note is the position drop at the beginning of the test for GU and RU which should be similar to that of LU and GD.

This test is repeated multiple times at different times with different room conditions

and the same results are obtained. The frequency of the sensors is varied and the same test is repeated. The results presented in Figure 5.25 present a very different behaviour from Figure 5.24. The temperature was dropped from 25°C to 20°C in over 1.2 hours.

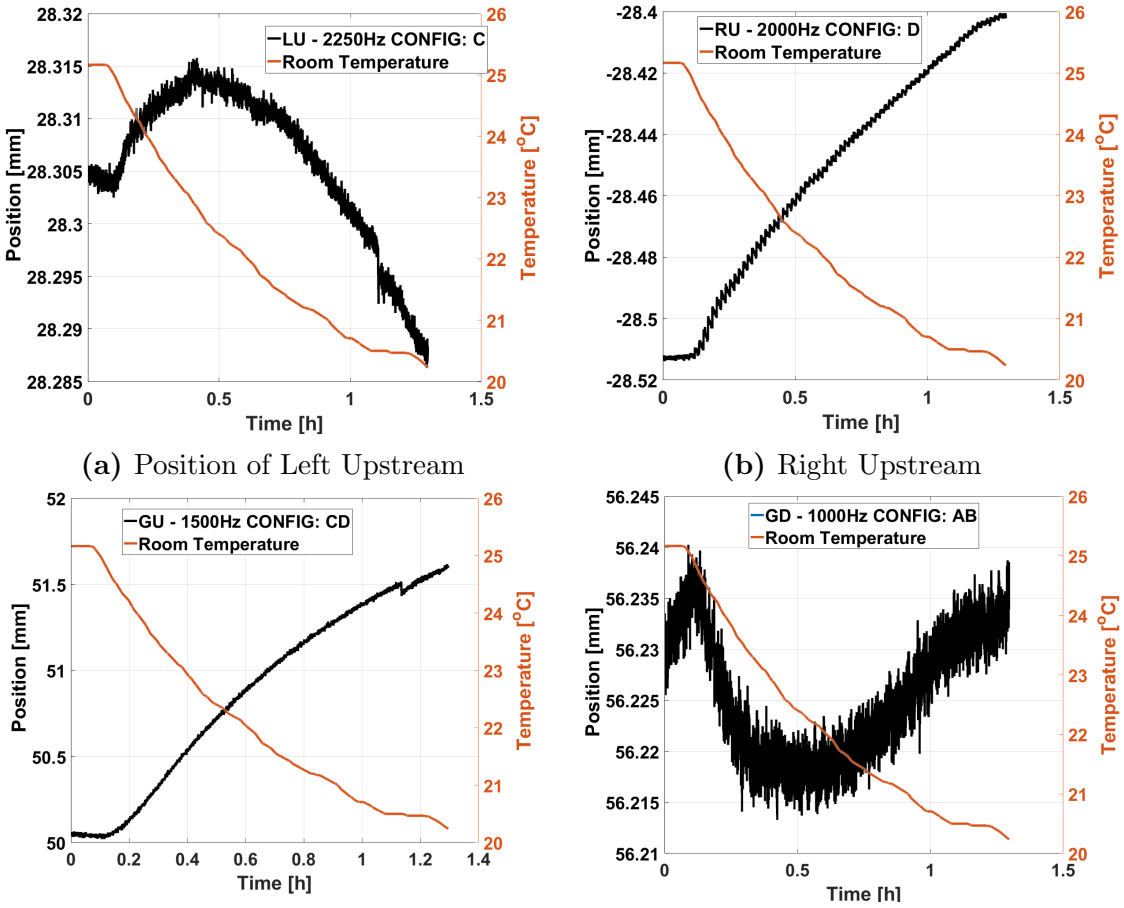

(a) Position of Left Upstream

(b) Right Upstream

(c) Gap Upstream

(d) Gap Downstream

Figure 5.25: A test where the room temperature was varied very slowly with the sensors at outer position.

Right Downstream (RD) suffers a bigger position change while before, at this frequency, it remained constant. On the other hand, GD is very stable with only 10 μm of position change. While the improvement of GD could be expected since the frequency was lowered, the stability of Left Upstream (LU) cannot be explained. Similarly, the high position change in Right Upstream (RU) can be attributed to the higher frequency but conversely while Gap Upstream (GU) is at a more stable frequency, it's position change is higher than in the previous test.

Keeping the same position while using the PT100 to measure and log the temperature of the room, a thermal camera is used to check the overall temperature. Figures 5.26 and 5.27 show two of the six sensors installed. It is noted that the sensors have local hot spots or gradients which differ from room temperature [98].

These hot spots are mainly due to the heat the stepper motors near the sensors generate, which is transferred through the aluminium body of the collimator to the sensor.

(a) Showing temperature at low spot

(b) Showing temperature at high spot

Figure 5.26: Thermal image of the Left Upstream sensor after jaw movement.

(a) Showing temperature at high spot

(b) Showing temperature at low spot

Figure 5.27: Thermal image of the Gap Downstream sensor after jaw movement.

This is a very important discovery since this explains a lot of strange position change phenomena that previously was uncorrelated to. The collimator is first set such that all jaws are at the outer switches. From the thermal camera it is noted that at this specific position, for this test bench, the moving coils for Left Downstream (LD), RU, RD, and GU are located in the part of the sensor which is similar to room temperature. For the results of Figure 5.24, the moving coil of all sensors is at thermal equilibrium at the initial state since after calibration the test was not started immediately but the jaws were moved by 5 mm to the outer switches. This is the reason why at the beginning there is a drift which is uncorrelated to the rest of the position change. The test of Figure 5.25 was initiated after a long time at the inner switches. This meant that the coils had changed temperature to match the previous one having GD, LU and LD at a stable temperature while RU, RD and GU at a different temperature. This led to

a high position change when at a different position. This test is repeated multiple times with variations to the position cycles and stable temperature times.

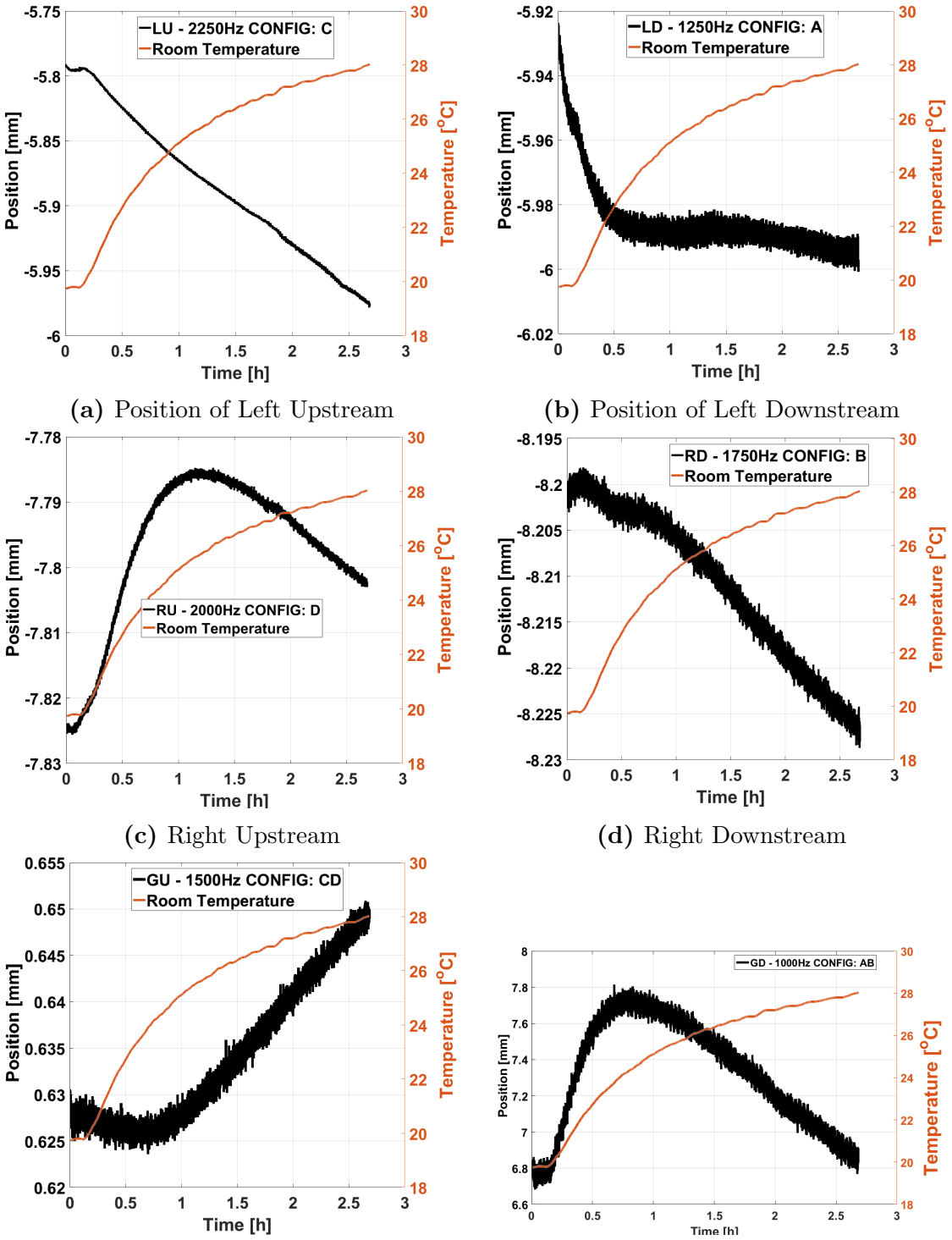

Figure 5.28: A test where the room temperature was varied very slowly with the sensors at outer position.

Figure 5.28 shows the position taken with the left jaws placed at the inner switches and the right jaws are placed 1 *mm* away from the left jaws, after moving the jaws

multiple times. The climate control in the room is set to heat it up from 20°C to 28°C as noted in Figure 5.28. In this case, LU suffers from a 180 μm position change while RU is very stable with a 40 μm position change and decreasing. All the sensor's behaviour depends on the thermal gradient they suffered. The moving coils of RU and GD were in a stable temperature and moved into a different temperature, which once achieved the same thermal temperature as the body it started decreasing. Others, such as LU and LD, are still drifting towards thermal equality while RD and GU were stable and are now changing temperature due to the new position of the sensor or the moving coil.

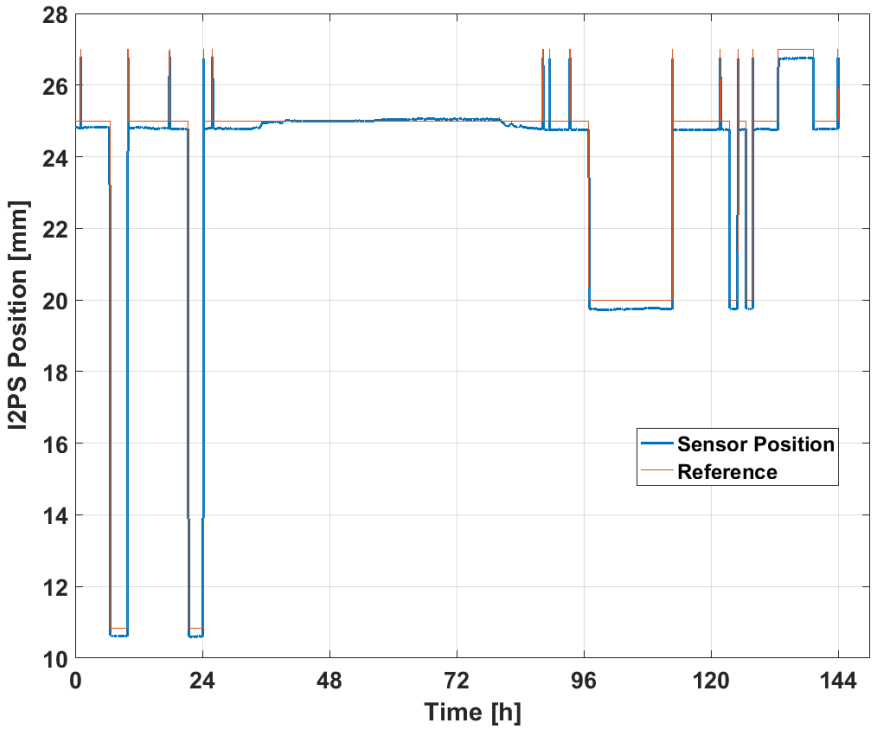

Figure 5.29: The read I2PS position from collimator during technical stop with respect to the read resolver position taken as the reference.

These results show that unlike in the oven, in the collimators the temperature change does not depend only on the frequency, the moving coil position and the ambient temperature but it also depends on the moving coil position with respect to the other collimator parts, as well as the status of the collimator. This explains why the position of multiple I2PS changes in a different way during the technical stop and returns back to normal after such as in Figure 5.29. Note that for the first 24 hours the position is much higher then the resolver position which can be considered a reference. This is because up till this point the LHC was operational. The position difference went to zero during this time since the collimator conditions where the same as during the commissioning. Then when the technical stop ended the position drifted back to an offset. Also note the continuous cycles that the

jaws move in. During operation, the collimator changes temperature due to its interaction with the beam also it is constantly being moved hence the motor's temperature is always high. This leads to variations in the temperature of the sensor. Furthermore, it explains the position change during a technical stop. In this period the beam is turned off, the collimator is not moved and the ambient temperature control is relaxed. This also explains why the position read after a movement by the jaws suffer an up till now un-explainable drop in position. The moving coil needs time to adapt to the thermal gradient it suffered. This also explains the strange position drift which does not match with the change in V_{dc} which is the average of the whole sensor and hence somewhat follows the ambient temperature.

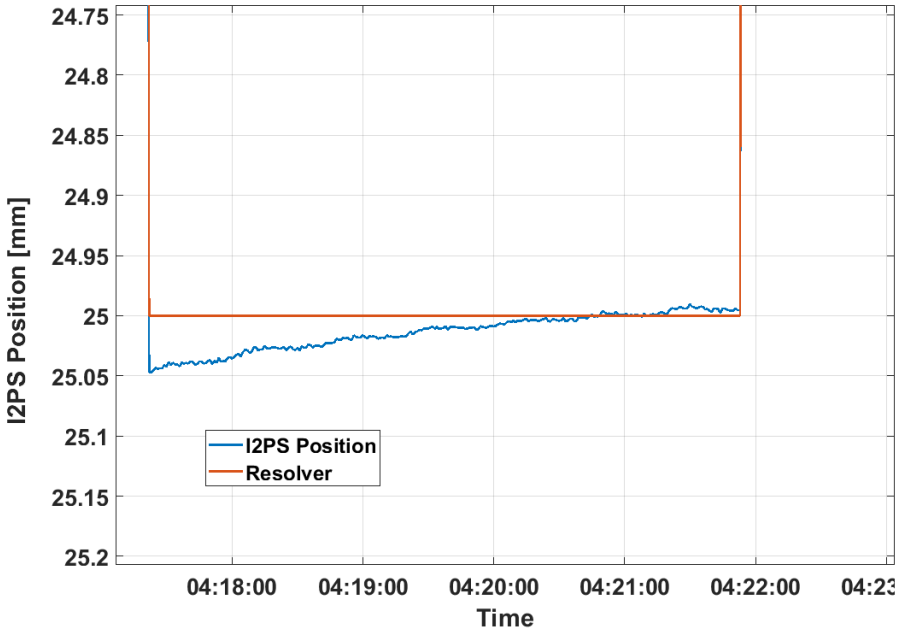

Figure 5.30: Position drift after short movement during operation

Unfortunately, there are very few viable options more than those that were tried already, especially since there is no control on how the temperature propagates in the collimator body. One possible solution is to insulate the sensor and change the flange. This reduces the temperature change due to conduction. However, since the sensor is open from the sides it is still susceptible to convection. Another possibility to test is to modify the moving coil by removing approximately half of the turns, and wind them in the opposite directions. This would in theory still allow the mutual inductance in the sensor but with temperature change both coils will get an increase in their current. The only difference would be that the current change will be opposite and hence it will cancel each other. These two modifications are installed on the LU and RU I2PS sensors of the test collimator.

Figure 5.31 shows one of the modified I2PS as installed in the test setup while Figures 5.32 present the thermal equivalent of this installation. These pictures are acquired after waiting for the temperature to settle. Moreover, the position set and room conditions is equivalent to the thermal images presented in Figure 5.26. The sensor's temperature is uniform with no high spots and low spots. The temperature difference between the two ends is $0.7^{\circ}C$. Additionally, the temperature of the flange is close to that of the I2PS body. It is important to note the temperature of the body of the collimator the flange is attached to and the rod attachment of the other sensor below the plastic flange, which are both higher by approximately $6^{\circ}C$.

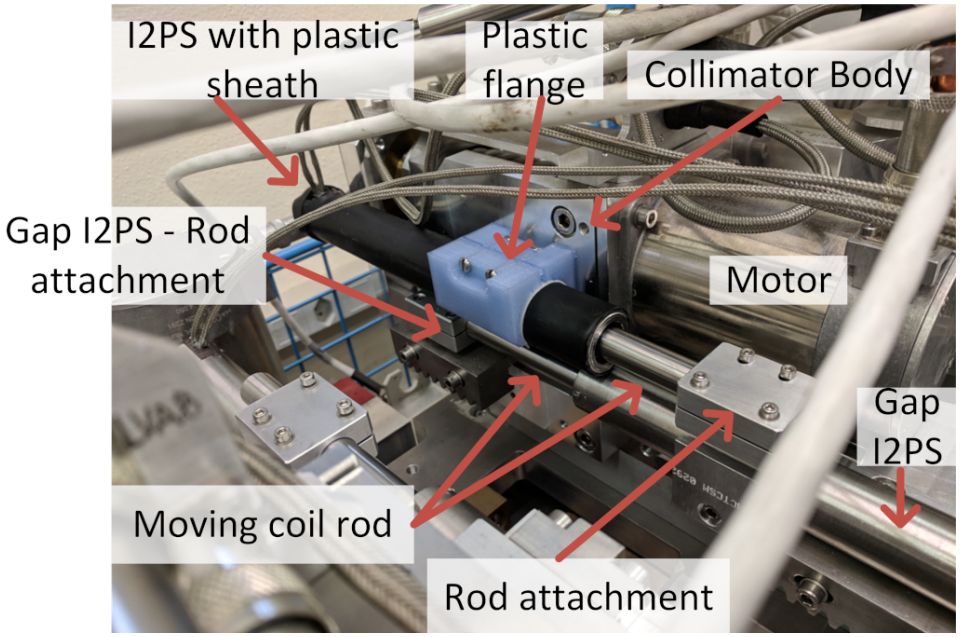

Figure 5.31: Photo of the plastic encased I2PS as installed on test setup with a plastic 3D printed flange.

(a) Thermal image of the Left Upstream sensor noting the uniformity of the temperature along the sensor.

(b) Thermal image of the Left Upstream sensor noting the uniformity of the temperature of the flange with the sensor.

Figure 5.32: Thermal images of modified I2PS

These two modifications result in a 160 μm of reduction in the position change over a temperature change of $8^{\circ}C$ for the LU and a 25 μm position change reduction for the RU. This can be observed in Figure 5.33. (Precautions are taken to record this data at the same conditions as without the modifications, the I2PS were calibrated followed by multiple jaw cycles before the test is initiated as done in the previous test. This is to ensure the same moving coil and sensor body conditions)

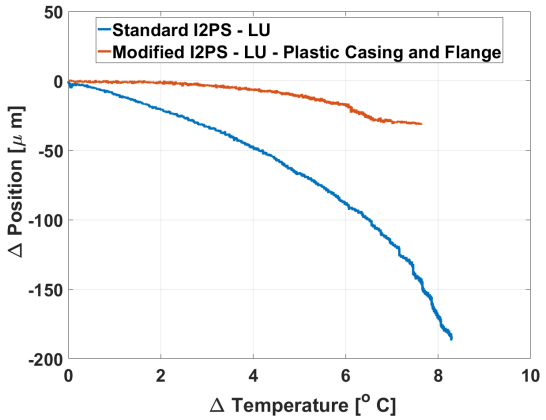

(a) Left Upstream (LU) sensor

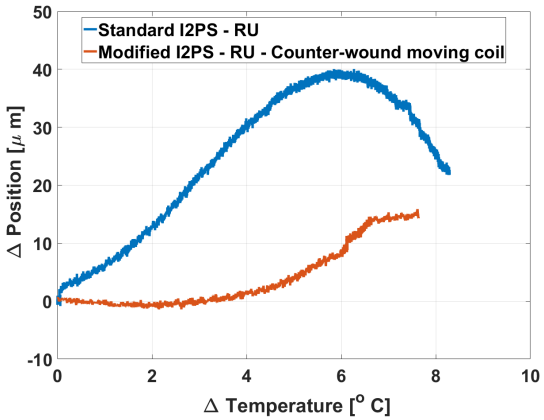

(b) Right Upstream (RU) sensor

Figure 5.33: Comparison of the position change of the I2PS with and without modification with respect to temperature

Finally, the modified moving coil, the plastic sheathed body and the 3D printed flange are installed on the LU sensor. The same tests are repeated and similar results are obtained, where over 160 μm position change is reduced. Figure 5.34 presents the results from a test conducted with this combination. In this test the jaw is left stationary for approximately an hour (during which time it was noted that the position change and temperature had stabilised). The jaws i.e. the I2PS are left at the same positions while the temperature in the room is

dropped by lowering the climate control temperature, presented in Figure 5.35. This test is conducted to investigate the stability of the modified sensor when only the ambient/overall temperature is changed. A sensor which exhibited more stable results during previous tests (RD) is used as a comparison and as a check for thermal drift.

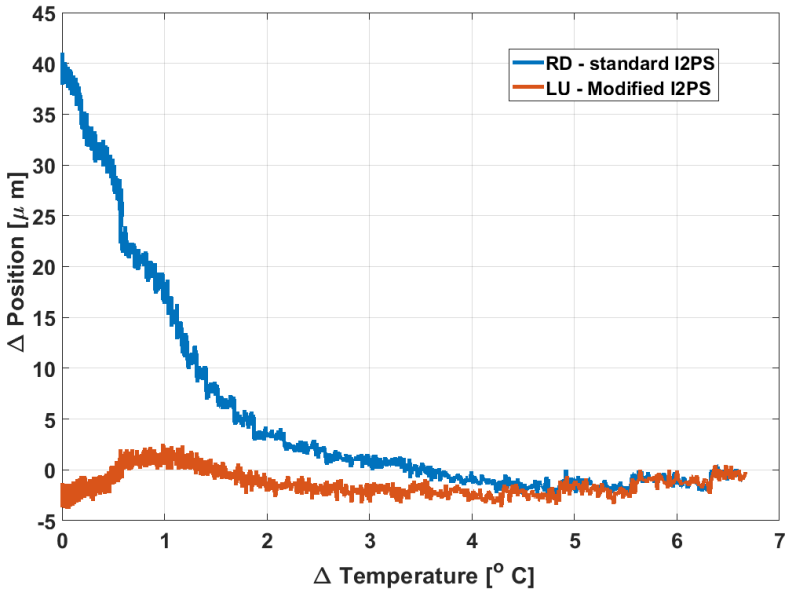

Figure 5.34: Difference between I2PS position and reference with respect to temperature. Comparison between RD which is a standard I2PS and LU which is a modified one.

Figure 5.34 compares a standard I2PS installed in RD with the modified I2PS. From this figure it is noted that while the position of the standard I2PS suffers a 40 μm change the modified one remains stable. Another interesting note is the V_{dc} recorded from the two sensors as presented in Figure 5.35. The standard I2PS voltage decreases with time in a similar way as the ambient temperature. Moreover, for a $7^{\circ}C$ change the voltage drops by 8 mV. The modified I2PS voltage change has a different profile as well as a smaller voltage drop. The latter reads an 1.2 mV voltage change for the same temperature change As explained in Section 4.3.2 the dc voltage read provides an average temperature reading along the whole sensor. Hence, while one side of the sensor is $5^{\circ}C$ higher than on the other end, the voltage will not reflect this gradient. On the other hand, if the temperature of the sensor is controlled as in the modified sensor and so allowing more time for the sensor to achieve a uniform temperature. Then the dc voltage read reflects the true average voltage of the sensor and the compensation algorithm provides better correction.

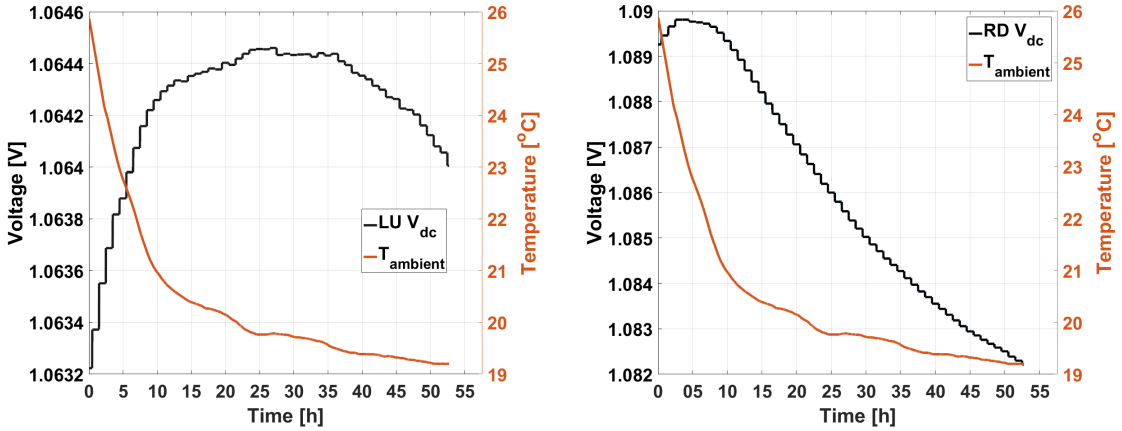

(a) The dc voltage of the modified I2PS when the room temperature is changed

(b) The dc voltage of the standard I2PS when the room temperature is changed

Figure 5.35: Temperature and dc voltage variation with time for stability test.

5.5 Summary

This chapter investigates multiple modifications to the ironless inductive position sensor with the aim of increasing its robustness to thermal drift. It shows that taking the necessary design steps, this transducer can successfully operate with a brass wound moving coil. Similarly, the I2PS can be successfully operated with a solid core made out of brass or copper. While the electrical performance is not degraded, the thermal aspect is not improved. This chapter also shows that multiple ironless inductive position sensors can be operated on the same collimator at the same frequency.

Finally, this chapter presents empirical results on temperature gradient which the sensor needs to operate in. The presented study provides explanation to multiple phenomena noted during operation. Furthermore, a simple mechanical solution is presented and the results from a prototype are discussed, showing a decrease in the position drift.

Chapter 6

Design engine development

The I2PS is being designed and manufactured with the aim of substituting a number of LVDTs found in the LHC collimators. The aim is to have a design tool that uses the theoretical models to design and optimise a new sensor for any application defined by the user. This tool must be able to accept the parameters defined by the user, suggest, where possible, calculated values and make the necessary checks such that the sensor design is viable. At the end, depending on the inputs, the tool must find the optimal solution.

The available I2PS theoretical models are written in Matlab Scripts. Although Matlab code is quite robust and offers a wide variety of functions, the computational requirements for such a script are very high. Consequently, designing an automatic design tool using Matlab would lead to long execution time and high computational resources. This is due to the electromagnetic model of the I2PS.

The basis of the I2PS' electromagnetic model is the calculation of the inductance between two circular conductors using elliptic integrals. This model needs the conductors to be coaxial but not concentric. This function is an integral part of the next one, a function that calculates the mutual inductance between two circular solenoids. These two functions are then used iteratively with different inputs to calculate the mutual inductance between the different layers, turns of the coils and the position of the moving coil. The same functions are also called when the self-inductance of a thick wall solenoid is calculated. In order to make these calculations faster, an approximation method has also been implemented so that the number

of calculations are reduced. At the end of the model, the voltages and currents in the coils are then calculated. This model provides the project with a relationship between the input parameters / constraints with respect to the output parameters of the sensor. The output parameters in this case are the parameters that need to be optimised.

Hence, the available models are transferred to a generic programming language. The transfer to C++ poses several problems, some of which include the need for an elliptic integral function, which is not easily found in C++ and various other ready made functions available in Matlab. The transfer is then verified through testing the C++ code in parts, making sure all functions are mirroring the Matlab functions and then testing them as a block, whilst comparing the outcomes with the result. The settings used for the benchmark are the parameters used in the past [56] to design the current I2PS being tested in the LHC (these parameters are also presented in Table 6.1).

Finally, a sequential approach is first investigated. The advantage of a sequential approach is that the minimum number of layers is always found. Firstly, the algorithm always starts from the smallest combination and ends when it reaches the target or the maximum value allowed. Secondly, the user has much more input to the choices done. The disadvantage is that due to its sequential nature, the algorithm does not have a holistic approach and it optimises values in bunches. Indeed, this may lead to dismissed good combinations. On the other hand, an optimisation algorithm considers all the variables at once. Another hindrance is an increase of the evaluation time and local optima i.e. the final value may not always be the global optimum.

In considering the above, this chapter first presents an introduction to optimisation algorithms with special attention to multi-objective optimisation and evolutionary algorithms. Then, an analysis of the building blocks of the I2PS is explained, with this leading also to a run-down of the algorithm implemented for the I2PS. Ultimately, the results obtained from the design engine are presented and explained.

6.1 Optimisation Algorithms

Optimisation algorithms [99] can be generally divided into two: deterministic and probabilistic. Deterministic algorithms can be defined as algorithms that in the execution of each step, there exists at most one-way to proceed. These algorithms do not use random number generation in order to decide how to modify the data. Furthermore, these algorithms will always produce the same results when given the same inputs. Hence, deterministic algorithms are most often used when a clear relation exists between the characteristics of the possible solution and their utility for a given problem.

In the case that the dimensionality of the search space is very high or the relation between a prospective solution and its fitness (i.e. how close a given design solution is to achieving the set aims) are too complicated or not so obvious, then it will not remain feasible any more to use deterministic algorithms to solve even a relatively small problem. Undoubtedly, probabilistic algorithms, as the name implies, depends more on probability. It makes use of random numbers and random processes, to decide the next execution. The purpose is to save time calculating the actual best choice and avoiding introducing a bias.

Figure 6.1 shows the optimisation algorithms classified according to their algorithmic structure and underlying principles. Most of the available algorithms fall under the probabilistic nature, as can be noted from Figure 6.1. On one side, algorithms based on stochastic processes can be found. These utilise statistics obtained from samples from the search space or based on a model of some natural phenomenon or physical process. Evolutionary algorithms, for example, copy the behaviour of natural evolution and treat solution candidates as individuals that compete in a virtual environment.

An important class of probabilistic Monte Carlo meta-heuristics is evolutionary computation. It encompasses all algorithms that are based on a set of multiple solution candidates (called population), which are iteratively refined. This field of optimisation is also a class of soft computing, as well as a part of the artificial intelligence area. Some of its most important members are evolutionary algorithms and swarm intelligence.

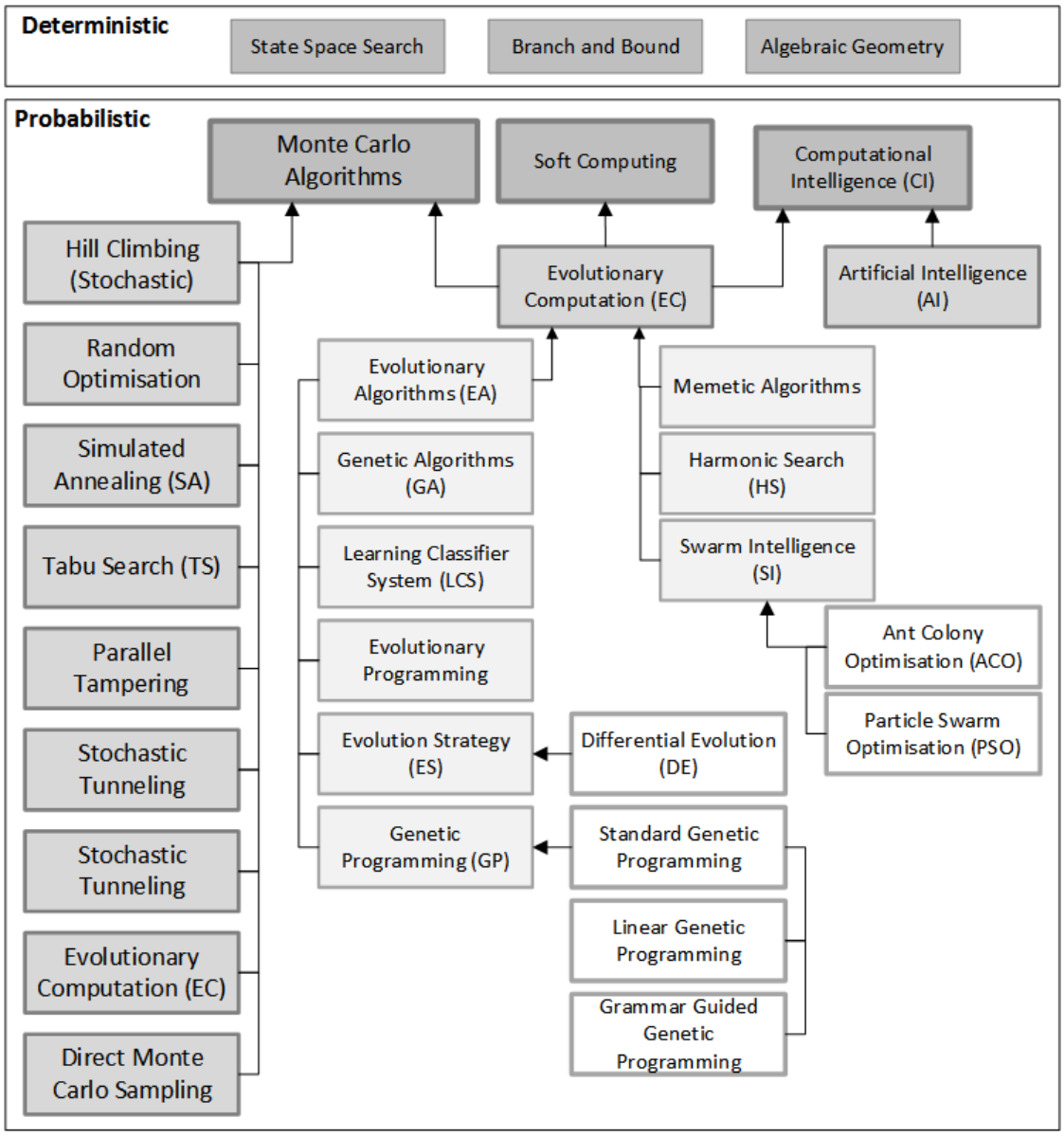

Figure 6.1: The taxonomy of global optimisation algorithms. Reproduced by author from [99]

6.1.1 Single-Objective Optimisation

As global optimisation [99, 100] is about finding the best possible solution for a given problem, it is important to define what makes a solution optimal. In the case of optimising a single criterion f, an optimum is either its maximum or minimum. In global optimisation, it is a convention that optimisation problems are most often defined as minimisations and if a criterion f is subject to maximisation, we simply minimise its negation ($\bar{f}$).

In optimisation, it is important to make distinction between local and global optima. A **global optimum** is an optimum of the whole domain $\mathbb{X}$ while a **local optimum** is an optimum of only a subset of $\mathbb{X}$.

A **local maximum** $\hat{x_l} \in \mathbb{X}$ of one objective function $f : \mathbb{X} \longmapsto \mathbb{R}$ is an input element with $f(\hat{x_l}) \geq f(x)$for all x neighbouring $\hat{x_l}$.

If $\mathbb{X} \subseteq \mathbb{R}^n$, we can write:

$$\forall\ \hat{x_l}\ \exists\ \varepsilon\ \ >\ \ 0 :\ f(\hat{x_l})\ \geq f(x)\ \forall\ x\ \exists\ \mathbb{X},\ |\ x\ -\ \hat{x_l}@|\ \ <\ \ \varepsilon \tag{6.1}$$

Similarly, a **local minimum** $\check{x_l} \in \mathbb{X}$ of one function $f : \mathbb{X} \longmapsto \mathbb{R}$ is an input element with $f(\check{x_l}) \leq f(x)$ for all x neighbouring $\hat{x_l}$.

If $\mathbb{X} \subseteq \mathbb{R}$, we can write:

$$\forall\ \check{x_l}\ \exists\ \varepsilon\ \ >\ \ 0 :\ f(\hat{x_l})\ \leq f(x)\ \forall\ x\ \exists\ \mathbb{X},\ |\ x\ -\ \check{x_l}@|\ \ <\ \ \varepsilon \tag{6.2}$$

Hence, the **local optimum** $x_l^\star \in \mathbb{X}$ of one objective function $f : \mathbb{X} \longmapsto \mathbb{R}$ is defined as either a local maximum or a local minimum.

A **global maximum** $\hat{x_l} \in \mathbb{X}$ of one objective function $f : \mathbb{X} \longmapsto \mathbb{R}$ is an input element with $f(\hat{x_l}) \geq f(x)\ \forall\ x \in\ \mathbb{X}$.

Similarly, a **global minimum** $\check{x_l} \in \mathbb{X}$ of one objective function $f : \mathbb{X} \longmapsto \mathbb{R}$ is an input element with $f(\check{x_l}) \geq f(x)\ \forall\ x \in\ \mathbb{X}$.

Therefore, a **global optimum** $\mathtt{x}^\star \in \mathbb{X}$ of one objective function $f : \mathbb{X} \longmapsto \mathbb{R}$ is either a global maximum or a global minimum.

Having defined this, a one-dimensional function $f : \mathbb{X} = \mathbb{R} \longmapsto \mathbb{R}$ may have more than one global maximum / minimum or both in its domain $\mathbb{X}$. A simple example is the cosine or sine function which have multiple repetitive global maxima and minima.

Furthermore, the exact meaning of optimal is problem dependent. In single-objective optimisation, it either means minimum or maximum. Then, in multi-objective optimisation, there exists a variety of approaches to define optima.

6.1.2 Multi-Objective optimisation

Real-world problems and decision making are not normally limited to finding the maximum or minima of a function. Finding maxima and minima in this case are applied to sets F consisting of $n = \|F\|$ objective functions f_i. Where each f_i represents one criterion to be optimised.

Therefore, $F = \{f_i \ : \ \mathbb{X} \longmapsto Y_i \ : \ 0 < i \leq n, Y_i \subseteq \mathbb{R}\}$. It may be the case in multi-objective optimisation that to find the global optimum would mean to maximise one function $f_i \in F$ and to minimise another $f_j \in F, (i \neq j)$. This continues to prove the point that it makes no sense to talk about a global minimum or a global maximum. This leads to the adoption of the set of optimal elements $x^\star \in X^\star \subseteq \mathbb{X}$. Multiple approaches exist to define what an optimum is as it depends on the way a compromise is reached for the conflicting criteria. These different definitions, in turn, lead to different sets $X^\star$. Some methods how to achieve a compromise between conflicting criteria are by using Weighted Sums (Linear aggregation) and pareto Optimisation.

In **linear aggregation** the optimal is found by computing a **weighted sum** $g(x)$ of all the functions $f_i(x) \in F$. In this method, each objective function f_i is multiplied with a weight w_i representing its importance. Therefore, this method allows for minimisation of one objective while maximisation of another, through the use of signed weights. This is achieved by, for example, multiplying an objective function f_a by a weight w_a and the weight $w_b = -1$ to objective function f_b. This will minimise the first while maximise the second function. Then, if they are revered the opposite will happen. Ultimately, the weighted Sums resolved to the following:

$$g(x) = \sum_{i=1}^{n} w_i f_i(x) \ = \ \sum_{\forall f_i \in F}^{max} w_i f_i(x) \tag{6.3}$$

$$x^\star \in X^\star \Leftrightarrow g(x^\star) \geq g(x) \forall x \in \mathbb{X} \tag{6.4}$$

Although it is easy to implement, this approach is not able to handle functions that rise or fall with different speed properly. Therefore, weighted sums are only suitable to optimise functions that at least share the same big-**O** notation[1]. Additionally,

[1] The big-**O** notation is a mathematical notation used to to describe the asymptotical upper

even if the shape of the objective functions and their complexity class were clear, the weights w still need to be properly set and remain open in most cases. Hence, with weighted sum approaches, not necessarily all elements considered optimal in terms of pareto domination, will be found.

Pareto optimality defines the frontier of solutions that can be reached by trading-off conflicting objectives in an optimal manner. To understand the notation of optimal in the pareto sense, the definition of domination must first be defined.

An element x_1 dominates an element x_2 ($x_1 \vdash x_2$) if x_1 is better than x_2 in at least one objective function and not worse with respect to all other objectives. Based on the set F of objective functions f, we can write:

$$x_1 \vdash x_2 \Leftrightarrow \forall i \ : \ 0 < i \leq n \Rightarrow w_i f_i(x_i) \leq w_i f_i(x_2) \ \wedge \ \exists j \\ : \ 0 < j \leq n : w_j f_j(x_1) < w_j f_j(x_2) \quad (6.5)$$

$$w_i = \begin{cases} 1, & \text{if } f_i \text{ should be minimised} \\ -1, & \text{if } f_i \text{ should be maximised} \end{cases}$$

It can be noted that unlike the weights in the weighted sum approach, the factors ω_i only carry sign information which allows some objectives to be maximised and to minimise some other criteria.

An element $x^\star \in \mathbb{X}$ is pareto optimal if it is not dominated by any other element in the problem space $\mathbb{X}$. In terms of pareto optimization, $X^\star$ is called the pareto set or the pareto Frontier.

$$x^\star \in X^\star \Leftrightarrow \nexists x \in \mathbb{X} \ : \vdash x^\star \quad (6.6)$$

The complete pareto optimal set obtained is often not the wanted result of an optimisation algorithm. Usually only some special areas of the pareto front are of interest.

bound of functions. $f(x) \in \mathbf{O}(g(x)) \Leftrightarrow \exists\, x_0, m \in \mathbb{R} : m > 0 \wedge |f(x)| \leq m\,|g(x)| \forall\, x > x_0$

After classifying optimisation algorithms and defining what makes the optimum choice, it is important to identify ways how the optimum is reached.

The following are a few optimisation techniques:

- Artificial bee colony algorithm
- Evolutionary algorithm
- Simulated annealing
- Firefly algorithm
- Greedy algorithm
- Particle swarm optimisation algorithm
- Artificial ant colony optimisation algorithm

Evolutionary Algorithms (EA) [101], however, are a very popular approach to obtain multiple solutions in a multi-modal optimisation task [102]. In the following subsection the genetic algorithm is explained since it is a subclass of evolutionary algorithms which concept is easily understood.

6.1.3 The Genetic Algorithm

Genetic Algorithm (GA) [99, 103, 104] are a subclass of evolutionary algorithms where the elements of the search space $\mathbb{G}$ are binary strings ($\mathbb{G} = \mathbb{B}^*$) or arrays of other elementary types. The search spaces $\mathbb{G}$ of genetic algorithms are referred to *genome* and its elements are called *genotypes*. Like their natural prototypes, the genomes in genetic algorithms are strings. They are linear sequences of certain data types. Due to this, these genotypes are often called *chromosomes*.

In genetic algorithms, we most often use chromosomes which are strings of one and the same data type, for example bits or real numbers. Hence, a string chromosome can be any of the following:

- A fixed-length tuple - The loci i of the genes g_i are constant and, hence, the tuples may contain elements of different types $\mathbb{G}_i$.

$$G = \{\forall(g[1], g[2], ..., g[n]) : g[i] \in \mathbb{G}_i \forall \in 1..n\}$$

- A variable-length list - The positions of the genes may shift when the reproduction operations are applied. Thus, all elements of such genotypes must have the same type GT.

$$G = \{\forall \text{lists} g : g[i] \in \mathbb{G}_T \forall 0 \leq i < len(g)\}$$

String chromosomes are normally bit strings, vectors of integer numbers, or vectors of real numbers. Genetic algorithms with numeric vector genomes in their natural representation, i. e., where $\mathbb{G} = \mathbb{X} \subseteq \mathbb{R}^n$ are called *real-encoded*.

Genetic algorithms are the original prototype of evolutionary algorithms and so they provide search operators which closely copy sexual and asexual reproduction schemes from nature. In such "sexual" search operations, the genotypes of the two parent genotypes will recombine. In asexual reproduction, mutations are the only changes that occur. It is very common to apply both principles in conjunction, i. e. to first recombine two elements from the search space and subsequently, make them subject to mutation.

Mutation is an important method for preserving the diversity of the solution candidates by introducing small, random changes into them. In fixed-length string chromosomes, this can be achieved by randomly modifying the value (allele) of a gene. For real-encoded genomes, modifying an element g_i can be done by replacing it with a number drawn from a normal distribution with expected value g_1, like $g^new_i \sim N(g_1, \sigma^2)$.

The **permutation operation** is an alternative mutation method where the alleles of two genes are exchanged. This is possible only if all genes have similar data types. Permutation is, for instance, useful when solving problems that involve finding an optimal sequence of items, like the travelling salesman problem.

Amongst all evolutionary algorithms, genetic algorithms have the recombination operation which probably comes closest to the natural paragon. The recombination of two string chromosomes, the so-called **crossover**, is performed by swapping parts of two genotypes. When performing single-point crossover, both parental chromosomes are split at a randomly determined crossover point. Subsequently, a new child genotype is created by appending the second part of the second parent to the first part of the first parent. In two-point crossover, both parental genotypes are split at two points and a new offspring is created by using parts number one and three from the first, and the middle part from the second parent chromosome. Therefore, in general, dividing from n different points is the n-point crossover operation, also called multi-point crossover. Indeed, for fixed-length strings, the crossover points for both parents are always identical.

The **fitness function** is a computation that evaluates the quality of the chromosome as a solution to a particular problem. A GA uses fitness as a discriminator of the quality of solutions represented by the chromosomes in a GA population. This implies that the selection component of a GA is designed to use the fitness of a chromosome to guide the evolution of chromosomes by selective pressure. Those with higher fitness have a greater chance of selection than those with lower fitness, thus creating a selective pressure towards more highly fit solutions. Selection is usually with replacement, meaning that highly fit chromosomes have a chance of being selected more than once or even recombined with themselves.

The traditional selection method used is roulette wheel selection. This allocates each chromosome a probability of being selected proportional to its relative fitness, which is its fitness as a proportion of the sum of fitnesses of all chromosomes in the population. If roulette wheel is not fit for the application there are many different selection schemes:

- Random Stochastic Selection - explicitly selects each chromosome a number of times equal to its expectation of being selected under the fitness proportional method.
- Tournament Selection - first selects two chromosomes with uniform probability and then chooses the one with the highest fitness.
- Truncation Selection - simply selects at random from the population having first eliminated a fixed number of the least fit chromosomes.

The typical design for a classical GA using complete replacement with standard genetic operators can be as follows:

1. **Randomly** generate an **initial** source population of P chromosomes.
2. **Calculate** the fitness, $F(c)$, of each chromosome c in the source population.
3. **Create** an empty successor population and then repeat the following steps until P chromosomes have been created.
   (a) Using proportional fitness selection, **select two chromosomes**, c_1 and c_2, from the source population.
   (b) **Apply** one-point **crossover** to c_1 and c_2 with crossover rate p_c to obtain a child chromosome c.
   (c) **Apply** uniform **mutation** to c with mutation rate p_m to produce c
   (d) **Add** c **to** the successor **population**.
4. **Replace** the source population **with the successor population**.
5. If stopping criteria have not been met, **return** to Step 2.

There are limitations in the use of a genetic algorithm compared to alternative optimisation algorithms. Some of these are listed below:

- Finding the optimal solution to complex high-dimensional, multi-modal problems often requires very expensive fitness function evaluations;
- In many problems, GAs may have a tendency to converge towards local optima or even arbitrary points rather than the global optimum of the problem;
- Operating on dynamic data sets is difficult, as genomes begin to converge early on towards solutions which may no longer be valid for later data;
- GAs cannot effectively solve problems in which the only fitness measure is a single right/wrong measure (like decision problems), as there is no way to converge on the solution;

6.2 I2PS variables and dependencies

6.2.1 Constants

Some parameters depend on where the sensor will be installed or whether there are constraints set by manufacturing or by the electronics available. These variables set the general structure and boundary conditions. These constants include the:

1. Geometrical size - Depends on the area of application
2. Bobbin & insulation - Depends on the manufacturer
3. Max supply V/I - Depends on the supply board/source
4. Max Sense Voltage - Depends on the acquisition board selected/available
5. Max number of layers - Depends on the manufacturer
6. Sampling time - Depends on the acquisition system

6.2.2 Variables to be optimised / calculated

The following is a list of all the variables that require calculation and setting. Moreover, the acronyms adopted are listed as well:

1. The Supply Coil Wire Diameter (wire dP). Depends on the sensor's diameter and current carrying capability;
2. The Sense Coil Wire Diameter (wire dS). Depends on the sensor's diameter;
3. The Moving Coil Wire Diameter (wire dC). Depends on the sensor's diameter and resistivity (must be as low as possible);
4. The Number of Layers of the Supply Coil (NLP). Depends on the diameter of the sensor and wire dP;
5. The Number of Layers of the Sense Coil (NLS). Depends on the diameter of the sensor and wire dS;
6. The Number of Layers of the Moving Coil (NLC). Depends on the diameter of the sensor and wire dC;

7. The Number of turns in the Supply Coil (NP). Depends on NLP and wire dP;
8. The Number of turns in the Sense coil (NS). Depends on NLS and wire dS;
9. The Number of turns of the Moving coil (NC). Depends on NLC and wire dC;
10. The Semi-length of the Supply and Sense Coil (ap/as). Depends on the length of sensor; and
11. The Semi-length of the Moving Coil (ac). Depends on the length of sense and supply coils , and sensor's sensitivity.

The NLP, NLS, NLC and ac will impact the output voltage produced, the sensitivity of the sensor and the NLE. In [56], it has been found out that the optimum choice for the coils length would be of:

$$ac \geq 2 \times P_{max}$$

Where P_{max} is the maximum range required / extreme position.

In addition, it has also been shown that the best ratiometric swing is given by:

$$as = ap = ac$$

Hence, the ratiometric swing, the extreme position effects and geometrical constraints impact the coils' lengths. While the diameter of the supply cable can be calculated depending on the supply current/voltage and the diameter of the sense cable can be selected to be the thinnest possible (as this gives very good sensitivity), the diameter of the moving coil needs to be optimised depending on the space required and output. The number of layers for all the coils have been identified to be another three parameters that need to be optimised depending on the output of the sensor. Finally, the length of the supply and sense coil can be set to be the sensor's length left when all bobbins and spacers are subtracted. Additionally, it may be the case as in the current LHC situation that the P_{max} is greater than the size allowed by the sensor's length. Therefore, the ac is the fourth parameter identified to be optimised depending on the output parameters. From this list the three output parameters that are required can also be identified. These three parameters are the output voltage, the NLE and the sensitivity. A minimum and maximum value of each parameter is presented in Table 6.1.

Table 6.1: List of constraints

Constraint	**Value**
Sensor Length	235 mm
Sensor Diameter	26 mm
Moving coil bobbin diameter	4 mm
Bobbin thickness	1.5 mm
Distance between coils	1 mm
Insulation thickness	0.05 mm
Range required	25 mm
Min Range required	18 mm
Max Output Voltage	10 V
Min Output Voltage	8.5 V
Max gain	-100
Min gain	-300
Max Nle	2
Supply Coil wire diameter	0.193 mm
Sense Coil wire diameter	0.045 mm
Moving Coil wire diameter	0.335 mm
Max Supply Coil Number of Layers	5
Min Supply Coil Number of Layers	2
Max Sense Coil Number of Layers	5
Min Sense Coil Number of Layers	1
Max Moving Coil Number of Layers	15
Min Moving Coil Number of Layers	3

In fact, Table 6.1 presents the constraints (which are input to the algorithm for the following tests) for the current I2PS design. As explained in Section 6.2.1 the geometrical constraints of the end application of the sensor limit the size of the sensor. In this case the sensor will be used in the LHC collimator where the size is very important. Furthermore, in this case the sensor will be mainly substituting existing LVDTs. For this reason the sensor length and diameter are set to be 235 mm and 26 mm respectively. Similarly the minimum range of the sensor is defined by the use case which in this application is required to be at least 18 mm. The moving coil bobbin diameter is one of the most important constraints set by the manufacturer. In this sensor the bobbin diameter should be as small as possible, the problem is that to successfully wind with the thick wire required by the moving coil a minimum bobbin diameter of 4 mm is required. Other constraints set by the manufacturer which vary from manufacturer to manufacturer and from design to design is the minimum and maximum number of layers a coil can be wound with.

The supply coil wire diameter is set by the current that is going to be applied and the sense coil wire diameter is restricted by manufacturer's minimum wire that can be wound. There are other constraints set by the manufacturer which effect the space constraints of the sensor, such as the minimum distance between two coils which are side by side which is 1 mm. Another constraint is the minimum thickness of the sense/supply coil bobbin. In this case the minimum possible is used which is 1.5 mm. The thinner the bobbin the less robust the end coil is, but by making it thicker ones important space inside the sensor. Finally, between each coil a thin wrapping of insulation is wound. This is selected to be only 0.05 mm thick but must be considered since it contributes to the overall space constraint.

6.3 Algorithm and Methods Implemented

From Section 6.2, it can be immediately understood that to design an I2PS, a multi-objective optimisation is required [105]. It can also be appreciated and understood that the objectives targeted at this point can be increased to the extent that new objects such as costs can also be considered.

The core of the optimisation of the I2PS revolves around the optimisation of the output parameters produced by the electromagnetic model of the I2PS. The former can be changed by changing the coil structures. A.Danisi showed [56] that the I2PS is highly sensitive to changes in the coil parameters. For this reason the mathematical model of the I2PS is used to calculate the output parameters depending on specific design inputs. Hence, a custom fitness function is built around the mathematical model. The algorithm works by solving the mathematical modelling and assigning the output a fitness value. The fitness value is defined by the following fitness function:

$$Fittness\ function = W_V \hat{f}_1 + W_{NLE} \hat{f}_2 + W_S \hat{f}_3 + W_{ac} \hat{f}_4 \tag{6.7}$$

where: W_V is the weighting of the output voltage, W_{NLE} is the weighting of the NLE, W_S is the weighting of the sensitivity and W_{ac} is the weighting of the moving coil length.

Furthermore,

$$\hat{f}_x = \frac{f_x}{||f_x||}$$

and

$$f_1 = V_{max} - V$$

$$f_2 = |NLE_{min} - NLE|$$

$$f_3 = |Sensitivity_{max} - Sensitivity|$$

$$f_4 = |Theoretical\ coil\ length - moving\ coil\ length|$$

Since each value changes at different speeds, each value is normalised depending on the constraints set by the user. To determine if only one solution exists to a specific sensor design a variable is varied while the remaining variables are kept constant. (In this case, NLP is set to 3, NLS is set to 3, NLC is set to 7 and ac is set to 0.045). Figure 6.2 plots the calculated fitness value against the variable being varied. These fitness are limited by the design requirements presented in Table 6.1. This is done such that an indicative convexity test is performed per variable.

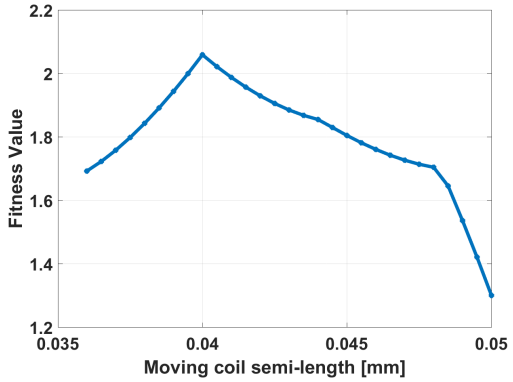

(a) The case where the moving coil semi-length is varied.

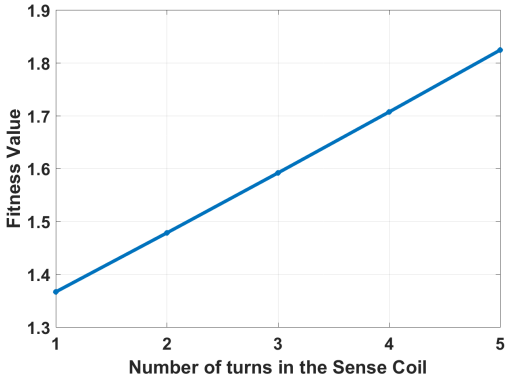

(b) The case where the number of sense coil layers is varied.

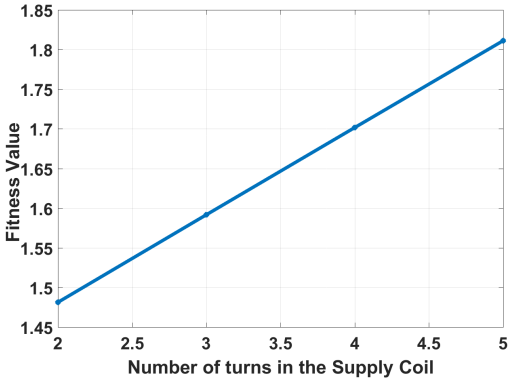

(c) The case where the number of supply coil layers is varied.

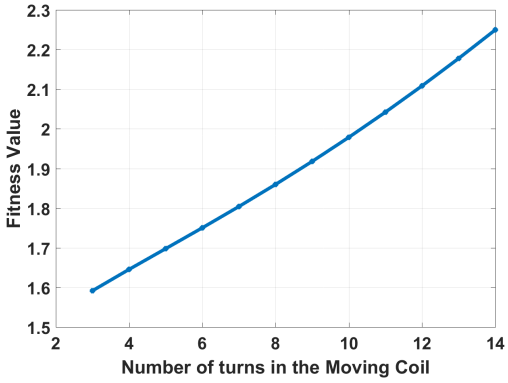

(d) The case where the number of moving coil layers is varied.

Figure 6.2: Convexity test per variable

This test yields results showing convexity however since this test is indicative of convexity it can't be conclusive. A probabilistic algorithm can be used to solve this problem. Traditional methods such as gradient based methods and direct search may not be the optimum method to be selected for this algorithm since they depend heavily on their initial values. Furthermore, since traditional methods are ways how to search (for example using random search or steepest-descent) the speed is low.

The optimisation problem of the I2PS requires a versatile method. A procedure that can work without satisfying mathematical properties such as differentiability, continuity and convexity. Moreover, it requires an algorithm which works well in noisy environments and is able to use a fitness score. A method which is modular, separate from application and which has a concept which is easy to understand and implement. Finally, this problem requires an optimisation method which supports multi-objective problems.

Various multi-objective methods have been identified and studied. It is noted that since the variables of the I2PS are often discrete and the constraints are not explicit, EA are more suitable for this task. In fact, EA [101], are a very popular approach to obtain multiple solutions in a multi-modal optimisation task [102]. Furthermore, an evolutionary algorithm uses a fitness score which is obtained from an objective function, without other derivative or auxiliary information.

Not every multi objective evolutionary algorithm is suitable for this application. One of the ways how this can be resolved is to use a GA method [103, 104, 106–108] which is selected in this case due to the ease of implementation with respect to other methods, such as the normal boundary intersection [109] or the multi-objective Particle Swarm Optimisation (PSO) [110, 111]. Since it is not necessarily the best solution this work will be used to see if this problem can be optimised using such method. Furthermore, genetic algorithms are inherently parallel, and use a parallel search space from random starting points. This provides the ability to avoid being trapped in local optimal solutions. Moreover, multiple additional methods exist which help avoid this problem. In this case, a custom made genetic algorithm is developed which uses chromosomes that are made of real numbers and are of a fixed-length, therefore, they will be real-coded.

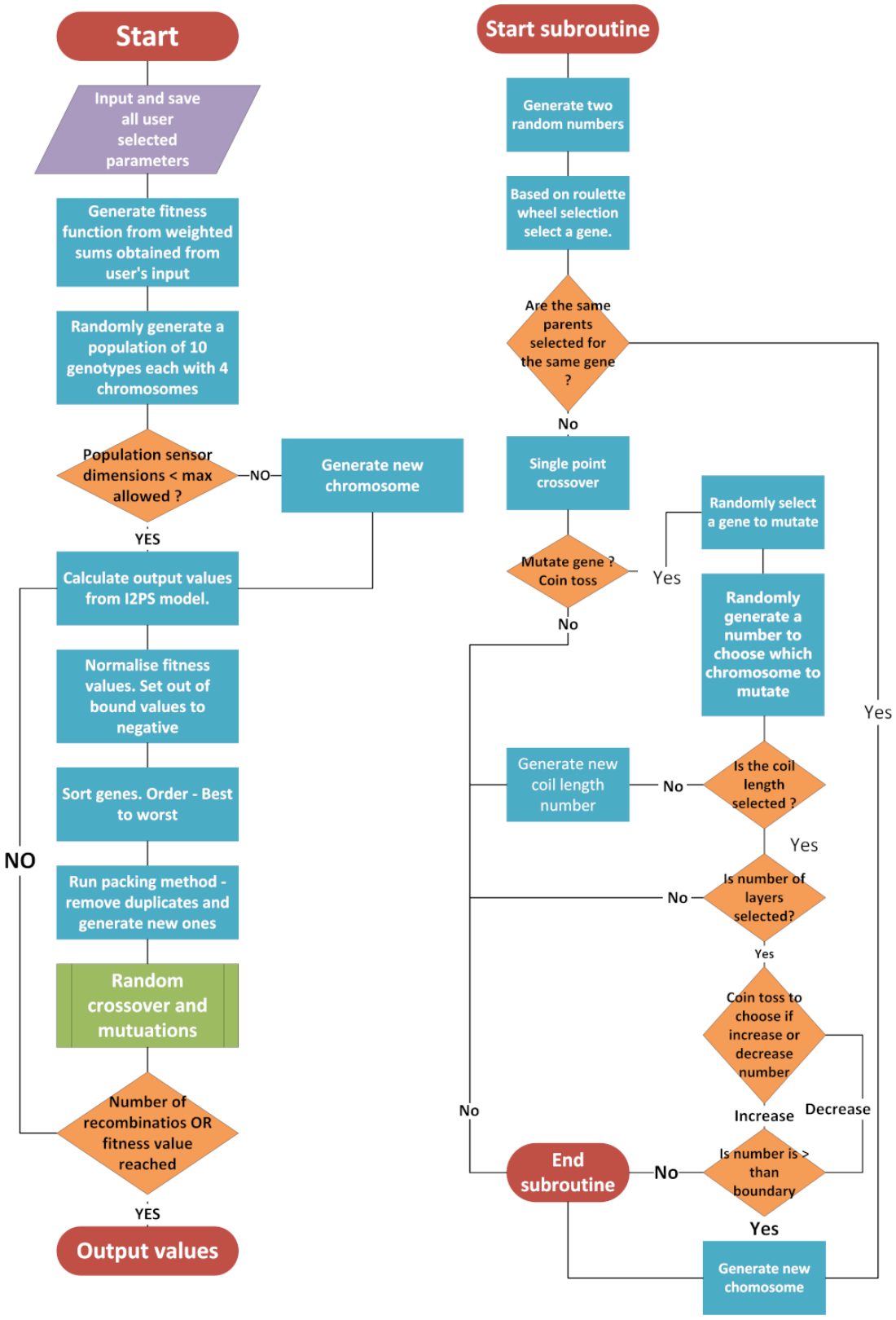

Figure 6.3: The optimisation algorithm

The user is required to select the weighting and, the number of recombinations, whilst also deciding if judgement day protocol is to be put in effect. If the latter is so, then the number of recombination on which judgement day takes place is to be set (judgement day is usually used when a high number of recombinations are set. Therefore, if the number of recombinations is less than ten it cannot be used and it is by default set to half the number of recombinations). At the set number of recombinations all the genes, except the best two, are destroyed and randomly repopulated. This is done to ensure genetic diversity and to avoid local minima. The user is also asked to select if he/she wishes to vary the coil length. The flowchart presented in Figure 6.3 presents a high level description of the algorithm.

During the process the application shows the user the combinations and the progress done so far. Table 6.2 & Figure 6.5 show an example of a generation of values after having their fitnesses assigned and the final fitness calculated. The engine outputs the best two combinations found as well as a list of the top combinations considered along the process. The tool also produces a list of dimension specifications of the sensor for FEM simulation and prototyping. Furthermore, it allows the user to produce the characteristic theoretical curve for the best sensor, to calculate the electrical parameters and it also generates a spice command package to simulate the sensor in spice.

As a test, the tool is run with fifty recombinations and with the judgement day protocol activated. Using the following weighting:

- voltage close to the max - weighting set to 1
- ac close to optimum ac = ap = as - weighting set to 1
- NLE - weighting set to 0.8
- Sensitivity - weighting set to 0.7

Therefore the algorithm is set to maximise the output voltage (in this case set to 10 V) and position range (the moving coil length - ac). Furthermore, the moving coil length is set to stay within ± 10 mm of the nominal value (as found in [28]), which states that all the coils should have the same length. The same input parameters as the manual optimisation method used before are set. This is done such that the manually optimised sensor is taken as a benchmark. Moreover, this same test was repeated multiple times to also test for convergence to the same design parameters.

Figure 6.4 shows the output after a run. The higher the fitness function, the closer the design of the sensor is to reaching the required optimum. A low fitness function means the design combination results in a design that falls outside of the design requirements. From the Figure 6.4, it is also observed that chromosomes six to ten are constantly changing values. This is because they are the freshly generated combinations. On the other hand, the first (1-5) chromosomes are the ones that have the highest fitness value and which is always on the increase. This means that for these chromosomes the design parameters are continuously being improved. The second chromosome is the healthiest one of the group. Furthermore, generations which seem to become similar to the the fittest chromosome, can also be noted. This happens when every parent becomes similar and hence crossover starts to happen with similar combinations. This becomes a repetitive loop and resultantly all individuals start becoming similar and converge towards a possible local maximum. Undoubtedly, this is avoided with the judgement day protocol which destroys all lineage and keeps only the fittest.

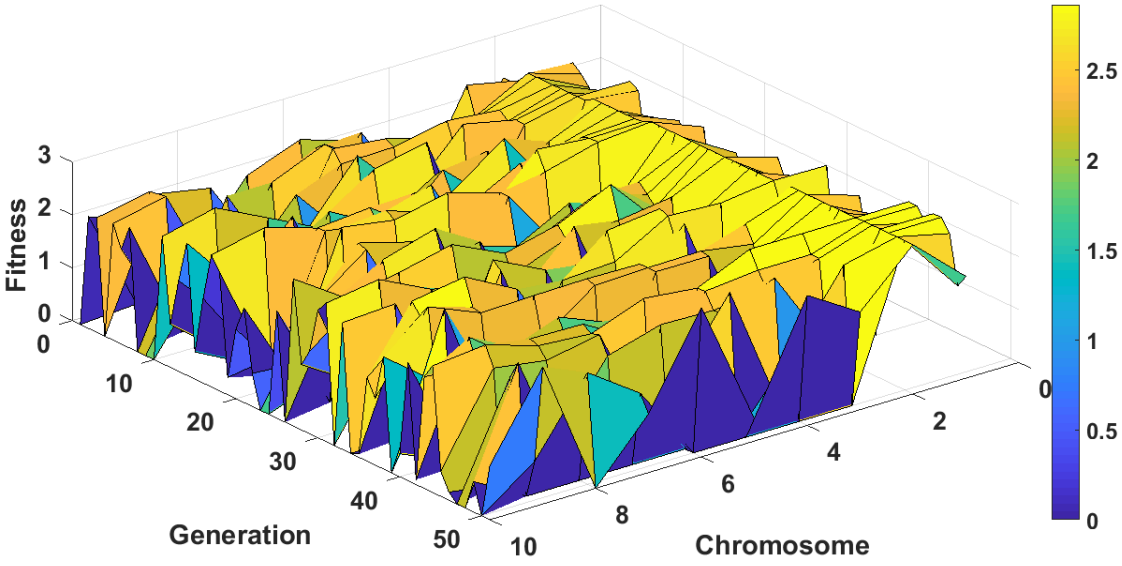

Figure 6.4: 3D plot representing the fitness of each chromosome for each generation

Table 6.2 is an example of a generation. The best fitness drafted in this case had an output voltage close to the nominal, a somewhat good NLE and sensitivity while the moving coil length used is close to the nominal.

Table 6.2: Example of a combination, with input/output values and fitness

№	NLP	NLS	NLC	ac[mm]	V[V]	NLE[%]	Sensitivity	Fitness
1	3	4	12	87.55	9.85	0.53	-217	2.37
2	3	3	14	76.98	8.50	0.725	-201	2.28
3	3	5	5	88.28	6.26	0.41	-304	1.981
4	4	2	13	95.93	7.04	0.26	-215	1.96
5	3	5	4	91.61	5.55	0.32	-329	1.80
6	3	4	4	91.71	4.41	0.33	-326	1.68
7	3	1	11	75.50	2.21	0.75	-218	1.521
8	5	3	10	84.88	10.24	0.59	-230	1.18
9	4	5	7	98.40	10.43	0.32	-279	0.55
10	5	5	10	98.45	17.35	0.33	-244	-6.34
M	4	3	14	90	9.82	0.3	-240	2.24

Figure 6.5 presents a graphical equivalent of Table 6.2. An illustration of how the algorithm is taking a holistic approach is probably seen in the third and fourth values. The third has lower output voltage, and higher NLE, and the sensitivity is less with respect to that of the fourth place. Yet the ac (the moving coil length) is closer to the optimum and hence it is assigned a higher fitness.

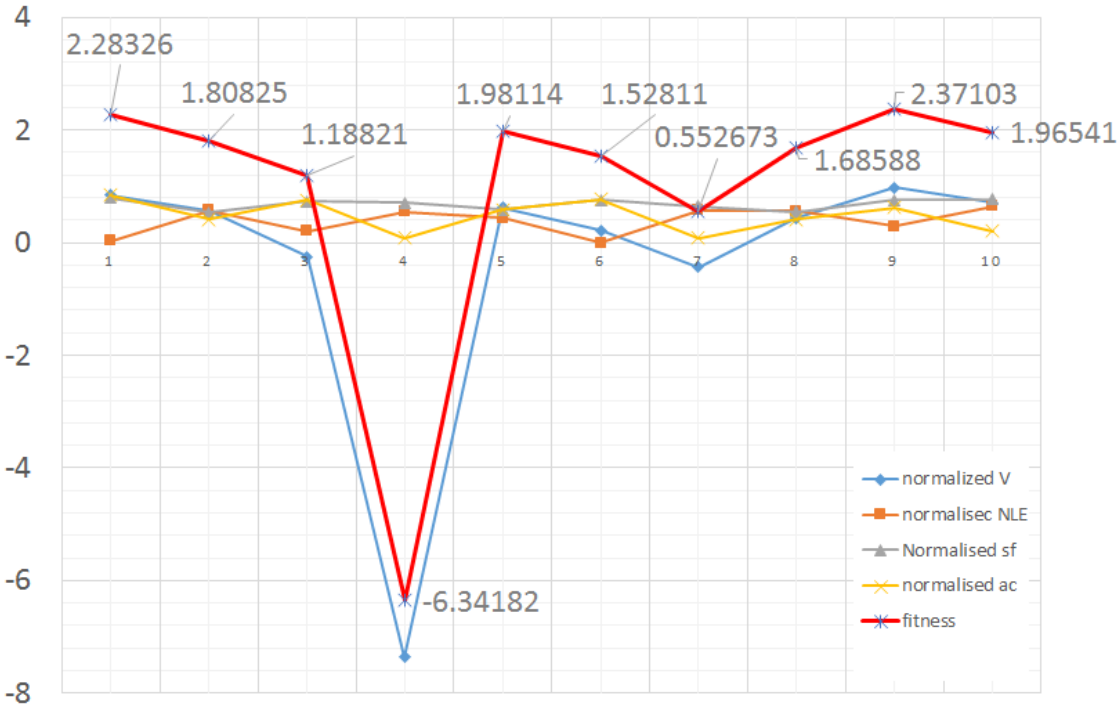

Figure 6.5: Example of a graph showing the normalised fitness of all values to be considered in optimisation and the final fitness value

It can be also be observed how voltage values greater than the maximum value

selected by the user are given low importance. For every value a tolerance is set, for example if the output voltages are greater than $\pm 0.5\ V$ of the specified maximum, their respective fitness value is set to negative. This leads to automatic elimination in the next generation. Finally, comparing the best obtained result, in Table 6.2, with manually optimised sensor (№: M), the number of layers vary but are close.

It is noticed that the number of layers and hence the number of turns for the supply and sense coils are swapped. In reality, from a manufacturing point of view this is better since it is easier to add a uniform layer with a very thin wire than a thicker wire. Similarly, for the number of turns of the moving coil, it is better to limit the number of layers, since this will reduce the inconsistencies in the winding. Moreover, the maximum output voltage is similar which is understandable since the ratio of layers is somewhat kept. Furthermore, this is the value that the design tool has the highest priority to. On the other hand, the non-linearity error and the sensitivity are degraded. This originates from the parameters of the moving coil. Since the moving coil parameters provide a shorter coil with a reduced number of turns the linearity close to the end of the sensor decreases as does the sensitivity.

Finally, curves Figures 6.6 and 6.7 present the characteristic and ratiometric index curves respectively. Since the output voltages and ratiometric are very similar these curves are also very similar with changes happening at the outer ends of the sensor.

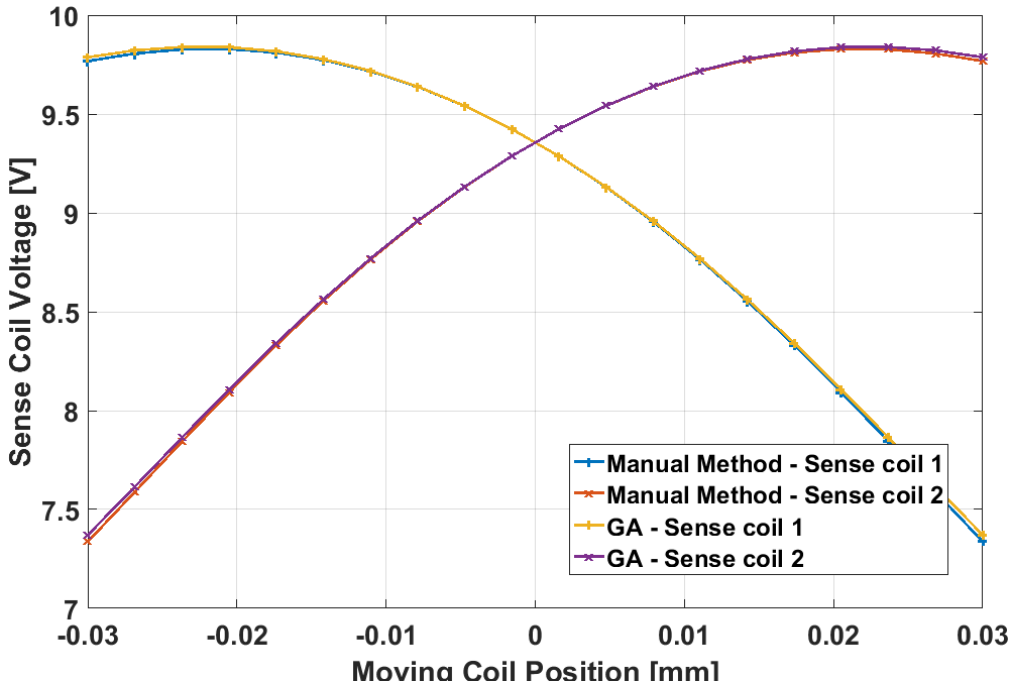

Figure 6.6: Comparison between the characteristic curves of the manual design and the result from the tool.

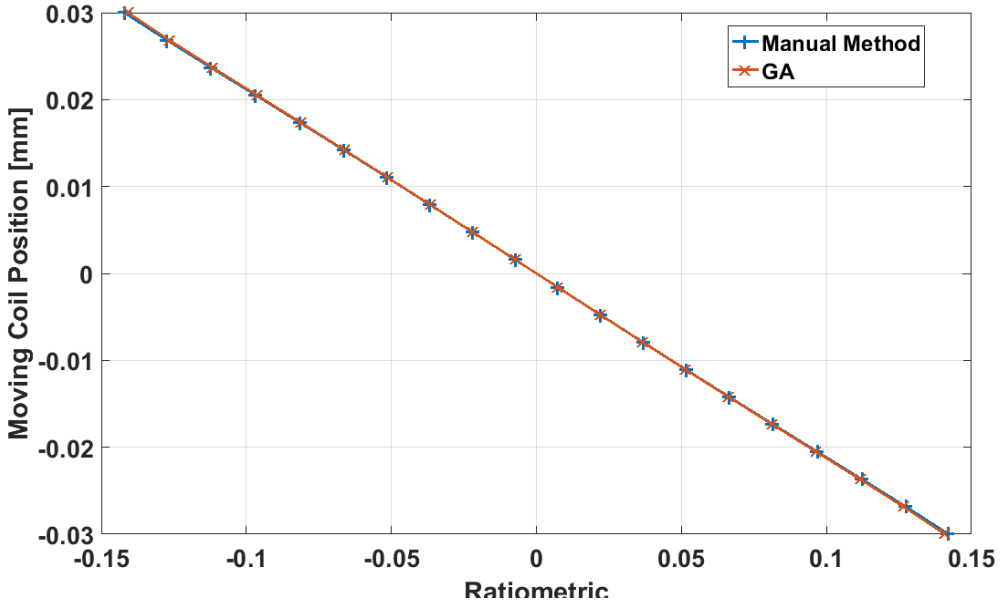

Figure 6.7: Comparison between the ratiometric index curves of the manual design and the result from the tool.

6.4 Summary

This chapter presents a novel weighted multi-objective genetic algorithm that optimises the sensor's parameters with minimal user intervention. The previous manual design procedure involves a long, iterative and manual procedure where the user needs to take all the decisions. The advantage of the new procedure is that through the multi-objective optimisation algorithm, an automated holistic approach is taken when designing the new sensor. This allows all parameters to be optimised at the same time. Furthermore, due to the migration to a generalised programming language, the computational resources required have reduced drastically. The results show that with a small number of re-combinations, i.e. in a short execution time of about twenty minutes, a similar design to the one optimised manually is obtained. Since a very rigorous and lengthy manual design was performed in the past with the manual method, an automated result close to the former is accepted. The value added is a comparable design that can be generated very quickly by a user with minimal training. However, while using a genetic algorithm provided a generic design tool that works well in this case, it may not be the optimal optimisation tool for this procedure. Hence, further work can be conducted to examine other optimisation methods that can be used to find a more appropriate algorithm for this tool.

Chapter 7

Conclusions and Outlook

7.1 Achieved results

The worst-case scenarios for a linear position sensor is to operate in such a wrong state that the interlocks in place from the PRS and the MDC do not recognise the wrong operation. In the case that the sensor drifts outside of the limits specified before operation, the interlocks immediately dump the beam and an investigation is launched. Then, in the case that a collimator's jaws are hit directly by a proton bunch, dangerous beam induced damages occur. These include, but are not limited to, severe damage to the collimator's jaws, magnet quenches and other equipment. The consequence of such a disaster, apart from loss of subsystem hardware and hence the capital required to fix them, would be the consequent downtime of the machine. This study is therefore focused on the improvement of the I2PS from operation-derived problems.

7.1.1 Analysis

Indeed, the position reading of the I2PS is susceptible to a number of external factors. One of these, like many other sensors, is the cable length connecting the sensor to its electronics. In the case of the I2PS this cable supplies and acquires the sensor's signals. No electronics can be close to any sensor installed in the collimator, especially semiconductors, since the radiation causes these devices to fail. As a result, all electronic boards are located hundreds of meters away in electronics rooms. The cables connecting them are multi-pair cables usually bundled together on racks or under false floors in order to be out of the way and reduce space consumption. This work first investigates the impact of these cables on the I2PS. It is noted that, as expected the output voltages are attenuated but it is still high enough for correct reading after proper calibration. Frequency analysis is performed to investigate the impact of the I2PS behaviour with the cable, as well as investigate the frequency range available for the sensor to work in. Up until now it was always considered that the best operating frequency of this sensor is between 1 kHz and it goes up to 2 kHz. It is observed that the frequency range limit is between 500 Hz and 2.75 kHz. This is very important since it provides a wider range of operability. Moreover, this study shows that whilst the sensitivity of the sensor does not vary with cable length, it shows that the cable does change the behaviour of the frequency response. Indeed, the bandwidth and gain decrease as the cable length increases. A comparison with the LVDT shows that the LVDT has a much flatter response and lower susceptibility to change when the moving coil changes. This is because in the case of the LVDT the whole operability depends on the magnetic core.

A SPICE simulation is designed for the I2PS mainly due to the need for a model, which is easy, fast and more flexible than the existing ones. The electromagnetic model is good for the design of new sensors but it is impossible to add electronic components and difficult to model other parasitics. Furthermore, the FEM, while being much more accurate in terms of electromagnetic behaviour and ideal sensor parasitics, it is slow, requires modelling, is more expensive both in terms of capital and in terms of computational resources and is finally much more difficult to simulate additional circuits. However, whilst a SPICE simulation is able to fulfil all the requirements, which these two existing models lack, it is much more difficult to model the electromagnetic part of the sensor. At the end, as presented in this study, a SPICE model in the free modeller LtSpice by LinearTech is developed which uses theoretical mutual inductance and capacitance values for the sensor while it

uses empirical values for the cable parasitics. Additionally, as presented in this study, the floating current supply and the acquisition are also modelled. Overall, the SPICE simulation provides very good results where generally the difference is small and acceptable.

Finally, during operation of the LHC, a flood occurred for a short period of time where the cables used for the I2PS are temporarily submerged in flood water. A position drift is noted and an investigation is launched. Studies show how cables can degrade or develop defects which leave the space in between the multi-pair cables exposed. It is shown that this leads to cable capacitance change in between the cables. While this is statistical in nature, it is very unlikely to be evenly distributed on all the multi-pairs. As a result, this study shows that the I2PS is highly sensitive to a change in this cable capacitance. Using the SPICE simulation, a countermeasure is developed and tested on the same set-up. It is observed that with the countermeasure in place, the sensor's sensitivity to cable capacitance change is reduced by 97%.

The next part of this study focuses on another external factor that influences the transducer's position. This is the thermal drift. Through constant monitoring, it is noted that the sensor exhibits drifts, which can only be associated with temperature. Although these drifts are within the acceptable limits, they are ideally reduced or removed. The commissioning stage of the LHC usually starts in January, just after the shut-down over the Christmas recess, and finishes at around March. During this time, the LHC tunnels are open and climate control is not in a closed loop controlled system. All the devices are tested and calibrated during this time. Various drifts are recognised during the I2PS operation. The shortest are peaks which the dc voltage, read by the sensor, registers but seem to be un-matching and uncompensated when compared with temperature. Longer drifts than the latter were until now, thought to be caused by day-night drifts. These are drifts that cause the position to increase during the day and drop during the night. Then there are longer drifts. These happen during the year where the base position, with respect to the resolver, slowly drifts away during the months, showing the biggest change during the month of August. Ultimately, it slowly drifts back towards the original position. Finally, the last drift noted happens when access to the tunnels is granted during technical stops and the climate control is stopped. Undeniably, all these indicate a strong correlation with ambient temperature.

Consequently, this study has performed a detailed analysis of the sensor's performance when the ambient temperature changes. This in-lab study provides a very important insight in the basic operation of this transducer. First, the transducer is analysed in its basic components and raw values. It is shown that while the change in inductance and resistance of the sense and supply coils impacts the sensors' behaviour in an unbalanced way, it is almost negligible if it is balanced. Moreover, the high sensitivity of the moving coil's parameters to temperature change has been shown. It is also observed that, as expected, the ac voltage of the sense coils changes both with moving coil position as well as with temperature. Moreover, empirical proof is provided that the dc voltage used for the temperature compensation algorithm, dubbed as the primary, is stable with respect to different frequencies, moving coil position and ac voltage. Additionally, the primary voltage swing from room temperature of approximately 20°C to 40°C is recorded. This has led to the first correction to the operation settings. In the past, a constant voltage reference based on calculated values was used for the compensation algorithm. Consequent to these measurements, a new operation standard is adopted which is to obtain and implement the primary voltage at the time of calibration and then calibrate.

The transducer is then analysed in the context of the position with special respect to definition of guidelines or improvements to the current compensation algorithm. Here a number of things are noted. First, the position change due to temperature drift depends on the moving coil position. It is observed that the position drift increases as the moving coil is positioned closer to the transducer's edges. A study of the compensation algorithm shows that the compensation factors do not compensate at all when the position is close to the electrical zero while it either over compensates or under-compensates close to the edges. It is also noted that the position drift changes with frequency as well. This has prompted a temperature study in the frequency range of the I2PS at 250 Hz intervals. The studies indicate that at a particular frequency, the position change is the same for all moving coil positions, and at another frequency, there is little to no position change. In general, the higher the frequency the higher the position change. Furthermore, the compensation factor ζ required to compensate correctly for temperature drift is obtained for different moving coil positions and frequencies. Here it is noted that a variable ζ is mostly required to compensate and not to be regarded as a single value. It is also observed that a big variation is usually required. The study is expanded by analysing the effect of increasing the dc current amplitude, which controls the dc voltage used for the compensation. Here it is observed that as the amplitude of the primary is increased, the compensation factor ζ required is

decreased, as well as the variation of the ζ required to correctly compensate the position change for different frequencies and temperature change. Consequently, a fixed ζ value at certain frequencies is derived and implemented on the collimator test bench.

This work has led to three studies where the first one investigates the effect of changing the material of the moving coil to one that has a lower thermal coefficient. Additionally, operation with a brass core instead of a coil is investigated. It is noted that the sensor still works with satisfactory sensitivity and the linearity of the output voltage is improved. However, it is found that there is no improvement thermally. Other variations include encapsulating the moving coil in a layer of plastic and closing the sensor's sides to add a thermal barrier and reduce air movement. These also lead to negligible improvement with respect to thermal drift.

The second work investigates the impact of operating two or more I2PS close to each other at the same frequency. It is observed that at close distance there is electromagnetic interference between the two. This is because the magnetic flux lines that are produced link together. Eventually, from this study, it is deduced that multiple I2PS can be operated at the same frequency if they are at least 35 cm apart.

Finally, with the knowledge obtained from the thermal analysis until this point, thermal tests are conducted on I2PS installed in a test collimator. These tests show that the collimator's body has local hot spots which lead to a gradient temperature in the sensor's body. The nearby motors are one of the main contributors of heat in the test set-up. In the real collimator, it is expected that the beam interaction with the jaws also generates heat in the collimator body propagating to the sensor. It is also noted that apart from the heat transfer through radiation and convection, the flange holding the sensor conducts a lot of heat from the body. Having said this, the flange is not always in the same position and hence it can create very strange thermal gradients. To make it worse, it is also noted that the moving coil changes temperature when it changes position. Hence, it creates position drifts which are independent of the ambient temperature change and the temperature read by the dc voltage used for the compensation. All of this leads to high temperature drifts which cannot be compensated. As a result, a mechanical solution is developed and tested where the transducer is thermally isolated by the use of a plastic sheath and flange. This leads to a drastic improvement of the sensor's performance.

Having said this, apart from enhancing the transducer in terms of reliability and performance, there is also the need of designing new transducers with different specifications. Not all situations require these particular requirements. There may be circumstances where a longer travel or a thinner sensor is required. The I2PS is designed, tested, and continuously optimised for one specific application. Consequently, it is recognised that the I2PS needs to be further industrialised. The first step taken in this study is to understand and convert all Matlab scripts into a general programming language hence obtaining independence from Matlab. All the variables, constants and constraints are understood and resultantly a procedure for new designs is compiled. During this process, it is realised that the manual approach used to date is slow and requires a well-trained person to be able to design new sensors even with the scripts. This is because each step requires precise modifications to the sensors' parameters. Consequently, a holistic approach is adopted which includes the use of an optimisation algorithm to be able to find the optimum solution. The algorithm is tested with the same input parameters taken when the first sensor was designed. Since the latter was heavily optimised over the years, it can be considered a good baseline to compare the tool's performance. In fact, the tool powered with a genetic algorithm produced a sensor whose characterisation curve and outputs are similar to that of the manually optimised one. Furthermore, the tool's specifications allow for easier manufacturing and hence a cheaper and faster procedure. Finally, the tool produces these results in a short time without any human intervention.

7.1.2 Summary of scientific contributions

The impact that parasitics of long cables have on the I2PS, and hence on the position reading, is understood from the electrical characterisation of the I2PS with long cables. This includes a frequency response characterisation of the I2PS and the development of a novel SPICE simulation which accurately models the I2PS and its phenomenon. Finally, a countermeasure to unbalanced change in the long cable's capacitance is devised.

To fulfil the project descriptions presented in Section 1.2 an extensive thermal characterisation is performed. This leads to a deeper understanding of the sensor's behaviour and the validity of the compensation algorithm. Indeed, a set of guidelines and procedures are defined from this work, namely, the definition of guidelines for correct operation when multiple I2PS, operating at same frequency, are installed in close proximity to each other. Moreover, guidelines on how to set the compensating factors are also defined. Also, alternative moving coil designs for the I2PS are investigated and a solution to temperature drifts, as noted on I2PS installed on the collimators, is developed.

Finally, a general model is obtained and hence a design engine for the manufacturing of optimised I2PS is developed. This engine provides an autonomous algorithm that holistically optimises the sensor's specifications with minimal direct intervention by the user.

7.2 Future Work

The work presented in the previous chapters consist of a detailed study where the ironless inductive position sensor could be optimised, giving the possibility to actually design and operate a transducer according to a particular task. However there are still some other aspects that can be considered for further research.

The application of the counter measure circuit for cable capacitance can be seriously taken into consideration in critical applications, which include long cabling systems that are exposed to environmental conditions. Nonetheless, this study considers only one particular frequency and one specific sensor design. Therefore, it can be applied to be a starting point where a more generalised approach or design procedure is formulated, to be able to apply it for newly designed sensors with different specifications and operating at different frequencies. While the design tool offers a very generic and optimised process further work needs to be done to examine the possible optimisation tools available and understand if the GA was the optimal tool for the task or if another optimisation algorithm is more appropriate. Finally, the design tool can be further enhanced by linking it to finite element modelling software in a closed loop, once the optimised set of specifications are obtained.

Indeed, the extended thermal model and compensation guidelines developed further enhance the stability of the transducer in normal scenarios, where ambient temperature variations happen continuously. The solution tested for the isolation from the collimator's body is a prototype. Further studies can be conducted to assess the material type and thickness needed for a robust shield which isolates the sensor. Additionally, the material needs to be able to withstand a high radiation dose. Of course, this work can be taken as a starting point to further the study in operating in cryogenic conditions.

References

[1] S. Redaelli. (2013) 'LHC Collimation Project'. [Online]. Available: http://lhc-collimation-project.web.cern.ch/lhc-collimation-project/. [Accessed: 10 January 2019].

[2] D. Goldberg, *The Standard Model in a Nutshell*. Princeton University Press, 2017.

[3] G. Elert. (2018) 'The Standard Model'. [Online Book]. Available: physics.info/standard/. [Accessed: 10 January 2019].

[4] CERN Official Website. (2019) 'About CERN'. [Online]. Available: home.cern/about. [Accessed: 10 January 2019].

[5] ATLAS Experiment. (2019) 'The Physics'. [Online]. Available: atlas.cern/discover/physics. [Accessed: 10 January 2019].

[6] R. C. M. Xabier Cid Vidal. (2014) 'The Accelerator Complex'. [Online]. Available: www.lhc-closer.es. [Accessed: 10 January 2019].

[7] S. Myers and E. Picasso, "The lep collider," *Scientific American*, vol. 263, no. 1, pp. 54–61, 1990.

[8] S. Myers and E. Picasso, "The Design, Construction and Commissioning of the CERN Large Electron-Positron Collider," *Contemporary Physics*, vol. 31, no. 6, pp. 387–403, 1990.

[9] G. Aad, J. Butterworth, J. Thion, U. Bratzler, P. Ratoff, R. Nickerson, J. Seixas, I. Grabowska-Bold, F. Meisel, S. Lokwitz *et al.*, "The ATLAS experiment at the CERN large hadron collider," *JINST*, vol. 3, p. S08003, 2008.

[10] K. Aamodt, A. A. Quintana, R. Achenbach, S. Acounis, D. Adamová, C. Adler, M. Aggarwal, F. Agnese, G. A. Rinella, Z. Ahammed *et al.*, "The ALICE experiment at the CERN LHC," *Journal of Instrumentation*, vol. 3, no. 08, p. S08002, 2008.

[11] S. Chatrchyan, E. de Wolf *et al.*, "The CMS experiment at the CERN LHC," *Journal of instrumentation.-Bristol, 2006, currens*, vol. 3, pp. S08 004–1, 2008.

[12] A. A. Alves Jr, L. Andrade Filho, A. Barbosa, I. Bediaga, G. Cernicchiaro, G. Guerrer, H. Lima Jr, A. Machado, J. Magnin, F. Marujo *et al.*, "The LHCb detector at the LHC," *Journal of instrumentation*, vol. 3, no. 08, p. S08005, 2008.

[13] G. Anelli, G. Antchev, P. Aspell, V. Avati, M. Bagliesi, V. Berardi, M. Berretti, V. Boccone, U. Bottigli, M. Bozzo *et al.*, "The totem experiment at the CERN large hadron collider," *Journal of Instrumentation*, vol. 3, no. 08, p. S08007, 2008.

[14] O. Adriani, T. Tamura, M. Bongi, L. Bonechi, Y. Itow, K. Kasahara, S. Torii, J. Velasco, T. Sako, Y. Muraki *et al.*, "Lhcf experiment: Technical design report," CERN, Tech. Rep., 2006.

[15] V. A. Mitsou, M. Collaboration *et al.*, "The MoEDAL experiment at the LHC: status and results," in *Journal of Physics: Conference Series*, vol. 873. IOP Publishing, 2017, p. 012010.

[16] LHC Machine Website. (2015) 'LHC machine outreach'. [Online]. Available: lhc-machine-outreach.web.cern.ch/lhc-machine-outreach/. [Accessed: 10 January 2019].

[17] G. Apollinari, O. Brüning, T. Nakamoto, and L. Rossi, "High luminosity large hadron collider hl-lhc," *arXiv preprint arXiv:1705.08830*, 2017.

[18] G. D'Amen, "Exploiting the ATLAS detector in a search for Stop Squark in a Compressed Mass Spectrum using the Higgs boson," Ph.D. dissertation, Alma Mater Studiorum - Università di Bologna, 2018.

[19] CERN Official Website. (2019) 'Cryogenics: Low temperatures, high performance'. [Online]. Available: https://home.cern/about/engineering/cryogenics-low-temperatures-high-performance. [Accessed: 10 January 2019].

[20] R. Assmann, M. Magistris, O. Aberle, M. Mayer, F. Ruggiero, J. Jiménez, S. Calatroni, A. Ferrari, G. Bellodi, I. Kurochkin *et al.*, "The Final Collimation System for the LHC," CERN, Tech. Rep., 2006.

[21] M. Cauchi, "Thermo-Mechanical Studies of Large Hadron Collider Collimators in Accident Scenarios," Ph.D. dissertation, University of Malta, 2015.

[22] C. Pralavorio, "Record luminosity: well done LHC," *https://home.cern/about/updates/2017/11/record-luminosity-well-done-lhc*, 2017, (Online; Last updated:14-December-2017, Last accessed 19-September-2018).

[23] J. Gillies, "Luminosity? Why don't we just say collision rate?" *https://home.cern/cern-people/opinion/2011/03/luminosity-why-dont-we-just-say-collision-rate*, 2011, (Online; Last updated:23-April-2013, Last accessed 19-September-2018).

[24] L. Rossi and O. Brüning, "High luminosity large hadron collider a description for the european strategy preparatory group," CERN, Tech. Rep., 2012.

[25] M. L. Reyes Alemany and S. Page, "Functional specification of LHC modes," CERN-AB-Note: LHC-OP-ES-0005 rev 1.0, Tech. Rep., 2007.

[26] Santamaria Garcia, Andrea, "Experiment and Machine Protection from Fast Losses caused by Crab Cavities in the High Luminosity LHC," Ph.D. dissertation, École Polytechnique Fdérale de Lausanne, 2018.

[27] R. Assmann, F. Zimmermann, F. Schmidt, and M. Zorzano-Mier, "Equilibrium beam distribution and halo in the LHC," in *Proceedings of EPAC 2002, Paris, France*, 2002.

[28] H. Burkhardt and R. Schmidt, "Intensity and luminosity after beam scraping," CERN-AB-Note-2004-054-ABP, Tech. Rep., 2004.

[29] B. Yee-Rendon, R. Lopez-Fernandez, J. Barranco, R. Calaga, A. Marsili, R. Tomás, F. Zimmermann, and F. Bouly, "Simulations of fast crab cavity failures in the high luminosity Large Hadron Collider," *Physical Review Special Topics-Accelerators and Beams*, vol. 17, no. 5, p. 051001, 2014.

[30] R. Schmidt, "Machine protection," *CERN Yellow Reports: School Proceedings*, vol. 3, p. 447, 2017.

[31] E. B. Holzer, B. Dehning, E. Effinger, J. Emery, G. Ferioli, J. L. Gonzalez, E. Gschwendtner, G. Guaglio, M. Hodgson, D. Kramer *et al.*, "Beam loss

monitoring system for the LHC," in *Nuclear Science Symposium Conference Record, 2005 IEEE*, vol. 2. IEEE, 2005, pp. 1052–1056.

[32] S. Redaelli, "Beam cleaning and collimation systems," *arXiv preprint arXiv:1608.03159*, 2016.

[33] G. A. R. Assmann, O. Aberle *et al.*, "LHC collimation: design and results from prototyping and beam tests," *IEEE Proceedings of the Particle Accelerator Conference, 2005. PAC 2005.*, pp. 1078–1080, 2005.

[34] C. Bracco, "Commissioning Scenarios and Tests for the LHC Collimation system," Ph.D. dissertation, École Polytechnique Fdérale de Lausanne, 2009.

[35] R. Assmann, "Operational experience with LHC collimation," in *Proceedings of PAC09, Vancouver, BC, Canada*, 2009.

[36] R. Assmann, J. Jeanneret, R. Schmidt, J. Wenninger, G. Burtin, M. Hayes, M. Brugger, R. Jung, B. Dehning, D. Kaltchev *et al.*, ""requirements for the lhc collimation system"," CERN, Tech. Rep., 2002.

[37] G. Robert-Demolaize, "Design and performance optimization of the LHC collimation system," Ph.D. dissertation, Universite Joseph Fourier, 2006.

[38] S. Redaelli, R. Losito, R. Assmann, and A. Masi, "Final implementation and performance of the LHC collimator control system," CERN, Tech. Rep., 2009.

[39] A. Danisi, "Simulation of DC interfering magnetic field effects on the LHC collimators' LVDT positioning sensors," *M. Sc., Electronic Engineering Department, University of Naples" Federico II", Naples, Italy*, 2009.

[40] A. Grima, A. Danisi, A. Masi, and N. Sammut, "Influence of External Conductive Objects on the Performance of an Ironless Inductive Position Sensor," *IEEE Sensors Journal*, vol. 17, no. 14, pp. 4500–4507, 2017.

[41] M. Martino, G. Golluccio, R. Losito, and A. Masi, "An analytical model of the effect of external DC magnetic fields on the AC voltages of an LVDT," in *Instrumentation and Measurement Technology Conference (I2MTC), 2010 IEEE*. IEEE, 2010, pp. 213–218.

[42] A. Masi, A. Danisi, R. Losito, M. Martino, and G. Spiezia, "Study of magnetic interference on an LVDT: FEM modeling and experimental measurements," *Journal of Sensors*, vol. 2011, 2011.

[43] M. Martino, A. Danisi, R. Losito, A. Masi, and G. Spiezia, "Design of a linear variable differential transformer with high rejection to external interfering magnetic field," *IEEE Transactions on Magnetics*, vol. 46, no. 2, pp. 674–677, 2010.

[44] A. Bertarelli, O. Aberle, M. Mayer, R. Perret, P. Sievers, E. Chiaveri, R. Assmann, and T. Kurtyka, "The mechanical design for the LHC collimators," CERN, Tech. Rep., 2004.

[45] J. J. Fuller and E. Marotta, "Thermal contact conductance of metal/polymer joints: an analytical and experimental investigation," *Journal of Thermophysics and Heat Transfer*, vol. 15, no. 2, pp. 228–238, 2001.

[46] R. Ostojic and P. Proudlock, "New Machine Layout in IR3 and IR7," CERN, Tech. Rep. LHC-LJ-EC-0002, 2004.

[47] A. Masi and R. Losito, "LHC collimators low level control system," in *Real-Time Conference, 2007 15th IEEE-NPSS*. IEEE, 2007, pp. 1–8.

[48] J. Serrano, P. Alvarez Sanchez, J. Lewis, and D. Dominguez, "Nanosecond level UTC timing generation and stamping in CERN's LHC," in *ICALEPCS*, 2007.

[49] R. W. Assmann, S. Redaelli, M. Lamont, and M. Jonker, "Application software for the LHC collimators and movable elements," CERN, LHC-TCT-ES-0001 rev 1.0, Tech. Rep., 2007.

[50] A. Masi, R. Losito, and S. Redaelli, "Measured performance of the LHC collimator low-level control system," *Proc. ICALEPCS09, Kobe, Japan*, 2009.

[51] M. Arruat, L. Fernandez, S. Jackson, F. Locci, J.-L. Nougaret, M. Peryt, A. Radeva, M. Sobczak, and M. V. Eynden, "Front-end software architecture," in *ICALEPCS*, vol. 7, 2007, p. 310.

[52] A. Masi, A. Brielmann, R. Losito, and M. Martino, "LVDT conditioning on the LHC collimators," *IEEE Transactions on Nuclear Science*, vol. 55, no. 1, pp. 67–75, 2008.

[53] A. Masi, A. Danisi, M. Di Castro, and R. Losito, "Real-time high-precision reading algorithm for the Ironless Inductive Position Sensor," *IEEE Transactions on Nuclear Science*, vol. 60, no. 5, pp. 3661–3668, 2013.

[54] TE connectivity. (2017) 'LVDT Tutorial'. [White Paper]. Available: https://www.te.com/global-en/industries/sensor-solutions/insights/lvdt-tutorial.html. [Accessed: 10 January 2019].

[55] W. contributors. (2018) 'Linear Variable Differential Transformer'. [Online]. Available: https://en.wikipedia.org/wiki/Linear_variable_differential_transformer. [Accessed: 10 January 2019].

[56] A. Danisi, "Ironless Inductive Position Sensor for Harsh Magnetic Environments," Ph.D. dissertation, EPFL, 2013.

[57] Nyce, David S, *Linear position sensors: theory and application*. John Wiley & Sons, 2004.

[58] Martino, M and Losito, R and Masi, A, "Analytical metrological characterization of the three-parameter sine fit algorithm," *ISA transactions*, vol. 51, no. 2, pp. 262–270, 2012.

[59] Wu, Shang-Teh and Hong, Jyun-Lang, "Five-point amplitude estimation of sinusoidal signals: With application to LVDT signal conditioning," *IEEE Transactions on Instrumentation and Measurement*, vol. 59, no. 3, pp. 623–630, 2010.

[60] Bertocco, Matteo and Narduzzi, Claudio, "Sine-fit versus discrete Fourier transform-based algorithms in SNR testing of waveform digitizers," *IEEE transactions on Instrumentation and Measurement*, vol. 46, no. 2, pp. 445–448, 1997.

[61] A. Masi, A. Danisi, R. Losito, M. Martino, and G. Spiezia, "Study of magnetic interference on a LVDT prototype," *IEEE Trans. Instrum. Meas.*, vol. 60, pp. 219–223, 2010.

[62] R. Wolf and W. Delsolaro, "Magnets Pre-Cycle for LHC Operation," CERN, Geneva, Switzerland, Tech. Rep., 2009.

[63] A. Danisi, A. Masi, and R. Losito, "Performance Analysis of the Ironless Inductive Position Sensor in the Large Hadron Collider Collimators Environment," *Sensors*, vol. 15, no. 11, pp. 28 592–28 602, 2015.

[64] M. Lamberti, R. Losito, M. Martino, and A. Masi, "Reduction of Magnetic Interference on the Position Sensors of the LHC Collimators," in *Conf. Proc.*, vol. 110904,IPAC-2011-TUPS039, 2011, pp. 1623–1625.

[65] H. Mandal, S. K. Bera, S. Saha, P. K. Sadhu, and S. C. Bera, "Study of a Modified LVDT Type Displacement Transducer with Unlimited Range," *IEEE Sensors Journal*, 2018.

[66] J. M. Maurio, C. C. McCarthy, and M. Mulhern, "Linear positioning system utilizing helically polarized magnet," Jun. 6 2017, uS Patent 9,671,472.

[67] J. Fraden, *Handbook of modern sensors: physics, designs, and applications*. Springer Science & Business Media, 2004.

[68] Y. Kim and H. Y. Choi, "Development of High-Temperature Position Sensors for Control of Actuators in Aerospace Systems," in *2018 9th International Conference on Mechanical and Aerospace Engineering (ICMAE)*. IEEE, 2018, pp. 6–10.

[69] B. Hufenbach, S. Habinc, and P. Vuillenmier, "Space applications for smart sensors," in *Keynote lecture, Proceed. Eurosensors XIII, 13th European Conf. On Solid-St. Transducers, den Haag, Holland*, 1999, pp. 3–6.

[70] L. K. Baxter, "Capacitive sensors," *Ann Arbor*, vol. 1001, p. 48109, 2000.

[71] E. Dimovasili, A. Herty, H. M. Durand, A. Marin, F. Ossart, and T. Wijnands, "Radiation induced effects on the sensors of the hydrostatic leveling system for the lhc low beta quadrupoles," in *Radiation and Its Effects on Components and Systems, 2005. RADECS 2005. 8th European Conference on*. IEEE, 2005, pp. PH2–1.

[72] Y.-J. Rao, "Recent progress in fiber-optic extrinsic fabry–perot interferometric sensors," *Optical Fiber Technology*, vol. 12, no. 3, pp. 227–237, 2006.

[73] X. Zhou and Q. Yu, "Wide-range displacement sensor based on fiber-optic fabry–perot interferometer for subnanometer measurement," *IEEE sensors journal*, vol. 11, no. 7, pp. 1602–1606, 2011.

[74] H. Eren, "Inductive displacement sensors," *The Measurement, Instrumentation and Sensors Handbook*, pp. 6–26, 1999.

[75] C. Mandel, B. Kubina, M. Schüßler, and R. Jakoby, "Passive chipless wireless sensor for two-dimensional displacement measurement," in *Microwave Conference (EuMC), 2011 41st European*. IEEE, 2011, pp. 79–82.

[76] L. W. Hobbs, F. W. Clinard Jr, S. J. Zinkle, and R. C. Ewing, "Radiation effects in ceramics," *Journal of Nuclear Materials*, vol. 216, pp. 291–321, 1994.

[77] A. Danisi, A. Masi, R. Losito, and Y. Perriard, "Design optimization of an Ironless Inductive Position Sensor for the LHC collimators," *Journal of Instrumentation*, vol. 8, no. 09, p. P09005, 2013.

[78] A. Danisi, A. Masi, R. Losito, and Y. Perriard, "Electromagnetic model of an Ironless Inductive Position Sensor," in *Instrumentation and Measurement Technology Conference (I2MTC), 2012 IEEE International*. IEEE, 2012, pp. 69–74.

[79] A. Danisi, A. Masi, R. Losito, and Y. Perriard, "Modeling and compensation of thermal effects on an Ironless Inductive Position Sensor," *IEEE Transactions on Industry Applications*, vol. 50, no. 1, pp. 375–382, 2014.

[80] A. Danisi, R. Losito, A. Masi and Y. Perriard, "Modeling of high-frequency electromagnetic effects on an ironless inductive position sensor," *IEEE Sensors Journal*, vol. 13, no. 12, pp. 4663–4670, 2013.

[81] A. Danisi, A. Masi, R. Losito, and Y. Perriard, "Electromagnetic analysis and validation of an Ironless Inductive Position Sensor," *IEEE Transactions on Instrumentation and Measurement*, vol. 62, no. 5, pp. 1267–1275, 2013.

[82] A. Masi, A. Danisi, R. Losito, and Y. Perriard, "Characterization of magnetic immunity of an Ironless Inductive Position Sensor," *IEEE Sensors Journal*, vol. 13, no. 3, pp. 941–948, 2013.

[83] L. Sabato, "Modelling parasitic capacitances effects on ironless inductive position sensor," *MSc Thesis. Universita degli studi del Sannio*, 2013.

[84] S. Troisi, "Modelling conductive shield effects in an ironless inductive position sensor," *MSc Thesis. Universita degli studi del Sannio*, 2012.

[85] C. Akyel, S. Babic, and S. Kincic, "New and fast procedures for calculating the mutual inductance of coaxial circular coils (circular coil-disk coil)," *IEEE Transactions on Magnetics*, vol. 38, no. 5, pp. 2367–2369, 2002.

[86] A. Danisi, A. Masi, R. Losito, and L. Sabato, "Modeling of moving coil capacitance in an Ironless Inductive Position Sensor," in *SENSORS, 2013 IEEE*. IEEE, 2013, pp. 1–4.

[87] A. Grima, M. Di Castro, A. Masi, and N. Sammut, "Experimental Thermal Characterisation of an Ironless Inductive Position Sensor," *Case Studies in Thermal Engineering*, Submitted for publication.

[88] National Instruments, *'NI 6143 Specifications'*, [Online]. Available: http://www.ni.com/pdf/manuals/370835a.pdf, 2004, [Accessed: 10 January 2019].

[89] E. Fraga, C. Prados, and D.-X. Chen, "Practical model and calculation of ac resistance of long solenoids," *IEEE Transactions on Magnetics*, vol. 34, no. 1, pp. 205–212, 1998.

[90] D. G. Johnson, *Solid State Tesla Coil*. Kansas State University, 2001, ch. 1, [Online Book]. Available: http://www.ece.k-state.edu/people/faculty/gjohnson/files/tcchap1.pdf [Accessed: 10 January 2019].

[91] J. Groszkowski, "The temperature coefficient of inductance," *Proceedings of the Institute of Radio Engineers*, vol. 25, no. 4, pp. 448–464, 1937.

[92] A. Grima, M. Di Castro, A. Masi, and N. Sammut, "Frequency response characterization of ironless inductive position sensors with long cables," *MATEC Web Conf. - Elsevier*, vol. 208, p. 03007, 2018.

[93] J. Sylculslci, E. Sykulska, and S. Hughes, "Application of finite element modelling in lvdt design," *COMPEL-The international journal for computation and mathematics in electrical and electronic engineering*, vol. 11, no. 1, pp. 73–76, 1992.

[94] M. Krízek and P. Neittaanmäki, *Mathematical and numerical modelling in electrical engineering theory and applications*. Springer Science & Business Media, 2013, vol. 1.

[95] W. contributors. (2018) 'Orders of magnitude (magnetic field)'. [Online]. Available: en.wikipedia.org/wiki/Orders_of_magnitude_(magnetic_field). [Accessed: 10 January 2019].

[96] A. Grima, M. Di Castro, A. Masi, and N. Sammut, "Design Enhancements of an Ironless Inductive Position Sensor," *IEEE Transactions on Instrumentation and Measurement*, Submitted for publication.

[97] P. Ripka, *Magnetic Sensors and Magnetometers*. Artech House, 2001.

[98] A. Grima, M. Di Castro, A. Masi, and N. Sammut, "Thermal Study of the Ironless inductive Position Sensor Installed on the LHC collimators," *IEEE Transactions in Nuclear Science*, Submitted for publication.

[99] Weise,Thomas, "Global optimization algorithms-theory and application," *Self-Published*, 2009.

[100] R. K. Arora, *Optimization: algorithms and applications*. Chapman and Hall/CRC, 2015.

[101] E. Zitzler and L. Thiele, "An evolutionary algorithm for multiobjective optimization: The strength pareto approach," *TIK-report*, vol. 43, 1998.

[102] Wikipedia Contributors. (2018) 'Mathematical Optimization'. [Online]. Available: https://en.wikipedia.org/wiki/Mathematical_optimization. [Accessed: 10 January 2019].

[103] McCall, John, "Genetic algorithms for modelling and optimisation," *Journal of Computational and Applied Mathematics*, vol. 184, no. 1, pp. 205–222, 2005.

[104] The Wikipedia Contributors. (2018) 'Genetic Algorithm'. [Online]. Available: https://en.wikipedia.org/wiki/Genetic_algorithm. [Accessed: 10 January 2019].

[105] A. Grima, M. Di Castro, A. Masi, and N. Sammut, "A Novel Holistic Design Optimisation Algorithm for the Ironless Inductive Position Sensor," *International Journal of Computer and Electrical Engineering*, vol. Vol 10, 2018.

[106] M. S. Circiu and F. Leon, "Comparative Study of Multiobjective Genetic Algorithms," *Buletinul Institutului Politehnic din Iaşi*, 2010.

[107] M. Mitchell, *An introduction to genetic algorithms*. MIT press, 1998.

[108] M. Gen and R. Cheng, *Genetic algorithms and engineering optimization*. John Wiley & Sons, 2000, vol. 7.

[109] I. Das and J. E. Dennis, "Normal-boundary intersection: A new method for generating the Pareto surface in nonlinear multicriteria optimization problems," *SIAM Journal on Optimization*, vol. 8, no. 3, pp. 631–657, 1998.

[110] J. Kennedy, "Particle swarm optimization," in *Encyclopedia of machine learning*. Springer, 2011, pp. 760–766.

[111] G.-c. Chen and J.-s. Yu, "Particle swarm optimization algorithm," *INFORMATION AND CONTROL-SHENYANG-*, vol. 34, no. 3, p. 318, 2005.

[112] L. Evans, "The large hadron collider," *New Journal of Physics*, vol. 9, no. 9, p. 335, 2007.

[113] O. Brüning, *Large Hadron Collider Design Report*. European Organization for Nuclear Research, 2004, vol. 1.

[114] K. Francis, "Results of beam tests of a prototype calorimeter for a Linear Collider," Ph.D. dissertation, Northern Illinois University, 2010.

[115] R. Assmann, R. Schmidt, O. Aberle, M. Mayer, F. Ruggiero, D. Schulte, O. S. Brüning, S. Calatroni, A. Ferrari, L. Bruno *et al.*, "An Improved Collimation System for the LHC," CERN, LHC Project Report 773, Tech. Rep., 2004.

[116] Massarini, Antonio and Kazimierczuk, Marian K, "Self-capacitance of inductors," *IEEE Transactions on Power Electronics*, vol. 12, no. 4, pp. 671–676, 1997.

[117] Spiezia, Giovanni and Losito, Roberto and Martino, Michele and Masi, Alessandro and Pierno, Antonio, "Automatic test bench for measurement of magnetic interference on LVDTs," *IEEE Transactions on Instrumentation and Measurement*, vol. 60, no. 5, pp. 1802–1810, 2011.

[118] S. J. Shah, "Field wiring and noise considerations for analog signals," *National Instruments-Application Note*, vol. 25, pp. 1–26, 1992.

[119] V. Wallder, "Polyethylene for wire and cable," *Electrical Engineering*, vol. 71, no. 1, pp. 59–64, 1952.

[120] Y. Deflandre, M. Hoffman, and G. Cyr, "Impedance compensation for a cable and connector," Mar. 12 2002, uS Patent 6,356,162.

[121] Hartlein, R and Hampton, N and Hernández, JC and Perkel, J, "Overview of cable system diagnostic technologies and application," *The National Electric Energy Testing Research and Applications Center (NEETRAC), Cable Diagnostic Focus Initiative Project (CDFI)*, no. 04-211, 2006.

[122] Fruth, B and Niemeyer, L, "The importance of statistical characteristics of partial discharge data," *IEEE Transactions on Electrical Insulation*, vol. 27, no. 1, pp. 60–69, 1992.

[123] Dissado, Len A and Fothergill, John C, *Electrical degradation and breakdown in polymers*. IET, 1992, vol. 9.

[124] S. Wang and F. C. Lee, "Analysis and applications of parasitic capacitance cancellation techniques for EMI suppression," *IEEE Transactions on Industrial Electronics*, vol. 57, no. 9, pp. 3109–3117, 2010.

[125] Sammut, Nicholas J and Benedico-Mora, Eva and Bottura, Luca and Galbraith, Peter and Giloteaux, David and Greco, Gabriele and Haverkamp, Markus and Marchesotti, Marco and Masi, Alessandro and Micallef, Joseph

and others, "A Hall Plate Based Instrument to Measure the Snapback in the Large Hadron Collider Superconducting Dipole Magnets," in *2006 IEEE Instrumentation and Measurement Technology Conference Proceedings*. IEEE, 2006, pp. 61–66.

[126] Lackner, Friedrich and Riegler, Werner and Osanna, P and Durakbasa, M, "High precision strain gauge based sensor for monitoring suspension forces at CERN," *Measurement Science Review*, vol. 8, no. 2, pp. 46–49, 2008.

[127] Karmjit Sidhu, "Position/Presence/Proximity Understanding Linear Position Sensing Technologies," *Sensors Online*, 2012, December 2016.

[128] Colonel Em. T. McLyman, *Winding Capacitance an Leakage Inductance*. Marcel Dekker, Inc., 2004, ch. 17, pp. 1–100.

[129] Burkes, Klaehn W and Makram, Elham B and Hadidi, Ramtin, "Water Tree Detection in Underground Cables Using Time Domain Reflectometry," *IEEE Power and Energy Technology Systems Journal*, vol. 2, no. 2, pp. 53–62, 2015.

[130] Chen, Qi and Burkes, Klaehn and Makram, Elham and Hadidi, Ramtin and Xu, Xufeng and others, "Capacitance of Water Tree Modeling in Underground Cables," *Journal of Power and Energy Engineering*, vol. 2, no. 11, p. 9, 2014.

[131] GanGuPomu, Ajay, "Multi-Winding Model with Direct Extraction of Parameters from Voltage Measurments," Master Dissertation, University of Florida, 2003.

[132] Helwig, Sabine and Branke, Jurgen and Mostaghim, Sanaz, "Experimental analysis of bound handling techniques in particle swarm optimization," *Evolutionary Computation, IEEE Transactions on*, vol. 17, no. 2, pp. 259–271, 2013.

[133] Engelbrecht, Andries, "Particle swarm optimization: Velocity initialization," in *Evolutionary Computation (CEC), 2012 IEEE Congress on*. IEEE, 2012, pp. 1–8.

[134] Rocha, Miguel and Neves, José", "Preventing premature convergence to local optima in genetic algorithms via random offspring generation," in *Multiple Approaches to Intelligent Systems*. Springer, 1999, pp. 127–136.

[135] Kureichick, V and Melikhov, AN and Miagkikh, VV and Savelev, OV and Topchy, AP, "Some new features in genetic solution of the travelling salesman

problem," in *Adaptive Computing in Engineering Design and Control*, vol. 96, 1996.

[136] Tom Peterson, Fermilab, "Magnet Quench," http://www.symmetrymagazine.org/article/november-2008/explain-it-in-60-seconds-magnet-quench, [Online; accessed 8 July 2015].

[137] CERN Official Website. (2019) 'Experiments'. [Online]. Available: home.cern/science/experiments. [Accessed: 10 January 2019].

[138] CERN Official Website. (2019) 'Applications of CERN Technologies in Society'. [Online]. Available: kt.cern/cern-technologies-society. [Accessed: 10 January 2019].

[139] Emily Baumgaertner. (2018) '3-D Color X-Rays Could Help Spot Deadly Disease Without Surgery'. [Online Article]. Available: https://www.nytimes.com/2018/07/17/health/3d-color-xrays-cern.html?rref=collection%2Ftimestopic%2FCERN. The New York Times. [Accessed: 10 January 2019].

[140] Wikipedia Contributors. (2018) 'Particle Swarm Optimization'. [Online]. Available: en.wikipedia.org/wiki/Particle_swarm_optimization. [Accessed: 10 January 2019].

[141] Robert Miller. 'Linear Position Sensor'. [Online]. Available: http://www.futureelectronics.com/en/sensors/linear-position.aspx.

[142] National Instruments, *'NI 6143 Specifications'*, [Online]. Available: http://www.ni.com/pdf/manuals/370835a.pdf, 2004, [Accessed: 10 January 2019].

[143] J. R. Matlack. (2016) 'LVIT Technology. What is it and where does it fit into the sensor world'. [White Paper]. Available: http://www.engineeringnews.co.za/article/lvit-technology—what-is-it-and-where-does-it-fit-into-the-sensor-world-2016-03-04. [Accessed: 10 January 2019].

[144] M. Engelhardt, "Using Transformers in LTspice/SwitcherCAD III," Linear Technology Magazine - Design Ideas, Tech. Rep., 2006.

[145] Jude Fischer, "Measuring Self Resonant Frequency," Coilcraft Inc, Tech. Rep. Document 363-3, 2003.

[146] A. Grima, M. Di Castro, A. Masi, and N. Sammut, "Electrical Metrological Characterization of Ironless Inductive Position Sensors with Long Cables," *IEEE Sensors Journal*, vol. 18, no. 17, pp. 7114–7121, 2018.

[147] ——, "Behaviour of Ironless Inductive Position Sensors in Close Proximity to Each Other," *IEEE Transactions on Industry Applications*, Submitted for publication.